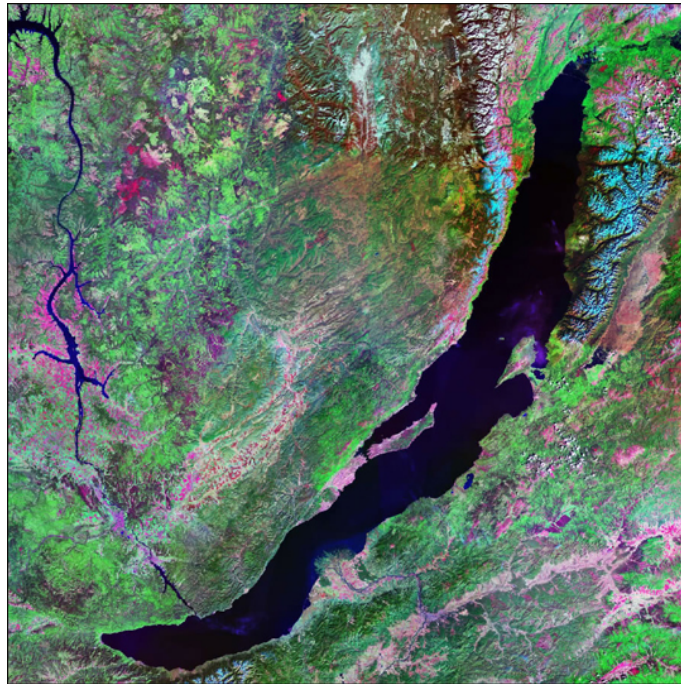


# **Deep ventilation in Lake Baikal: a simplified model for a complex natural phenomenon.**

Sebastiano Piccolroaz



UNIVERSITÀ DEGLI STUDI DI TRENTO

Dipartimento di Ingegneria Civile,  
Ambientale e Meccanica

2013

Doctoral thesis in **Environmental Engineering** (XXV cycle)

Department of Civil, Environmental and Mechanical Engineering, **University of Trento**

Year: **2013**

Supervisor: **Dr. Marco Toffolon**

On the cover: Lake Baikal from space. *Source: <http://consciouslifestylesradioblog.com>*

Università degli Studi di Trento, Italy

Trento, Italy

2013



*A te che stai per nascere.*

21 febbraio 2013

*From all directions  
winds bring petals of cherry  
into the grebe lake.*

(Matsuo Bashō, 1644-1694)



**Abstract -** *Lake Baikal (Southern Siberia) is the world's oldest, deepest and largest freshwater body by volume. In spite of its enormous depth, episodically (i.e. almost twice a year) large volumes of surface, cold and oxygenated water sink towards the bottom of the lake. This phenomenon is known as deep ventilation and determines the periodical, partial renewal of deep water, playing a key role in the ecology of the whole lacustrine system. Despite deep ventilation has been widely observed, still significant uncertainties exist about the detailed characterization of deep downwellings.*

*In order to tackle this issue, a simplified, one-dimensional numerical model has been developed, which allows for a suitable simulation of deep ventilation in profound lakes. Three main algorithms are at the basis of the model: a reaction-diffusion equation for temperature and other tracers (e.g. dissolved oxygen), and two Lagrangian algorithms, the first to handle buoyancy-driven convection due to density instability (including thermobaric effects) and the other to reproduce the deep downwelling mechanism. Thanks to its simple structure, such a model ensures a considerable computational speed that makes it suitable to perform long-term simulations (i.e. decades, centuries). At the same time, it has been shown to be appropriate for quantitatively and qualitatively simulating deep ventilation, well capturing the relative contribution of the different processes involved.*

*The model has been applied to investigate deep ventilation in the South Basin of Lake Baikal. The numerical results have been shown to be in good agreement with observed data (concerning temperature, CFC-12 and dissolved oxygen profiles), indicating a proper performance of the core algorithms. The analysis of results allowed for a detailed description of the major mixing and thermal dynamics of the lake, and for an in-depth characterization of deep water renewal (e.g. typical downwelling temperatures and volumes, vertical distribution of sinking water, energy balance). Numerical simulations have been performed under current conditions and climate change scenarios, thus permitting to assess the future behavior of the lake and the possible impact on deep ventilation, in response to the expected evolution of climate.*

*In addition to the main results discussed above, this study provided some additional outcomes: a simplified lumped model to convert air temperature into surface water temperature of lakes, and a novel downscaling procedure to transform meteorological data (i.e. wind speed and air temperature) from the global scale to the lake scale.*

*In the light of the proven performance of the deep ventilation model, further improvements of the model could bring to the development of a suitable module to simulate biogeochemical processes in the lake, thus providing valuable information to assess the role of deep ventilation in affecting the lake ecosystem.*



# Contents

<b>1</b>	<b>Introduction</b>	<b>1</b>
<b>2</b>	<b>Lake Baikal and deep ventilation</b>	<b>5</b>
2.1	Lake Baikal . . . . .	7
2.1.1	Geography and Morphology . . . . .	7
2.1.2	Climate . . . . .	9
2.1.3	Ice Conditions . . . . .	12
2.1.4	Biodiversity of Lake Baikal . . . . .	13
2.2	Deep ventilation . . . . .	14
2.2.1	Physical properties of water and thermobaricity . . . . .	15
2.2.2	Local stability . . . . .	17
2.2.3	Thermal regime . . . . .	20
2.2.4	Thermobaric instability . . . . .	22
2.2.5	Vertical diffusivity . . . . .	25
<b>3</b>	<b>A simplified 1D model for the numerical simulation of deep ventilation</b>	<b>29</b>
3.1	Background and state of the art . . . . .	31
3.2	Formulation of the model . . . . .	32
3.2.1	Reaction-diffusion equation solver . . . . .	33
3.2.2	Stability algorithm . . . . .	35
3.2.3	Downwelling algorithm . . . . .	37
3.2.4	Wind-based parameterization . . . . .	39
3.3	External forcing and internal dynamics . . . . .	41
3.3.1	Initial conditions, boundary conditions and reaction terms . . . . .	42
3.3.2	Reconstruction of external forcing . . . . .	43
3.4	Diapycnal diffusivity derivation . . . . .	46
3.4.1	Richardson number-based schemes . . . . .	46
3.4.2	Shear frequency . . . . .	47

Contents

3.4.3	Dynamical reconstruction of the diffusivity profile . . . . .	49
3.5	Concluding remarks . . . . .	51
<b>4</b>	<b>A simple lumped model to convert air temperature into surface water temperature in lakes</b>	<b>53</b>
4.1	Introduction . . . . .	55
4.2	The heat budget of lakes . . . . .	57
4.3	Formulation of the model . . . . .	60
4.3.1	A simplified heat budget scheme . . . . .	60
4.3.2	A suitable parameterization of the epilimnion thickness . . . . .	61
4.3.3	Definition of the parameters . . . . .	62
4.4	Study site . . . . .	64
4.5	Sensitivity analysis and model calibration . . . . .	66
4.5.1	8-parameter model . . . . .	68
4.5.2	From 8 to 4 parameters . . . . .	71
4.6	Model validation . . . . .	73
4.7	Discussion . . . . .	74
4.8	Concluding remarks . . . . .	79
<b>5</b>	<b>Available datasets and data processing</b>	<b>81</b>
5.1	An overview of available data . . . . .	83
5.1.1	Measurements and observations . . . . .	84
5.1.2	Re-analysis dataset . . . . .	90
5.1.3	Future climate projections . . . . .	91
5.2	Data processing . . . . .	92
5.2.1	Present conditions . . . . .	93
5.2.2	Future scenarios . . . . .	96
5.3	Concluding remarks . . . . .	105
<b>6</b>	<b>Results: deep ventilation under different climatic conditions</b>	<b>109</b>
6.1	Model calibration and validation . . . . .	111
6.1.1	Medium-term simulations . . . . .	112
6.1.2	Long-term simulations . . . . .	116
6.1.3	Sensitivity analysis . . . . .	119
6.2	Current climate conditions . . . . .	121
6.2.1	Seasonal dynamics . . . . .	123
6.2.2	In-depth analysis of deep ventilation . . . . .	132



6.3	Climate change projections . . . . .	140
6.3.1	Vertical profiles . . . . .	140
6.3.2	Downwelling characterization . . . . .	143
6.3.3	Effect of wind intensity and seasonality . . . . .	148
6.4	Concluding remarks . . . . .	150
<b>7</b>	<b>Conclusions and future developments</b>	<b>153</b>
	<b>Acknowledgments</b>	<b>159</b>
	<b>Bibliography</b>	<b>161</b>

*Contents*

## List of Figures

2.1	Bathymetric map of Lake Baikal, and its location on the globe. . . . .	8
2.2	Cross sections of Lake Baikal. . . . .	9
2.3	3D bathymetry and topography of Lake Baikal. . . . .	10
2.4	Ice cover on Lake Baika. . . . .	13
2.5	Some of the endemic animal species of Lake Baikal: an amphipod, Baikal oilfish (golomyanka) and Baikal seal (nerpa). . . . .	14
2.6	Schematic representation of deep ventilation. . . . .	16
2.7	Conditions for local stability. . . . .	19
2.8	Typical winter and summer temperature profiles measured at the South Basin. . . . .	21
2.9	Possible types of thermobaric instability in deep dimictic lakes. . . . .	24
2.10	Seasonal evolution of the depth of the mesothermal maximum. . . . .	26
2.11	Vertical diffusivity profiles estimated by <i>Ravens et al.</i> [2000] and <i>Wüest et al.</i> [2005].	27
3.1	Hypsometric curve of the South Basin of Lake Baikal. . . . .	34
3.2	Staggered grid used to solve the reaction-diffusion equation. . . . .	35
3.3	Sketch for the stability evaluation procedure. . . . .	37
3.4	Schematic representation of the parameters used to describe the energy transferred by the wind to the surface layers of the lake. . . . .	40
3.5	Vertical variation of the geothermal heat flux and vertical profile of oxygen consumption rate. . . . .	43
3.6	Diapycnal diffusivity as a function of the local Richardson number. . . . .	48
3.7	Reference diffusivity profile, $D_{z,r}$ , compared with the profiles estimated by <i>Ravens et al.</i> [2000] and <i>Wüest et al.</i> [2005]. . . . .	51
4.1	Schematic of the main heat fluxes affecting the surface layer. . . . .	58
4.2	Schematic of the seasonal evolution of the dimensionless thickness $\delta$ . . . . .	63
4.3	Lake Superior with the location of the gauging stations used in this work. . . . .	65

List of Figures

4.4	Dotty plots of efficiency indexes ( $E$ ) for the 8-parameters model during the calibration period 1985-2002. . . . .	69
4.5	Comparison between simulated and observed (buoy station) surface water temperature during the calibration period 1985-2002. . . . .	69
4.6	Dotty plots of efficiency indexes ( $E$ ) for the 4-parameters model during the calibration period 1985-2002. . . . .	73
4.7	Comparison between simulated and observed surface water temperature during the validation period 2003-2011 (NDBC simulation). . . . .	74
4.8	Evolution of the dimensionless depth $\delta$ over the period 2003-2011. . . . .	75
4.9	Comparison between simulated and observed surface water temperature during the calibration period 1994-2005 (GLERL simulation). . . . .	76
4.10	Comparison between simulated and observed surface water temperature during the validation period 2006-2011 (GLERL simulation). . . . .	77
4.11	Comparison of the hysteresis cycles between air and surface water temperatures, as derived by the data and by the 8- and 4-parameters versions of the model. . . . .	78
5.1	Seasonal cycle of the surface water temperature. . . . .	85
5.2	Seasonal distributions of wind speed and duration. . . . .	87
5.3	<i>CFC-12</i> vertical profiles and surface boundary condition. . . . .	88
5.4	Vertical profiles of dissolved oxygen concentration (from the literature). . . . .	89
5.5	Comparison between the ECMWF ERA-40 re-analysis and the historical CNRM-CM5 datasets. . . . .	91
5.6	Graphical illustration of quantile-mapping downscaling procedure. . . . .	95
5.7	Curves used for the downscaling of wind speed, under climate change. . . . .	98
5.8	Graphical illustration of the procedure used for the downscaling of wind speed, under climate change. . . . .	99
5.9	Future projections of air temperature for the different climate scenarios. . . . .	101
5.10	Mean annual cycles of air and surface water temperature. . . . .	102
5.11	Comparison of the hysteresis cycles between air and surface water temperatures, as derived by the data and by the temperature conversion model. . . . .	102
5.12	Future projections of surface water temperature for the different climate scenarios. . . . .	103
6.1	Comparison of simulated <i>CFC-12</i> profiles with measured data during the period from 1988 to 1996. . . . .	112
6.2	Overall evolution of <i>CFC-12</i> concentrations from 1958 to 1998. . . . .	113
6.3	Comparison of simulated temperature profiles with measured data, for the 40-years simulation ranging from 1988 to 1996. . . . .	114

6.4	Time evolution of deep water temperature, from 1958 to 2002. . . . .	115
6.5	Comparison of simulated <i>DO</i> profile with measured data, for the 40-years simulation.	116
6.6	Long-term evolution of deep water temperature (averaged values beneath 1000 <i>m</i> depth), for a 1000-year simulation. . . . .	117
6.7	Comparison of simulated temperature profile and measured data, for a 1000-year simulation starting from an isothermal profile at $T = 3.98^{\circ}\text{C}$ . . . . .	118
6.8	Comparison of simulated <i>DO</i> profile with measured data, for a 1000-year simulation starting from an anoxic profile, $DO = 0\text{mgO}_2\text{ l}^{-1}$ . . . . .	119
6.9	Mean annual cycle of model calculated vertical temperature profiles. . . . .	120
6.10	Mean annual cycle of measured vertical temperature profiles. . . . .	120
6.11	Map of residuals between the mean annual cycles of modeled and measured temperature profiles. . . . .	121
6.12	Sensitivity analysis on the temperature profile for a 40-year simulation. . . . .	122
6.13	Sensitivity analysis on the <i>CFC-12</i> profile for a 40-year simulation. . . . .	123
6.14	Mean annual cycle of temperature profile, <i>T</i> , within the hypolimnion (beneath 500 <i>m</i> depth). . . . .	124
6.15	Mean annual cycle of dissolved oxygen concentration profile, <i>DO</i> . . . . .	125
6.16	Mean annual cycle of the squared Brunt-Väisälä buoyancy frequency, $N^2$ . . . . .	127
6.17	Mean annual cycle of the squared shear frequency, $S^2$ . . . . .	128
6.18	Mean annual cycle of the Richardson number, <i>Ri</i> . . . . .	128
6.19	Mean annual cycle of the diapycnal diffusivity profile, $D, z$ . . . . .	129
6.20	Mean annual cycle of the diapycnal diffusivity profile, $D_z$ , within the uppermost 400 <i>m</i> . . . . .	130
6.21	Typical diapycnal diffusivity profiles in different periods of the year. . . . .	131
6.22	Annual evolution of the thickness of the epilimnion. . . . .	132
6.23	Typical timing of deep downwellings throughout the year. . . . .	133
6.24	Vertical distribution of downwellings along the water column. . . . .	134
6.25	Boxplots of mean annual sinking volume and mean annual downwelling temperature.	136
6.26	Relationship between downwelling temperature ( $T_d$ ) and the energy per unit volume required to reach the compensation depth ( $e_c$ ). . . . .	137
6.27	Relationship between temperature profile and the energy per unit volume required to move surface water to the compensation depth: warm season. . . . .	138
6.28	Relationship between temperature profile and the energy per unit volume required to move surface water to the compensation depth: cold season. . . . .	139
6.29	Winter and summer temperature profiles simulated under different climate scenario.	141
6.30	Mean annual dissolved oxygen profiles simulated under different climate scenario.	143

*List of Figures*

6.31	Evolution of the annual cumulative energy input provided by the wind, during the 21 <sup>st</sup> century. . . . .	145
6.32	Schematic representation of the main physical processes and their interactions controlling transport and mixing in the lake. . . . .	147
6.33	Correction functions associated to the different scenarios. . . . .	150

# List of Tables

3.1	Boundary conditions and reaction term for temperature, dissolved oxygen and <i>CFC</i> concentration . . . . .	42
4.1	Summary of the datasets adopted and their main statistics. . . . .	70
4.2	Estimated model parameters and efficiency indexes during calibration and validation periods. . . . .	70
5.1	Summary of the available datasets of water temperature, $T_w$ , air temperature, $T_a$ , and wind speed, $W$ . . . . .	84
5.2	Expected increase of surface water temperature for the future periods and scenarios.	105
5.3	Characteristic properties of surface water under current conditions, and for future periods and different scenarios. . . . .	105
5.4	Guidelines for the interpretation of Figures 5.7 - 5.9 and 5.12 in this section, and figures in Section 6. . . . .	105
6.1	Calibrated values of the model parameters. . . . .	112
6.2	Different sets of parameters used in the sensitivity analysis. . . . .	122
6.3	Comparison between numerical results and literature estimations of the main parameters characterizing deep ventilation in Lake Baikal. . . . .	135
6.4	Main parameters characterizing deep ventilation the different scenarios and current conditions. . . . .	145

*List of Tables*



# 1 Introduction

Transport and mixing phenomena are among the most important physical processes that regulate chemical and biological dynamics in lacustrine systems [Imboden and Wüest, 1995]. These processes are mainly driven by the combination of turbulent diffusion and convection, which, in turn, are strictly interlinked with the intrinsic properties of the water body (e.g. diffusivity, thermal structure, stratification, geometric features) and are primarily controlled by the external conditions (e.g. wind action, surface/bottom heat exchange, river inflow/outflow). Depending on the particular features of each lake, the dynamics that regulate the transfer of mass, momentum and energy within the water body can be different, giving rise to the existence of a wide variety of peculiar, sometimes singular, natural phenomena. These phenomena are often complex, due to the strong interactions between the various physical processes that take place in lakes. For these reasons, an in-depth investigation of their main causes and consequences can be difficult and not always straightforward. Generally, comprehensive three-dimensional numerical models are able to reproduce the overall circulation pattern of lakes, thus possibly providing valuable insight into the understanding of these phenomena. Notwithstanding, for a proper implementation of such type of models a large amount of data is usually required both as input and for model calibration and validation. Since sufficient information are often not available, especially for large basins located in scarcely monitored regions, a valid alternative is the use of physically-based, simplified models able to capture the major processes of interest and their mutual interactions. The development of reliable simplified models to investigate complex phenomena in natural aquatic systems is a great challenge, which also represents the major concern of the present work.

This study focuses on the investigation of the phenomenon of deep ventilation in Lake Baikal, the oldest ( $\sim 25$  millions years), deepest (max depth  $1\,642\text{ m}$ ) and most voluminous ( $23\,615\text{ km}^3$ ) lake in the world. Lake Baikal is a large, temperate lake located in the Southern Siberia, which contains about the 20% of the world's unfrozen freshwater reserve and is the habitat of many limnic animals and plants species, most of them endemic [Martin, 1994; Timoshkin, 1997; Bondarenko *et al.*, 2006; Moore *et al.*, 2009]. Thanks to the unique ecosystem that has been evolved during millions of years and adapted to singular, sometimes extreme, conditions, Lake Baikal was declared an UNESCO World Heritage Site in 1996. Besides it is world-wide known for its astonishing

ecosystem, numerous outstanding physical phenomena occur within this massive lake, which captured the attention of the scientific research community. Concerning hydro-thermodynamic phenomena, several field observations and measurements have been conducted [e.g. *Weiss et al.*, 1991; *Shimaraev et al.*, 1993; *Hohmann et al.*, 1997; *Ravens et al.*, 2000; *Wüest et al.*, 2000, 2005; *Schmid et al.*, 2008; *Shimaraev et al.*, 2009, 2011a,b, 2012], and many mathematical and numerical studies have been performed [e.g. *Killworth et al.*, 1996; *Tsvetova*, 1999; *Peeters et al.*, 2000; *Botte and Kay*, 2002; *Lawrence et al.*, 2002].

Deep ventilation (often referred to as deep water renewal or deep downwelling), is certainly the most famous and widely investigated physical process. This phenomenon consists in a large scale, turbulent convective mixing capable of renewing profound water by replacing and mixing it with colder and more oxygenated surface water. Indeed, in spite of its enormous depth and the fact that the seasonal convective mixing is limited to the uppermost part of the water column, periodically (i.e. nearly twice a year) large volumes of surface water sink towards the bottom of the lake.

Numerous are the consequences on the physical, chemical and biological properties, among which the most evident is the high oxygen content (up to the 80% of saturation [*Weiss et al.*, 1991]) along the entire water column, which allows for the existence of aquatic fauna down to huge depths. Thermobaric instability, which is due to the combined dependence of water thermal expansion on temperature and pressure (i.e. thermobaricity [*McDougall*, 1987]), has been identified as the mechanism responsible for the periodical deep downwellings [*Weiss et al.*, 1991]. This kind of instability is likely to occur when the lake is inversely stratified (i.e. temperature increases with depth), if surface water is displaced downwards to a critical depth where it becomes conditionally unstable. Different hypothesis have been proposed to explain the causes at the basis of thermobaric instability, wind-induced vertical mixing being the most probable and accepted [*Weiss et al.*, 1991; *Killworth et al.*, 1996; *Botte and Kay*, 2002; *Wüest et al.*, 2005; *Schmid et al.*, 2008].

Deep intrusions of cold water have been regularly observed [e.g. *Weiss et al.*, 1991; *Peeters et al.*, 2000; *Wüest et al.*, 2005; *Schmid et al.*, 2008; *Shimaraev et al.*, 2011a,b], especially in the South Basin of the lake. Notwithstanding, some degree of uncertainty still exists in evaluating the extension of deep downwelling volumes, which is confirmed by the wide range of estimates proposed in the literature [*Peeters et al.*, 2000; *Wüest et al.*, 2005; *Schmid et al.*, 2008; *Shimaraev et al.*, 2011a]. One of the main difficulties in properly investigating and characterizing deep ventilation of Lake Baikal is represented by the limited availability of measurements and observations. As a matter of fact, due to the impressive dimension of the lake and the fact that it is located in a very remote region, much of the basin is unmonitored and only a few datasets are available. These data present significant spatial and/or temporal resolution limitations, which are one of the major obstacles to their effective use.

The general aim of this study is to characterize deep ventilation in detail and describe the typical mixing and thermal regimes of Lake Baikal, both under current and projected climate conditions. In order to achieve this main objective, a simplified, one-dimensional numerical model has been developed, which is able to properly simulate deep ventilation in profound lakes. The model has been developed with a simple computational structure in order to perform long-term simulations (hundreds of years), requiring a low computational cost. At the same time, it has been designed to deal with a limited amount of information, according to the few available measurements.

The model is used here to investigate deep ventilation of Lake Baikal, but in principle it could represent a suitable tool to study the mixing dynamics of other very deep lakes in the world.

Beyond the introductory remarks, the thesis is organized into the following chapters.

In Chapter 2 a general description of Lake Baikal is provided. The first part is devoted to a brief overview concerning the geography and morphology, the regional climate, the surface ice conditions and the aquatic ecosystem of the lake. In the second part of the chapter, the main physical processes occurring in the lake are described, with particular emphasis on thermobaric instability and deep ventilation.

The simplified, one-dimensional model to simulate deep ventilation in profound lakes is presented and discussed in Chapter 3: the mathematical model is formulated, describing the core algorithms and the specific parameterizations that have been included.

Chapter 4 is devoted to the presentation of a simplified, physically-based model to estimate surface water temperature based on air temperature only. The model has been applied to the case of Lake Superior, for which long-term datasets of air and water temperature are available. The model is used in Chapter 5 to estimate surface water temperature of Lake Baikal under future climate change scenarios.

Chapter 5 focuses on the description, analysis and processing of the available data. In particular, a large portion of the chapter is devoted to the downscaling of available re-analysis data and future climate projections from their coarse spatial resolution to a more suitable lake scale. In this regard, a novel downscaling procedure has been developed which is suitable for the downscaling of climate change scenarios.

Results are presented in Chapter 6. Besides the calibration of the main parameters of the model, the chapter focuses on the description of the numerical results concerning the behavior of the lake under current and expected climate conditions. Numerical results allowed for a detailed description of the actual mixing regime and thermal dynamics of the lake (e.g. seasonality of temperature and diffusivity profiles), and for a statistical characterization of deep ventilation (e.g. mean annual downwelling volume and temperature, deep ventilation timing). Furthermore, the impact that climate change is likely to have on deep water renewal and on the general behavior of the lacustrine

## 1. Introduction

---

system is analyzed.

Finally, concluding remarks are addressed in Chapter 7.

A detailed introduction is given at the beginning of each individual chapter.

## 2 Lake Baikal and deep ventilation

**Abstract** - *Lake Baikal is located in the Southern Siberia and is famous for being the world's oldest, deepest and largest freshwater basin in terms of volume. It contains about the 20% of the world's unfrozen freshwater reserve, roughly equivalent to the water volume in the Great Lakes taken all together, which are 8 times more extended than the Siberian lake. Despite its enormous depth, the lake's waters are well-mixed and well-oxygenated throughout the entire water column, with dissolved concentrations up to the 80% of saturation. This feature, together with the singular, sometimes extreme, environmental conditions (e.g. the enormous depth, several months of ice cover, high water clarity, low nutrient concentrations) gave rise to a unique ecosystem and an astonishing aquatic environment, which earned it to be declared as a World Heritage Site by UNESCO in 1996.*

*The high oxygen concentration and the intense mixing observed along the entire water column are determined by a periodic renewal of deep water. Indeed, large volumes of superficial, cold and oxygenated water regularly (i.e. nearly twice a year) sink to the bottom of the lake, mixing and replacing hypolimnetic water. This peculiar phenomenon is known as deep ventilation or deep water renewal, and is caused by deep downwellings due to thermobaric instability. Thermobaricity is the coupled dependence of water density on temperature and pressure, thus acquires fundamental importance in very profound lakes, as is the case of Lake Baikal.*

*This chapter is structured in two main parts. In Section 2.1 Lake Baikal is presented, and its main characteristics and features are described: geography and morphology, regional climate, surface ice conditions and aquatic ecosystem. The second part, Section 2.2, is devoted to the characterization of the thermal regime of the lake and to the description of the physical processes occurring in its waters, with particular emphasis on thermobaric instability and deep ventilation.*

## 2. Lake Baikal and deep ventilation

---

## 2.1 Lake Baikal

### 2.1.1 Geography and Morphology

Lake Baikal is situated almost in the center of the Asian continent (Siberia), in the foothills of the East Sayan Mountains, 455.5 m above the sea level (Figure 2.1). It lies in the Baikal Rift Zone, the largest active continental rift system in Eurasia [Lesne *et al.*, 1998]. Lake Baikal is the world's oldest ( $25 \times 10^6$  years), deepest (1642 m) and largest ( $23615 \text{ km}^3$ ) freshwater body in terms of volume [The INTAS Project 99-1669 Team, 2002]. The freshwater basin runs from North-East to South-West for about 650 km, between  $51^\circ 28'$  and  $55^\circ 47'$  N and  $103^\circ 43'$  and  $109^\circ 58'$  E. The average width of the Baikal depression is about 49.3 km, with a maximum of 81 km in its central part, and a narrowing of 27 km in front of the Selenga River [Shimaraev *et al.*, 1994]. The length of the shoreline is about 1 800 km, and there are 22 islands with a total area of  $716 \text{ km}^2$  [Shimaraev *et al.*, 1994], the largest being Olkhon Island with a surface area of about  $700 \text{ km}^2$ .

Lake Baikal receives every year  $60 \text{ km}^3$  of water from more than 300 tributaries [Bradbury *et al.*, 1994], which drain an immense catchment area of about  $540000 \text{ km}^2$ . The Selenga River provides more than 50 % of tributary inflow, thus representing the most important tributary river of the lake, while the Angara River is the only river flowing out of Lake Baikal, at its southernmost end (see Figure 2.2).

Two submerged sills divide the lake into three sub-basins of similar size (see Figure 2.2): the South Basin (SB, max depth 1 461 m), the Central Basin (CB, max depth 1 642 m) and North Basin (NB, max depth 904 m). The average depths of the two sills are 300 – 400 m (see Figure 2.2), thus direct inter-basin exchange of water masses beneath this depth are excluded [Shimaraev *et al.*, 1994; Peeters *et al.*, 2000]. The South Basin stretches from the southern end of the lake to the Selenga River delta, where the bottom of the lake is higher than the adjacent parts (the Selenga Shallows). The middle cavity is located between the Selenga River and the north sill (the Academician Ridge), which extends from the Olkhon Island north-eastwards towards the Ushkanyi islands archipelago. The North Basin stretches from the Ushkanyi islands archipelago to the northern end of the lake. The separation of the lake in three sub-basins is clearly visible in the bathymetry (see Figures 2.1, 2.2 and 2.3).

The lake is completely surrounded by mountains (see Figure 2.3). Two coastal mountain belts, the Baikalskii and Primorskii, border the west coast of the lake, with benchmark elevations ranging from 700 to 1 500 m, and from 1 500 to 2 500 m, respectively. In the east, coastal plains separate the shore from the Barguzinskii, Ulan-Burgasy, and Khamar-Daban mountain ranges. The underwater part of the basin reflects the surrounding topography, resulting in an asymmetric bathymetry: the western shore is characterized by a steep border faults (slope up to  $60^\circ$ , average  $30 - 35^\circ$ , Shimaraev *et al.* [1994]) and the shallow water platform is not developed, while the eastern side is more gently

## 2. Lake Baikal and deep ventilation

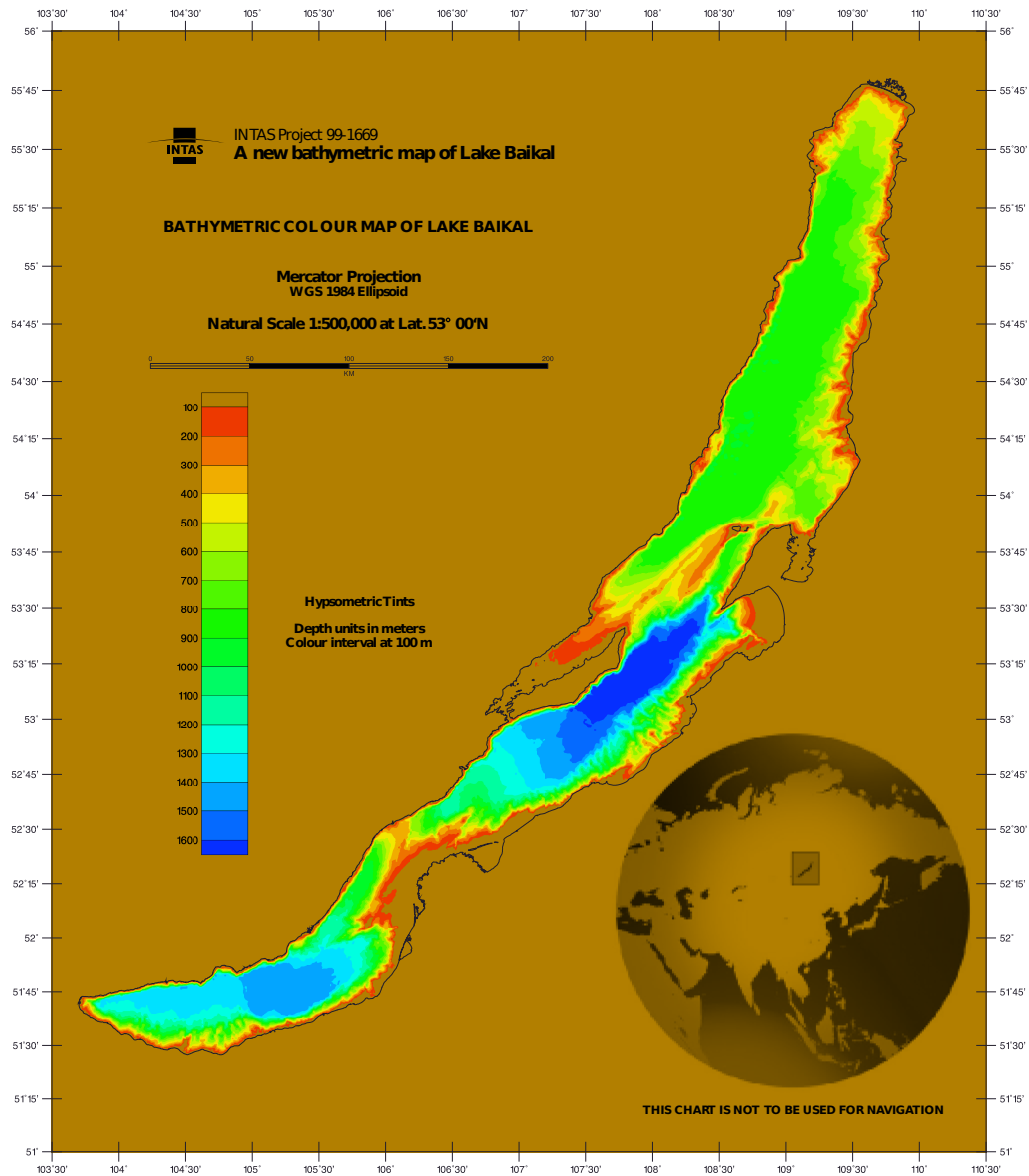


Figure 2.1: Bathymetric map of Lake Baikal, and its location on the globe (modified from *The INTAS Project 99-1669 Team* [2002]).

sloping (average slope of about  $7 - 10^\circ$ ) and the coastal shelf on it is much more greatly developed [Galaziya, 1993] (see Figures 2.2 and 2.3). The bottom of the lake is a vast underwater plain, with a little incline westwards where the maximum depths of the lake are localized. Thanks to the very steep sides and the flat bottom, the average depth of Lake Baikal is about 744 m.

Beneath its bottom, the Baikal depression is filled with a large volume of sediments. The typical thickness of the sediments layer has been estimated as equal to about 7 km [e.g. Hutchinson *et al.*,



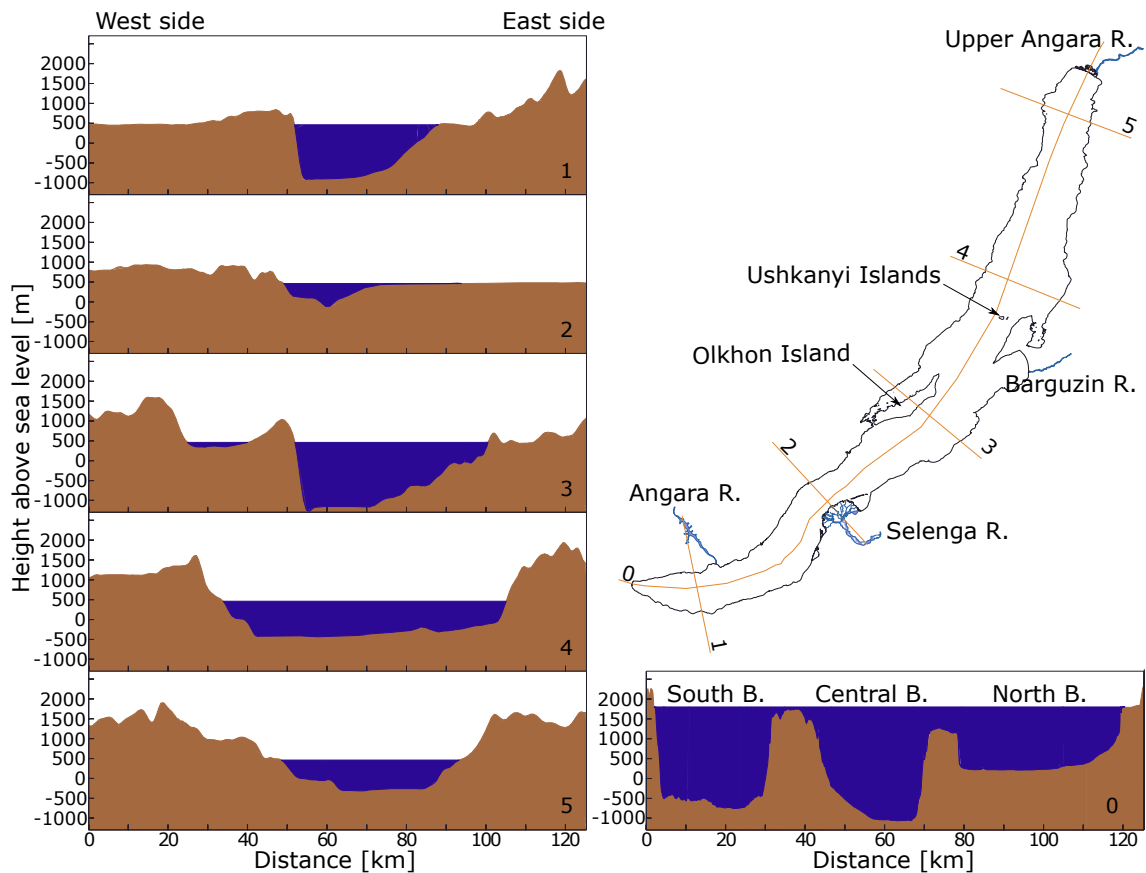


Figure 2.2: Cross sections of Lake Baikal: a) cutting planes, b) transverse sections, and c) longitudinal section (modified from *The INTAS Project 99-1669 Team* [2002]).

1992; Scholz *et al.*, 1993], with a maximum value of more than 9 km in some localities around the Selenga Delta [Scholz and Hutchinson, 2000]. The layer of accumulated sediments is a significant source of gas, oil and bitumens in the lake [Klerkx *et al.*, 2006; Khlystov *et al.*, 2007; Kontorovich *et al.*, 2007], and represents a valuable archive to investigate the history of local climate [Kashiwaya *et al.*, 2001].

### 2.1.2 Climate

The climate of South-East Siberia is continental, but the thermal inertia of the lake's enormous water mass and the peculiarities of its mountainous surroundings create an unusual microclimate, which has some signs of a maritime climate.

**Air temperature** The huge volume of water contained in Lake Baikal influences the processes of heat exchange between the lake and the atmosphere, and hence has significant thermal effects on

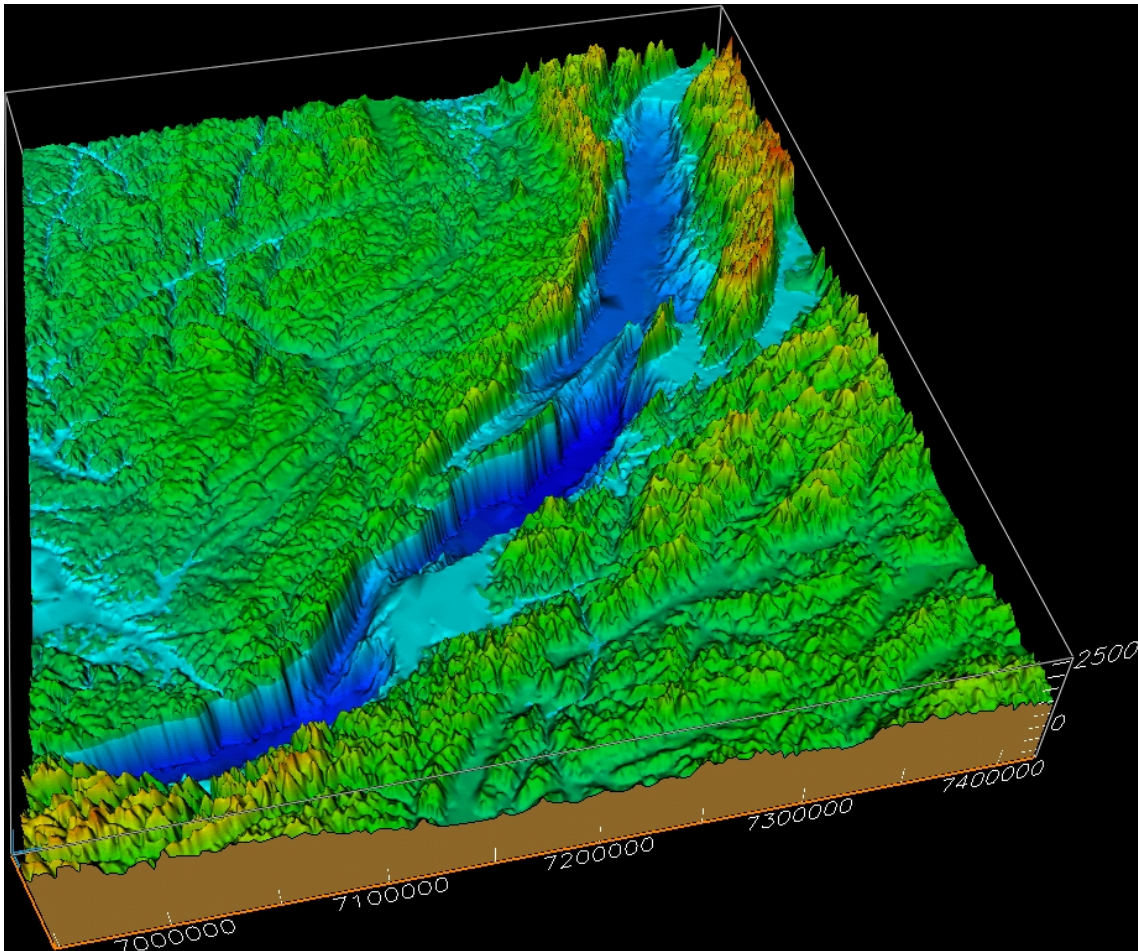


Figure 2.3: 3D bathymetry and topography of Lake Baikal [*The INTAS Project 99-1669 Team, 2002*].

the air temperature above the lake and the coastal areas. The sharp difference between summer and winter temperatures, which is typical of continental climates, is considerably reduced: if compared to the surrounding regions, air temperature over the lake is 6–8°C colder in summer, and 10–15°C warmer in late autumn and early winter. As a consequence, the annual amplitude of temperature variation is smaller close to the lake (30–38°C) than above the neighboring areas (41–50°C) [*Shimaraev et al., 1994*], resulting in cooler summers and milder winters.

Due to the huge dimension of the lake, the non-uniform topography and the complex local atmospheric circulation patterns, air temperature changes considerably moving from one place to another over the lake. In particular, the great latitudinal extent of the basin (the lake spans more than 4° of latitude) determines a clear trend towards a decrease of air temperatures from the South Basin to the North Basin. Mean temperatures observed during the past century at the South, Central and

North Basins are respectively  $-14.5^{\circ}\text{C}$ ,  $-15.3^{\circ}\text{C}$  and  $-17.4^{\circ}\text{C}$ , in winter, and  $10.5^{\circ}\text{C}$ ,  $9.6^{\circ}\text{C}$  and  $8.4^{\circ}\text{C}$  in summer, with mean annual temperature of  $-1.3^{\circ}\text{C}$ ,  $-1.9^{\circ}\text{C}$  and  $-3.2^{\circ}\text{C}$ , respectively [Shimaraev *et al.*, 1994].

Finally, not only the large volume of water has a tempering effect on air temperature, but the presence of the lake also determines a delay in the annual temperature cycle. Indeed, above and close to the lake, the maximum and minimum air temperatures occur nearly a month later than in the surrounding territories: the warmest month being August (it is rather warm still in September), and the coldest month being February.

**Atmospheric precipitation** The distribution of precipitation over the lake is largely determined by the effects of the topography and the orientation of the slopes as related to the direction of the atmospheric circulation patterns. In general, precipitation caused by global atmospheric circulation occurs when large-scale cyclonic flows of moist air cross the mountain ridges at the north-west shore, which are almost perpendicular to the predominant north-western transference of air masses in all seasons. On the other hand, precipitation from local atmospheric circulations are caused by thermal convection currents and unstable air masses, the latter being closely connected with mountain-valley circulations and ascending and descending breezes [Afanasyev and Leksakova, 1973].

Shimaraev *et al.* [1994] analyzed the annual distribution of atmospheric precipitation, finding a remarkable spatial and temporal variability. The heaviest precipitation (up to  $1400\text{ mm y}^{-1}$ ) is observed at the Khamar-Daban mountain range, whereas the precipitation rate over the surface of the lake is comprised between 200 and  $500\text{ mm y}^{-1}$ , with the least precipitation observed over the Central Basin. The most of the precipitation falls during the warm season (from April to October), with a peak in July (13 – 20 % of the annual total). During the cold season, atmospheric precipitation is low due to the development of anticyclonic circulations, with a minimum precipitation rate in February (1 – 3 % of the annual total).

**Winds** Lake Baikal has a very complicated regime of locally variable winds, which appear suddenly and blow in various directions [Ivanov, 2012]. Depending on their direction, winds can be categorized as lengthwise and cross winds. Rzhaplinsky and Sorokina [1977] provided a valuable description of the typical wind patterns over the lake, which is integrated with long-term statistics of wind speed and duration associated to each of them. During the ice-free period (May-December) two different regimes are clearly distinguishable: weak and unstable winds predominate from May to September, whereas from October to December there is a strong incidence of north-west and, to some extent, north-east winds [Shimaraev *et al.*, 1994]. The strongest, most severe and dangerous wind is the one blowing from north-west, named *Gornaya* (the mountain wind, in Russian *gornyy*

stays for *mountain*), which can reach velocities up to  $30 - 40 \text{ m s}^{-1}$  [Ivanov, 2012].

Winds are strongly influenced by the topography and the gradients of pressure due to the considerable differences of temperature between the lake and the surrounding regions. From May to July, the thermal effect of the huge mass of water produces a localized high pressure region over the lake, which generates on-shore winds. On the contrary, from October to January the thermal contrast of land and surface water temperatures leads to a localized low pressure system over the lake, and the enhancement of off-shore winds.

Wind velocities are higher over the Central and South Basins, while lower values can be observed at the North Basin, due to the sheltering effect of local topography that isolate the lake from the general circulation [Shimaraev *et al.*, 1994].

### 2.1.3 Ice Conditions

Every year Lake Baikal is covered by ice for several months. Due to the extraordinary latitudinal extent of the lake and the diversity of physical and geographical conditions in various parts of the freshwater basin, there is a north-south gradient in both the time of freeze-up and the time of break-up [Shimaraev *et al.*, 1994; Livingstone, 1999] (see Figure 2.4a). Indeed, the ice-cover period ranges from 4 to 4.5 months in the south part, and from 6 to 6.5 month in the northern part [Kouraev *et al.*, 2007a].

The timing of freeze-up depends mainly on the intensity of the lake cooling at the end of the year, thus making air temperature in November and December the main meteorological driving factor [Kouraev *et al.*, 2007a]. Freezing starts from late October to early November in small shallow bays, and most of the northern part is usually frozen over by early December, whereas the surface of the South Basin freezes completely about one month later, from late December to early January [Shimaraev *et al.*, 1994; Livingstone, 1999]. The maximum ice thickness varies from about 100 *cm* in the northern basin to 80 *cm* in the southern basin [Livingstone, 1999; Todd and Mackay, 2003], and is subjected to inter-annual variability, with thickness typically ranging between 50 and 110 *cm* [Shimaraev *et al.*, 1994].

The ice cover starts to break-up in the southern part in late March or early April, and by the middle of May the South and Central Basins are generally free of ice. In the northern basin the thaw of ice occurs from 2-3 weeks up to 1 month later, and the basin is free of ice in early June [Shimaraev *et al.*, 1994; Todd and Mackay, 2003]. Ice break-up depends on several factors, among which: the heat exchange between ice and water, the influence of solar radiation during ice melt, the ice thickness, the presence/absence of snow cover, the wind action, and the thermal and dynamical influence of the river inflows. During the melting season, when the ice sheet is thin, huge circles in the ice cover have been observed, which have a typical radius of about 2.5 – 3 *km* (see Figure 2.4b). The mechanisms involved in the formation of the rings have not been fully clarified yet, the

most likely hypothesis being the hydrothermal activity in Lake Baikal and the intense gas venting [Balkhanov *et al.*, 2010; Ivanov, 2012]

Baikal ice is peculiar because of its high degree of transparency (especially off the west coast and in the central part of the lake, Shimaraev *et al.* [1994]), which is very important for the development of phytoplankton, zooplankton, and benthos that begins in late winter/early spring, when the lake is still ice covered [Kouraev *et al.*, 2007a; Moore *et al.*, 2009]. Ice and snow conditions also influence the living conditions of the only Baikal mammal - the Baikal seal (*Phoca sibirica*, see Section 2.1.4). Indeed the seals give birth to their offspring in the snow caves on the ice from the end of February to the beginning of April, whereas during winters with thin snow cover it is difficult for the seals to construct these snow caves, thus leaving baby seals vulnerable to predators, such as crows [Kouraev *et al.*, 2007b; Moore *et al.*, 2009].

Finally, the ice cover is also important for fishing activities, tourism and transport; indeed, during winter the ice is strong enough to support roads, and the narrow lake width allows to more rapidly reach the opposite coast by crossing the lake instead of driving along the coast (see Figure 2.4c).

### 2.1.4 Biodiversity of Lake Baikal

Besides being known for its extreme depth and enormous volume, Lake Baikal is also famous for its outstanding aquatic ecosystem, which is closely connected with its great age and unique natural heritage. Indeed, aquatic life has adapted over the centuries to singular, sometimes extreme, environmental conditions (e.g. the enormous depth, several months of ice cover, low nutrient concentrations, high oxygen concentration along the entire water column) giving rise to an astonishing aquatic environment. Lake Baikal is extremely rich in biodiversity, most likely the lake that harbors more species than any other lake in the world [Moore *et al.*, 2009]. Numerous studies have been undertaken to assess the number of endemic species in Lake Baikal [e.g. Martin, 1994; Timoshkin, 1997], recently Bondarenko *et al.* [2006] estimated that its waters are home for approximately 2500 animal species, 82% of which are endemic, and about 1000 species of plants, 30% of which are endemic. The fauna of Lake Baikal one of the most diverse in the world with, for example, 255 species of shrimp-like amphipod several of which exhibit gigantism (e.g. *Acanthogammarus maximus*, see Figure 2.5a), 80 species of flatworm and 33 species of sculpin fishes, including the deep-dwelling translucent golomyanka (*Comephorus baicalensis* and *Comephorus dybowskii*) that resemble abyssal marine fishes [Brunello *et al.*, 2006; Hampton *et al.*, 2008] (Figure 2.5a). The most famous aquatic species is the Baikal seal (*Phoca sibirica*), the world's only freshwater pinniped, which is known locally as nerpa (Figure 2.5c).

Thanks to exceptional endemism of Lake Baikal, in 1996 the lake was added to the United Nations Educational, Scientific, and Cultural Organization (UNESCO) list of World Heritage Sites

## 2. Lake Baikal and deep ventilation

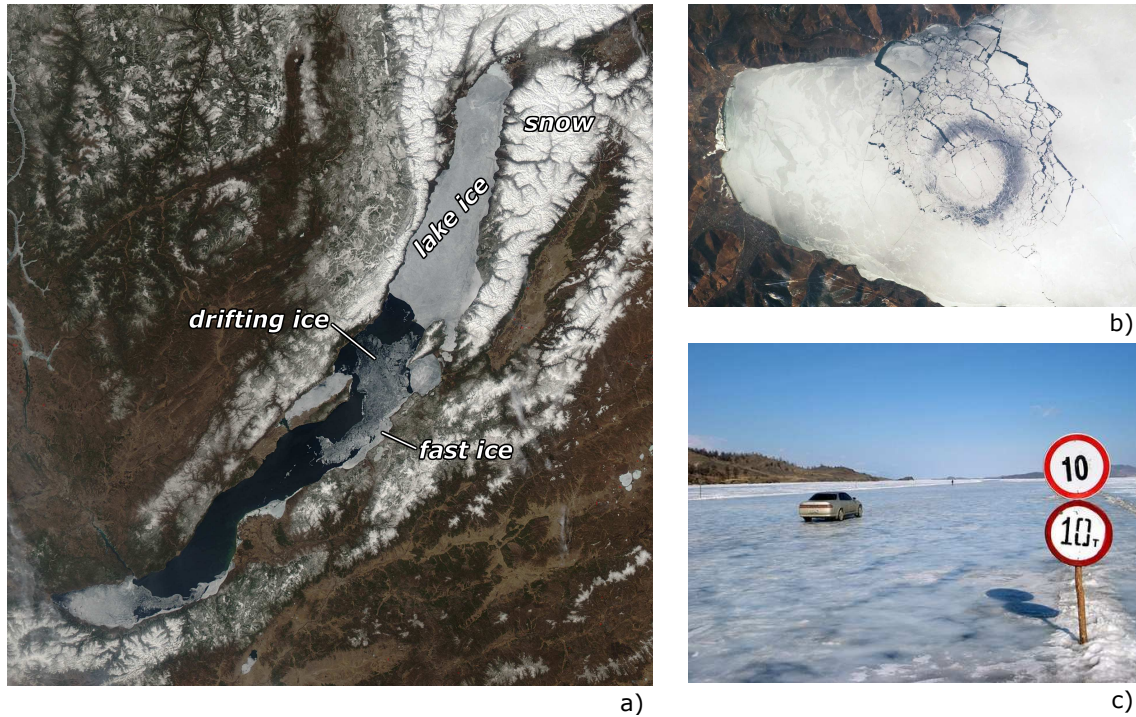


Figure 2.4: Ice cover on Lake Baikal: a) ice breaking up in the central part of the lake on May 4, 2012 (source: NASA image by Jeff Schmaltz, LANCE/EOSDIS MODIS Rapid Response; link: [www.earthobservatory.nasa.gov/IOTD](http://www.earthobservatory.nasa.gov/IOTD)), b) strange circular area of thinned ice in the southern end of Lake Baikal on April 25, 2009 (source: Astronaut photograph ISS019-E-10556, provided by the ISS Crew Earth Observations experiment and Image Science & Analysis Laboratory, Johnson Space Center; link: [www.earthobservatory.nasa.gov/IOTD](http://www.earthobservatory.nasa.gov/IOTD)), and c) ice highway on Lake Baikal (photo credit: Thomas Hack; link: [www.pinterest.com/pin/57350595224731816](http://www.pinterest.com/pin/57350595224731816)).

(WHS) which cited Lake Baikal as *"the most outstanding example of a freshwater ecosystem"* [UNESCO, 1996].

In conclusion, it is worth noting that the presence of high oxygenated deep water, a trait shared with oceans but unique among deep lakes ( $> 800\text{ m}$ ), is a key factor for the existence of multicellular life and the evolution of an extensive, mostly endemic fauna in the lake's profundal depths [e.g. Moore *et al.*, 2009]. The high oxygen content down to the deepest layers of Lake Baikal is a consequence of deep ventilation, a singular phenomenon that is exhaustively presented and described in Section 2.2.



Figure 2.5: Some of the endemic animal species of Lake Baikal: a) an amphipod on a sponge (source [ferreekeeper.files.wordpress.com](http://ferreekeeper.files.wordpress.com)), b) Baikal oilfish (golomyanka), the famous translucent abyssal fish (source [www.irkutsk.org](http://www.irkutsk.org)), and c) Baikal seal or Nerpa (*Pusa sibirica*) the only exclusively freshwater pinniped species (source [www.askbaikal.com](http://www.askbaikal.com)).

## 2.2 Deep ventilation

Due to its huge dimension and the large amount of wide-ranging physical and ecobiological phenomena occurring in it, Lake Baikal has caused a great interest in the international scientific community. Concerning hydro-thermodynamic phenomena, one of the most studied processes is deep water ventilation, which is the episodic sinking of large volumes of surface water down to the hypolimnion of the lake (see Figure 2.6 for a schematic illustration). Indeed, despite its enormous depth and the fact that the seasonal convective mixing is limited to the uppermost active layer (first 250 m depth), Lake Baikal is characterized by an intense renewal of deep water. As a consequence, the hypolimnetic layers are oxygenated even down to the bottom of the lake, with concentrations of dissolved oxygen generally greater than 80% of saturation [Weiss *et al.*, 1991]. In addition, the existence of regular deep intrusions is responsible for a permanent, even if weak, deep water stratification.

Deep intrusions of cold water have been regularly observed, usually during the period of convective surface mixing: in June (after the melting of the ice cover) and in December/January (before the surface freezes) when the surface layer is well mixed, thus having a quasi-uniform temperature profile. Thermobaric instability, which results from the decrease in the temperature of maximum density,  $T_{\rho,max}$ , with increasing depth (see Sections 2.2.1 and 2.2.4 for a detailed description), has been identified as the mechanism responsible for deep ventilation [Weiss *et al.*, 1991]. Notwithstanding, it has not been fully clarified yet which physical process may provide sufficient energy to the system to trigger this kind of instability. In this regard, many possibilities have been suggested: cabbeling instability of spring thermal bars [Shimaraev *et al.*, 1993], dense water plume formation in correspondence of the inflow regions [Hohmann *et al.*, 1997], water exchange over the sill between the Central and North Basins at Academician Ridge [Peeters *et al.*,

## 2. Lake Baikal and deep ventilation

1996; Hohmann *et al.*, 1997] and wind-induced vertical mixing [Weiss *et al.*, 1991; Killworth *et al.*, 1996; Botte and Kay, 2002; Wüest *et al.*, 2005; Schmid *et al.*, 2008].

Cold downwellings have been found to be more frequent and to have a greater cooling effect of deep water in the South Basin of Lake Baikal than in other parts of the lake [e.g. Shimaraev *et al.*, 2011b]. For this reason, and because measurements and observations at the South Basin are more available than in the central and northern basins, the present study is primarily focused on this part of the lake.

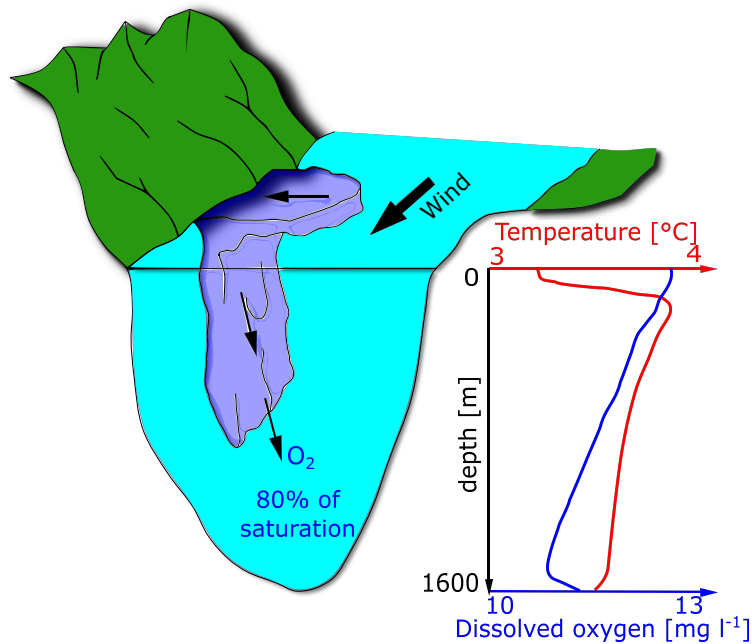


Figure 2.6: Schematic representation of deep ventilation: the sinking water cools and oxygenates the deep layers of the lake. For simplicity of representation and comprehension, the sketch shows a downwelling event occurring at the shore in presence of a wind blowing parallel to the coast, that generates inshore Ekman transport (i.e. coastal downwelling).

### 2.2.1 Physical properties of water and thermobaricity

The density of water,  $\rho$ , depends on temperature,  $T$ , pressure,  $P$ , and its physicochemical properties (e.g. salinity,  $S$ ). In order to adequately determine pressure, volume and temperature properties of lake water, Chen and Millero [1986] proposed an equation of state for freshwater that is valid over the range appropriate for most freshwater lakes: 0 – 0.6‰ salinity, 0 – 30°C, and



0 – 180 bar [see also *Chen and Millero, 1977*]. The equation is in the form

$$\rho^P = \rho^0 \left( \frac{P}{K} \right), \quad (2.1)$$

where  $\rho^P$  and  $\rho^0$  are the densities of water at the pressure  $P$  and at the sea level ( $P = 0$  bar), and both  $\rho^0$  and  $K$  are functions of  $T$ ,  $P$  and  $S$ . In this study, all the thermophysical properties of water (e.g. density  $\rho$ , thermal expansivity  $\alpha$ , specific heat capacity  $c_p$ ) have been calculated using this equation, which is widely accepted and utilized among limnologists. In the light of previous studies [*Killworth et al., 1996; Wüest et al., 2005*], salinity has been assumed to contribute little to the stratification of Lake Baikal, thus its role in the equation of state has been neglected (see also Section 3.2). On the contrary, the dependence on pressure had to be necessarily considered due to the enormous depth of the lake.

The coefficient of thermal expansion of water,  $\alpha$ , is expressed in units of  $[K^{-1}]$  and is defined by

$$\alpha = -\frac{1}{\rho} \left. \frac{\partial \rho}{\partial T} \right|_p, \quad (2.2)$$

where the subscript indicates that the derivative is calculated by keeping pressure constant. The coefficient  $\alpha$  is in close relation with one of the most important anomalous properties of water: the density of water is non-linearly dependent on its temperature. As pure water (i.e.  $S = 0$ ) at  $0^\circ C$  at the sea level is warmed, it increases in density until a maximum of  $999.972 \text{ kg m}^{-3}$  is reached at  $3.9839^\circ C$  [*Chen and Millero, 1986*]. Above this point, a further rise in temperature results in a decrease of density. In other words,  $\alpha$  changes sign at the temperature of maximum density  $T_{\rho,max}$ , which for pure water at the sea level is  $T_{\rho,max} = 3.9839^\circ C$ : for  $T < T_{\rho,max}$  density increases with increasing temperature and hence  $\alpha < 0$ , whilst for  $T > T_{\rho,max}$  density decreases with increasing temperature and thus  $\alpha > 0$ .

Pressure (and salinity) has an important influence on water density, which, in turn, results in a significant effect on both  $T_{\rho,max}$  and  $\alpha$ . Concerning the temperature of maximum density, its dependence on pressure can be determined by solving the equation  $(\partial \rho / \partial T)|_p = 0$ , which, in the case of the [*Chen and Millero, 1986*] equation of state, yields

$$T_{\rho,max} = 3.9839 - 1.9911 \times 10^{-2} P - 5.822 \times 10^{-6} P^2, \quad (2.3)$$

where we recall that  $P$  is in bar. Note that  $T_{\rho,max}$  decreases with increasing pressures, thus with increasing depth, by approximately  $0.2^\circ C$  for every 100 m of depth ( $100 \text{ m} \simeq 9.81 \text{ bar}$ ).

Due to the non linearity of the equation of state, lateral fluxes of heat (and salt) can cause vertical advection of fluid, which are related to two different physical processes. The fact that  $\alpha$  is a

function of temperature (and salinity) causes the so called cabbeling effect, while the combined dependence of  $\alpha$  on temperature and pressure is referred to as thermobaricity [McDougall, 1987]. Both processes are important in oceans and deep lakes, since they are often the cause of deep vertical convection and significantly enhance vertical mixing [e.g. Garwood *et al.*, 1994; Løyning and Weber, 1997; Weber and Løyning, 2006]. Indeed, it is not uncommon for cabbeling and thermobaricity to cause downwelling velocities of about  $10^{-7} \text{ m s}^{-1}$  [McDougall and You, 1990].

### 2.2.2 Local stability

A water column is said to be locally stable if a fluid parcel that is displaced isentropically (i.e. without exchange of heat and salt with the surrounding water) from its initial position by an infinitesimal vertical distance  $dz$  experiences a restoring force [Peeters *et al.*, 1996].

For an easier comprehension, local stability can be described considering two water parcels separated by a very small vertical distance. Imagine that the upper parcel is moved isentropically to the depth of the lower one, where the density of the two parcels are compared. If the density of the upper parcel is smaller than the density of the one at the lower position, the water column is said to be locally stable: because of buoyancy, the displaced parcel is pushed back to its original position, thus the displacement is reversible. In case the density difference is zero, the water column is referred to as neutrally stable: the two water parcels can exchange position without altering the potential energy of the system. Finally, if the displaced water parcel is heavier than the one at the lower position, the water column is said to be unstable: as a consequence of this exchange of positions, a spontaneous convection is initiated. The convection continues until the water column reaches a stable configuration, which has a lower potential energy compared to the initial condition. Since the displacement of the water parcels are infinitesimally small, the stability depends on the local density gradient, hence the expression local stability [Imboden and Wüest, 1995].

The correct criterion for local stability in a stratified fluid is [Landau and Lifshitz, 1987; Osborn and LeBlond, 1974]

$$\left. \frac{d\rho}{dT} \right|_P \frac{ds}{dz} > 0, \quad (2.4)$$

where  $z$  is the vertical coordinate defined as positive downward, and  $s$  is the entropy. When the left hand side of (2.4) is negative the water column is unstable, whilst when it is equal to zero the water column has neutral stability.

In freshwater, the temperature of maximum density is above the freezing point and thus the first term of Equation (2.4) cannot be neglected when studying local stability in lakes. Expanding the

entropy gradient, the stability condition can be rewritten as

$$\frac{d\rho}{dT}\bigg|_P \left( \frac{\partial s}{\partial T}\bigg|_p \frac{dT}{dz} + \frac{\partial s}{\partial p}\bigg|_T \frac{dp}{dz} \right) = \frac{d\rho}{dT}\bigg|_P \left( \frac{c_p}{T} \frac{dT}{dz} + \frac{g}{\rho} \frac{\partial \rho}{\partial T}\bigg|_p \right) > 0, \quad (2.5)$$

where  $c_p = c_p(T, P)$  is the specific heat capacity at constant pressure [e.g. see *Landau and Lifshitz*, 1987, for further details]. Substituting the definition of the thermal expansivity given in (2.2) into (2.5), and after some algebraic manipulations, the stability condition becomes

$$-\alpha \left( \frac{dT}{dz} - \Gamma \right) > 0, \quad (2.6)$$

where  $\Gamma$  is the adiabatic temperature gradient, which is defined as [e.g. *Imboden and Wüest*, 1995]

$$\Gamma = \frac{dT}{dz}\bigg|_{ad} = \frac{g\alpha(T + 273.15)}{c_p}. \quad (2.7)$$

It is worth noting that, by definition,  $\Gamma$  corresponds to the vertical in situ temperature gradient in a neutrally stable water column. As a matter of fact, when  $dT/dz$  is equal to  $\Gamma$ , the left hand side of Equation (2.6) is zero, which is the condition for neutral stability. Furthermore, from Equation (2.7) it is easy to see that the sign of  $\Gamma$  is given by the sign of  $\alpha$ , and in particular:  $\alpha$  and  $\Gamma$  are negative for  $T < T_{p,max}$ , and positive for  $T > T_{p,max}$  (see Figure 2.7).

In the literature, local stability is generally assessed by means of the squared Brunt-Väisälä buoyancy frequency  $N^2$  [Gill, 1982], which is nothing but the left hand side of expression (2.6) multiplied by the gravitational constant  $g$

$$N^2 = -g\hat{\alpha} \frac{d\Theta}{dz} = -g\alpha \left( \frac{dT}{dz} - \Gamma \right), \quad (2.8)$$

where  $\hat{\alpha}$  is the thermal expansion coefficient for the potential temperature [see *Peeters et al.*, 1996, for details] and  $\Theta$  is the potential temperature, which for a fluid parcel at the pressure  $P$  is defined as the temperature that this parcel would have if adiabatically brought to a reference pressure  $P^r$  (the potential density can be defined analogously)

$$\Theta(z) = T(z) - \int_z^{z^r} \Gamma dz'. \quad (2.9)$$

Since  $g$  is a positive constant, according to Equation (2.6) the water column is stable when  $N^2$  is positive, and neutral or unstable depending if  $N^2$  is zero or negative, respectively.

Alternatively, the squared Brunt-Väisälä frequency can be expressed in terms of the density

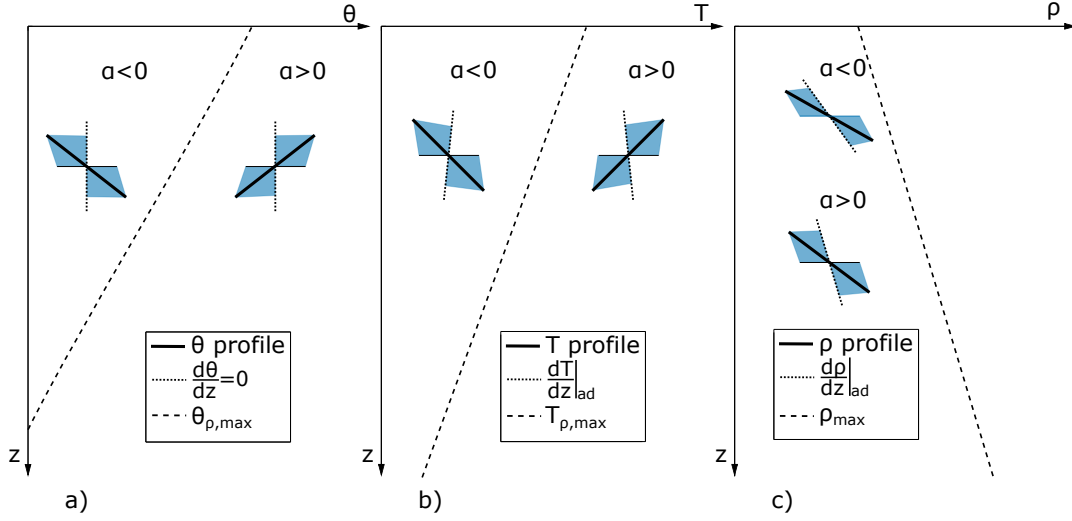


Figure 2.7: Conditions for local stability (shaded regions) for the cases of: a) potential temperature ( $\Theta$ ), b) real temperature ( $T$ ), and c) density ( $\rho$ ). Modified from *Imboden and Wüest [1995]*.

through the following Equation [e.g. *Peeters et al., 1996*]

$$N^2 = \frac{g}{\rho} \left( \frac{d\rho}{dz} - \frac{d\rho}{dz} \Big|_{ad} \right), \quad (2.10)$$

where  $\frac{d\rho}{dz} \Big|_{ad}$  is the adiabatic density gradient.

The regions of local stability for  $\Theta$ ,  $T$  and  $\rho$  are schematically presented in Figure 2.7, depending on the sign of  $\alpha$ .

The adiabatic term in Equation (2.8) is often neglected because it is usually much smaller compared to the real temperature gradient, especially in correspondence to  $T_{\rho,max}$  at which  $\alpha$  approaches zero. Neglecting  $\Gamma$  in the (2.8) corresponds to neglecting the adiabatic density gradient in Equation (2.10), which reduces to

$$N^2 = \frac{g}{\rho} \frac{d\rho}{dz}. \quad (2.11)$$

Although this approximated definition of  $N^2$  is widely used in limnology and oceanography applications, it is inadequate for small temperature gradients [*Osborn and LeBlond, 1974*]. As a matter of fact, under these conditions the real and adiabatic gradients of temperature and density have a similar order of magnitude, thus the adiabatic terms cannot be neglected. In conclusion, for an accurate assessment of local stability, an increasing density with depth ( $\frac{d\rho}{dz} > 0$ ) is not a sufficient condition. On the contrary, a minimum threshold on the density gradient is required to be satisfied, which is that corresponding to the adiabatic temperature gradient ( $\frac{d\rho}{dz} > \frac{d\rho}{dz} \Big|_{ad}$ ) [*Osborn*

and LeBlond, 1974].

As far as Lake Baikal is concerned, the thermal structure of the water column is characterized by small temperature gradients when water temperature approaches  $T_{\rho,max}$  and within the hypolimnion, with typical values of  $dT/dz \sim O(10^{-4} \div 10^{-5}) \text{ } ^\circ\text{C m}^{-1}$ . These values are comparable with the adiabatic temperature gradients  $\Gamma \sim O(10^{-5} \div 10^{-6}) \text{ } ^\circ\text{C m}^{-1}$  at the same depths, thus making the inclusion of  $\Gamma$  crucial to assess the stability of the water column. It is worth noting that a precise estimation of the main thermophysical properties (density  $\rho$ , thermal expansibility  $\alpha$ , specific heat capacity  $c_p$ ) is essential to accurately evaluate  $\Gamma$ , thus to evaluate the stability of the water column.

### 2.2.3 Thermal regime

The thermal regime of Lake Baikal can be classified as dimictic [e.g. *Hutchinson and Löffler, 1956; Lewis, 1983*]. Dimictic lakes are stably stratified in winter (inverse stratification) and in summer (direct stratification), and circulate twice a year at the transition between the two states.

According to the stability condition discussed in the previous section, deep dimictic lake present two different stable thermal profiles in summer and winter (for the sake of simplicity and ease of explanation, the contribution of  $\Gamma$  to local stability is neglected in the following discussion, without loss of qualitative generality). In summer, when water temperature is warmer than  $T_{\rho,max}$  (i.e.  $\alpha > 0$ ) at any depth, temperature decreases with increasing depth, and the lake is referred to as directly or regularly stratified.

On the contrary in winter, when water temperature in the epilimnion is colder than  $T_{\rho,max}$  (i.e.  $\alpha < 0$ ), the water column is stable if temperature increases with depth. Under these conditions the water column is said to be inversely stratified. Beneath the epilimnion, however, deep water is not much affected by the seasonal changes at the surface, and it remains directly stratified throughout the year, with temperatures above  $T_{\rho,max}$  (i.e.  $\alpha > 0$ ). The condition for stable stratification implies that the vertical temperature gradient changes sign at the depth at which the in situ temperature meets  $T_{\rho,max}$  ( $\alpha = 0$ ), where also the sign of  $\alpha$  changes. Therefore, it is evident that at this intersection water temperature has its local maximum [e.g. *Boehrer and Schultze, 2008*], the so called mesothermal maximum [*Shimaraev et al., 1994*].

This is the only temperature profile that is compatible with the stability condition. As a matter of fact any vertical displacement of the mesothermal maximum away from the  $T_{\rho,max}$  line would lead to a specific form of convective turbulence known as thermobaric instability, which is essentially caused by thermobaricity (see Section 2.2.1 for the definition). Since the water column is never at rest, the mesothermal maximum is constantly exposed to this kind of instabilities, which causes the continuous mixing with surrounding water. As a consequence, the mesothermal maximum is not a well-defined point, but rather a well-mixed layer of almost homogeneous temperature, which

## 2. Lake Baikal and deep ventilation

thickness provides an indication for the largest amplitudes of the vertical displacement at that depth [Wüest *et al.*, 2005].

The typical thermal profiles that occur at the South Basin of Lake Baikal are shown in Figure 2.8, both for the warm (line with squares) and the cold (line with dots) season. During the cold season, the mesothermal maximum is typically located at a depth of about 200 – 250 *m*, and has a temperature of  $\simeq 3.55^\circ\text{C}$ . Beneath that depth, deep temperature profile is permanently, weakly stratified over the whole year, and maintains a typical background temperature of about  $3.38^\circ\text{C}$  [Schmid *et al.*, 2008].

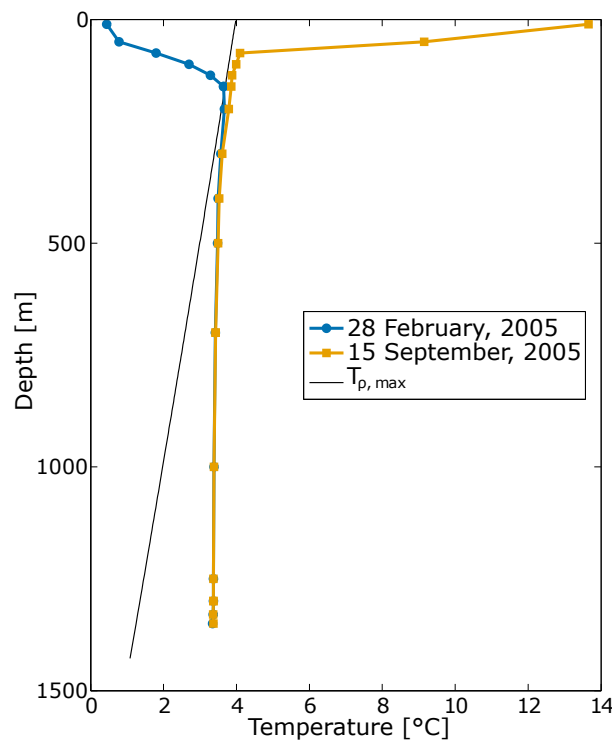


Figure 2.8: Temperature profiles measured (data courtesy of A. Wüest) on: 28 February 2005, during the cold season the surface layer (above 250 – 300 *m* depth) is inversely stratified and the maximum of the temperature profile lies on the temperature of maximum density curve,  $T_{p, max}$ ; 15 September 2005, during the warm season the surface layer is directly stratified. Deep water (beneath 300 *m* depth) is permanently, weakly stratified over the year.

When surface water temperature approaches  $T_{p, max}$  and the water column is nearly isothermal (twice a year in dimictic lakes), the stable stratification weakens and the water column undergoes complete or partial vertical mixing. In profound dimictic lakes (as is the case of Lake Baikal) only the surface layer regularly turns over, while the deep water is just episodically and partially

renewed [e.g. *Farmer and Carmack*, 1981; *Boehrer and Schultze*, 2008; *Crawford and Collier*, 1997; *Shimaraev et al.*, 1994]. This is also the case of Lake Baikal. As a matter of fact, due to the enormous depth of the lake, during homothermy the wind-induced convection is limited to the upper 250-300 m [*Shimaraev et al.*, 1994]. Hence, only the epilimnion typically mixes, while the hypolimnion is affected by an occasional, large-scale, convective mixing, which is known as deep ventilation or deep water renewal. *Weiss et al.* [1991] observed this turbulent convective process in Lake Baikal, and explained it as a consequence of thermobaric instability (see Section 2.2.4 for an in-depth description).

#### 2.2.4 Thermobaric instability

Thermobaric instability can be qualitatively described as follows. Consider a deep lake characterized by a typical winter temperature profile (e.g. line with dots in Figure 2.8) in which the epilimnion is inversely stratified and its mean temperature is colder than the bottom water temperature. If a volume of epilimnetic water is mixed and pushed downward by the action of an external forcing, it can become conditionally unstable when it reaches the depth at which its density matches the density of the local deep water. This critical depth is known as compensation depth,  $h_c$ , and depends on the temperature of the sinking water volume and on the temperature profile. In correspondence to  $h_c$ , the descending water shows a temperature colder than  $T_{\rho,max}$  while, on the contrary, the local water is warmer. If the sinking water volume reaches and oversteps  $h_c$ , thermobaric instability is triggered: the sinking water is heavier than the surrounding water and starts to sink freely until, along its descending path, it encounters deep water having the same temperature, thus density (see Figure 2.9a). If the sinking water is heavier than the deep water, it sinks until the very bottom of the lake (see Figure 2.9b). In both cases, as the descending volume sinks, it is replaced either by water flowing from the sides or from above  $h_c$ ; in the latter case, this may perpetuate the deep intrusion of water as the cold fluid crosses its compensation depth and becomes unstable [*Watts and Walker*, 1995].

In general, deep ventilation is capable of renewing profound water by replacing and mixing it with colder and more oxygenated surface water. As a consequence, despite its enormous depth, Lake Baikal is characterized by strong vertical exchanges that ensure high oxygen and low nutrients concentrations along the entire water column. The surprising high oxygenation of deep water (i.e. dissolved oxygen concentration up to the 80% of saturation, *Weiss et al.* [1991]) plays a crucial role for the existence of deep water aquatic life.

Deep downwelling events triggered by thermobaric instability are likely to happen during the transition between the two seasonal stratification periods, when the lake is nearly isothermal [e.g. *Weiss et al.*, 1991; *Shimaraev et al.*, 1994]. In late autumn and late spring the temperature gradient within the epilimnion is progressively lowered, thus the density stratification weakens. Under these

conditions less energy is required to overcome the stabilizing effect of buoyancy, the convective mixing is enhanced and the turbulent diffusivity increases. Moreover, as surface water temperature approaches  $T_{\rho,max}$ , the difference between surface and deep water temperature reduces, and hence  $h_c$  becomes shallower (see Figure 2.9), further contributing to the diminishing the external energy input required to trigger thermobaric instability.

On the contrary, when the epilimnion shows a strong inverse thermal stratification, in winter, turbulent mixing is inhibited, thus reducing the diapycnal transfer of momentum, heat and mass tracers. Under these conditions, the eddy size and hence the turbulent diffusivity are suppressed by the presence of strong, stabilizing buoyancy forces. In addition, the surface water is much colder than deep water, thus resulting in a deepening of  $h_c$  and in a consequent increasing demand for the external energy input necessary to initiate thermobaric instability. Hence, during the winter stratification period, only shallow, partial downwellings are allowed: the surface water is pushed until a certain depth  $< h_c$  (depending on the energy input), where it is still buoyant and hence is forced to rise back (see Figure 2.9c).

Finally, when the epilimnion is directly stratified, in summer, thermobaric instability cannot occur since temperature is always warmer than  $T_{\rho,max}$  and no compensation depth  $h_c$  can be defined. In this period of the year, only shallow convective mixing occurs, which result from the balance between wind mixing and buoyancy fluxes (Figure 2.9d).

A schematic representation of the four possible types of thermobaric instability that can occur in deep dimictic lakes is shown in Figure 2.9. The vertical movement of the water volume is depicted from its initial (IP) to its final position (FP), passing through the depth at which the water volume is forced to sink as a result of the external energy input, which is referred to as arrival position (AP). For the sake of simplicity, in the figure the vertical displacement of the water volume follows an adiabatic path. Hence, the heat exchanged with the surrounding water is not accounted for in the drawing, whilst, in the reality, turbulence and mixing are enhanced during unstable conditions when buoyancy acts as an additional source of turbulent kinetic energy [e.g *Lorke et al.*, 2005].

In addition to the above considerations, meteorological conditions play a fundamental role: deep downwellings are favored during the transition seasons also because strong winds affect Lake Baikal in those periods of the year. As a matter of fact, the long term observations during the past century provided by *Rzheplinsky and Sorokina* [1977] show pronounced seasonal variations, with a general increase of wind speed and duration in May and, even more, from October to December (see Section 5.1.1), when the water column is nearly isothermal. It is evident that stronger and more persistent winds guarantee a major energy input at the surface, increasing the turbulent diffusivity and the momentum transfer within the wind-affected layer.



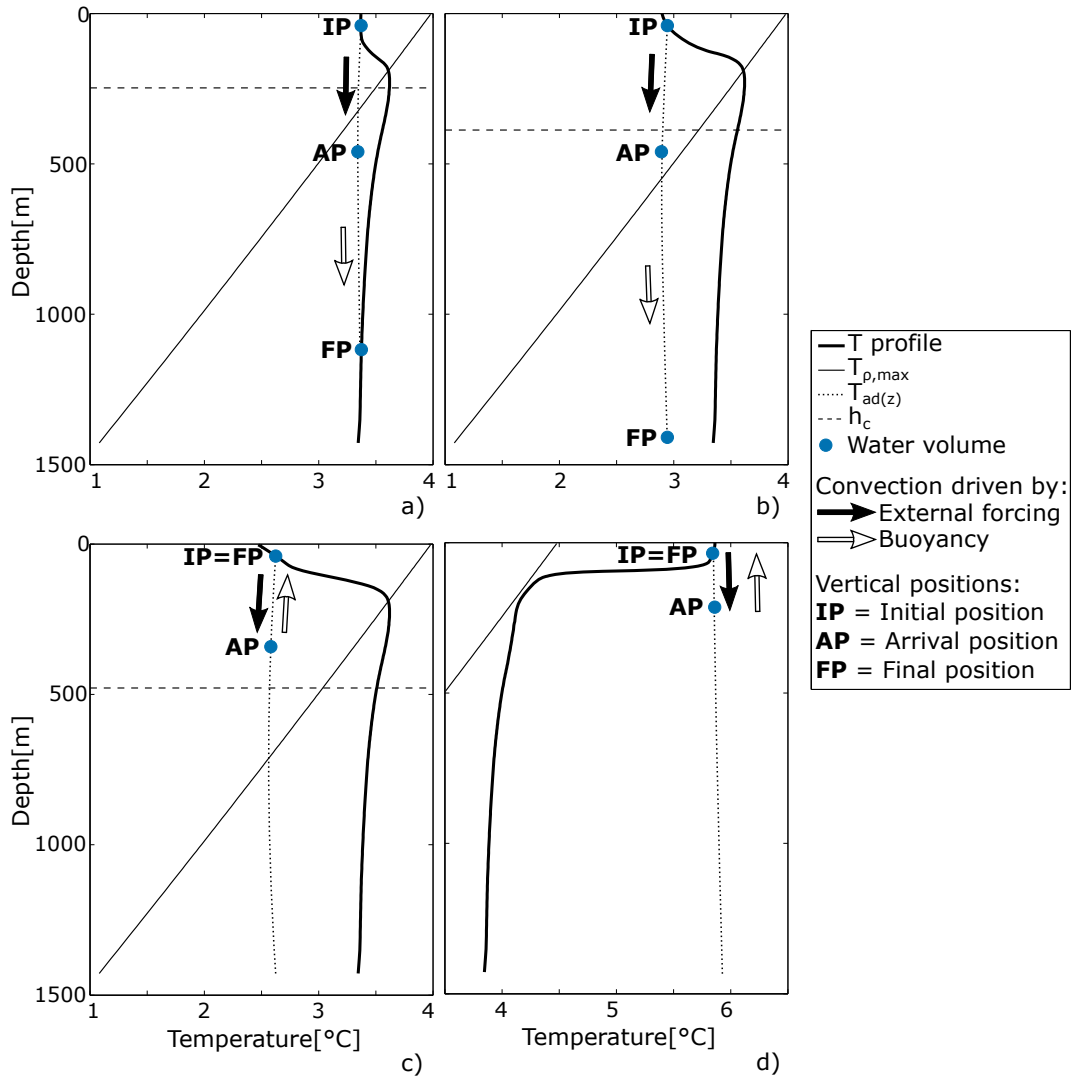


Figure 2.9: Possible types of thermobaric instability in deep dimictic lakes: when the lake is nearly isothermal (late autumn and late spring) the surface water volume moving along an adiabatic path crosses the compensation depth  $h_c$  and a) stops when encounters local water having the same temperature or b) sinks until the bottom of the lake; when the upper part of the lake is strongly stratified, thermobaric instability does not occur, c) neither in winter when  $h_c$  is deep and thus the energy demand is high, d) nor in summer when  $h_c$  cannot be defined. In these last two cases, strong stabilizing buoyancy forces reestablish the initial condition.

Finally, thermobaric instability plays an important role in establishing the depth of the mesothermal maximum, which is not constant throughout the whole cold season. Moving from winter to spring, the progressive rise in surface water temperature implies unstable conditions. As a consequence, the epilimnion mixes and the mixing layer deepens, reaching its maximum thickness (200 – 250 m) when the mean surface temperature approaches that of the mesothermal maximum. A further heating at the surface will progressively rise the temperature of the mesothermal maximum, and contextually the depth at which the temperature profile intersects the  $T_{p,max}$  line gets shallower, following the evolution of surface water temperature. The upper layer is well mixed and maintains a nearly constant temperature. Under these conditions, the depth of the mesothermal maximum and the compensation depth  $h_c$  almost coincide, and any weak perturbation (e.g. wind induced instability, internal waves, day/night thermal cycle) generates local thermobaric instability at that depths. This will yields an upper temperature profile that follows the  $T_{p,max}$  line up to the surface [Weiss *et al.*, 1991; Boehrer *et al.*, 2008] (see Figure 2.10a).

After summer and autumn, during which lake is directly stratified, surface water begins to cool, causing the gradual thickening of the mixing layer. Eventually, the epilimnion starts to stratify inversely, and the mesothermal maximum appears at the very surface. Progressively it deepens generating local unstable regions as it moves down, until it stabilises at the depth of about 200 – 250 m (see Figure 2.10b).

### 2.2.5 Vertical diffusivity

Small-scale vertical diffusion is a key process in Lake Baikal, and is highly correlated with the extremely weak (even though permanent) stratification of deep water (i.e. beneath  $\sim 250$  m) that allows for the existence of large turbulent eddies [Wüest *et al.*, 2005]. As a consequence, in the deep part of the water column strong diffusive-type vertical fluxes are enhanced, which are able to compensate the advective-type ones caused by deep downwellings [Ravens *et al.*, 2000; Wüest *et al.*, 2005]. Close to the bottom of the lake, turbulence is enhanced due to friction-induced shear stress, thus determining a significant increase of turbulent diffusivity [Wüest *et al.*, 2000].

Different empirical techniques have been adopted to evaluate the vertical transfer of momentum, heat and tracers in Lake Baikal: performing temperature microstructure profiles and inertial dissipation measurements [Ravens *et al.*, 2000], using CFCs,  $^3H$ ,  $^3He$  or dissolved oxygen as tracers [Killworth *et al.*, 1996; Peeters *et al.*, 1997, 2000], with temperature profile modeling [Lawrence *et al.*, 2002], and balancing biogeochemical water constituents [Wüest *et al.*, 2000]. The various studies (except for the results of Killworth *et al.* [1996] that are characterized by smaller values) lead to deep water diffusivity estimates on the order of  $10^{-4}$  to  $10^{-3} m^2 s^{-1}$  within the middle part of the deep water mass (roughly 500 – 1200 m depth) and an increase up to  $10^{-2} m^2 s^{-1}$  [Wüest *et al.*, 2000] near the bottom.

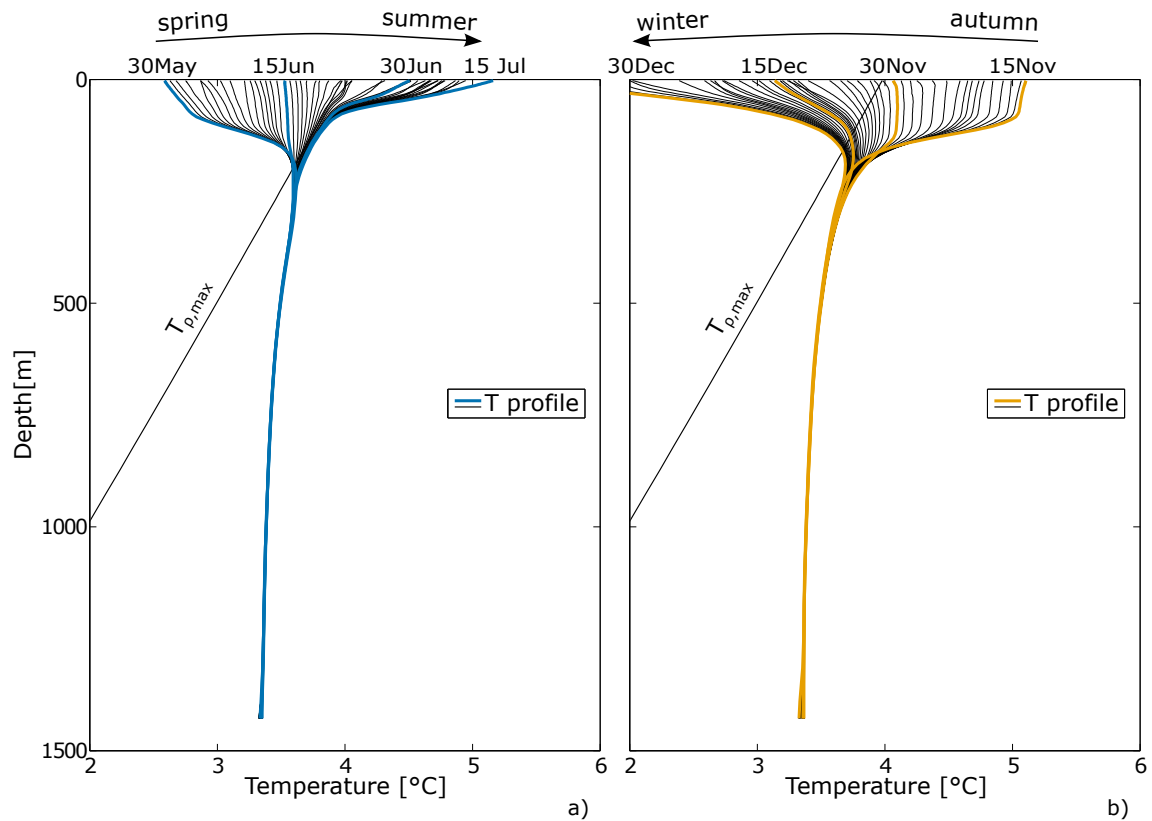


Figure 2.10: Seasonal evolution of the depth of the mesothermal maximum: a) moving from late spring to early summer, the mesothermal maximum gets shallower and warmer; b) moving from early autumn to winter, the mesothermal maximum gets colder and deepens until it stabilises at the depth of about 200 – 250 m. Temperature profiles has been obtained using the model presented in Section 3.

## 2. Lake Baikal and deep ventilation

---

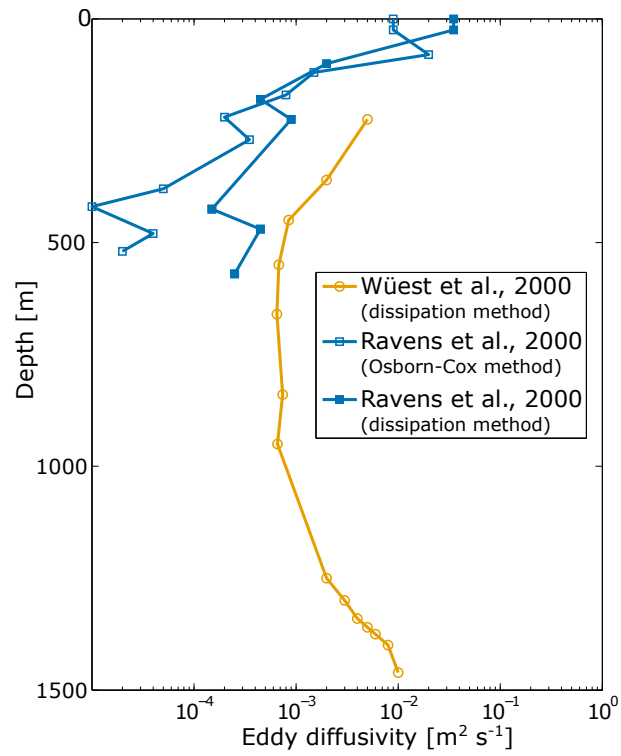


Figure 2.11: Vertical diffusivity profiles estimated by *Ravens et al.* [2000] and *Wüest et al.* [2005].

Figure 2.11 shows the diapycnal diffusivity profiles estimated by *Ravens et al.* [2000] and *Wüest et al.* [2000].

## 3 A simplified 1D model for the numerical simulation of deep ventilation

**Abstract** - *In the previous chapter, the phenomenon of deep water renewal in Lake Baikal has been described, focusing on its underlying causes, and highlighting its main consequences. A proper description of deep ventilation process and a careful quantification of the effects that large-scale, convective, deep intrusions have on the physical, chemical and biological variables are mandatory in order to determine and comprehend the behavior of the overall limnological system.*

*In this chapter an original one-dimensional model is presented, which simulates the ventilation mechanism occurring in deep lakes. The model numerically computes the evolution of the temperature vertical profile taking into account the stability of the water column and the occurrence of deep water intrusions. Given the required information (boundary and initial conditions, internal parameters) the model allows one to simulate the temporal evolution of any tracer (e.g. dissolved oxygen, salinity, biological tracers, etc.) in addition to the temperature  $T$ . In spite of its simple structure, such a model represents a comprehensive tool able to effectively capture the feedback loops among the main physical processes (downwelling, mixing, thermobaric instability). Climate dynamics are included not only assuming that the external forcing can evolve (e.g. by accounting for seasonal or climatic fluctuations of the boundary conditions), but also consistently adapting the internal properties of the lake. Indeed, in order to account for the effect of the variability of meteorological forcing, a novel and expeditious approach has been developed to self-consistently reconstruct the diapycnal diffusivity profile given the system and the external conditions. Thanks to these key properties, the model is appropriate to analyze limnic systems under different climatic conditions.*

*The chapter is structured as follows. A brief introduction on the state of the art concerning the investigation of deep ventilation is given in 3.1, highlighting the main difficulties and major methodological limitations. In Section 3.2, the mathematical model is formulated, describing the governing equations and the algorithms to handle the vertical convection due to the instability of the water column and the downwelling intrusions. Section 3.3 describes how external forcing (i.e. the wind) and internal dynamics (e.g. oxygen depletion rate) are accounted for in the model. Initial and boundary conditions are commented as well. The procedure to self-consistently reconstruct the diapycnal diffusivity profile is formulated in Section 3.4. Finally, concluding remarks are given in Section 3.5.*

*A paper describing the model presented here and its application to Lake Baikal is ready to be submitted to a refereed journal for consideration [Piccolroaz and Toffolon, 2013]. The model has been described also in Piccolroaz and Toffolon [2011] and Piccolroaz and Toffolon [2012c].*

### 3. A simplified 1D model for the numerical simulation of deep ventilation

---

### 3.1 Background and state of the art

Deep ventilation of Lake Baikal has long fascinated the scientific community. During the last decades, several mathematical models and numerical simulations have been performed [Killworth *et al.*, 1996; Tsvetova, 1999; Peeters *et al.*, 2000; Lawrence *et al.*, 2002; Botte and Kay, 2002], and many field observations and measurements have been conducted [Weiss *et al.*, 1991; Shimaraev *et al.*, 1993; Hohmann *et al.*, 1997; Ravens *et al.*, 2000; Wüest *et al.*, 2000, 2005; Schmid *et al.*, 2008; Shimaraev *et al.*, 2009, 2011a,b, 2012]. It is evident that, since deep water renewal has been shown to have significant effects on the ecobiology of the whole lake (one of the most important being the high oxygen content throughout the entire water column), a proper description of this process and a careful quantification of its consequences on physical, chemical and biological variables is needed. However, despite this phenomenon has been widely observed and investigated, still significant uncertainty exists in evaluating the extension of the downwelling events. For instance, the volume of typical intrusions in the SB has been estimated in a wide range, from  $10\text{km}^3$  to  $100\text{km}^3$  [Peeters *et al.*, 2000; Wüest *et al.*, 2005; Schmid *et al.*, 2008; Shimaraev *et al.*, 2011a]. Furthermore, as far as we know, no specific studies have been carried out to investigate, and possibly evaluate, the possible effects of climate change on deep ventilation and, in turn, on the intrinsic properties of the lake (e.g. thermal and mixing regimes, temperature and oxygen vertical profiles).

One of the main difficulties in properly investigating and characterizing deep ventilation of Lake Baikal is represented by the limited availability of measurements and observations, concerning both the lake thermal structure and the meteorological forcing. As a matter of fact, due the impressive dimension of the lake and the fact it is located in a very remote region, much of the basin is unmonitored. Only a few datasets are available (see Chapter 5), which, among others, provide important information about water temperature vertical profiles, seasonal cycle of air temperature, typical wind speed and wind patterns over the lake. Anyway, these data present significant spatial and/or temporal resolution limitations, which are one of the major obstacles to their effective use.

Data analysis using sophisticated statistical techniques is a powerful tool that in principle could be adopted to investigate deep ventilation and its possible effects on the limnic ecosystem. Nevertheless, since the significant variables are numerous and the data resolution is poor, data analysis could give rise to controversial results, especially when applied to reconstruct medium- and long-term trends (tens of years to centuries). This suggests numerical modeling as a worthwhile approach to be adopted for simulating the lake behavior over an extended time horizon. Unfortunately, due to the large extension of Lake Baikal and the lack of data (especially about the spatial distribution of the wind) also the application of a three-dimensional model for a rigorous thermo-hydrodynamic study represents a hard task. A huge amount of input data would be necessary (basically, field measurements to estimate the main parameters, define the initial and boundary conditions and

### 3. A simplified 1D model for the numerical simulation of deep ventilation

---

calibrate the model), but sufficient information is not available. As a matter of fact, the main numerical works on deep ventilation adopting 2D or 3D models have been performed referring to very simplified and/or partial domains and considering idealized external conditions (e.g. constant and uniform wind) [Akitomo *et al.*, 1995; Watts and Walker, 1995; Botte and Kay, 2002].

Under these conditions, it is often difficult and uncertain to obtain a rigorous representation of the processes occurring in the real basin, suggesting the development of simplified numerical models as an interesting alternative, coherently with the available measurements and without the need of introducing fictitious spatial distributions of unknown external conditions.

In this study, a one-dimensional, simplified numerical model has been developed, which is suitable to simulate deep ventilation in lakes. It is important to note that the aim is not to reproduce and simulate the complex three-dimensional structure of the process in detail (which would be impossible using a 1D model since the physical phenomenon is inherently three-dimensional), but to investigate its effect over a large spatial scale (i.e. basin scale) and a long temporal horizon (i.e. tens to hundreds of years). For these purposes, only a few data in input are required (consistently with the available measurements), and a simplified structure has been developed, which permits both to reduce the need of artificial parameterization and to ensure a considerable computational time saving.

## 3.2 Formulation of the model

A time-dependent, one-dimensional vertical model has been developed to analyze the phenomenon of deep water renewal occurring in profound lakes. The model consists of three main parts: 1) a reaction-diffusion equation solver for any tracer considered (including temperature); 2) a re-sorting algorithm handling the vertical movements of water volumes due to density instability; and 3) an algorithm reproducing the deep downwelling mechanism. In order to suitably simulate the convective mixing processes, the last two algorithms have been developed following a Lagrangian scheme. This approach represents the major difference from the models previously proposed in the literature [e.g. Killworth *et al.*, 1996; Peeters *et al.*, 1997, 2000; Wüest *et al.*, 2000], which are generally based upon an advection-diffusion equation. Furthermore, a wind-based parameterization derived from physical considerations has been formulated, which is aimed at estimating the major variables characterizing the occurrence of a deep downwelling: the downwelling volume,  $V_d$ , and the energy input from external factors,  $E_w$ . The three core algorithms and the wind-based parameterization are described in Sections 3.2.1, 3.2.2, 3.2.3 and 3.2.4, respectively, while the current section outlines the general features and relevant assumptions of the model.

All the thermophysical properties (e.g. density  $\rho$ , thermal expansivity  $\alpha$ , specific heat capacity



### 3. A simplified 1D model for the numerical simulation of deep ventilation

---

$c_p$ ) are derived from the *Chen and Millero* [1986] equation of state for freshwater (see Section 2.2.1). Following *Killworth et al.* [1996] and *Wüest et al.* [2005], salinity has been assumed to contribute little to the density stratification of Lake Baikal, thus its contribution has been neglected. On the contrary, the dependence of density on pressure has been retained, since it is crucial for the onset of thermobaric instability and thus for the occurrence of deep ventilation (see Section 2.2.4 for a detailed description of the phenomenon). The pressure  $P$  is assumed as hydrostatic:

$$\frac{dP}{dz} = \rho g, \quad (3.1)$$

where  $z$  is the vertical coordinate defined positive downward ( $z = 0$  at the free surface),  $g$  is the gravitational acceleration and  $P = 0$  at the lake surface (coherently with the equation of state by *Chen and Millero* [1986]). The hydrostatic approximation is convenient and justified for investigations of processes where the horizontal scale is large enough and the instantaneous behavior is not essential.

The stability of the water column is assessed by means of the rigorous definition of the squared Brunt-Väisälä buoyancy frequency  $N^2$  given in Equation (2.8), which includes the effect of the adiabatic temperature gradient  $\Gamma$ . As already mentioned in Section 2.2.2,  $\Gamma$  is known to be small, in particular for water temperatures approaching values near  $T_{\rho,max}$ , where it vanishes. However, especially if thermal stratification is weak,  $\Gamma$  could be close to the actual temperature gradient, thus becoming important for the analysis of the local stability of the water column.

The physical domain is vertically discretized using a finite volume scheme, which divides the entire water body into  $n$  sub-volumes having the same volume. Such a constant-volume discretization scheme leads to an easy management of both the mixing due to density instability and the downwellings due to deep ventilation: in both cases, the column of sub-volumes is reorganized by simply rearranging the sub-volumes involved in the process. The number of sub-volumes is decided *a priori* looking for a compromise between a good resolution and little computational efforts. It is worth to notice that since in natural freshwater basins the horizontal cross section is generally not constant (diminishes) with depth, the use of a constant-volume discretization will inevitably lead to sub-volumes having a vertical dimension that varies (increases) with depth, with a rate that depends on the hypsometric curve of the lake. In this study, the model has been applied to the case of the South Basin of Lake Baikal (having a maximum depth of 1461 m and a volume of about 6360 km<sup>3</sup>), whose hypsometric curve is shown in Figure 3.1. In this case, the domain has been discretized into 159 sub-volumes (having the same volume of 40 km<sup>3</sup>), characterized by minimum, maximum and mean vertical dimension of about 5 m, 66 m and 9 m, respectively.

### 3. A simplified 1D model for the numerical simulation of deep ventilation

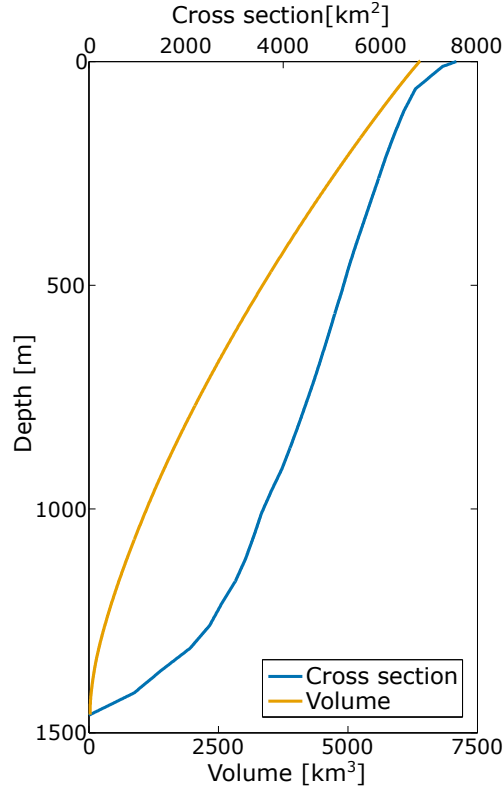


Figure 3.1: Hypsometric curve of the South Basin of Lake Baikal: variation of the cross section and of the cumulative water volume with depth [from the bathymetry provided by *The INTAS Project 99-1669 Team*, 2002]

#### 3.2.1 Reaction-diffusion equation solver

The dynamics of a generic tracer  $C$  (e.g. temperature, dissolved oxygen, salinity, biological tracers, etc.) is described by a reaction-diffusion equation

$$\frac{\partial C}{\partial t} = -\frac{1}{A} \frac{\partial(A\phi_C)}{\partial z} + R, \quad (3.2)$$

$$\phi_C = -D_z \frac{\partial C}{\partial z}, \quad (3.3)$$

where  $t$  is the temporal variable,  $A$  is the horizontal surface at a fixed depth,  $\phi_C$  is the vertical diffusive flux,  $D_z$  is the diapycnal turbulent diffusivity, and  $R$  is the reaction (source) term. Note that the vertical axis  $z$  is positive downward. Equation (3.2) is defined over the entire water column  $[0, Z]$ , where  $Z$  is the maximum depth of the basin.

As regards the reaction (source) term  $R$ , it depends on the type of tracer and on the physical, chemical and biological processes involved. In general, it is reasonable to define  $R$  as the combina-

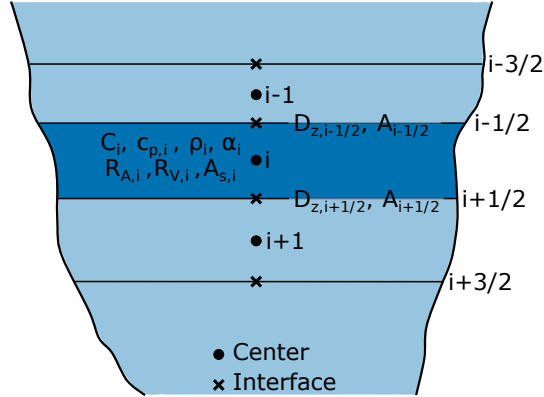


Figure 3.2: Staggered grid used to solve the reaction-diffusion equation.

tion of a volumetric contribution  $R_V$ , due to the processes occurring within the sub-volume, and of an areal contribution  $R_A$  (having the dimension of a flux), which quantifies the reactions taking place at the sediment-water interface [Livingstone and Imboden, 1996; Peeters et al., 2000]. For the  $i^{th}$  sub-volume

$$R_i = R_{V,i} + R_{A,i} \frac{dA_{S,i}}{dV_i}, \quad (3.4)$$

where  $dV_i$  and  $dA_{S,i}$  are the water volume and the surface area of the sediment-water interface, respectively, of the  $i^{th}$  sub-volume (note that the subscript  $i$  associated to  $dV$  is unnecessary, since the water column is discretized into sub-volumes having the same volume). The volumetric and areal reaction terms for the variables examined in this work (temperature  $T$ , dissolved oxygen  $DO$  and  $CFC-12$  concentration) are summarized in Table 3.1.

An implicit scheme (backward Euler) has been used to solve the reaction-diffusion equation, which ensures an unconditionally stable numerical solution, and hence does not require any restriction on time step,  $\Delta t$ . Aimed at guaranteeing both good temporal resolution of the results and little computational cost, a time step of half a day has been chosen ( $\Delta t = 12h$ ). Such a time step is an appropriate time scale for the physical processes included in the model: diffusive processes, stabilization of unstable regions, wind forcing and surface temperature variation. Both the reaction-diffusion solver and the stability algorithm handling buoyant mixing are solved with this temporal step. On the other hand, the algorithm handling deep ventilation uses a different time step,  $\Delta t_{down}$ , which is a multiple of  $\Delta t$  and represents the temporal scale of the downwelling events.  $\Delta t_{down}$  has been fixed equal to three days ( $\Delta t_{down} = 72h$ ), as further discussed in Section 3.3.2.

For the numerical solution of Equation (3.2), a staggered grid has been used, in which the generic tracer  $C$ , the thermophysical variables ( $\rho$ ,  $\alpha$  and  $c_p$ ) and the reaction terms ( $R_V$  and  $R_A$ ) are defined at the center of each sub-volume and the turbulent diffusivity  $D_z$  at the interfaces, thus allowing for a mass-conservative definition of the fluxes (Figure 3.2).

### 3.2.2 Stability algorithm

At each time step  $\Delta t$ , the entire water column is tested for static stability by analyzing in pairs each couple of neighbor sub-volumes  $i$  and  $i + 1$  (respectively centered in  $z_i$  and  $z_{i+1}$ , see Figure 3.3). Both the sub-volumes are ideally shifted toward their mid-depth  $z_{i,mid}$ . Following the adiabatic transformation (2.7), in  $z_{i,mid}$  two new values of temperature are computed:  $T_{i,down}$  of the upper sub-volume ( $i$ ) displaced downward, and  $T_{i+1,up}$  of the lower sub-volume ( $i + 1$ ) displaced upward. Finally, the density associated to each sub-volume is computed with the new values of temperature and pressure at  $z_{i,mid}$ , and the local stability is tested according to the following condition

$$\begin{aligned} \Delta\rho(T,P)|_{z_{i,mid}} &> 0 \rightarrow \textit{stable} \\ \Delta\rho(T,P)|_{z_{i,mid}} &= 0 \rightarrow \textit{neutral} \\ \Delta\rho(T,P)|_{z_{i,mid}} &< 0 \rightarrow \textit{unstable} \end{aligned} \quad (3.5)$$

where

$$\begin{aligned} \Delta\rho(T,P)|_{z_{i,mid}} &= \\ \rho(T_{i+1,up}, P(z_{i,mid})) &- \rho(T_{i,down}, P(z_{i,mid})). \end{aligned} \quad (3.6)$$

Starting by the pair of sub-volumes showing the higher instability, the water column is progressively adjusted by simply exchanging the unstable sub-volumes until a stable configuration is achieved. In performing this operation, a mixing coefficient  $c_{mix}$  is introduced, which accounts for the mixing exchanges occurring between each couple of unstable sub-volumes. As a matter of fact, buoyancy-driven convection in a conditionally unstable water column acts as an additional source of turbulent kinetic energy, thus enhancing turbulence and mixing [e.g *Lorke et al.*, 2005]. For the generic tracer  $C$ , the correction due to mixing is calculated as

$$C_i^* = C_{i+1} - c_{mix}\Delta C, \quad (3.7)$$

$$C_{i+1}^* = C_i + c_{mix}\Delta C, \quad (3.8)$$

where  $\Delta C = C_{i+1} - C_i$  and  $C^*$  indicates the corrected value of  $C$ . Note that by performing this operation the overall mass of the generic tracer  $C$  is conserved as volumes are equal. For the specific case of temperature, Equations (3.7) and (3.8) are modified by including the contribution of the adiabatic transformation  $\Gamma$ , which arises from switching each couple of unstable sub-volumes

$$T_i^* = T_{i+1} - \Gamma_{i+1}dz - c_{mix}\Delta T, \quad (3.9)$$

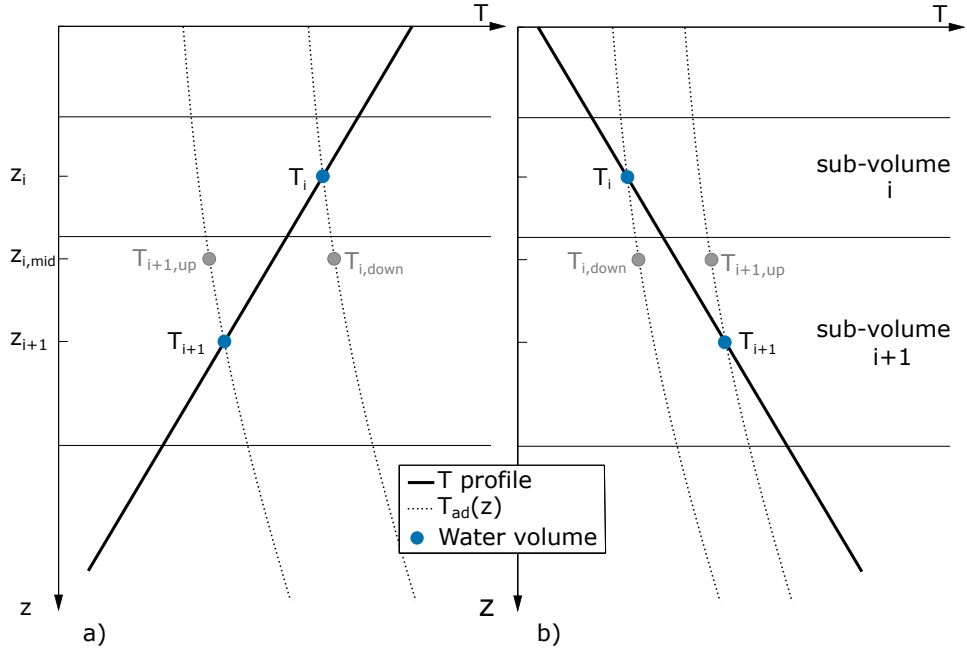


Figure 3.3: Sketch for the stability evaluation procedure (for the case  $\alpha > 0$ ): a) stable profile ( $\Delta\rho(T, P_{i,mid}) > 0$ ), b) unstable profile ( $\Delta\rho(T, P_{i,mid}) < 0$ ). The dashed lines represent the adiabatic path.

$$T_{i+1}^* = T_i + \Gamma_i dz + c_{mix} \Delta T, \quad (3.10)$$

where  $\Delta T = T_{i+1} - T_i$ ,  $dz = z_{i+1} - z_i$ ,  $\Gamma_i$  and  $\Gamma_{i+1}$  are the adiabatic temperature gradients calculated for the sub-volumes  $i$  and  $i + 1$ , respectively, and  $T^*$  indicates the corrected value of  $T$ .

### 3.2.3 Downwelling algorithm

In order to handle the convective flows due to deep ventilation, a Lagrangian-based algorithm is performed at every downwelling time step  $\Delta t_{down}$ . Each sub-volume is temporarily discretized in  $m$  homogeneous, smaller parts (hereafter subparts) having the same value of  $C$  as that of the initial sub-volume. For the specific application to the South Basin of Lake Baikal, each sub-volume ( $40 \text{ km}^3$ ) has been divided in 8 subparts having a volume,  $\delta V$ , of  $5 \text{ km}^3$  each. This allows one to solve deep convection using a finer spatial resolution, with an acceptable increase of the computational time.

On the basis of the phenomenological description of thermobaric instability given in Section 2.2.4, it is evident that deep ventilation can occur when the lake is relatively weakly stratified and a sufficient amount of energy is transferred from the external forcing (primarily the wind) to the lake. Hence, at a given time, the process is completely determined when the following three information

### 3. A simplified 1D model for the numerical simulation of deep ventilation

---

are known: the temperature profile, the sinking volume  $V_d$  and the amount of energy input  $E_w$  provided by external forcing. The temperature profile, is given by the solution of Equation (3.2, and hence is known at every time step  $\Delta t$ , while both  $V_d$  and  $E_w$  need to be estimated at every downwelling time step,  $\Delta t_{down}$ , for instance by means of the wind-based parameterization proposed in Section 3.2.4. As a matter of fact, the most important source of kinetic energy for lakes is generally the wind [e.g. *Imboden and Wüest, 1995*], and also in the case of Lake Baikal it has been identified as the major driving force for diapycnal mixing [*Wüest et al., 2000*].

Provided the temperature profile and the sinking volume  $V_d$ , the downwelling temperature  $T_d$  and the compensation depth  $h_c$  are calculated respectively as: 1) the mean temperature of the uppermost part of the water column that corresponds to a volume of  $V_d$ , and 2) the depth at which the sinking volume  $V_d$  shows the same density as the surrounding water. Note that, because of the typical thermal profile during downwelling events, the temperature of the ambient water at  $h_c$  and that of the descending volume are usually different, being the former above  $T_{\rho,max}$  and the latter below  $T_{\rho,max}$ .

Based upon these information, it is possible to determine the energy per unit volume  $e_c$  required for triggering thermobaric instability (the subscript  $c$  standing for critical or for compensation), which is the amount of energy necessary for the descending water volume  $V_d$  to overcome the buoyancy forces and reach the compensation depth  $h_c$ . This is calculated by summing the energy variations of all the consecutive switches of positions between sub-volumes parts to bring  $V_d$  from the surface down to  $h_c$ . We recall that all sub-volumes parts are characterized by the same  $\delta V$ .

Since the potential energy of a generic subpart  $i$  is  $e_i = \rho_i g z_i$ , where  $z_i$  is the depth of its barycenter and  $\rho_i = \rho(i)$  its density, each switch from a stable condition to a temporarily unstable one (resulting from moving lighter water from the position  $i$  downward to  $i + 1$ ) requires an external energy input  $\delta e_{i,i+1} = g(\rho_{i+1} - \rho_i)(z_{i+1} - z_i)$ , which is positive since  $\rho_{i+1} > \rho_i$  in locally stable conditions. Therefore, for a generic subpart  $i_d$  composing  $V_d$ , the required energy is

$$e_c(i_d) = \sum_{i=i_d}^{i_c-1} g[\rho(i+1) - \rho^*(i; i_d)] (z_{i+1} - z_i), \quad (3.11)$$

where  $i_c$  is the index of the subpart corresponding to the compensation depth  $h_c$ , and  $\rho^*(i; i_d)$  is the density of the descending subpart, whose initial density may change in each adiabatic switch due to the effect of increasing pressure.

Assuming that the downwelling is composed by  $m_d$  subparts, i.e.  $V_d = m_d \delta V$ , the specific energy required as a whole is

$$e_c = \frac{1}{V_d} \sum_{i_d=1}^{m_d} e_c(i_d) \delta V = \frac{1}{m_d} \sum_{i_d=1}^{m_d} e_c(i_d), \quad (3.12)$$

which can be reasonably approximated by a single estimate of Equation (3.11) where  $i_d$  is chosen as the subpart corresponding to the barycenter of  $V_d$ .

It is clear that thermobaric instability (thus deep ventilation) can occur when sufficient total energy  $E_w$  is provided by the external forces, hence when  $E_w > e_c V_d$ .

Introducing  $e_w = E_w/V_d$  as the specific external energy available to displace the volume  $V_d$ , a downwelling can occur only partially if  $e_w < e_c$  (see Figure 2.9c,d). In this case the arrival depth  $h_s$  ( $< h_c$ ) can be defined as the position at which the sinking surface water volume  $V_d$  stops because of the lack of external energy. The downwelling water is shifted until this depth, where it results lighter than the surrounding water. On the contrary, if  $e_w > e_c$  a complete downwelling occurs, and the surface water volume  $V_d$  is displaced beneath  $h_c$ , where its density becomes larger than the ambient water (2.9a,b). In both cases, the downward displacement of  $V_d$  follows an adiabatic transformation corrected by the introduction of a mixing coefficient  $c'_{mix}$ , which allows one to consider partial exchanges between the ambient water and the volume  $V_d$  during its descent. Such a correction has been applied to all tracers, adopting the same procedure as in Equations (3.7)–(3.10). It is important to note that  $c_{mix}$  is inherently different from  $c'_{mix}$ , as they refer to two different mixing processes: the first coefficient is related with the relatively slow mixing following the stabilization of large, widespread unstable water layers (e.g. convective instabilities arising from the daily cycle of surface temperature, a relatively slow process during which the mixing is intense), while the second is linked to the intrusion of relatively small and localized unstable volumes. In case the background turbulence of the deep layer (i.e. beneath  $h_c$ ) is small, the sinking volume may penetrate to depth without appreciable mixing with the surrounding stable water [Garwood *et al.*, 1994], which suggests that  $c'_{mix}$  is expected to be smaller than  $c_{mix}$ .

In general, both for  $e_w < e_c$  and  $e_w > e_c$ , the temperature profile subsequent the sinking of  $V_d$  is unstable, and the downwelling procedure is completed running the stability algorithm previously discussed, but retaining the mixing coefficient  $c'_{mix}$  instead of  $c_{mix}$ .

The downwelling procedure is concluded by re-establishing the former spatial discretization, re-combining together the subparts in groups of  $m$  elements and computing the mean value of the generic tracer  $C$  for each group. In this way, all the variables are conserved. Furthermore, the overall procedure implicitly accounts for the compensating upwelling of water resulting as a consequence of deep downwellings through the Lagrangian switch of the subvolumes, and hence allows to conserve the total volume of the system.

#### 3.2.4 Wind-based parameterization

In order to separately estimate the wind energy input per unit volume  $e_w$  and the downwelling volume  $V_d$ , two relationships are needed, depending by at least two quantities. The natural choice is to select wind speed and duration as independent variables. With the aim of facing the lack of

### 3. A simplified 1D model for the numerical simulation of deep ventilation

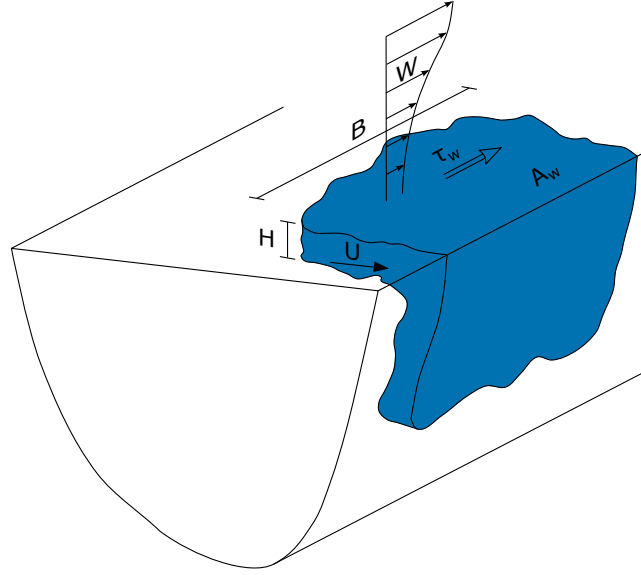


Figure 3.4: Schematic representation of the parameters used to describe the energy transferred by the wind to the surface layers of the lake. For simplicity of representation, the drawing shows a coastal downwelling due to inshore Ekman transport generated by a wind blowing parallel to the coast.

data and the complexity of the physics involved, the following simplified approach is proposed, where physically based relations are introduced and only two calibration parameters are needed.

The energy input  $\delta E_w$  transferred from wind to the water mass in the time step  $\delta t$  can be estimated as

$$\delta E_w \sim \tau_w A_w U \delta t, \quad (3.13)$$

where  $\tau_w$  is the wind shear stress,  $U$  is the mean water velocity within the wind-driven layer, and  $A_w$  represents the portion of water surface affected by wind.  $U \delta t$  is the displacement of the volume of water  $\delta V_d$  moved by the wind force  $\tau_w A_w$ . Analogously, the displaced volume  $\delta V_d$  could be approximated as

$$\delta V_d \sim H B U \delta t, \quad (3.14)$$

where  $H$  is the depth of the surface wind-affected layer and  $B$  is the extension of the wind affected area in the direction perpendicular to the water movement (see Figure 3.4 for a conceptual sketch, see also *Boehrer and Schultze [2008]*). The external specific energy input  $e_w$  is obtained by (3.13) and (3.14) as

$$e_w \sim \frac{\delta E_w}{\delta V_d} = \tau_w \frac{A_w}{H B}, \quad (3.15)$$

where the time  $\delta t$  disappears.



The frictional transfer of momentum from wind to water takes place within the wind-driven boundary layer  $H$ . In geophysical flows, the length scale of this layer is often assumed as that of the surface Ekman layer, thus  $H \propto u_*/f$ , where  $u_* = \sqrt{\tau_w/\rho}$  is the friction velocity and  $f$  the Coriolis frequency. Substituting this relationship into Equation (3.15) and defining  $\tau_w = \rho_a C_D W^2$ , where  $W$  is the wind velocity,  $C_D$  is the wind drag coefficient, and  $\rho_a$  the air density, gives

$$e_w = \xi \sqrt{C_D} W. \quad (3.16)$$

where  $\xi$  is a parameter that needs to be calibrated since a rigorous physical evaluation is not possible on the basis of the available data. We assume (3.16) as a general relationship, independent of the specific mechanism,  $\xi$  representing the geometry of the portion of lake surface involved in the deep ventilation process.

Assuming that the mean water velocity  $U$  is proportional to  $u_*$ , with the same definition of  $H$  as above, Equation (3.14) yields

$$V_d = \eta C_D W^2 \Delta t_w, \quad (3.17)$$

where  $\eta$  is the second parameter to be calibrated. A constant value of  $\eta$  implies that a typical average value of  $B$  is fixed.

The problem is finally closed by assuming an empirical relationship for the drag coefficient: given the uncertainties in the derivation, a linear dependence  $C_D = a + bW$  (where  $a = 0.8$  and  $b = 0.065$ , *Wu* [1982]) is probably sufficient.

As a whole the proposed parameterization, composed of Equations (3.16) and (3.17), allows for the estimation of the specific external energy,  $e_w$ , and of the sinking volume,  $V_d$ , using two quantities, namely the wind velocity,  $W$ , and the wind duration,  $\Delta t_w$ . Wind direction is not explicitly included in the model since data are not available, however its overall contribution to the downwelling process is implicitly accounted for in the calibration parameters.

### 3.3 External forcing and internal dynamics

The simple structure of the 1D model presented in the previous section allows for its application over long-term temporal horizons with a reasonable computational cost. The large amount of information that is theoretically required to calibrate and validate a model for long term simulations, is significantly reduced thanks to the different modules (vertical diffusion, density stabilization, downwelling displacement and triggering of the process by wind forcing), which have been developed with the aim to reduce the amount of input data needed by the overall model. Still there are some internal parameters to be calibrated, like the vertical diffusivity profile, the parameters  $c_{mix}$  and  $c'_{mix}$ , introduced in Sections 3.2.2 and 3.2.3 respectively, and  $\xi$  and  $\eta$  introduced in Section

### 3. A simplified 1D model for the numerical simulation of deep ventilation

Table 3.1: Boundary conditions and reaction term for temperature, dissolved oxygen and *CFC* concentration

Variable	Surface B.C.	Bottom B.C.	$R_V$	$R_A$
Temperature	$T = T_{\text{surf}}$	$\phi_T _Z = -\frac{q_{\text{geo}}}{c_p \rho _Z}$	$R_{V,T} = 0$	$R_{A,T} = \frac{q_{\text{geo}}}{c_p \rho}$
Dissolved Oxygen	$DO = DO_{\text{surf}}$	$\phi_{DO} _Z = R_{A,DO}$	$R_{V,DO} =$ volumetric oxygen consumption	$R_{A,DO} =$ sediment oxygen consumption
<i>CFC</i> -12 Concentration	$CFC = CFC_{\text{surf}}$	$\phi_{CFC} _Z = 0$	$R_{V,CFC} = 0$	$R_{A,CFC} = 0$

3.2.4. Once these quantities are calibrated, the only additional data required by the model is the climate forcing: lake surface temperature (and surface boundary conditions for any other tracer) and wind velocity and duration.

#### 3.3.1 Initial conditions, boundary conditions and reaction terms

**Initial and boundary conditions** - Initial and boundary conditions are required in order to solve Equation 3.2. For the generic tracer  $C$ , the initial condition is provided by vertical profiles based on available measurements, while the boundary conditions at the free surface and at the bottom are respectively fixed through: 1) the assignment of the value of the generic tracer  $C = C_{\text{surf}}$  at the surface, according to measures or analytical relationships; and 2) by the imposition of a Neumann condition assigning the flux  $\phi_C$  at the bottom of the lake. During the ice cover period, the no flux condition has been assumed at the surface for the generic tracer  $C$  other than temperature.

Three variables have been examined in this work: temperature  $T$ , dissolved oxygen concentration  $DO$ , and dichlorodifluoromethane concentration *CFC*-12. The boundary conditions for each variable are listed in Table 3.1, together with the reaction terms  $R_V$  and  $R_A$  introduced in Equation (3.4). Note that for all variables,  $R_A = 0$  at the lowest sub-volume since it is included as the flux imposed in the bottom boundary condition.

Initial and surface boundary conditions are shown and discussed in details in Chapter 5, where the available data are presented.

**Reaction terms** - Concerning temperature, the only source term is that at the sediment-water interface (i.e.  $R_V = 0$ ) and is determined by the geothermal heat flux  $q_{\text{geo}}$ . Observations conducted on the lake revealed mean  $q_{\text{geo}}$  values ranging from about  $80 \text{ mW m}^{-2}$  at the bottom to about  $55 \text{ mW m}^{-2}$  at the sides of the lake [Dorofeeva and Lysak, 1989; Lysak, 2002; Golubev, 2010]. The vertical variation of  $q_{\text{geo}}$  considered in this work is shown in Figure 3.5, and has been determined as a result of the model calibration procedure (see Chapter 6), performed on the basis of these observations in the literature. Analogously, the vertical profile of oxygen consumption rate has been calibrated assuming as reference values the volumetric and areal depletion rates proposed by Peeters *et al.* [1997]:  $R_V = 44 \pm 3 \text{ mgO}_2 \text{ m}^{-3} \text{ yr}^{-1}$  and  $R_A = 17000 \pm 3000 \text{ mgO}_2 \text{ m}^{-2} \text{ yr}^{-1}$ . The

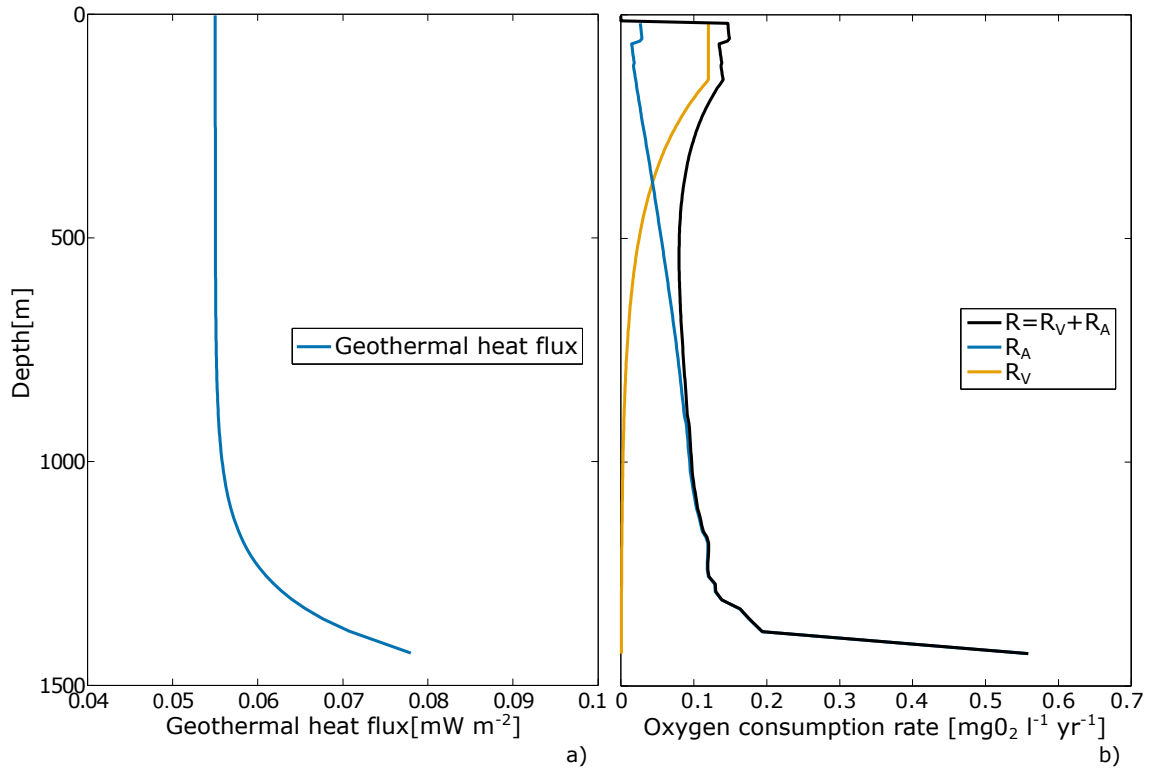


Figure 3.5: a) Vertical variation of the geothermal heat flux and b) vertical profile of oxygen consumption rate. Both profiles have been obtained through the model calibration procedure, assuming observations and estimates available in the literature as reference values.

resulting volumetric, areal and total depletion rate curves are shown in Figure 3.5. According to *Peeters et al.* [1997], the net oxygen flux has been assumed to be zero within the uppermost layers of the lake, where oxygen depletion and oxygen production are likely to be comparable. Beneath that depths and within the upper 150 – 200 m, the oxygen depletion is likely to increase due to the high ratio of sediment area to water volume [*Hohmann et al.*, 1997], and because of the oxidation of organic matter sedimenting from the surface into deep water. In the interior of the lake the total consumption rate diminishes, whilst it sharply increases near the bottom, as a consequence of the large sediment surface per unit volume that characterizes the bottom layers of the lake [*Peeters et al.*, 2000]. The mean value of oxygen depletion rate in the hypolimnion is about  $0.1 \text{ mgO}_2 \text{ l}^{-1} \text{ yr}^{-1}$ , which agrees well with the values of  $0.075 \div 0.1 \text{ mgO}_2 \text{ l}^{-1} \text{ yr}^{-1}$  determined by *Peeters et al.* [1997, 2000], and the estimates of *Weiss et al.* [1991]; *Hohmann et al.* [1997] that range from  $0.12 \text{ mgO}_2 \text{ l}^{-1} \text{ yr}^{-1}$  to  $0.14 \text{ mgO}_2 \text{ l}^{-1} \text{ yr}^{-1}$ .

#### 3.3.2 Reconstruction of external forcing

Estimating the wind forcing is one of the main problems. As it has been anticipated (see Section 3.2.4), determining the exact amount of energy transferred from the wind to the lake on the basis of measurements is almost impossible. Theoretically, information about wind is required on the whole lake surface, in continuous and for long time periods. However, the only viable alternative is to reconstruct a time series of spatially averaged values of wind speed. As direct measurements are not accessible (see Chapter 5), such operation can be carried out only by either using reconstructed series of data or by developing a probabilistic approach, depending on which data are available. Analogously, the same considerations can be addressed for surface water temperature.

In this study, time series of spatially averaged wind forcing (speed and duration) and temperature are available for the periods of interest. As a matter of fact, the model has been calibrated using historical re-analysis dataset for the period 1958 – 1998, and successively applied to investigate the future behavior of the lake in response to different climate change scenarios for the 21<sup>st</sup> century. Both the datasets provide a chronological description of the series of meteorological conditions in Lake Baikal region, holding information about wind speed and temperature with a temporal resolution of 6 hours (see Chapter 5 for a detailed description of the data). With these information, the external forcing can be reconstructed as follows. At every time step  $\Delta t$ , the corresponding value of surface water temperature  $T_{surf}$  is assigned in the upper layer, thus defining the surface boundary condition. Concerning the wind forcing, at each downwelling time step ( $\Delta t_{down}$ ),  $n_w$  subsequent values of wind speed,  $W$ , are extracted from the chronological sequence of events. Each wind event is characterized by a specific duration  $\Delta t_w$ , which in this case is constant and equal to 6 hours (i.e. the temporal resolution of re-analysis and climate scenarios datasets). Accordingly, the number of events throughout the downwelling time step is defined as  $n_w = \Delta t_{down} / \Delta t_w$ .  $\Delta t_{down}$  has been fixed considering the typical time scale of deep downwelling events, which is a few days [Wüest *et al.*, 2005]. In the light of past observations,  $\Delta t_{down}$  has been chosen equal to three days, which is reasonably long to ensure sufficient transfer of energy from wind to water and sufficiently short to permit a good resolution in simulating deep ventilation. It is worth to note that  $\Delta t_{down}$  does not have the meaning of a mere computational time step, but is rather a physical parameter representing the time scale of the deep ventilation process.

Associated to each  $j^{th}$  value of wind speed  $W_j$ ,  $j = [1, n_w]$ , the corresponding values of specific energy input  $e_{w,j}$  and sinking volume  $V_{d,j}$  are calculated from Equations (3.16) and (3.17), respectively. Successively, the  $n_w$  results obtained for both physical quantities are combined to calculate the global values of  $e_w$  and  $V_d$  referred to the temporal interval  $\Delta t_{down}$ , which are used as input in

the downwelling algorithm (see Section 3.2.3)

$$V_d = \sum_{j=1}^{n_w} V_{d,j}, \quad (3.18)$$

$$e_w = \sum_{j=1}^{n_w} e_{w,j} V_{d,j} / V_d. \quad (3.19)$$

Analogously, the effective wind speed,  $W_{eff}$ , is computed

$$W_{eff} = \frac{e_w}{\xi \sqrt{C_D}}, \quad (3.20)$$

where  $C_D$  is a function of  $W_{eff}$  (i.e. the equation is implicit).

The reconstruction of wind forcing is only applied during the ice free season, while during the ice cover period the wind effect does not drives any circulation due to the ice sheltering. In order to establish when the lake surface is frozen or not, a threshold temperature in the upper layer have been introduced. Such a value has been set to  $1^\circ\text{C}$  on the basis of observations on ice cover formation and break-up [Peeters *et al.*, 2002] (see Figure 5.1 and Section 5.1.1 for further details).

On the other hand, if only probabilistic distributions of surface water temperature and wind speed and duration are known, a different procedure should be adopted, which is based on a stochastic reconstruction of the two climatic variables. At each simulation year, an annual cycle of surface water temperature is randomly interpolated from those available, and it is assigned as water temperature in the upper layer. Concerning the wind forcing, at every downwelling time step  $n_w$  values of wind speed,  $W$ , are randomly extracted from the available probabilistic curve (note that in principle more than one probabilistic curve of wind speed may be used, depending on whether the seasonality of wind is important or not). The wind duration  $\Delta t_{w,j}$ ,  $j = [1, n_w]$ , corresponding to the  $j$ th wind event is randomly sampled from the probabilistic curve of wind duration associated with the wind class whose  $W, j$  belongs. The random sampling stops when the cumulative duration of the  $n_w$  wind events achieve the downwelling time step  $\Delta t_{down}$ . Note that, since  $\Delta t_{w,j}$  are not constant,  $\sum_{j=1}^{n_w} \Delta t_{w,j}$  could be greater than  $\Delta t_{down}$ . In this case, the wind duration excess is transferred to the next downwelling time step.

Eventually, the specific energy input  $e_w$ , sinking volume  $V_d$  and effective wind speed  $W_{eff}$  are calculated through Equations (3.18), (3.19) and (3.20), respectively.

Both the reconstruction of the chronological series of events and the probabilistic approach have been tested, obtaining good results in the two cases. However, only the first approach allows for a consistent chronological description of the meteorological conditions occurred during a defined

historical period, which is an essential prerequisite for a robust calibration. For this reason, in this work the external forcing has been reconstructed through the first, more rigorous procedure. An application of the stochastic approach can be found in *Piccolroaz and Toffolon [2011]*.

## 3.4 Diapycnal diffusivity derivation

In stratified natural waters, diffusivity is influenced by the combination of turbulence at the boundaries and in the interior of the water body [*Wüest and Lorke, 2003*], which, in turn, are controlled by boundary layer processes and internal mixing mechanisms. As a consequence, the diapycnal diffusivity profile is characterized by a clear annual pattern, which is primarily controlled by its strong dependence on stratification. Furthermore, diffusivity profile may undergo significant inter-annual variability, due to changes in external forcing (e.g. inter-annual fluctuations, climate change), and possibly due to the memory of past downwelling events. Aimed at incorporating these features, a simple procedure has been developed with the purpose to dynamically reconstruct the seasonal and inter-annual evolution of diapycnal diffusivity.

### 3.4.1 Richardson number-based schemes

Parameterization of turbulent vertical mixing remains a main issue in hydrodynamic modeling. Among the several methods proposed in the literature, a simple and widely used approach has been assumed, in which the vertical turbulent diffusivity is calculated accounting for the relative importance of buoyancy forces and shear effects in the water column. According to this approach, the vertical turbulent diffusivity,  $D_z$ , is obtained multiplying a reference value  $D_{z,r}$  by a damping function of the Richardson number

$$Ri = \frac{N^2}{S^2} = \frac{N^2}{(dU/dz)^2}, \quad (3.21)$$

where  $N$  is the Brunt-Väisälä buoyancy frequency, defined as in Equations (2.10) and (2.8),  $U$  is the horizontal velocity of water and  $S$  is the shear frequency, defined as in Section 3.4.2. A negative value of  $Ri$  indicates unstable density gradients (i.e.  $N^2 < 0$ ) with active convective overturning. When  $Ri$  is small (smaller than about 0.25 according to the classical theory), then velocity shear is considered sufficient to overcome the stabilizing effects of stratification, and some mixing will generally occur. Finally, when  $Ri$  is large, turbulent mixing across the stratification is generally suppressed.

The following well-known empirical formula based on *Munk and Anderson [1948]*,

$$D_z = \frac{D_{z,r}}{(1 + aRi^b)^c} + D_{z,bg}, \quad (3.22)$$

has been used, where  $D_{z,r}$  represents the upper limit for turbulent diffusivity,  $D_{z,bg}$  is a background value of diapycnal diffusivity (introduced in the formulation given by *Pacanowski and Philander* [1981]), and  $a$ ,  $b$ , and  $c$  are positive parameters ( $a = 10/3$ ,  $b = 1$  and  $c = 3/2$ , in the original formulation by *Munk and Anderson* [1948]). These parameters do not have specific values but rather can vary in a wide range, depending on which of the several relationships in the literature is considered [e.g. *Deardorff*, 1967; *Sundaram and Rehm*, 1971; *Pacanowski and Philander*, 1981; *Henderson-Sellers*, 1982].

*Large et al.* [1994] proposed an alternative Richardson number-dependent parameterization of  $D_z$ , which is basically a modification of Equation (3.22)

$$\begin{aligned}
 D_z &= D_{z,r} + D_{z,bg}, & Ri < 0 \\
 D_z &= D_{z,r} \left[ 1 - \left( \frac{Ri}{Ri_0} \right)^2 \right]^3 + D_{z,bg}, & 0 < Ri < Ri_0 \\
 D_z &= +D_{z,bg}, & Ri_0 < Ri
 \end{aligned} \tag{3.23}$$

where  $Ri_0 = 0.7$  is a threshold value for  $Ri$ . This scheme is commonly used to parametrize the shear-induced mixing in the ocean's interior, but it found wide application also in numerical modeling of lakes [e.g. *Sheng and Rao*, 2006; *Bennington et al.*, 2010].

For the purposes of this work, the vertical mixing parameterization proposed by *Large et al.* [1994] has been rewritten into the form of Equation (3.22), thus removing the threshold on  $Ri$  and providing an asymptotic trend for high  $Ri$  values. Expanding Equations (3.22) and (3.23) in Taylor series, and taking the limit  $Ri \rightarrow 0$  yields

$$\frac{D_z}{D_{z,r}} = 1 - ac Ri^b + O(Ri^{2b}), \tag{3.24}$$

$$\frac{D_z}{D_{z,r}} = 1 - 3 \left( \frac{Ri}{Ri_0} \right)^2 + O(Ri^5), \tag{3.25}$$

whose comparison leads to  $a = 1/Ri_0^2$ ,  $b = 2$  and  $c = 3$ . Figure 3.6 shows the variation of  $D_z$  as a function of  $Ri$ , calculated using the formulations of *Munk and Anderson* [1948] and *Large et al.* [1994], and solving Equation (3.22) with the parameters  $a$ ,  $b$  and  $c$  specified above ( $a = 1/Ri_0^2$ ,  $b = 2$  and  $c = 3$ ). In all cases,  $D_{z,r} = 8 \times 10^{-4} \text{ m}^2 \text{ s}^{-1}$  and  $D_z = 5 \times 10^{-5} \text{ m}^2 \text{ s}^{-1}$  have been assumed, which are consistent with previous estimates available in the literature [e.g. *Wüest et al.*, 2000; *Schmid et al.*, 2007].

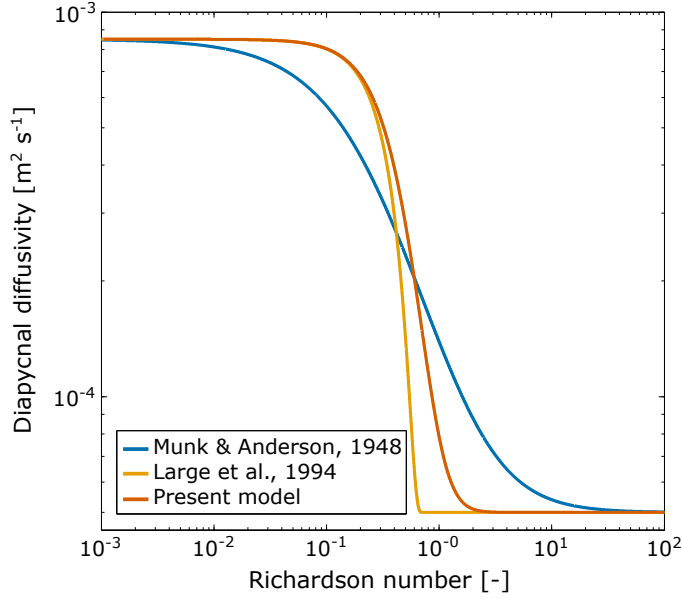


Figure 3.6: Diapycnal diffusivity as a function of the local Richardson number, following the models proposed by *Munk and Anderson* [1948] and *Large et al.* [1994], and as calculated solving Equation (3.22) with  $a = 1/Ri_0^2$ ,  $b = 2$ ,  $c = 3$ ,  $D_{z,r} = 8 \times 10^{-4} \text{ m}^2 \text{ s}^{-1}$  and  $D_{z,bg} = 5 \times 10^{-5} \text{ m}^2 \text{ s}^{-1}$ .

### 3.4.2 Shear frequency

In order to evaluate the Richardson number  $Ri$  from its definition in Equation (3.21), the shear frequency  $S$  is needed, besides the Brunt-Väisälä buoyancy frequency  $N$ . As the simplified 1D model does not solve the flow field, in principle no information about the shear stress are available. Hence,  $S$  cannot be calculated according to its physical definition  $S = dU/dz$ , but a further parameterization is required. Adapting a formulation proposed by *Mellor* [1989], the following expression for  $S^2$  is suggested, which accounts for the combination of three main terms

$$S^2 = S_{Iw}^2 + S_{iw}^2 + S_{bg}^2, \quad (3.26)$$

where  $S_{Iw}$  indicates the shear induced by the wind,  $S_{iw}$  is the shear generated by internal waves and  $S_{bg}$  is a background value.

Wind-induced shear stress within the upper part of the water column can be calculated using the law of the wall

$$S_{Iw}(z) = \frac{dU(z)}{dz} = \frac{\tau_w}{\rho \kappa z}, \quad (3.27)$$

where  $U$  is the horizontal velocity of water,  $\tau_w$  is wind stress and  $\kappa = 0.41$  is the von Kàrmàn constant.



Concerning the contribution of internal waves  $S_{iw}$ , *Mellor* [1989] suggested to include the following correction term

$$S_{iw}(z)^2 = \gamma N(z)^2, \quad (3.28)$$

where  $\gamma$  is a constant and is equal to 0.7. For the specific case of Lake Baikal, the correction term  $S_{iw}$  has been included only during the ice free period, when internal waves can be generated by wind forcing. On the contrary,  $\gamma$  has been set equal to 0 when the lake is ice covered.

Finally, a background squared shear frequency  $S_{bg}^2 = 2 \times 10^{-7} s^{-2}$  has been assumed, which is in close agreement with the value suggested by *Lawrence et al.* [2002].

### 3.4.3 Dynamical reconstruction of the diffusivity profile

As far as Equation (3.22) is adopted to calculate diapycnal diffusivity, it is clear that in the limit of an unstratified/weakly stratified system and/or high vertical shear stress (i.e.  $Ri \rightarrow 0$ )  $D_z$  approaches the upper values  $D_{z,r}$ . On the contrary  $D_z$  approaches the background values  $D_{z,bg}$  if stratification overcomes the effects of velocity shear and inhibits vertical mixing (i.e.  $Ri \gg 1$ ). It is evident that a proper definition of  $D_{z,r}$  and  $D_{z,bg}$  is needed. The reference diffusivity profile  $D_{z,r}$  represents an upper limit for turbulent diffusivity, thus is generally chosen to fall within the range of the maximum observed values [*Large et al.*, 1994], while on the contrary, the background value  $D_{z,bg}$  is typically chosen on the order of  $10^{-5} m^2 s^{-1}$  [*Pacanowski and Philander*, 1981]. In the case of Lake Baikal, as a result of the calibration procedure described in Section 6.1 the background diffusivity value,  $D_{z,bg}$ , has been taken equal to  $5 \times 10^{-5} m^2 s^{-1}$ . This is consistent with the typical values  $\sim O(10^{-5}) m^2 s^{-1}$  suggested by *Pacanowski and Philander* [1981] and with previous estimates available in the literature [*Schmid et al.*, 2007].

The reconstruction of  $D_{z,r}$  has been based on the few estimates of turbulent diffusivity available in literature [*Ravens et al.*, 2000; *Wüest et al.*, 2000] (Figure 2.11). These diffusivity profiles are particularly suited to identify reasonable values of  $D_{z,r}$ , as the three of them have been estimated from temperature microstructure measurements collected during near isothermal conditions and close to an observed downwelling occurrence, thus when turbulent diffusivity was high (from *Wüest et al.* [2000]: microstructure profiles 26-28 June, 1996; from *Wüest et al.* [2005]: downwelling occurrence 22-26 June, 1996). In the lake interior and close to the bottom ( $z > 500 m$ ),  $D_{z,r}$  has been defined following the profile proposed by *Wüest et al.* [2000](Figure 2.11). On the contrary, these information are not sufficient to properly describe  $D_{z,r}$  within the upper part of the lake, which is strongly affected by the mixing processes driven by wind, and influenced by thermal stratification. Aimed at reproducing the seasonal variation of  $D_{z,r}$  within the superficial region of the lake, an original procedure based on a wind speed-dependent parameterization has been introduced. Within

### 3. A simplified 1D model for the numerical simulation of deep ventilation

---

the Ekman depth,  $H_E = 0.4u_*/f$ , a constant value of turbulent diffusivity is assigned

$$D_E = \frac{1}{f} \left( \frac{\rho_a C_D}{\rho k} \right)^2 W_{eff}^2, \quad z \leq H_E, \quad (3.29)$$

where  $k$  is a constant that fall in the range  $1 \times 10^{-2} \leq k \leq 4 \times 10^{-2}$  [Kullenberg, 2011] and has been chosen equal to  $2 \times 10^{-2}$ . Based on the existing data (Figure 2.11), a lower bound on the value of  $D_E$  has been fixed equal to  $10^{-2} m^2 s^{-1}$  during the ice free season. For sake of precision, Equation (3.29) has been originally derived for the eddy viscosity ( $v_z$ ) [Kullenberg, 2011], but, as a first approximation and according to the widely used Reynolds analogy, it is proposed here to estimate eddy diffusivity. Such choice is justified by the fact that the turbulent Prandtl number  $Pr = v_z/D_z$  is closed to unity for weakly stratified conditions, as is typically the case of the Ekman layer  $H_E$  [Venayagamoorthy and Stretch, 2010].

Beneath  $H_E$ , the diffusivity profile decreases depending on the stratification conditions occurring during the year. Such conditions are assessed at every time step looking at the well-mixed surface layer thickness,  $H_{ml}$  (epilimnion), which is evaluated as the maximum depth between  $H_E$  and the surface unstable region that results by performing the stability algorithm. Thus,  $D_{z,r}$  is reduced exponentially from the value  $D_E$  at the depth  $H_E$  to the value of  $D_{z,r}$  at a depth proportional to the thickness of the epilimnion  $\beta_{ml}H_{ml}$ , where  $\beta_{ml}$  is a constant suitably assumed equal to 1.25. When a nearly homogeneous temperature profile is approached (i.e. the absolute value of the difference between water temperature at the surface and at the mesothermal maximum is lower than  $1^\circ C$ ), more complicated mixing patterns can develop, that are not directly captured by the model. Aimed at including the increase of turbulent diffusivity subsequent to these conditions, diffusivity is reduced exponentially from  $D_E$  at  $H_E$  to the value of  $D_{z,r}$  at  $\max[\beta_{ml}H_{ml}, \beta_{mm}H_{mm}]$ , where  $H_{mm} = z(\alpha = 0)$  is the mesothermal maximum depth and  $\beta_{mm}$  is a constant assumed equal to 1.5. This empirical approach has been developed testing different solutions, and is a result of the calibration procedure discussed in Section 6.1.

No specific model is considered for the turbulent processes within the benthic boundary layer. Nevertheless, the increase of diffusivity close to the bottom is already embodied in the shape of the reference profile, and has only a short time influence on the reestablishment of the temperature profile after cold downwelling events.

Finally, during the ice cover period, a low  $D_{z,r}$  profile is assumed (surface value equal to  $3 \times 10^{-4} m^2 s^{-1}$ ), which accounts for the suppression of the wind-induced mixing due to the ice cover. In order to avoid an abrupt transition from ice free to ice cover conditions (and vice-versa), an exponential decay law is used, with a mean lifetime of about 1 month.

The range of variability of the reference diffusivity profile,  $D_{z,r}$ , is shown in Figure 3.7, together with the diffusivity profiles available in literature.

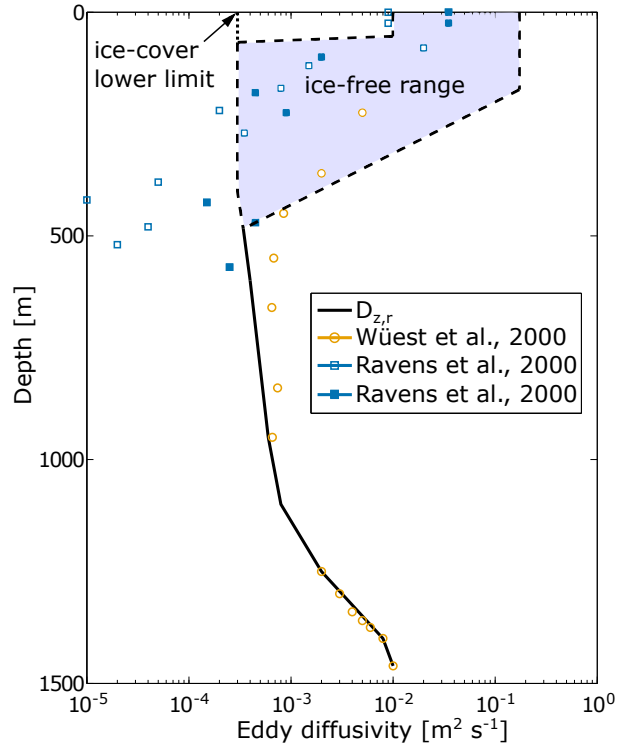


Figure 3.7: Reference diffusivity profile,  $D_{z,r}$ , compared with the profiles estimated by *Ravens et al.* [2000] and *Wüest et al.* [2005]. The shaded area indicates the possible range of variation of  $D_{z,r}$ , according to the 1 000-year simulation discussed in Section 6.1.2.

In order to account for the memory of the system through the evolution of its past states,  $D_z$ ,  $D_{z,H}$ ,  $H$  and  $S_{lw}(z)$  (introduced in this section and in Section 3.4.2) are defined at every time step as the average between the profiles computed at current and previous steps.

### 3.5 Concluding remarks

A simplified one-dimensional model has been proposed to analyze deep water renewal occurring in deep, temperate lakes due to thermobaric instability. The model numerically computes the evolution of the vertical temperature profiles (and of any other tracer) taking into account the stability of the water column and the occurrences of deep water intrusions. For this purpose, the model includes two specific sorting algorithms, which allows for a suitable reproduction of the major processes occurring in the lake: vertical stabilization of the unstable regions of the water column, deep downwellings triggered by thermobaric instability, compensating upwelling generated by deep ventilation and seasonal wind-driven mixing. Furthermore, the model is provided with a self-consistent procedure to reconstruct the diapycnal diffusivity profile, which allows to account for the seasonal and inter-annual dynamics on turbulent diffusivity. The model handles a few data in input (according to the reduced information often available for large basins) and has a simplified structure. Together these features ensure a significant computational time saving, while the accuracy of the results is consistent with that of the input data.

Two main quantities characterize and quantify the downwelling events: the specific energy input  $e_w$  and the downwelling volume  $V_d$ . At each downwelling time step  $\Delta t_{down}$ , these quantities are calculated by means of two simplified equations, whose input data are the wind speed and duration. To link wind speed and duration to the correspondent specific energy and sinking volume, the model requires the calibration of only two calibration parameters ( $\xi$  and  $\eta$ ), mainly depending on geometric features.

Due to the considerable computational speed, the model is suitable to analyze the future behavior of the lake and its response to climate change scenarios by performing long time simulations (i.e. hundreds of years). These tasks, as well as the calibration of the model parameters, are presented and discussed in Chapter 6.

## 4 A simple lumped model to convert air temperature into surface water temperature in lakes

**Abstract** - *In the previous chapter, a simplified 1D model to simulate deep ventilation in profound lakes has been presented. The model shows a simple computational structure and requires only a few data in input: besides wind forcing, which represents the major factor responsible for the occurrence of deep downwellings, surface water temperature is the only variable required to impose the boundary conditions at the atmosphere-lake interface. Unfortunately, long term records of surface water temperature are usually not easily available, and the estimates from climate models coupling lake and atmosphere are still affected by significant uncertainties. As a matter of fact, water temperature in lakes is governed by a complex heat budget, where the single fluxes are hardly assessable over long time periods in the absence of high accuracy data and high spatial resolution (i.e. lake scale).*

*In order to address this issue, we developed a simple physically-based model to relate the temperature of the lake superficial layer (epilimnion) to air temperature only. The model accounts for the overall heat exchanges with the atmosphere and the deeper layer of the lake (hypolimnion) by means of simplified relationships, which contain a few parameters (from four to eight in the different proposed formulations) to be calibrated with the combined use of air and water temperature measurements. In particular, the calibration of the parameters in a given case study allows one to estimate, in a synthetic way, the influence of the main processes controlling the lake thermal dynamics, and to recognize the atmospheric temperature as the main factor driving the evolution of the system. In fact, the air temperature variation implicitly contains proper information about the variation of other major processes, and hence in our approach is considered as the only input variable of the model. Furthermore, the model can be easily used to predict the response of a lake to climate change, since projected air temperatures are usually available by large-scale global circulation models.*

*Since short series of data are available for Lake Baikal, the model has been tested on Lake Superior (USA - Canada) considering a 27-year record of measurements, among which 18 years are used for calibration and the remaining 9 years for model validation. The results show a remarkable agreement with measurements, over the entire data period.*

*The chapter is structured as follows. The heat budget is presented in detail in Section 4.2. In Section 4.3 the governing equations are presented, and the model is formulated. Section 4.4 provides a general description of the data used to test the model. The results concerning model calibration and validation are presented in Sections 4.5 and 4.6 with reference to the different versions of the model. Results are further discussed in Section 4.7, where the model is also tested using a different dataset (i.e. surface water temperature estimates from satellite imagery). Finally, the main conclusions are drawn in Section 4.8.*

*The results presented here have been submitted to a refereed journal for consideration [Piccolroaz et al., 2013a], and some applications of the model has been presented in Piccolroaz and Toffolon [2012a] and Piccolroaz et al. [2013b], as far as Lake Superior (USA - Canada) and Lake Garda (Italy) are concerned, respectively.*

#### 4. A simple lumped model to convert air temperature into surface water temperature in lakes

---

## 4.1 Introduction

Water temperature is crucial for lakes physical, chemical and biological dynamics, indeed temperature is the primary driver of the vertical stratification, thus directly affects vertical exchanges of mass, energy and momentum within the water column. Water temperature plays a key role influencing the aquatic ecosystem of lakes, which usually adapts to a specific range of physical and environmental conditions. As a matter of fact, water temperature can affect both the chemical (e.g. dissolved oxygen concentration) and biological (e.g. fish growth) processes occurring in the water body. Recent studies demonstrate that lakes are highly sensitive to climate, and their physical, chemical, and biological properties respond rapidly to climate-related changes [Adrian *et al.*, 2009]. In the light of these considerations, it is evident that any significant modification to current environmental conditions may influence the limnic system, with direct impacts on the composition and richness of its ecosystem [MacKay *et al.*, 2009]. There are indeed several reasons to look for a reliable tool to have information about the dependence of water temperature on the various factors influencing the heat balance of the lake compartments.

Water temperature in lakes follows complex dynamics and is the result of a combination of different fluxes, whose sum is often small compared to the single terms. This is particularly true for the temperature of the well-mixed surface layer, usually termed as epilimnion during stratified conditions, which experiences strong oscillations at a variety of temporal scales: from short (a few days) to long (annual and interannual) up to climatic (decades to centuries). Closing the heat balance correctly at the different scales and predicting the future trend of surface water temperature is therefore challenging, but some difficulties are essentially harder to tackle. As a consequence, some hydrodynamic lake models prescribe surface water temperature as surface boundary condition instead of computing the net heat flux at the water-atmosphere interface (e.g. Goudsmit *et al.* [2002] and the simplified model presented in the previous chapter, see also Piccolroaz and Toffolon [2013]). On one hand, large uncertainties are associated to the estimates of the various heat exchange components, whereas on the other, the variables involved in the different processes are either not all independent from each other or do not present strong interannual variations, suggesting that some simplifications can be possibly adopted. For instance, shortwave solar radiation substantially depends on the latitude of the lake, but has a rather regular annual trend. Deep water temperature typically changes on time scales much longer than surface water, thus the heat exchanged with the hypolimnion can be reasonably assumed as constant in many situations. On the contrary, air temperature is a significant index of the overall meteorological conditions and can be reasonably assumed as the main variable influencing the heat balance of the surface layer of the lake [Livingstone and Padisák, 2007].

Thankfully, long-term, high-resolution air temperature observational datasets are in general

#### 4. A simple lumped model to convert air temperature into surface water temperature in lakes

---

available, both for historical periods adopted to calibrate General Circulation Models (GCMs) and Regional Climate Models (RCMs), and for future periods where air temperature is a variable commonly derived from GCMs or RCMs projections. On the other hand water temperature measurements are far less available, and future projections are less reliable than modeled air temperature. The latter point is particularly true for climate change studies based on GCMs, whose mesh size is normally too coarse for explicitly including even some of the biggest lakes on Earth. These evidences explain why air temperature is typically used to derive surface temperature of water bodies.

Regression models [see *Sharma et al.*, 2008, for a review] are typically adopted for this scope, but their use may be questionable especially when it is necessary to extrapolate temperature values beyond the maximum (or minimum) limit of the measured time series. This is often the case in climate change studies, where the regression relationships built upon current climate condition are applied to estimate surface water temperature for different climate change scenarios, with the possibility that the projected air temperature may cover a wider interval of values. Regression-type models, either linear or non-linear, have been successfully applied to estimate the temperature of rivers and streams, giving rise to a rich literature [e.g. *Kothandaraman and Evans*, 1972; *Crisp and Howson*, 1982; *Webb et al.*, 2003; *Benyahya et al.*, 2007; *Morrill et al.*, 2005]. Notwithstanding, significant error may arise by adopting this approach, especially for those water basins that have a significant seasonal hysteresis. As a matter of fact, the variety of processes of heat exchange across the lake surface and the thermal inertia of the water mass cause an annual phase lag between air and water temperatures, which is hard to consider in regressions. In many cases simplistic linear regressions are adopted for the conversion, following the assumption of a direct monotonic relationship between air temperature and surface water temperature [e.g. *Shuter et al.*, 1983; *Livingstone and Lotter*, 1998; *Livingstone et al.*, 1999], which do not allow for capturing the hysteresis cycle. In other cases, seasonal hysteresis is solved by estimating different seasonal regression relationships, one for each branch of the hysteresis loop (e.g. one for the ascending and another for the descending branch) [e.g. *Webb*, 1974], or by using linear regressions to estimate the monthly means of surface water temperature from the monthly means of measured air temperature data [*McCombie*, 1959].

Besides regression analysis, water temperature of lakes can be estimated by means of process-based numerical models [e.g. *Arhonditsis et al.*, 2004; *Fang and Stefan*, 1999; *Peeters et al.*, 2002; *Martynov et al.*, 2010; *Bonalumi et al.*, 2012], possibly coupled with an atmospheric model [e.g. *Goyette and Perroud*, 2012; *Martynov et al.*, 2012] aimed at including the mutual interaction between water and atmosphere. This kind of models can provide exhaustive information about the thermal structure of lakes, and accurately characterize the different energy fluxes involved in the lake temperature dynamics. The major drawback of the process-based models is the requirement



of detailed time series of meteorological data in input (e.g. wind speed, humidity, cloudiness etc. besides air temperature), which are often not available or not accurate enough.

In order to overcome the limitations of traditional approaches (both regression- and process-based models), semi-empirical models based on physical principles may represent a valid alternative, having the key advantage of requiring less data in input than deterministic models, whilst preserving a clear physical basis. Recently, *Kettle et al.* [2004] proposed a simple empirical model to estimate mean daily water temperature, using only air temperature and the theoretical clear-sky solar radiation as input information. The model is based on the sensible heat exchange model of *Rodhe* [1952] [see also *Bilello*, 1964], and implicitly accounts for the main heat exchange processes through 4 parameters. The model has good performances, but its application is limited to specific periods of the year with nearly uniform stratification conditions (it has been tested from late June to early September, long after ice melts, when water temperature is always above 4°C). Indeed, it does not account for the seasonal evolution of the thermal structure of the lake, and hence of the mixing depth (i.e. the depth of the epilimnion), which determines the volume of water responding to external forcing and has a significant influence on the seasonal patterns of atmosphere-lake heat exchange.

In the attempt to reliably estimate the cycle of surface water temperature of lakes from air temperature measurements/projection only, both under past, current and projected climate conditions, a simplified model has been developed. Such a model is primarily based on the energy balance between atmosphere and lake surface water (Figure 4.1), but avoids the need to take into account all heat budget terms explicitly. A simple parameterization of the seasonal evolution of the mixing depth is included in the model equations, which only depend upon air temperature. This allows for a consistent description of the physical principles governing lake surface temperature, and ensures a general applicability of the model (e.g. over the entire year).

## 4.2 The heat budget of lakes

The net heat flux  $H_{net}$  in the surface layer of a lake results from the combination of the different fluxes entering and exiting the upper water volume. The main heat exchanges occur at the interface between the epilimnion and atmosphere and deep water, respectively. Indicating with  $H$  the generic heat flux per unit surface [ $W m^{-2}$ ], defined as positive when it is directed towards the considered layer, the net flux is assessed accounting for the following main terms

$$H_{net} = H_s + H_a + H_w + H_e + H_c + H_p + H_i + H_d, \quad (4.1)$$

#### 4. A simple lumped model to convert air temperature into surface water temperature in lakes

where  $H_s$  is the net short-wave radiative heat flux due to solar radiation (considering only the incoming radiation that is actually absorbed),  $H_a$  is the net long-wave radiation emitted from the atmosphere toward the lake,  $H_w$  is the long-wave radiation emitted from the water,  $H_e$  is the latent heat flux (due to evaporation/condensation processes),  $H_c$  is the sensible heat flux (due to convection),  $H_p$  is the heat flux due to precipitation onto the water surface,  $H_i$  is the effect of the throughflow of water by inlets and outlets, and  $H_d$  is the heat flux exchanged with deep water. Figure 4.1 shows a schematic representation of the heat exchanges at the epilimnion/atmosphere and epilimnion/hypolimnion interfaces. All the components of Equation (4.1) are analyzed in detail below to point out the main variables and physical parameters involved in the heat exchange process.

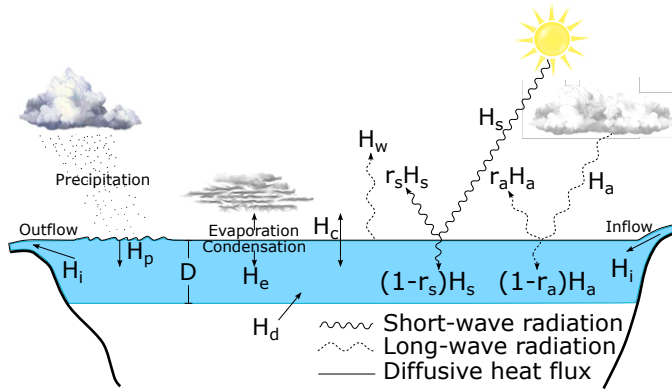


Figure 4.1: Schematic of the main heat fluxes affecting the surface layer.

The incident short-wave solar radiation approximately follows a sinusoidal annual cycle. Considering the short-wave reflectivity  $r_s$  (albedo), which is a function of the solar zenith angle and of the lake surface conditions (e.g. water waves height), the net solar radiation  $H_s$  reads

$$H_s = (1 - r_s) \left[ s_1 \cos \left( \frac{2\pi(t - s_2)}{t_y} \right) + s_3 \right], \quad (4.2)$$

where  $t$  is time,  $t_y$  is the duration of a year in the units of time considered in the analysis, and  $s_1, s_2, s_3$  are coefficients that primarily depends on the latitude and the shadowing effects of the local topography. The effects of cloud cover, which could be accounted for by means of empirical relationships, are not explicitly considered in the present analysis.

Long-wave radiation terms are calculated according to the Stefan-Boltzmann law, yielding to the following formulations

$$H_a = (1 - r_a) \epsilon_a \sigma (T_K + T_a)^4, \quad (4.3)$$

#### 4. A simple lumped model to convert air temperature into surface water temperature in lakes

$$H_w = -\varepsilon_w \sigma (T_K + T_w)^4, \quad (4.4)$$

where  $r_a$  is the long wave reflectivity, generally assumed to have a constant values [Henderson-Sellers, 1986],  $\varepsilon_a$  and  $\varepsilon_w$  are the emissivities of atmosphere and lake surface, respectively,  $\sigma$  is the Stefan-Boltzmann constant ( $5.67 \times 10^{-8} \text{ W m}^{-2} \text{ K}^{-4}$ ),  $T_K = 273.15 \text{ K}$ ,  $T_a$  and  $T_w$  are the temperatures of air and water expressed in Celsius [ $^{\circ}\text{C}$ ]. The emissivity  $\varepsilon_w$  is essentially constant and close to unity, as water is nearly a black body, while  $\varepsilon_a$  is more variable and depends on several factors among which the most important are air temperature, humidity and cloud cover [Imboden and Wüest, 1995].

Air and water temperatures can be decomposed into a reference value representative of the specific case study ( $\bar{T}_a$  and  $\bar{T}_w$ ) and a fluctuation ( $T'_a$  and  $T'_w$ ). Hence, considering that  $T'_a/(T_K + \bar{T}_a)$  and  $T'_w/(T_K + \bar{T}_w)$  are small parameters, the long-wave fluxes (4.3) and (4.4) can be linearised using a Taylor expansion as

$$H_a \simeq \tilde{\varepsilon}_a \sigma (T_K + \bar{T}_a)^4 \left( 1 + 4 \frac{T'_a}{T_K + \bar{T}_a} \right), \quad (4.5)$$

$$H_w \simeq -\varepsilon_w \sigma (T_K + \bar{T}_w)^4 \left( 1 + 4 \frac{T'_w}{T_K + \bar{T}_w} \right), \quad (4.6)$$

where  $\tilde{\varepsilon}_a = (1 - r_a)\varepsilon_a$ . By choosing  $\bar{T}_a = \bar{T}_w = \bar{T}$  (hence  $T'_a = T_a - \bar{T}$  and  $T'_w = T_w - \bar{T}$ ), the terms  $H_a$  and  $H_w$  can be easily combined to yield the following equation

$$H_a + H_w \simeq 4\sigma\tilde{\varepsilon}_a(T_K + \bar{T})^3 \cdot \left[ \frac{\tilde{\varepsilon}_a - \varepsilon_w}{4\tilde{\varepsilon}_a} (T_K + \bar{T}) + \frac{\tilde{\varepsilon}_a - \varepsilon_w}{\tilde{\varepsilon}_a} (T_w - \bar{T}) + T_a - T_w \right]. \quad (4.7)$$

The sensible ( $H_c$ ) and latent ( $H_e$ ) heat fluxes are calculated through bulk semi-empirical relations that can be derived from turbulence theory [Henderson-Sellers, 1986]

$$H_c = \alpha_c (T_a - T_w), \quad (4.8)$$

$$H_e = \alpha_e (e_a - e_w), \quad (4.9)$$

where  $\alpha_c$  [ $\text{W m}^{-2} \text{ K}^{-1}$ ] and  $\alpha_e$  [ $\text{W m}^{-2} \text{ hPa}^{-1}$ ] are transfer functions primarily depending on wind speed and other meteorological parameters,  $e_a$  is the vapor pressure in the atmosphere and  $e_w$  is the water vapor saturation pressure at the water temperature (both in [ $\text{hPa}$ ]). The ratio  $\alpha_c/\alpha_e$  is known as Bowen coefficient and is often taken to be constant ( $\approx 0.61 \text{ hPa K}^{-1}$ ) [Imboden and Wüest, 1995]. The saturated water pressure  $e_w$  is a function of temperature, and can be calculated

## 4. A simple lumped model to convert air temperature into surface water temperature in lakes

---

through several empirical formulas, as for example the exponential law

$$e_w = a \exp\left(\frac{bT_w}{c + T_w}\right), \quad (4.10)$$

where  $a = 6.112 \text{ hPa}$ ,  $b = 17.67$  and  $c = 243.5^\circ\text{C}$  [Bolton, 1980].

In order to keep the formulation of the model as simple as possible, Equation (4.10) can be linearized by Taylor series expansion around a reference temperature, which can be assumed equal to  $\bar{T}$

$$e_w \approx a \exp\left(\frac{b\bar{T}}{\bar{T} + c}\right) \left(1 + \frac{bc}{(\bar{T} + c)^2}(T_w - \bar{T})\right). \quad (4.11)$$

Finally, the heat exchange with deep water  $H_d$  can be formulated, as a first approximation, as the combination of a constant contribution and a contribution depending on the gradient of temperature between surface and hypolimnetic water. Considering that deep water has a temperature that is approximately constant during the year, the second component of  $H_d$  is essentially dependent on surface water temperature  $T_w$ . The term  $H_d$  is usually small with respect to the flux components exchanged with the atmosphere, which have been described above. Analogously, the contribution  $H_p$  of precipitation onto the lake surface and the heat  $H_i$  exchanged with the inflows and the outflows are only rarely significant, thus are not explicitly included in the balance. As a matter of fact, changes in surface temperature during rainy periods generally result from changes of the main terms  $H_w$ ,  $H_c$  and  $H_e$ , and  $H_i$  is only important in lakes with high flushing rate [Imboden and Wüest, 1995].

### 4.3 Formulation of the model

#### 4.3.1 A simplified heat budget scheme

According to the simplifications discussed in Section 4.2, the net heat flux at the surface  $H_{net}$  introduced in Equation (4.1) can be suitably written as the combination of linear and sinusoidal functions

$$H_{net} = c_1 \cos\left[\frac{2\pi(t - c_2)}{t_y}\right] + c_3 + c_4(T_a - T_w) + c_5T_w, \quad (4.12)$$

where  $t$  is time,  $t_y$  is the duration of the year expressed in suitable time units,  $T_a$  and  $T_w$  are air and water temperature (expressed in Celsius [ $^\circ\text{C}$ ] for simplicity), respectively, and  $c_i$  ( $i$  from 1 to 5) are coefficients with a physical correspondence. These coefficients result by appropriately combining together the physical parameters that appear in Equations (4.2) - (4.11), and their definitions are given in Section 4.3.3.

Note that Equation (4.12) accounts for a sinusoidal annual forcing term with amplitude  $c_1$  and

#### 4. A simple lumped model to convert air temperature into surface water temperature in lakes

---

phase  $c_2$ , an exchange air-water term  $c_4(T_a - T_w)$ , a constant term  $c_3$  and a residual correction  $c_5T_w$  dependent on the water temperature. The only meteorological variable included in the model is  $T_a$ , while the remaining meteorological forcing (primarily wind, which is a major driving force for lakes) are inherently accounted for in the model's parameters. The formulation implicitly accounts for the seasonal patterns of external forcing, while higher frequency fluctuations are not considered, consistently with the main aim of the model, which is to reproduce the evolution of  $T_w$  at long time scales (i.e. seasonal, annual, interannual).

##### 4.3.2 A suitable parameterization of the epilimnion thickness

Considering the upper layer of the lake, the volume-integrated heat equation can be expressed as follows

$$\rho c_p V \frac{dT_w}{dt} = H_{net} A, \quad (4.13)$$

where  $\rho$  is the water density,  $c_p$  is the specific heat at constant pressure,  $V$  and  $A$  are the volume and the surface area of the layer, respectively. Both  $V$  and  $A$  can be left undetermined in the analysis if we define the depth of the well-mixed surface layer (i.e. the epilimnion thickness) as follows

$$D = \frac{V}{A}. \quad (4.14)$$

The depth  $D$  typically depends on the stratification of the water column and is characterized by a clear seasonal behavior. In order to include this essential feature, a suitable parameterization of  $D$  in time is required. The most appropriate choice is to estimate  $D$  as a function of the thermal stratification, thus of the vertical temperature gradient. As a first approximation, the strength of the stratification can be evaluated as proportional to the difference between the surface water temperature  $T_w$  and a reference value  $T_r$ .  $T_r$  is representative of deep water temperature, thus can be suitably chosen depending on the thermal regime of the lake (for a classification of lakes refer to *Hutchinson and Löffler* [1956]; *Lewis* [1983]). In the case of cold monomictic lake (i.e. never over the temperature of maximum density  $T_{\rho,max} \approx 4^\circ C$ , stably stratified in winter and circulating in summer; in these lakes the thermal stratification is referred to as inverse since water temperature at the surface,  $T_w$ , is colder than in the hypolimnion)  $T_r$  can be assumed as the maximum surface temperature registered during the year. In the case of warm monomictic lakes (i.e. always above  $4^\circ C$ , circulating in winter and stably stratified in summer; in these lakes the thermal stratification is referred to as direct since water temperature at the surface,  $T_w$ , is warmer than in the hypolimnion)  $T_r$  can be assumed as the minimum surface temperature registered during the year. Finally  $T_r$  can be assumed equal to the temperature of maximum density  $T_{\rho,max} \approx 4^\circ C$  for the case of dimictic lakes (i.e. inversely stratified in winter, stably stratified in summer and circulating twice a year at

#### 4. A simple lumped model to convert air temperature into surface water temperature in lakes

---

the transition between the two states, at about  $4^\circ\text{C}$ ). In all cases, when the water column is nearly isothermal (i.e.  $T_w \rightarrow T_r$ ), close to the onset of the seasonal turnover, the thermal stratification weakens and, as a consequence, the surface mixed layer  $D$  reaches its maximum thickness  $D_r$ . On the contrary, we assume that the stronger is the stratification (i.e.  $|T_w - T_r| \gg 0$ ), the thinner is the surface mixed layer  $D$ .

For the period of direct stratification ( $T_w > T_r$ ), the evolution of  $D$  has been described using the simple exponential decay law

$$D(t) = D_r \exp\left(-\frac{T_w(t) - T_r}{\tau_{warm}}\right), \quad (4.15)$$

where  $\tau_{warm}$  [ $^\circ\text{C}$ ] is the inverse of the decay rate (the subscript *warm* refers to the case  $T_w > T_r$ : direct stratification) and  $D_r$  indicates the maximum thickness of the mixed layer. With the aim to consider the variation of  $D$  when the lake is inversely stratified (i.e.  $T_w < T_r$ , subscript *cold*), a modified version of Equation (4.15) has been derived,

$$D(t) = D_r \left[ \exp\left(-\frac{T_r - T_w(t)}{\tau_{cold}}\right) + \exp\left(-\frac{T_w(t) - 0^\circ\text{C}}{\tau_{ice}}\right) \right], \quad (4.16)$$

where  $\tau_{cold}$  [ $^\circ\text{C}$ ] and  $\tau_{ice}$  [ $^\circ\text{C}$ ] are the inverse of decay rates. In principle,  $\tau_{cold}$  is not necessarily equal to  $\tau_{warm}$ , since the evolution of  $D$  below and above  $T_r$  is possibly different. In addition, the second term in the exponential function has been introduced to account for the potential formation of the ice cover at the surface. In this case, as  $T_w$  tends to  $0^\circ\text{C}$ ,  $D$  thickens, and in our scheme this indirectly takes into account the inhibition of the air-water heat flux due to the presence of ice and snow covers. It is worth noting that  $\tau_{ice}$  should have an upper bound (approximately equal to  $0.5^\circ\text{C}$  in our case), in order to include the effect of ice only when the lake is inversely stratified, and avoid a discontinuity in  $D$  at the transition from direct to inverse stratification (i.e. when  $T_w = 4^\circ\text{C}$ ).

By substituting Equations (4.12), (4.14), (4.15) and (4.16) into Equation (4.13) we obtain

$$\frac{dT_w}{dt} = \frac{1}{\delta} \left\{ p_1 \cos\left[\frac{2\pi(t - p_2)}{t_y}\right] + p_3 + p_4(T_a - T_w) + p_5 T_w \right\}, \quad (4.17)$$

with

$$\begin{aligned} \delta &= \exp\left(\frac{T_r - T_w}{p_6}\right), & (T_w \geq T_r) \\ \delta &= \exp\left(\frac{T_w - T_r}{p_7}\right) + \exp\left(-\frac{T_w}{p_8}\right), & (T_w < T_r) \end{aligned} \quad (4.18)$$

where the model parameters  $p_i$  ( $i = 1, 3, 4, 5$ ) are the coefficients  $c_i$  present in Equation (4.12) normalized by the maximum mixing depth  $D_r$ ,  $p_2 = c_2$ ,  $p_6 = \tau_{warm}$ ,  $p_7 = \tau_{cold}$ ,  $p_8 = \tau_{ice}$ , and  $\delta$  is

#### 4. A simple lumped model to convert air temperature into surface water temperature in lakes

the normalized depth  $\delta = D/D_r$ , whose seasonal evolution is schematically represented in Figure 4.2 for the case of dimictic lakes (monomictic regimes are particular cases of the dimictic regime, which represents the most general case).

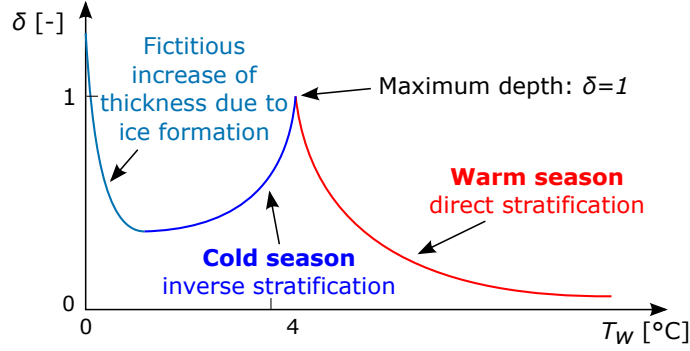


Figure 4.2: Schematic of the seasonal evolution of the dimensionless thickness  $\delta$  of the surface well-mixed layer for the general case of a dimictic lake.

#### 4.3.3 Definition of the parameters

The semi-empirical lumped model presented in the previous section requires the calibration of 8 parameters  $p_i$  ( $i = 1, \dots, 8$ ), whose possible ranges of values can be reasonably estimated based upon their physically-based derivation.

According to the definition of Equation (4.17), parameters  $p_i$  ( $i = 1, \dots, 5$ ) are determined once the corresponding coefficients  $c_i$  in Equation (4.12) and the maximum mixing depth  $D_r$  are known. Coefficients  $c_i$  ( $i = 1, \dots, 5$ ) have been defined by rearranging the heat balance given in Equation (4.1) into the form of Equation (4.17), using the expressions in (4.2) - (4.11) to specify the main heat flux terms. Furthermore, the parameters in Equations (4.2) - (4.11) that are influenced by meteorological (e.g. wind and precipitation patterns) and astronomical phenomena (i.e.  $r_s$ ,  $\alpha_c$ ,  $\alpha_e$ ,  $e_a$ ) have been assumed to consist of a constant (indicated by an overline) and a periodic (indicated by a prime) component. The resulting expressions for the coefficients  $c_i$  are given below

$$c_1 \approx (1 - \bar{r}_s)s_1 + f(\bar{r}'_s, \alpha'_c, \alpha'_e, e'_a), \quad (4.19)$$

$$c_2 \in [0, 1], \quad (4.20)$$

$$c_3 \approx (1 - \bar{r}_s)s_3 + \sigma(\tilde{\epsilon}_a - \epsilon_w)(T_K + \bar{T})^3(T_K - 3\bar{T}) - \bar{\alpha}_e \left[ \bar{e}_a - a \exp\left(\frac{b\bar{T}}{\bar{T} + c}\right) \left(1 - \frac{bc}{(\bar{T} + c)^2}\bar{T}\right) \right], \quad (4.21)$$

$$c_4 \approx 4\sigma\tilde{\epsilon}_a(T_K + \bar{T})^3 + \bar{\alpha}_c, \quad (4.22)$$

$$c_5 \approx 4\sigma(T_K + \bar{T})^3(\tilde{\epsilon}_a - \epsilon_w) - \bar{\alpha}_e a \exp\left(\frac{b\bar{T}}{\bar{T} + c}\right) \left(\frac{bc}{(\bar{T} + c)^2}\right). \quad (4.23)$$

It is evident that a straightforward quantification of these coefficients is not trivial. In fact, most of the physical parameters involved do not have a single, unambiguous value, but rather they span a range of values that depends on several factors, often difficult to specify (e.g. cloud cover). Therefore, each coefficient  $c_i$  is defined over a range of possible values, which is specific of each case study and, thanks to the physical interpretation of Equations (4.19)-(4.23), is physically reasonable. The possible ranges of variation can be easily determined by considering the lake location properties (e.g. latitude, climate, typical temperatures) and by using parameter values taken from the literature [e.g. *Henderson-Sellers, 1986; Imboden and Wüest, 1995; Martin and McCutcheon, 1998*]. Analogous consideration can be addressed for the estimation of  $D_r$ .

As far as the the remaining parameters are concerned,  $p_6$  and  $p_7$  have been allowed to range within a wide interval comprised between 0 and 15 °C, while  $p_8$  between 0 and 0.5 °C. As already mentioned in Section 4.3, the range of  $p_8$  has been set narrower (more stringent upper bound), aimed at confining the correction due to ice only when the lake is inversely stratified ( $e^{-4/0.5} = O(10^{-4}) \ll 1$ ). These ranges of variation have been shown to be sufficiently wide to permit a suitable sensitivity analysis of the model's parameters (see results in Sections 4.5.1 and 4.5.2).

Finally, it is worth noting that the first term on the right hand side of Equation (4.12) is a periodic term accounting for all seasonal patterns of meteorological variables other than air temperature (e.g. wind speed, air humidity, cloudiness, see the definition of  $c_1$ ). As a first approximation, these components have been treated as sinusoidal functions having the same frequency of the solar radiation (i.e. a period equal to one year), but possibly different amplitudes and phases. Based upon purely algebraic considerations, the sum of such a set of functions produces another sinusoid having the same frequency but different amplitude (i.e.  $c_1$ ) and phase (i.e.  $c_2$ ).

## 4.4 Study site

In order to apply the model described in Section 4.3, only two series of data are required: air temperature as input forcing, and surface water temperature for calibration purpose. A sufficiently



#### 4. A simple lumped model to convert air temperature into surface water temperature in lakes

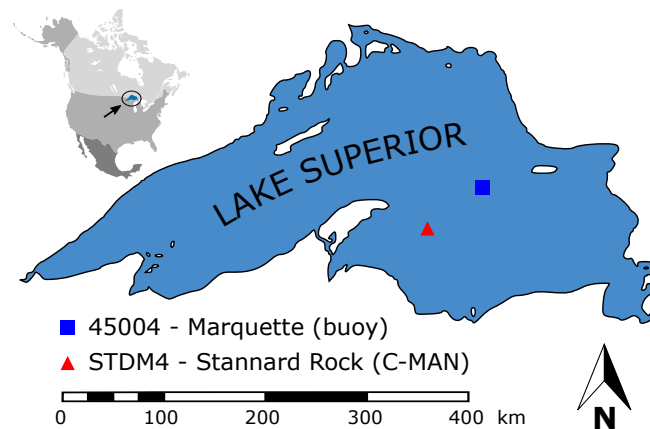


Figure 4.3: Lake Superior with the location of the NDBC stations (45004 - Marquette and STD4 - Stannard Rock) used in this work. The inset shows the location of lake Superior in North America.

long dataset (i.e. more than one year) is an essential prerequisite to perform a robust model calibration and validation procedure. Moreover, a long-term dataset provides a clear picture of the possible interannual temperature variability, thus allowing for the identification of a set of parameters that is appropriate to investigate long-term climate dynamics.

The model has been tested on Lake Superior (Surface area:  $82\,103\text{ km}^2$ ; Volume:  $12\,000\text{ km}^3$ ; Maximum depth:  $406\text{ m}$ ), the largest of the five Great Lakes of North America (see Figure 4.3), and the largest freshwater basin in the world by surface area. Lake Superior is a dimictic lake: the temperature of the epilimnion is warmer than  $4^\circ\text{C}$  in summer and cools below  $4^\circ\text{C}$  in winter. While the surface water temperature varies seasonally, the temperature of the hypolimnion is almost constant over the year at about  $4^\circ\text{C}$ . Twice a year, in December and in June, surface water reaches the temperature of  $4^\circ\text{C}$ , thus the thermal stratification weakens. Under these conditions, and in the presence of a sufficiently strong wind blowing at the surface, the entire lake can mix.

Long-term temperature data (both for air and surface water) have been obtained from the National Data Buoy Center (NDBC) and from the Great Lakes Environmental Research Laboratory (GLERL), which are part of the National Oceanic and Atmospheric Administration (NOAA). In particular, the NDBC provides historical meteorological and oceanographic data for a network of offshore buoys and Coastal Marine Automated Network (C-MAN) which are installed all over the world, while the GLERL, through the CoastWatch program, releases daily digital maps of the Great Lakes surface water temperature and ice cover (i.e. the Great Lakes Surface Environmental Analysis - GLSEA). For the purpose of this work, only air and surface water temperatures are required, thus other variables are not presented here.

#### 4. A simple lumped model to convert air temperature into surface water temperature in lakes

---

Concerning NDBC dataset, two different stations have been used: (a) 45004 - Marquette, an offshore mooring buoy that provides water temperature measured at 1 *m* below the water surface, and (b) STD4 - Stannard Rock, a C-MAN station installed on a lighthouse that provides air temperature series measured at about 35 *m* above the lake surface. These two stations have been chosen from the many that are available for Lake Superior (both offshore buoys and C-MAN), because of their central location (see Figure 4.3) and long-term data availability, but time series registered in other stations present similar behavior (not presented here). The observational dataset cover a 27-year long period, from 1985 to 2011, and consists of measurements with a one-hour temporal resolution. Since NDBC buoys in the Great Lakes are removed during winter to prevent damage from icing, no measurements are available at the 45004 - Marquette during winter months (except for 1991), while the STD4 - Stannard Rock measurements do not show significant gaps.

Concerning GLERL dataset, daily temperature maps have been used for the period 1994 to 2011. Data refer to the daily lake average surface water temperature obtained from NOAA polar-orbiting satellite imagery. The series is almost continuous, and does not present significant gaps. *Schwab et al.* [1999] compared GLERL surface water temperatures estimates with water temperatures measured at some of the NDBC buoys, finding an overall good agreement, with a mean difference between the two of less than 0.5°C and a root mean square differences ranging from 1.10 to 1.76°C. The close correspondence between the two sets of data is confirmed in Figure 4.8a where NDBC and GLERL dataset considered in the present study are compared for the period 2003-2011.

As customary, the available datasets have been divided into two parts: the first part, containing around two thirds of the available data, is used for model calibration and sensitivity analysis, while the second part, containing the remaining one third, is used for model validation. The datasets used in this work are listed in Table 4.1, together with their main statistics.

The differential Equation (4.17) has been solved numerically by using the Euler explicit numerical scheme, with a daily time step (concerning NDBC data, mean daily temperatures have been preliminary calculated from the original data).

### 4.5 Sensitivity analysis and model calibration

Inverse modeling of complex systems, as such as those encountered in hydrological applications, is inherently ill posed problem, as the information provided by observational data is insufficient to identify the parameters without uncertainty. In a typical situation many different combinations of the parameters may provide similar fitting to the observational data. For example, even a simple model with only four or five parameters to be estimated may require at least ten hydrographs for a robust calibration [e.g. *Hornberger et al.*, 1985].

This identification problem can be alleviated by reducing the number of parameters used in the

#### 4. A simple lumped model to convert air temperature into surface water temperature in lakes

model, for example through sensitivity analysis, which is the typical methodology used for this purpose [e.g. *Majone et al.*, 2010]. In this case we perform sensitivity analysis by using Generalized Likelihood Uncertainty Estimation (GLUE), a methodology proposed by *Beven and Binley* [1992] that requires the identification of a validity range for each parameter, a strategy for sampling the parameter space and finally a likelihood measure to be used in order to rank the different parameters sets. We carried out 100000000 Monte Carlo model realizations using uniform random sampling across specified parameter ranges selected according to physical limitations of model's parameters. Indeed, the physical meaning of the parameters allowed for a reasonable definition of the possible range of variability of each of them. Finally, we used as likelihood measure the Nash-Sutcliffe model efficiency coefficient,  $E$ , which is a widely used metric adopted in hydrological applications [e.g. *Nash and Sutcliffe*, 1970; *Majone et al.*, 2012, and many others]

$$E = 1 - \frac{\sigma_e^2}{\sigma_o^2} = 1 - \frac{\sum_{i=1}^n (\hat{T}_{w,i} - T_{w,i})^2}{\sum_{i=1}^n (\hat{T}_{w,i} - \bar{T}_w)^2}, \quad (4.24)$$

where  $n$  is the number of data,  $\sigma_e^2$  and  $\sigma_o^2$  are the variance of the residuals and of the observations, respectively,  $\hat{T}_{w,i}$  and  $T_w$  are the observed and simulated surface water temperature at time  $t_i$ , and  $\bar{T}_w$  is the average of  $\hat{T}_{w,i}$ . Note that the residual is defined as the difference between the observational data and the model's prediction, and a parameter set identifies a point in the space of parameters.

The Nash-Sutcliffe efficiency index ranges from  $-\infty$  to 1. An efficiency equal to 1 ( $E = 1$ ) corresponds to a perfect match between measured and simulated values, whilst  $E = 0$  indicates that the model prediction is as accurate as the mean of observations. Efficiency values lower than 0 ( $E < 0$ ) occurs when  $\sigma_e^2$  is larger than  $\sigma_o^2$ , thus when the mean of observations is a better estimator than the model itself.

Since its introduction in 1992, GLUE has found wide applications and it is recognized as a useful methodology for uncertainty assessment in many fields of study especially in non-ideal situations [e.g. *Beven*, 2006]. Nevertheless, the goal of this work is not to adopt a complete informal Bayesian approach to estimate uncertainty of model predictions, but rather to assess the impact of changes in uncertain parameter values on model output. Hence, the purpose is to set up a general and effective strategy to select which are the most sensitive parameters of the model, and to define which should be suitably adjusted in a calibration process. Indeed, the GLUE methodology is a powerful and effective tool that can be also used for model calibration besides uncertainty estimation procedures and sensitivity analysis.

One of the most acknowledged limitation of the GLUE methodology is the dependence on the number of Monte Carlo simulation, especially in the presence of complex models with high computational demand. However, in our case we were able to fully explore parameter response surfaces by adopting a significantly high number of realizations. Therefore, the use of the GLUE

#### 4. A simple lumped model to convert air temperature into surface water temperature in lakes

---

methodology, not only for parameter identifiability purposes but also as a calibration tool, appears appropriate. Just as a sidenote, 100000000 model runs over a period of 18 years with a daily time step and adopting Intel(R) Xeon(R) CPU X5680 @ 3.33GHz took around 2 hours.

Furthermore, in the attempt to test reliability and predictive capability of the model, a validation procedure was undertaken by running the model on validation datasets (see Table 4.1) by using the sets of parameters which maximize the efficiency  $E$  during the calibration periods (i.e. the set of parameters with the highest likelihood obtained through the GLUE methodology).

In the ensuing sections, the GLUE methodology is presented for different model configurations (from 8 to 4 parameters), with reference to the calibration periods of the NDBC and GLERL datasets, respectively (see Table 4.1).

As a final comment, we point out that the first year of each time series is used as warm-up period (i.e., excluding the period from the calculation of the Nash-Sutcliffe efficiency index  $E$ ), in order to remove any transient effect due to the initial condition.

##### 4.5.1 8-parameter model

A first-step sensitivity analysis has been carried out by solving Equation (4.17) over the calibration period (18 years, from 1985 to 2002) using randomly sampled set of parameters. We recall here that each of the 8 parameters has been allowed to vary over physically reasonable ranges of values, whose determination is discussed in Section 4.3.3.

In the light of the results obtained from the first-step sensitivity analysis, the ranges of variability of each parameter were narrowed, thus allowing for a detailed investigation of parameters space regions associated with high values of  $E$ . Subsequently, a second-step sensitivity analysis has been undertaken by sampling further 100000000 parameters sets from the narrowed parameters ranges.

Figure 4.4 shows the dotted plots of the efficiency index  $E$  for each of the 8 parameters of the model, corresponding to the narrowed ranges (second-step performance analysis). For the sake of clarity in the presentation of results, Figure 4.4 (as well as Figure 4.6) shows only the set of parameters with  $E$  larger than 0.8. Model simulation during the calibration period 1985-2002 using the best set of parameters is illustrated in Figure 4.5, which shows a noticeable agreement between simulated and observed values, with an efficiency index  $E > 0.9$  (see Table 4.2 for a summary of the results).

#### 4. A simple lumped model to convert air temperature into surface water temperature in lakes

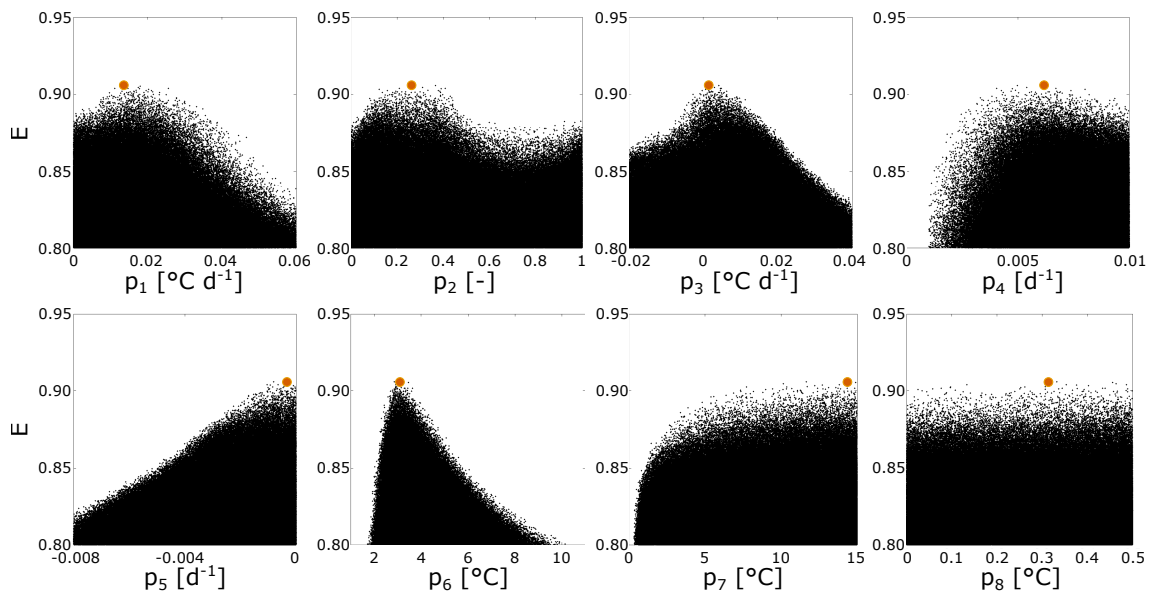


Figure 4.4: Dotty plots of efficiency indexes ( $E$ ) for the 8-parameters model during the calibration period 1985-2002 (NDBC simulation). Highest efficiency is presented with an orange dot.

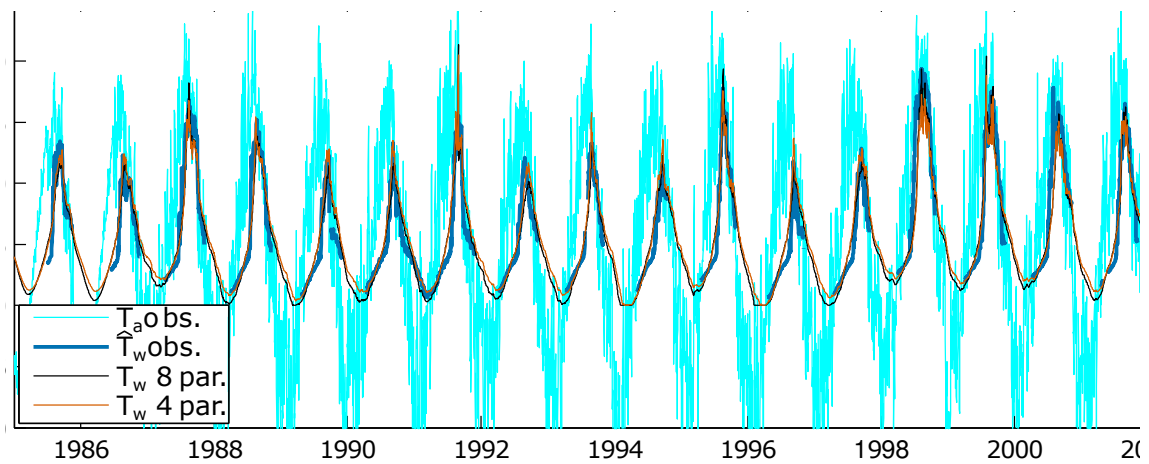


Figure 4.5: Comparison between simulated and observed surface water temperature during the calibration period 1985-2002 (NDBC simulation). Simulated curves refer to the full 8-parameter and the simplified 4-parameter models, respectively. Observed air temperature data are also presented with cyan line.

Table 4.1: Summary of the datasets adopted in this study, and their main statistics.

Source	Variable	Device	Period	Duration	(cal + val)	Frequency	Missing data	Mean value [°C]	Std [°C]
NDBC	$T_w$	Buoy	1985-2011	27 years	(18 + 9)	Hourly	46%	7.18	4.66
NDBC	$T_a$	C-MAN	1985-2011	27 years	(18 + 9)	Hourly	9%	5.39	8.97
GLERL	$T_w$	Satellite	1994-2011	18 years	(12 + 6)	Daily	5%	6.52	5.26

Table 4.2: Estimated model parameters and efficiency indexes during calibration and validation periods (NDBC and GLERL simulations).

n par.	$p_1$ [°C d <sup>-1</sup> ]	$p_2$ [-]	$p_3$ [°C d <sup>-1</sup> ]	$p_4$ [d <sup>-1</sup> ]	$p_5$ [d <sup>-1</sup> ]	$p_6$ [°C]	$p_7$ [°C]	$p_8$ [°C]	$E$ cal	$E$ val
<i>NDBC (cal: 1985-2002; val: 2003-2011)</i>										
8	$1.35 \times 10^{-2}$	$2.62 \times 10^{-1}$	$1.47 \times 10^{-3}$	$6.18 \times 10^{-3}$	$-3.26 \times 10^{-4}$	3.08	14.41	0.31	0.91	0.90
6	$1.56 \times 10^{-2}$	$2.83 \times 10^{-1}$	$1.23 \times 10^{-3}$	$5.95 \times 10^{-3}$	$-2.36 \times 10^{-4}$	3.01	-	-	0.91	0.90
4	-	-	$1.41 \times 10^{-2}$	$5.87 \times 10^{-3}$	$-2.23 \times 10^{-3}$	2.77	-	-	0.89	0.89
<i>GLERL (cal: 1994-2005; val: 2006-2011)</i>										
8	$1.75 \times 10^{-2}$	$4.67 \times 10^{-1}$	$2.30 \times 10^{-2}$	$6.55 \times 10^{-3}$	$-2.57 \times 10^{-3}$	3.50	13.32	0.44	0.95	0.97
6	$2.36 \times 10^{-2}$	$4.37 \times 10^{-1}$	$1.93 \times 10^{-2}$	$5.91 \times 10^{-3}$	$-2.16 \times 10^{-3}$	3.65	-	-	0.95	0.97
4	-	-	$2.57 \times 10^{-2}$	$9.63 \times 10^{-3}$	$-2.73 \times 10^{-3}$	3.54	-	-	0.95	0.97
<i>GLERL<sub>my</sub> (cal: mean year 1994-2005; val: 2006-2011)</i>										
8	$1.31 \times 10^{-2}$	$2.32 \times 10^{-1}$	$1.55 \times 10^{-2}$	$8.47 \times 10^{-3}$	$-1.09 \times 10^{-3}$	3.26	11.93	0.45	0.99	0.97
6	$2.01 \times 10^{-2}$	$2.06 \times 10^{-1}$	$1.49 \times 10^{-2}$	$9.69 \times 10^{-3}$	$-7.58 \times 10^{-4}$	3.75	-	-	0.99	0.97
4	-	-	$2.77 \times 10^{-2}$	$9.16 \times 10^{-3}$	$-2.87 \times 10^{-3}$	3.13	-	-	0.99	0.97

#### 4. A simple lumped model to convert air temperature into surface water temperature in lakes

---

A visual inspection of dot plots of model efficiency can provide useful information on the identifiability of each parameter. According to Figure 4.4, all the parameters are characterized by a good identifiability with the exception of parameters  $p_7$  and  $p_8$ . This can be explained if we consider that NDBC dataset presents few values of water temperature during winter periods. In particular, no data (except for one single year out of 18) are available when surface water temperature approaches  $0^\circ\text{C}$ , which corresponds to the period of the year when the parameter  $p_8$  is relevant. We remark here that  $p_8$  is the parameter associated to ice formation at the surface of the lake. Although to a minor extent, also  $p_7$  does not show a clear identifiability, probably as a consequence of the importance that this parameter assumes during winter time (it plays a role only when  $T_w < 4^\circ\text{C}$ ), that is when water temperature measurements are not available. However, by analyzing the dot plot an important information can be inferred: efficiency increases for higher values of  $p_7$ , and approaches a nearly asymptotic high efficiency trend when  $p_7 \gtrsim 5^\circ\text{C}$ . Looking at the physical meaning of the parameter (see Equation (4.18)), this means that model performance improves as the mixed depth  $D$  approaches its maximum value  $D_r$  when the lake is inversely stratified ( $T_w < 4^\circ\text{C}$ ).

In the light of these evidence, in the ensuing section the full 8-parameter version of the model has been simplified by neglecting parameters  $p_7$  and  $p_8$ .

##### 4.5.2 From 8 to 4 parameters

On the basis of the results discussed in the previous section, not all the model parameters seem to be significant and clearly identifiable. In particular, the parameter  $p_8$  has been found to be insensitive to the model, and parameter  $p_7$  provides an overall high performance over most of its variability domain ( $p_7 \gtrsim 5^\circ\text{C}$ ). The peculiar behavior of these parameters, together with the fact that both appear in the definition of the mixing depth  $D$  when the lake is inversely stratified, suggests that a simplification of the model may be possible by considering a different (simpler) expression for  $D$ . As far as parameter  $p_8$  is concerned, since it is not significant for the model, it can be easily neglected, thus eliminating the effect of ice formation. On the other hand, according to Equation (4.18) high values of  $p_7$  mean small decay rates of  $D$ , thus thick mixing depths when the lake is inversely stratified. In the light of these considerations, we derived a first simplified version of the model, where the mixing depth is assumed to be constant and at its maximum thickness  $D = D_r$  when the lake is inversely stratified ( $T_w < T_r$ ). Thanks to this simplification  $p_7$  and  $p_8$  are removed and the number of parameters diminishes from 8 to 6.

As for the case of the full 8-parameter version of the model, the same sensitivity analysis described in Section 4.5.1 has been carried out also for the simplified 6-parameter version. The set of parameters presenting the highest efficiency index during the calibration period is summarized in Table 4.2, whilst dot plots deriving from the application of GLUE methodology and the comparison between simulated and measured surface water temperature during the same period

#### 4. A simple lumped model to convert air temperature into surface water temperature in lakes

---

are not presented here for the sake of brevity. Indeed, results are essentially equivalent to those obtained using the full 8-parameter model, which is confirmed by the close similarity between the best set of parameters and the efficiency indexes obtained in the two cases (see Table 4.2). The similarity of results supports the idea that the 6-parameter model is a reasonable simplification, at least in the case considered herein where the winter data are not abundant (see also Section 4.7 for further discussion).

The number of parameters can be further diminished from 6 to 4 by eliminating the parameter  $p_1$  and, as a direct consequence,  $p_2$ , besides  $p_7$  and  $p_8$ . This simplification is justified since three periodic terms appear in the model as characterized by an annual periodicity: the forcing term  $p_1 \cos(2\pi(t - p_2))$ , the exchange term  $p_4(T_a - T_w)$  and the residual correction  $p_5 T_w$ . The simultaneous co-presence of all these terms may be considered redundant in those cases in which the annual cycles of  $T_w$  and/or of  $T_a - T_w$  can be suitably approximated as sinusoids. Indeed, the sum of sinusoidal functions with the same frequency, but different amplitude and phase, yields another sinusoid with different amplitude and phase but same frequency. Therefore, two sinusoids are sufficient, and the forcing term  $p_1 \cos(2\pi(t - p_2))$  can be removed, relieving the overall annual variations on the periodic terms controlled by the model variable  $T_w$  and the external forcing  $T_a$ . Following this logic, the term  $p_5 T_w$  could be neglected alternatively (on the contrary  $p_4(T_a - T_w)$  cannot since it is the only term that includes information about the external forcing), but this assumption would remove only one parameter ( $p_5$ ) instead of two ( $p_1$  and  $p_2$ ), thus making it less attractive. In principle, both  $p_1 \cos(2\pi(t - p_2))$  and  $p_5 T_w$  could be neglected contemporaneously, but in this case the phase of the overall periodic term would be forced to that of the temperature difference. It is worth noting that in the 4-parameter version of the model (retaining  $p_3$ ,  $p_4$ ,  $p_5$  and  $p_6$ ), the meaning of the parameters is distorted, as the processes that were accounted in  $p_1$  are now included in  $p_4$  and  $p_5$ .

Figure 4.6 shows the dotted plots of the efficiency indexes  $E$  for the 4-parameter version of the model, where only the parameters  $p_3$ ,  $p_4$ ,  $p_5$  and  $p_6$  are retained. In this case, since the number of random samplings has been kept unchanged (i.e., 100 000 000), the predictions of the Monte Carlo realisations appear much less sparse (i.e. denser dotted plots) if compared to the case of the 8-parameter version. Notice that all the parameters are characterized by high identifiability and the model does not present signs of overparameterization. Figure 4.5 shows the comparison between observed and simulated surface water temperatures during the calibration period 1985-2002 for the 4-parameter and the full 8-parameter models, respectively. The difference is little, and mainly localized during the winter period, when no surface water temperature data are available for comparison. During the rest of the year, when measurements are available and  $E$  index can be effectively calculated, the two solutions are comparable and the efficiency indexes are similar (just slightly lower for the simplified 4-parameter version of the model, see Table 4.2).



#### 4. A simple lumped model to convert air temperature into surface water temperature in lakes

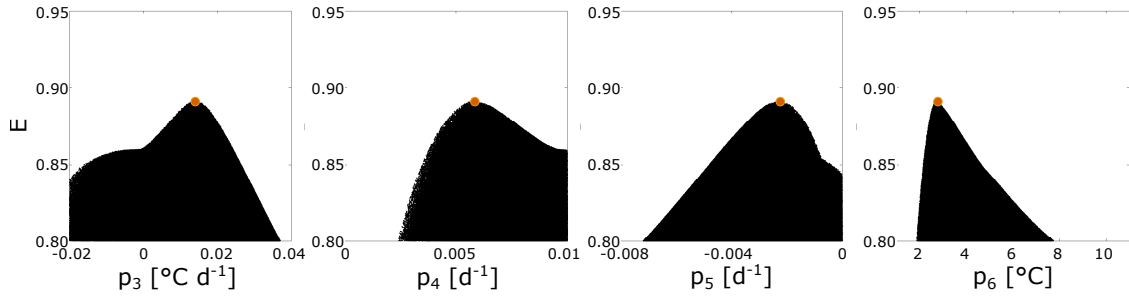


Figure 4.6: Dotty plots of efficiency indexes ( $E$ ) for the 4-parameters model during the calibration period 1985-2002 (NDBC simulation). Highest efficiency is presented with an orange dot.

### 4.6 Model validation

The best set of parameters obtained during the calibration period for the different versions of the model (with 8, 6 and 4 parameters, see Table 4.2) have been used to run the model during the validation period 2003-2011 (see Table 4.1). In all the cases, simulations have been characterized by high efficiency indexes, comparable to those obtained with the best simulations during the calibration period ( $E \simeq 0.9$ , see Table 4.2). In Figure 4.7 simulated water temperatures (for the versions with the 8 and 4 parameters) are compared with observations showing an overall very good agreement. Results confirm the reliability of the model as a valuable tool for surface water estimation over long-term periods with different model configurations.

Besides the evaluation of the surface water temperature, the model provides additional relevant information regarding the annual evolution of the epilimnion thickness. In fact, as discussed in Section 4.3, the model explicitly includes a suitable parameterization of the seasonal behavior of the mixing depth through Equation (4.18). In particular, the normalized thickness of the epilimnion  $\delta = D/D_r$  is automatically determined once the parameters  $p_6$ ,  $p_7$  and  $p_8$  are defined. Furthermore, it is evident that if an estimate of the reference mixing depth  $D_r$  were known, the actual thickness of the well-mixed layer  $D$  could be evaluated as well. With reference to the NDBC dataset Figure 4.8b shows the evolution of  $\delta$  over the validation period 2003-2011, for the 8- and 4-parameter versions of the model (continuous lines). In the first case (8 parameters) the fictitious increase of depth due to the presence of ice is evident (peaks at values greater than 1). We recall here that in the 8-parameter version of the model, the formation of ice is modeled by increasing the depth  $D$  of the surface layer, thus the volume of water involved in the heat balance (see Figure 4.2). Thanks to this assumption the model accounts for the insulation effect due to the presence of ice, which may be even more significant when the ice surface is snow-covered, and the penetration of solar

radiation is strongly attenuated.

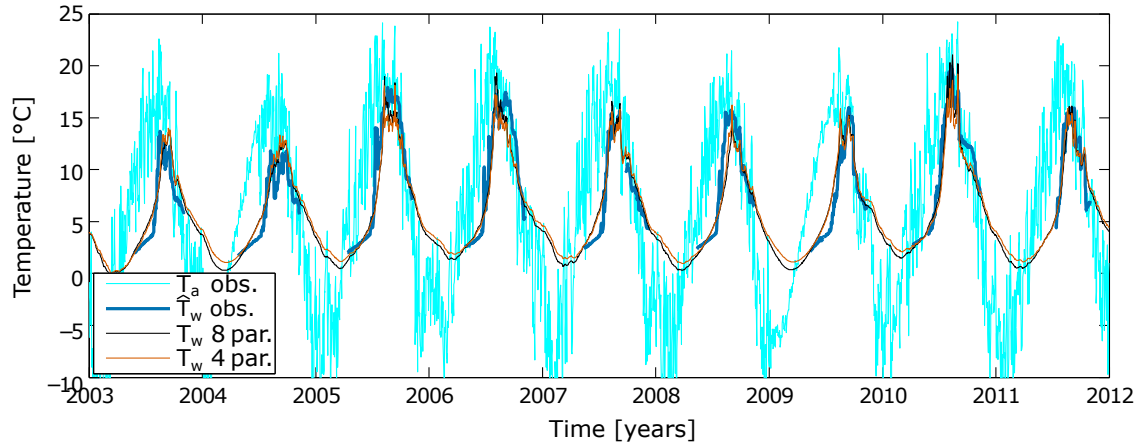


Figure 4.7: Comparison between simulated and observed surface water temperature during the validation period 2003-2011 (NDBC simulation). Simulated curves refer to the full 8-parameter and the simplified 4-parameter models, respectively. Observed air temperature data are also presented with cyan line.

## 4.7 Discussion

The physically-based, semi-empirical model presented here has been shown to provide an accurate description of surface water temperature of lakes, with high values of Nash-Sutcliffe efficiency index  $E \simeq 0.90$ , and a root-mean-square error between observations and simulations of the order of  $1^\circ\text{C}$  (results not presented here). This error in prediction capability is comparable to those obtainable using process-based numerical models [e.g. *Fang and Stefan, 1996; Stefan et al.*]. However, these kinds of models have the strong limitation of requiring high resolution weather data.

Results are remarkable both using the full 8-parameter version and the simplified 6- and 4-parameter versions of the model. In particular, little difference has been found regarding the best set of parameters and the efficiency indexes obtained using the 8- and the 6-parameter versions (see Table 4.2). Therefore, one may infer that no significant advantages can be expected by using a more accurate expression for  $D$  during the winter period (8-parameter version), instead of a constant value (6-parameter version). However, it is not possible to state this conclusion by simply analyzing results presented in Sections 4.5.1, 4.5.2 and 4.6. Indeed, no surface water temperature measurements are available during the winter period for the NDBC dataset, except for the year

#### 4. A simple lumped model to convert air temperature into surface water temperature in lakes

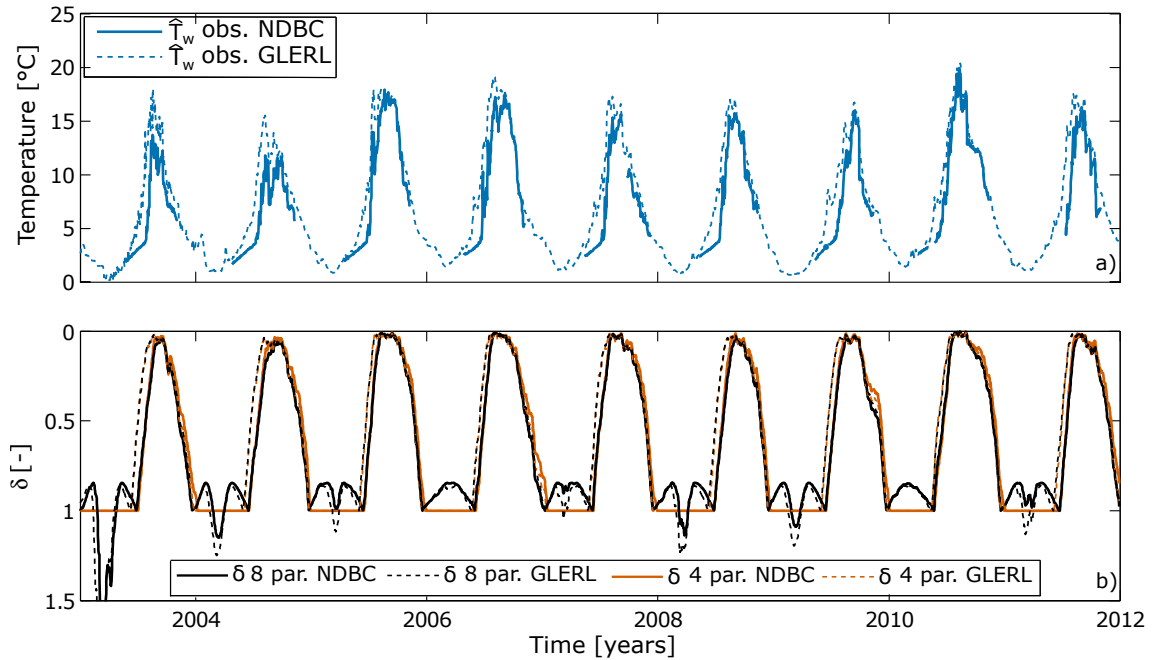


Figure 4.8: Evolution of the dimensionless depth  $\delta$  over the period 2003-2011: comparison between results for the full 8- and simplified 4-parameter versions of the model obtained from NDBC and GLERL simulations. a) Comparison of observed water temperature time series during the period 2003-2011 for the NDBC and GLERL dataset, respectively. b) Evolution of the dimensionless depth  $\delta$  over the period 2003-2011 for the full 8- and simplified 4-parameter versions of the model (NDBC and GLERL simulations).

1991, thus the model efficiency has not been tested during the period of inverse stratification. Aimed at overcoming this limitation, a new dataset of surface water temperature has been used, which does not have significant data gaps: the daily lake-averaged surface water temperature based on satellite imagery provided by the GLERL (see Table 4.1). The same GLUE procedure discussed in Section 4.5 has been performed by adopting the GLERL dataset as reference surface water temperature data and by repeating the implementation details described in Section 4.5.1. The simulations (hereafter referred to as GLERL) have been run over the calibration period 1994-2005, using as input forcing the air temperature data retrieved from the NDBC dataset (C-MAN station, see Table 4.1). The 8-, 6- and 4-parameter versions of the model have been tested, obtaining remarkable efficiency indexes ( $E > 0.95$ ), which are higher with respect to the previous applications (i.e. using NDBC dataset). Validation procedure has been conducted with reference to the period 2006-2011, confirming high performances of the model ( $E > 0.97$ ). The parameters sets providing the highest efficiencies during the calibration period and the associated  $E$  values are given in Table 4.2, while comparison between

#### 4. A simple lumped model to convert air temperature into surface water temperature in lakes

simulated and observed surface water temperature data for the 8- and 4-parameter versions of the model are shown in Figures 4.9 and 4.10 for the calibration and validation periods, respectively. Finally, the seasonal evolution of  $\delta$  is shown in Figure 4.8b for both versions of the model (dashed lines), and it is compared with those obtained from the application of the model to the NDBC dataset. Results are consistent, with the slight difference in the onset of summer stratification being due to the earlier increase of water temperature in the GLERL dataset compared to the NDBC dataset (see 4.8a).

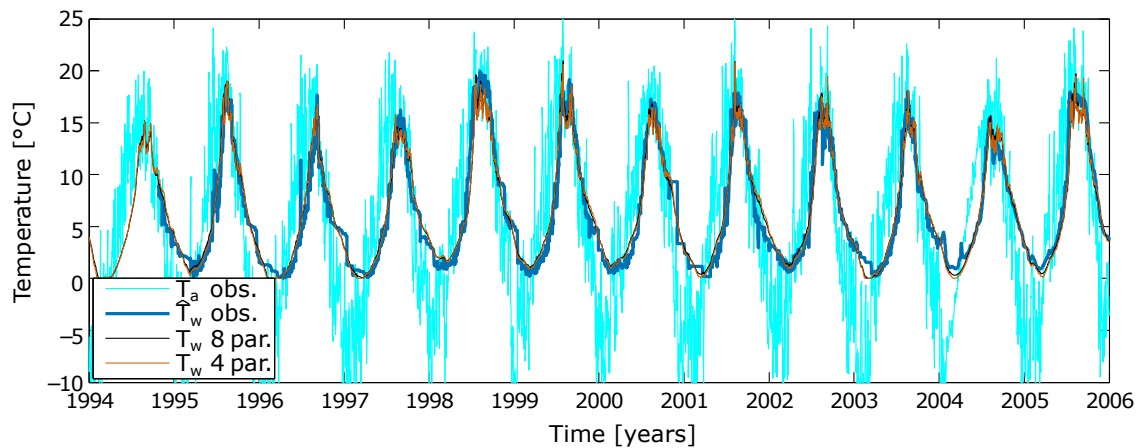


Figure 4.9: Comparison between simulated and observed surface water temperature during the calibration period 1994-2005 (GLERL simulation). Simulated curves refer to the full 8-parameter and the simplified 4-parameter models, respectively. Observed air temperature data are also presented with cyan line.

So far, the model has been tested with long-term series of data (NDBC: 27 year, and GLERL: 18 years), however long-term records are often not available, or are characterized by significant gaps due to missing data. Instead, it is relatively easier to have access to mean annual cycles of temperature (both of surface water and air), whose determination also represents a valuable strategy to overcome the possible lack of data. Therefore, a conversion model that could be calibrated on mean annual cycles, and successively applied over long-term periods without compromising the correct estimation of the interannual fluctuations, would represent a valuable tool. For this purpose, the mean annual cycle of surface water temperature has been derived from GLERL data during the calibration period 1994-2005, and the corresponding cycle of air temperature from NDBC dataset (C-MAN station). A Monte Carlo sensitivity analysis (hereafter referred to as  $GLERL_{my}$ , the subscript  $my$  staying for mean year) has been carried out following the same procedure adopted in the previous sections, but using mean annual cycles of air and water temperature as forcing and

#### 4. A simple lumped model to convert air temperature into surface water temperature in lakes

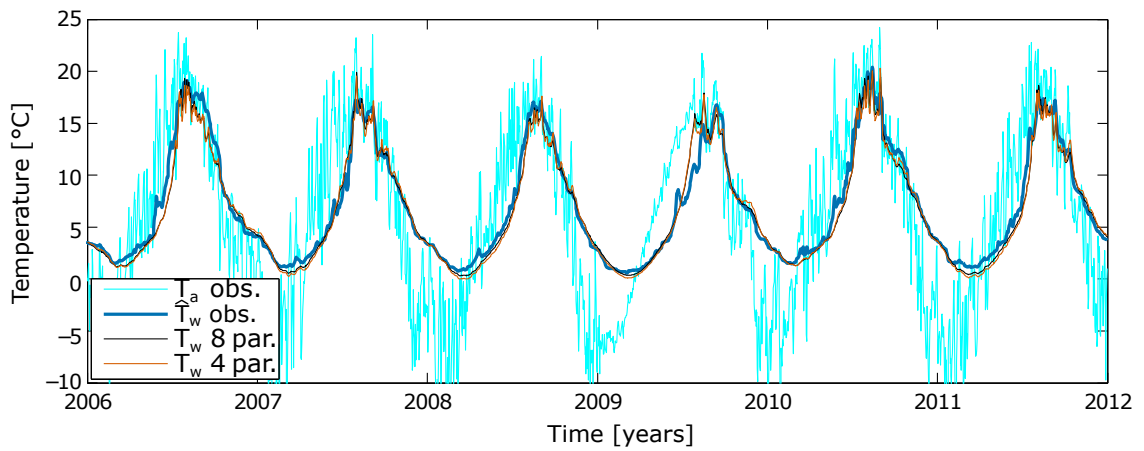


Figure 4.10: Comparison between simulated and observed surface water temperature during the validation period 2006-2011 (GLERL simulation). Simulated curves refer to the full 8-parameter and the simplified 4-parameter models, respectively. Observed air temperature data are also presented with cyan line.

reference data, respectively. In order to eliminate the influence of initial conditions the temperature cycles have been replicated for two years with the first one used as a “warm-up”. Results obtained by adopting the parameters providing the highest efficiency (see Table 4.2) are presented in Figure 4.11, which shows the hysteresis cycles between air and surface water temperatures derived from measurements and model estimates (8- and 4-parameter versions). A very high efficiency index ( $E \simeq 1.0$ ) is achieved, and both versions of the model are able to satisfactorily capture the seasonal pattern of thermal hysteresis. The parameters sets providing the highest efficiency during the calibration process with the mean annual temperature data and the associated  $E$  value are summarized in Table 4.2.

Afterwards, a validation procedure has been conducted for  $GLERL_{my}$  during the period 2006-2011 (the same as GLERL simulations, thus results can be compared). Results are characterized by remarkable efficiency indexes ( $E \simeq 0.97$ ), only slightly lower than the values obtained with the simulations presented in the previous sections. Indeed, the model calibrated on the mean year is able to well capture the interannual variabilities, producing remarkable results not dissimilar from those shown in Figure 4.10 (for this reason are not presented here). Furthermore, parameters values are significantly similar to those obtained calibrating the model with the whole 12-year series of data (GLERL simulation, see Table 4.2).

In the light of the results presented in this section, we assert that the model can be calibrated and adopted using data of different origin (measurements at buoys and coastal stations, satellite

#### 4. A simple lumped model to convert air temperature into surface water temperature in lakes

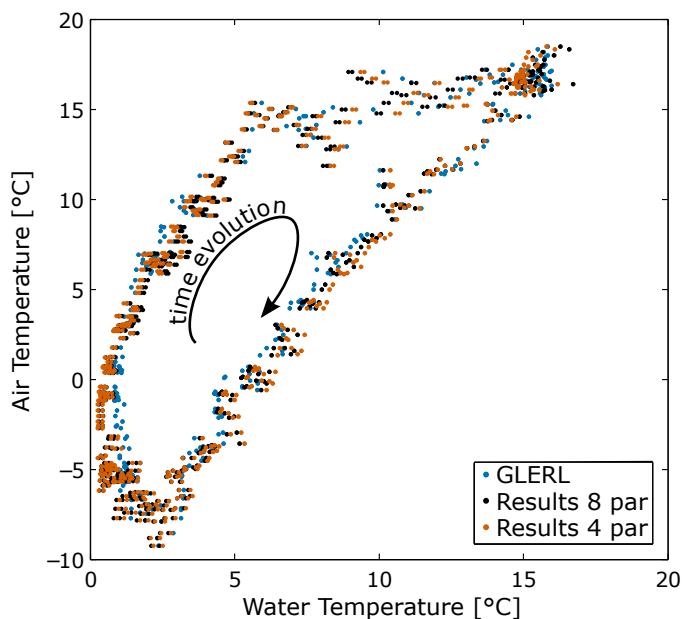


Figure 4.11: Comparison of the hysteresis cycles between air and surface water temperatures, as derived by the data and by the 8- and 4-parameters versions of the model. Hysteresis cycles refer to the mean year, calculated over the period 1994-2005, using GLERL and NDBC data for  $T_w$  and  $T_a$ , respectively (GLERL<sub>my</sub> simulation).

estimates) and nature (long-term series of data, mean annual cycle of temperature). This conclusion is corroborated by the excellent results (not shown here for the sake of brevity) of the performance analysis (entirely comparable to those presented in the present paper) obtained using different datasets: (a) air temperature from a different C-MAN station (the PILM4 - Passage Island), whose sensor is installed at a different high (22m) respect to the Stannard Rock station (35m), (b) air temperature data measured at the 45004 - Marquette offshore buoy station at only 4 m from the lake surface, and (c) water temperature measured at a different off shore buoy (the 45001 - Hancock). Furthermore, in all cases, even if the calibration is performed considering mean annual cycles of temperature, the model suitably captures the interannual variations that are likely to occur. On the basis of these evidence, we can assert that in principle this simple model may be used with different temperature datasets as input. As a matter of fact, unlike process-based models, it can be calibrated using any dataset, independently of its physical representativeness (e.g. point measurements vs. spatial averages). Air temperature series provided by general atmospheric models or climate projections derived from GCMs and RCMs can be used as well. In this regard, the model is particularly attractive for climate change impact studies, since predictions of air temperature are usually more reliable than other meteorological variables [e.g. Gleckler *et al.*, 2008].

## 4.8 Concluding remarks

In this chapter a simple, physically-based model has been described, which is able to reproduce observed water temperature of lakes with limited information on external meteorological forcing. As a matter of fact, the only input required is air temperature.

Starting from the zero-dimensional heat budget, we derived a simplified first-order differential equation for water temperature forced by a few terms representing the combined effects of the seasonally varying external term and the exchange terms explicitly dependent on the difference between air and water temperatures. Assuming annual sinusoidal cycles of the main heat flux components 8 parameters have been identified, which can be calibrated if temporal series of air and surface water temperature are available. Such a calibration is supported by the physical interpretation of the parameters, which provides reasonable initial conditions for the parameters ranges.

The relative importance of the model's parameters have been evaluated by using the GLUE methodology. Thanks to this analysis we were able to identify and neglect parameters that, under different conditions, appears less significant in the model formulation leading to two simplified versions retaining 6 and 4 parameters, respectively.

The model has been applied to the case of Lake Superior (USA - Canada) with reference to different types of datasets, and all the versions of the model have shown to perform well in reproducing the measured water temperature data. This model has proved to be robust and able to reproduce well the lake's response to meteorological forcing, including interannual variability, representation of the variability of the epilimnion thickness, and the inverse stratification process which typically occurs in dimictic lakes.

In the light of these results, the model can represent a valuable tool in climate change impact studies allowing for predictions of future trends of lake surface water temperature, given future projections of air temperature only. In this regard, the model has been used here to construct possible scenarios of surface water temperature of Lake Baikal (see Chapter 5), used to investigate the future response of the lake to climate change (see Chapter 6).

#### 4. A simple lumped model to convert air temperature into surface water temperature in lakes

---



## 5 Available datasets and data processing

**Abstract** - *In the first part, the present chapter provides a review of the data available for Lake Baikal. The main emphasis is on wind and surface water temperature, which are the major forcing of the system, and the primary information needed for the model presented in Chapter 3. Owing to the fact that Lake Baikal is huge and located in a very remote region, it is only partially monitored. As a consequence, the available measurements and observations are few, and not sufficient for the purposes of this study. Therefore, these data have been integrated with historical re-analysis series, a long-term record of data that describes the climate conditions occurred in the past half century in the region of Lake Baikal. Future projections of wind and temperature under global climate change scenarios have been considered as well, aimed at simulating the effects on deep ventilation driven by plausible changes in the climate forcing. Finally, besides data about surface water temperature and wind forcing, also measurements concerning the vertical profiles of temperature, CFC-12 and dissolved oxygen concentration are presented and discussed.*

*Since both re-analysis series and future projections have a coarse spatial resolution, they are not representative of the conditions at the lake surface (i.e. local scale), but rather of the processes occurring at a wider spatial scale (i.e. regional scale). Furthermore information about surface water temperature of lakes are generally not available, but only air temperature is provided. In the attempt to overcome these data constraints, two basic operations are required. The first is the downscaling of data, which consists in extrapolating coarse-grid climatic variables to a finer scale, whereas the second is the conversion of air temperature series into the corresponding values of surface water temperature. The downscaling and conversion procedures employed in this study are described into details in the second part of this chapter. Different approaches have been used depending on the type of data to be processed: wind speed or temperature, past records or future scenarios. In general, the downscaling/conversion of data has been obtained integrating well-known downscaling techniques into newly developed methodologies.*

*The chapter is structured as follows. The available data are presented and described in Section 5.1, starting from measurements and observation in Section 5.1, to continue with re-analysis dataset and the future climate scenarios in Sections 5.1.2 and 5.1.3, respectively. Section 5.2 deals with the processing of re-analysis and future projections datasets. In particular, the procedures devised to downscale/convert historical data are presented in Section 5.2.1, while those for future conditions are described in Section 5.2.2. Finally, concluding remarks are given in Section 5.3.*



## 5.1 An overview of available data

Several measurement campaigns have been being carried to characterize the physical and chemical limnology of Lake Baikal. In particular, during the last decades numerous expedition cruises have been organized and some measurement stations have been installed, primarily by Russian, Swiss and American scientists, often working in close cooperation with each other [e.g. Weiss *et al.*, 1991; Shimaraev *et al.*, 1994; Killworth *et al.*, 1996; Hohmann *et al.*, 1997; Peeters *et al.*, 1997, 2000; Wüest *et al.*, 2005; Hampton *et al.*, 2008; Schmid *et al.*, 2008; Shimaraev *et al.*, 2011a,b, 2012]. These field campaigns were mainly designed to measure vertical temperature profiles and collect water samples for the analysis of tritium, helium isotopes, dissolved oxygen, *CFCs*, and other noble gases. As a whole, the existing measurement data are sufficiently detailed to provide a general characterization of the vertical thermal and chemical structure of the South, Central and North basins. Nevertheless, the temporal resolution of the measurements is generally low, consisting in only a couple of vertical profiles per year. The only exception is for the measurements collected at the permanent stations [e.g. Schmid *et al.*, 2008; Shimaraev *et al.*, 2011b, 2012], which have been installed in the South Basin since 2000, and provide vertical profiles of temperature with a high frequency (i.e.  $O(10^1)$  min). In conclusion, continuous series of measurements are available just from 2000, and only for temperature.

As far as meteorological conditions (e.g. air temperature, wind speed and direction, humidity, solar radiation) are concerned, only few observations are available. The existing data have been generally recorded at weather stations installed around the lake [e.g. Wüest *et al.*, 2005; Schmid *et al.*, 2008], however there exist also a few measurements collected offshore, from ships or mooring stations [e.g. Rzhaplinsky and Sorokina, 1977]. Unfortunately, these latter data are scarce, fragmentary and difficult to access. On the other hand, data from meteorological stations along the coast are relatively more abundant, but it is evident that they are not likely to be fully representative of the actual conditions over the lake. Wind speed and direction, for example, are strongly affected by mountain ridges, which often modulate the background wind field and produce highly variable local winds of different strengths and directions [Ivanov, 2012]. To conclude, long-term continuous series of meteorological data representative of the conditions over the lake are not available or accessible, at least to our knowledge.

If on one hand available data are few and cover limited periods, on the other long-term series of data are required for a robust calibration of the simple 1D model presented in Chapter 3. The calibration procedure has been performed assuming, besides temperature, *CFCs* concentration as the main tracer. Indeed, *CFCs* are not known to be influenced by biological processes and are characterized by a high chemical stability, thus serve as relatively unambiguous tracers [e.g. England, 2001]. The attempt is to adjust the model's parameters to suitable values in order to

## 5. Available datasets and data processing

Table 5.1: Summary of the available datasets of water temperature,  $T_w$ , air temperature,  $T_a$ , and wind speed,  $W$ .

Dataset	Variables	Resolution	Time period
EAWAG	Surface water temperature	Sub-basin scale, 12h	2000-2008
<i>Rzheplinsky and Sorokina</i> [1977]	Wind speed and duration	Lake scale	1959-1968
ECMWF ERA-40	Wind speed and air temperature	Regional scale, 6h	1958-2002
CNRM-CM5 (historical)	Wind speed and air temperature	Regional scale, 3h	1960-2005
CNRM-CM5 (RCP2.6, RCP4.5 and RCP8.5)	Wind speed and air temperature	Regional scale, 3h	2026-2046, 2081-2101

contemporaneously obtain a good description of the thermal structure of the lake and a reliable reconstruction of the historical evolution of *CFCs* concentrations in deep water. Therefore, for calibration purposes, the series of data, besides covering long periods, should also appropriately describe the historical meteorological conditions that actually occurred at the lake surface.

In order to overcome some of the constraints related to the scarcity of data, available measurements and observations had to be integrated with additional, more detailed, information. In this regard, re-analysis datasets have been used to calibrate the model and hindcast past conditions of the lake. Re-analysis datasets consist of long-term record of data, which provide a consistent chronological description of climate conditions that actually occurred in the past. Therefore, this kind of data allows for the imposition of appropriate upper boundary conditions to properly simulate the evolution of *CFCs* concentrations in Lake Baikal, and hence calibrate the model. Furthermore, aimed at investigating the behavior of the lake in response to changing external forcing, future projections of meteorological variables under global climate change scenarios have been considered. The datasets used in this work are summarized in Table 5.1 and discussed in the following sections, starting from the measurements and observations, to proceed with re-analysis datasets and future climate scenarios. Measured profiles of temperature and species concentrations are reported and discussed only with reference to the South Basin of the lake, which is the part of the lake considered in this study.

### 5.1.1 Measurements and observations

**Water temperature** Concerning water temperature,  $T_w$ , a 9-year set of vertical temperature profiles are available for the period ranging from 2000 to 2008. The data were collected at a distance of 3.2 km from the northern shore of the South Basin [see *Schmid et al.*, 2008, for details], where a mooring station equipped with a chain of high accuracy and resolution thermistors was installed. The vertical positions of the moored instruments changed slightly from year to year, but always keeping the deepest measurement point at  $\sim 1350m$  depth. The entire dataset is courtesy of Prof. A. Wüest and his research team at EAWAG, Switzerland.

For the aims of the model, measurements were re-sampled to a resolution 12 h, according to

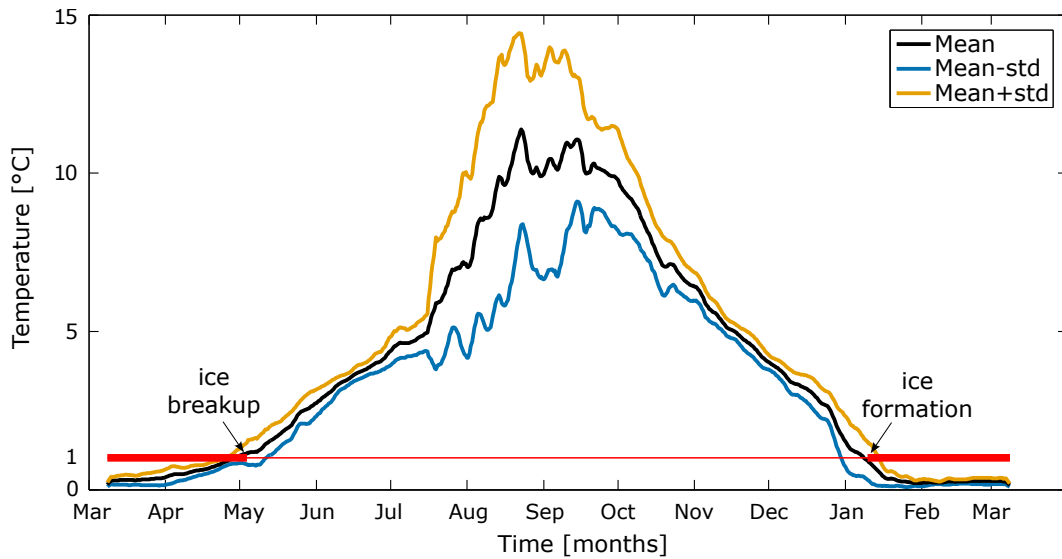


Figure 5.1: Seasonal cycle of the surface water temperature: mean temperature and range of variability ( $\pm$  standard deviation) for the period from 2000 to 2008 (courtesy of A. Wüest). For the sake of clarity, data are filtered with a 7 days moving average. The horizontal line indicates the threshold temperature for ice formation in the model: thick and thin parts respectively represent the duration of the ice covered and ice free periods, as reported by *Peeters et al.* [1997].

the time step used in the model ( $\Delta t = 12 h$ ). Furthermore, measurements from the uppermost instrument have been used to construct a statistical distribution of the seasonal cycle of surface water temperature (see Figure 5.1), which have been used to impose the surface boundary condition in the model.

The use of surface water temperature as boundary condition instead of determining the net heat exchange at the lake-atmosphere interface (see Section 4.2 for further details) has the key advantage that the uncertainties in the estimation of the heat fluxes can be avoided [*Goudsmit et al.*, 2002]. This is particularly true in all those cases where the available data are scarce and hence significant hypotheses and simplifications are introduced in order to solve the heat budget at the surface.

In this case, the upper boundary condition for temperature used in the model is not the temperature of the very surface waters of the lake, but rather the temperature of the uppermost part of the well-mixed surface layer. As a matter of fact, the measurements used to construct the annual cycle of surface water temperature shown in Figure 5.1 refer to a depth of 16.9 m below the surface of the lake. This depth corresponds to a mean value for the 9-year period of measurements, since the position of the uppermost instrument varied from a minimum depth of 9.0 m to a maximum depth of 30 m. It is worth to notice that using this value of temperature instead of the actual surface water temperature (which anyway is not available) has the convenience to inherently account only

for those heat flux components that are not confined to the very surface waters (e.g. long wave radiation emitted by the lake), but rather can penetrate downward, involving a thicker layer (e.g. short-wave solar radiation).

Finally, in order to simulate the dynamics of the ice cover, a temperature threshold is required to link the physical condition at the surface (i.e. formation/melting of the ice cover) to the upper boundary condition. This threshold value is not necessarily equal to  $0^{\circ}\text{C}$ , since, as already discussed, the upper boundary condition is derived from measurements collected at about  $\sim 17\text{ m}$  below the surface. Based upon observations of ice cover formation and break up given by [Peeters *et al.*, 1997], and combining these information with the mean annual cycle of surface water temperature (black curve in Figure 5.1), a threshold temperature of  $1^{\circ}\text{C}$  has been identified.

**Wind action** Long-term series of measurements concerning the wind forcing are not available. However, precious observations are reported in *Rzheplinsky and Sorokina* [1977] about the monthly frequency of speed and duration (not used here) of six different types of wind. The data cover the period ranging from 1959 to 1968 and refer to the whole Lake Baikal, giving important information about the seasonality and the intensity of winds at the lake surface. Measurements have been collected from fixed stations (at the coast and on the islands) and ships, during the ice free season (May - December).

Two distinct seasonal patterns are clearly recognizable [Shimaraev *et al.*, 1994], which allow for the definition of two complete (i.e. comprehensive of all wind types) cumulative frequency distributions of wind speed, one for the warm season (May - September) and the other for the cold season (October - December, see Figure 5.2a).

In the absence of wind data when the lake is ice covered (i.e. January - April), the validity period of each curve has been extended to cover the whole year (warm season curve from mid February to September, and cold season curve from October to mid February). We recall here that wind action is not included in the model during the ice cover period (see Sections 3.3 and 3.4), thus this expedient is only required to ensure that a wind probabilistic curve is always defined when the lake is ice free (accounting for the possible effects of inter-annual climate variability that can slightly hasten or postpone the ice melting and formation, respectively). More importantly, wind information covering the entire year is necessary for the construction of climate change scenarios. Indeed, ice formation and melting dynamics are likely to be significantly modified in the next future.

The cumulative frequency distributions of wind speed have been used to downscale the data provided by the re-analysis datasets and the climate scenarios, which are introduced in the next paragraphs (see Section 5.2 for further details concerning the downscaling procedure).

Finally, Figure 5.2b,c shows the cumulative frequency distribution of wind duration for different

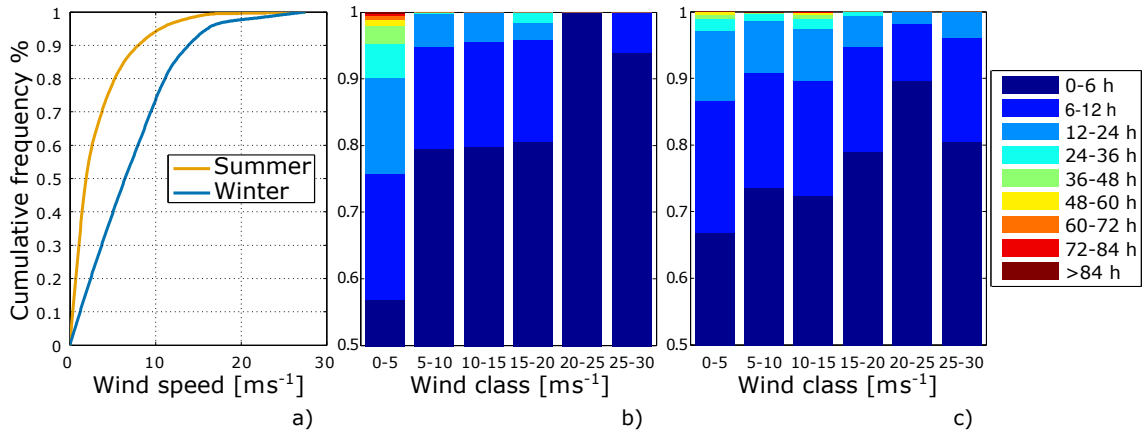


Figure 5.2: Seasonal distributions of wind speed and duration (data from *Rzheplinsky and Sorokina* [1977]): a) cumulative frequency distribution of wind speed for summer (May-September) and winter (October-December), b) summer and c) winter cumulative frequency distributions of wind duration for each wind speed class.

classes of wind speed and for both the warm and cold seasons. This information would be required if wind forcing were reconstructed by means of the stochastic approach discussed in Section 3.3.2, and used in *Piccolroaz and Toffolon* [2011]. However, in this case the reconstruction of wind action has been based upon the complete series of wind events contained in the re-analysis dataset, which provide a value of wind speed with a time resolution of 6 hours (see Section 5.1.2). Therefore, the statistics concerning the observations of wind duration are not used here.

**CFCs profiles** Chlorofluorocarbons (*CFCs*) have been released into the atmosphere since their industrial production, in the early 1930s. *CFCs* concentration significantly increased in the atmosphere until they were progressively banned in the 1990s. Such anthropogenic trace gases dissolved into surface waters and accumulated there. Upper level traces of *CFCs* get redistributed vertically by convection, and then horizontally by interior currents and mixing. Ventilated waters in oceans and deep lakes are therefore characterized by relatively high concentrations of these anthropogenic gases.

Unlike the majority of ocean tracers (e.g. tritium -  $^3H$ , radiocarbon -  $^{14}C$ , helium -  $^3He$ ), *CFCs* are not known to be influenced by biological processes and have high chemical stability. They therefore serve as relatively unambiguous tracers of the present day circulation patterns in oceans and lakes. *CFCs* are presently the best available tracers for decadal to interdecadal model validation [*England, 2001*], and have been extensively used to determine the age of water and analyze deep water ventilation.

Among the others, in past studies *CFC-12* has been successfully used as limnological tracer to

## 5. Available datasets and data processing

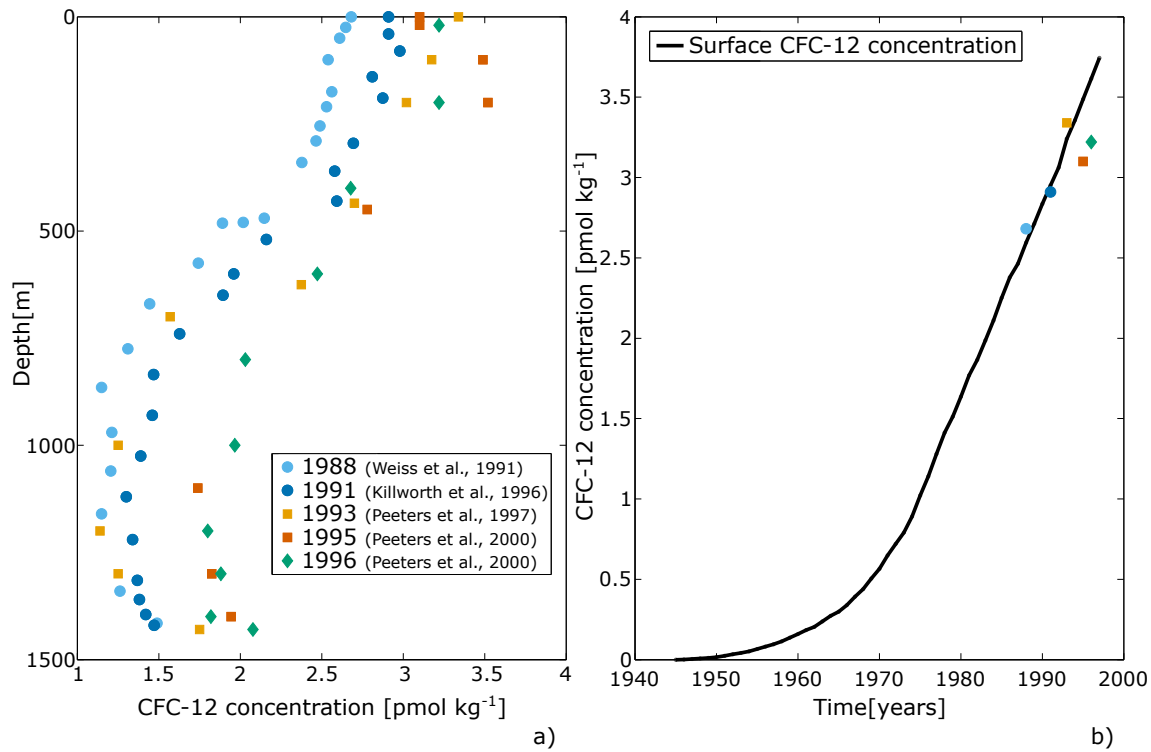


Figure 5.3: a) *CFC-12* vertical profiles measured in 1988, 1991, 1993, 1995 and 1996 (data from *Weiss et al.* [1991]; *Killworth et al.* [1996]; *Peeters et al.* [1997, 2000]); b) *CFC-12* upper boundary condition derived from data by *Peeters et al.* [1997].

investigate deep water renewal of Lake Baikal and estimate ventilation rates [*Weiss et al.*, 1991; *Killworth et al.*, 1996; *Peeters et al.*, 1997, 2000]. In the light of these evidences, *CFC-12* has been chosen, together with temperature, as the main tracer for the calibration of the model.

A few vertical profiles of *CFC-12* concentration have been extracted from the literature [*Weiss et al.*, 1991; *Killworth et al.*, 1996; *Peeters et al.*, 1997, 2000] for the years 1988, 1991, 1993, 1995 and 1996. This has allowed for a fairly good representation of the evolution of *CFC-12* concentration profiles during the 1990s (see Figure 5.3a). The upper boundary condition for *CFC-12* is shown in Figure 5.3b, for the period ranging from 1940 to 1997. This curve has been determined from the mean values of *CFC-12* concentration given by *Peeters et al.* [1997] for the upper 300 m of the lake. Starting from these values, the corresponding concentrations at the surface (i.e. the upper boundary condition) have been estimated by performing multiple runs of the model, until achieving a satisfactory agreement between simulated and reference mean *CFC-12* concentrations within the upper 300 m depth layer. We obtain a reliable trend of *CFC-12* concentrations, which compares well with measurements collected at the surface in 1988, 1991 and 1993 (see Figure 5.3b). We recall here that during the ice cover season the no flux condition has



been imposed at the surface.

**Dissolved oxygen profiles** Analogously to the case of *CFC-12*, vertical profiles of *DO* have been reconstructed on the basis of literature data [Killworth *et al.*, 1996; Peeters *et al.*, 2000] (see Figure 5.4, whereas the upper boundary condition is obtained by imposing saturation at the water surface. Oxygen saturation is determined at each time step depending on the following empirical equation proposed by Weiss [1970]

$$\ln(DO_{sat}) = 0.5513 \frac{P}{T} \left[ A_1 + \frac{A_2 100}{T} + A_3 \ln \left( \frac{T}{100} \right) + A_4 \frac{T}{100} \right], \quad (5.1)$$

where  $DO_{sat}$  is the oxygen saturation concentration in [mg l],  $T$  is surface water temperature in Kelvin,  $P$  is the atmospheric pressure in [mmHg] and  $A_1$ - $A_4$  are empirical coefficients ( $A_1 = -173.4292$ ,  $A_2 = 249.6339$ ,  $A_3 = 143.3483$  and  $A_4 = -21.8492$ ). As for *CFC-12*, during the ice cover period, the no flux condition has been assumed at the surface.

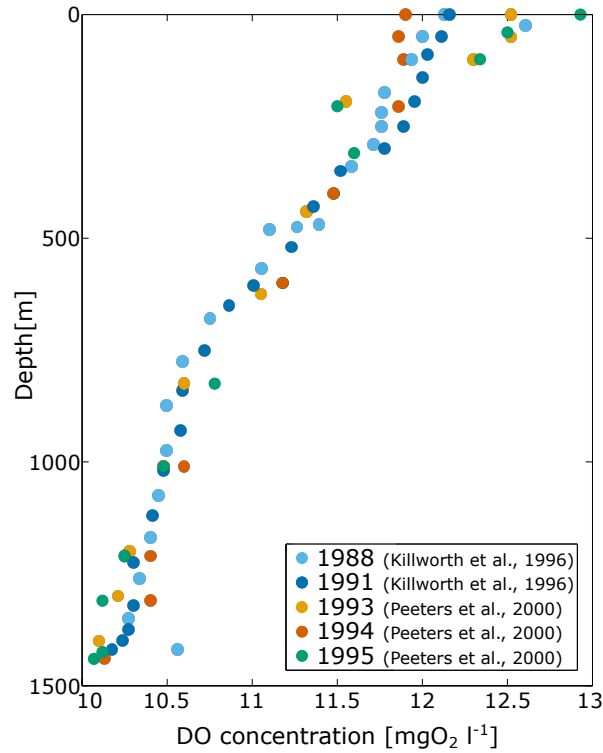


Figure 5.4: Vertical profiles of dissolved oxygen concentration available from the literature (data from Killworth *et al.* [1996] and Peeters *et al.* [2000]).

As already mentioned in the previous paragraph, the calibration of the model has been based mainly on *CFC-12* profiles (besides  $T$ ) because of its non reactive dynamics. On the contrary, the

uncertainties in the *DO* depletion rates do not allow for a robust estimate of the model parameters. As a matter of fact, these rates are not likely constant along the water column, and need themselves to be calibrated. The oxygen depletion rate curve obtained through the model calibration is shown in Figure 3.5.

### 5.1.2 Re-analysis dataset

Re-analysis is the combination of information from past meteorological observations with modern forecast models, using data assimilation techniques originally developed for numerical weather prediction. The output is an integrated dataset describing the evolution of the climate system over recent decades.

The horizontal resolution of re-analysis data is that of the atmospheric model used to generate the dataset: a macro-regional scale (100 to 200 km), which is generally too coarse to explicitly account for the presence of lakes on the continental land surface, and hence quantify their effects on the climate system [MacKay *et al.*, 2009]. As a consequence, in most global and even regional climate models lakes are often not explicitly resolved but parameterized. In order to overcome these limitations, in the last years several attempts were made to explicitly include lakes in climate modeling studies [e.g. Pitman, 1991; Ljungemyr *et al.*, 1996; Goyette *et al.*, 2000; MacKay, 2012; Samuelsson *et al.*, 2010], although still significant uncertainties exist in the estimation of surface water temperature. Finally, in many cases, information about surface water temperature are not available, as is the case of the re-analysis dataset described below.

In this study, the well-known ECMWF ERA-40 dataset has been used, which has been obtained from the ECMWF Data Server (link: <http://data-portal.ecmwf.int/>). Wind speed,  $W$ , and air temperature,  $T_a$ , data are available for the period 1958-2002 with a temporal resolution of 6 hours. The horizontal resolution is  $1.125^\circ \times 1.125^\circ$  (roughly  $125\text{ km} \times 125\text{ km}$ ), and the model cell (barycenter:  $53.375^\circ\text{N}$ ,  $108.125^\circ\text{E}$ ) is not specific for the lake itself but rather covers a wider region. In spite of the coarse grid and the differences between measurements at the meteorological stations and re-analysis data, Kouraev *et al.* [2007a] suggest that the ECMWF ERA-40 dataset is suitable to assess seasonal or interannual changes in air temperature of Lake Baikal.

ECMWF ERA-40 data for both  $W$  and  $T_a$  have been used to accomplish two main tasks: 1) calibrate the numerical model and 2) specify the future climate scenarios. In the first case, re-analysis data were necessary as they provide information about the actual historical series of climatic events occurred during the second half of the last century, which coincides with the calibration period. Whereas in the second case, re-analysis data were used to define appropriate boundary conditions for different climate projections, taking advantage of their characteristic of representing realistic chronological series of meteorological events (see Section 5.1.3).

In both cases, due to their coarse spatial resolution, re-analysis data require to be downscaled,

moving from the ECMWF ERA-40 resolution to a more suitable lake scale. Furthermore, re-analysis data of air temperature are also required to be converted into surface water temperature, which is needed in the model as surface boundary condition. Different streamlined statistical downscaling procedures have been devised, each one being appropriate for a specific type of data that is analyzed: historical conditions, future scenarios, air temperature or wind speed. All procedures only rescales the value of climate variables, while the temporal series of events is kept unchanged. These procedures, as well as the conversion of the temperature of air, are discussed in detail in Sections 5.2.1 and 5.2.2.

### 5.1.3 Future climate projections

Future projections about climate change scenarios are based on the outputs from Global Climate Models (GCMs) forced with different levels of GHG concentrations. These datasets have the same limitations with respect to the spatial resolution as those typical of re-analysis data. In this work, the scenarios have been constructed on the basis of the outputs of the CNRM-CM5 model [Voldoire *et al.*, 2012], a GCM developed jointly by CNRM and Cerfacs that provides wind speed and air temperature for historical conditions and future scenarios with a temporal resolution of 3 hours. The data refer to a region of about  $125\text{ km} \times 125\text{ km}$  area, centered in  $53.929^\circ\text{N}$ ,  $108.281^\circ\text{E}$  (thus roughly corresponding to that of the ECMWF ERA-40 dataset). Historical climate conditions have been obtained forcing the model with emissions observed in the period 1960-2005. After the historical period, three different climate change scenarios have been assumed, which refer to different GHG concentration scenarios, the so-called Representative Concentration Pathways (RCPs). Depending on the different projected concentrations of GHG in the atmosphere, the scenarios are indicated as RCP2.6, RCP4.5 and RCP8.5, the number being an indicator of the radiative forcing, thus of GHG concentration (detailed information about the different RCPs can be found in IPCC [2008]). CNRM-CM5 provides results for two future periods: from 2026 to 2045 and from 2081 to 2101.

It is important to note that the CNRM-CM5 historical dataset is inherently different from the re-analysis dataset, the first being obtained running GCMs forced with observed GHG concentrations, while the second being the result of the combination of climate observations and weather forecast modeling. Relevant differences can be seen in Figure 5.5, where the annual cycles of air temperature and wind speed are compared between the two datasets (data have been averaged over the overlapping period, 1960 – 2002). Strong biases are evident for both air temperature and wind speed, in the first case mainly in the ascending branch, while in the second case during the whole year. Moreover, it is important to stress that GCM outputs do not include any reliable information about the chronological series of meteorological events, which, together with the coarse spatial resolution, represents the major limitation of this source of information.

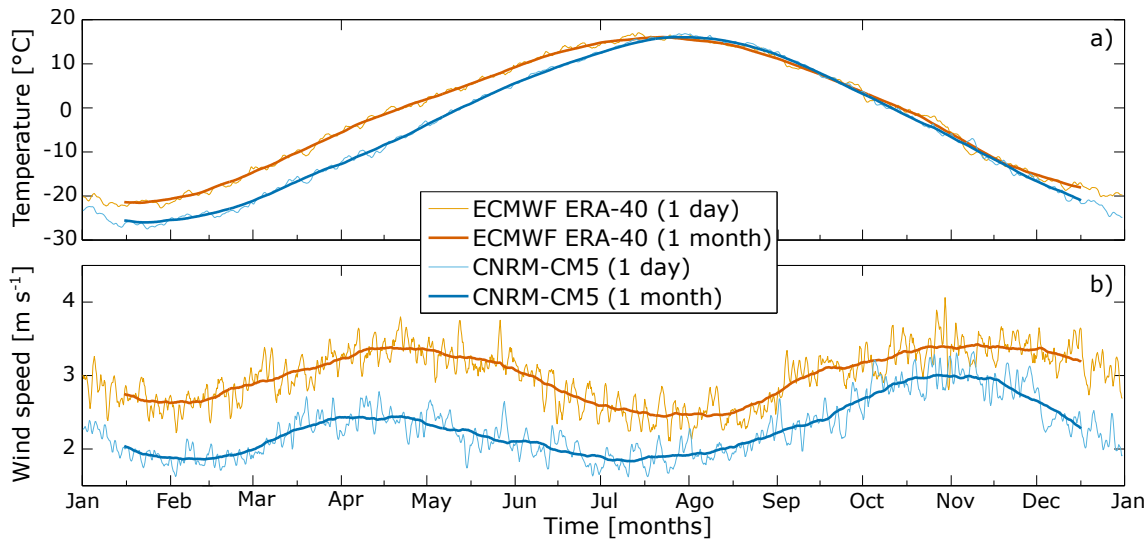


Figure 5.5: Comparison between the ECMWF ERA-40 re-analysis and the historical CNRM-CM5 datasets: a) air temperature and b) wind speed averaged over the period 1960-2002. Data have been smoothed using 1 day (thin lines) and 1 month (thick lines) moving average.

## 5.2 Data processing

Nowadays, climate analysis and modeling is a main issue, both for the analysis of past decades (re-analysis datasets) and the prediction of future climate scenarios. Re-analysis datasets and climate projections are normally obtained through the application of global scale numerical models, whose coarse horizontal resolution represents the main obstacle to their straightforward implementation for impact studies on local environmental systems. As a matter of fact, the mismatch existing between the actual capacity of numerical models (both weather forecast models and GCMs) and the scale resolution desired for many studies of local impact is a couple of orders of magnitude ( $10^2 km$  vs.  $10^0 \div 10^1 km$ ). Furthermore, the numerical results are inevitably affected by systematic biases due to the inadequate knowledge of key physical processes (e.g., cloud physics) and the simplification of the natural heterogeneity of the climate system that exists at finer spatial scales [Li *et al.*, 2010].

For these reasons, the processing of outputs is generally required in order to correct possible biases and achieve a finer spatial resolution. This can be obtained by two main approaches [Mearns *et al.*, 1999]: 1) physical process-based dynamical downscaling, and 2) statistical downscaling. The first technique involves nesting of high resolution Regional Climate Models (RCMs) within weather forecast models or GCMs (which provide the boundary conditions) over the region of interest. This approach allows for high spatial and flexible temporal resolution outputs, but it is

extremely computationally demanding and requires detailed surface climate data. On the other hand, statistical downscaling directly transforms coarse-resolution datasets to a finer scale through the use of statistical relationships between the two spatial scales. The key advantage of the latter family of methods is the extremely low computational cost and easy implementation. Moreover, statistical downscaling normally involves the contemporary removal of biases from re-analysis datasets and GCMs outputs, while dynamical downscaling may still include modeling inconsistencies. In the light of these evidences, statistical downscaling has been chosen to process both ECMWF ERA-40 and CNRM-CM5 datasets.

Concerning the downscaling of re-analysis data, the expeditious and well-known quantile-mapping approach [*Panofsky and Brier, 1968*] has been adopted (see Section 5.2.1), both for wind speed and temperature. For the particular case of temperature, the procedure involves the contemporary downscaling and transformation of air temperature (provided by the re-analysis dataset) into surface water temperature (which is requested by the model as surface boundary condition). Indeed, statistical downscaling tools can be applied also if the predictor variable does not coincide with the downscaled parameter, but the two have an understandable physical relation [*Hewitson and Crane, 2006*], as is the case of surface water temperature and air temperature [e.g. *Adrian et al., 2009*].

On the other hand, the downscaling of future climate scenarios requires the development of a more sophisticated procedure. *Chen et al. [2011]* applied numerous methods to quantify the local impact of climate change on the main hydrological variables, finding a certain degree of uncertainty added by the method that is adopted. In general, the choice of a downscaling method is critical and specific for any singular application, and not all of them are indicated to be applied in climate change studies. Indeed, many of the existing statistical methods do not account for changes in the probabilistic distributions of future scenarios. Only recently, and thanks to the increasing interest in climate change, more complex statistical approaches have been developed [e.g. *Li et al., 2010*]. Inspired by these works, and based on the quantile-mapping approach, an original downscaling procedure for the wind speed has been devised, aimed at being applied to climate change conditions (see Section 5.2.2). As regards temperature, the contemporaneous downscaling and conversion of future air temperatures into surface water temperatures has been required, in close analogy to the downscaling of re-analysis data. This conversion has been carried out by coupling the standard quantile-mapping approach with the physically-based empirical model presented in Chapter 4 [see also *Piccolroaz et al., 2013a*]. In particular, the model has been used to assess the change of water temperature due to climate change (see details in Section 5.2.2).

### 5.2.1 Present conditions

The transfer function method is a simple and effective statistical downscaling technique that establishes a relationship between the cumulative distribution functions (CDFs) of observed local climate variables (predictands) and the CDFs of large-scale model outputs (predictors)

$$CDF_{obs} = TF \cdot CDF_{mod}, \quad (5.2)$$

where the subscript *obs* is for observations, *mod* stands for model (in this case refers to both re-analysis and future scenarios datasets), and *TF* is the transfer function. The easiest way is to assume a transfer function equal to 1, obtaining the so-called quantile-mapping approach. In this way, the distribution of the model entirely matches that of the observations, and all the moments of the model distribution are adjusted, while maintaining the rank correlation between model and observations [Li *et al.*, 2010]. This method implicitly assumes that climate patterns do not significantly change over time, thus it is not recommended to be applied over long-term series, which are likely affected by climate modifications. For this reason, the quantile-mapping approach has not been used to downscale future scenarios. On the other hand, it has been applied to current climatic conditions (i.e. re-analysis data), despite the ECMWF ERA-40 dataset covers a relatively long time period (45 years). This choice, that may seem controversial, has been necessary since the available measurements do not provide any information about past climate trends, thus implementing a more sophisticated downscaling procedure (as the one described in Section refs5:fut) would have not been possible. In fact, the only information about wind at the lake scale is provided by the overall probabilistic distribution of wind speed during a long-term observational period during the last century [Rzheplinsky and Sorokina, 1977] (1959-1968), without any information about the inter-annual variations (such information would be available for the following period, 1968-2007, but only for the mean annual values [Shimaraev and Starygin, 2010]). Similarly, the surface water temperature dataset consists in a 9-year series (2000-2008), too short to perform any trend analysis. Therefore, climate evolution could not be included in the downscaling procedure for hindcasting. In conclusion, observations have been necessarily assumed to be representative of the re-analysis period, and climate conditions have been considered stationary during this time window. Under these hypotheses, the quantile-mapping approach has been used to downscale wind speed,  $W_{re}$ , and convert air temperature  $T_{a,re}$  (the subscript *re* staying for re-analysis) into surface water temperature.

The predictors are represented by re-analysis data ( $W_{re}$  and  $T_{a,re}$ ) while the predictands are, respectively, the observed wind speed  $W_{obs}$  given by Rzheplinsky and Sorokina [1977] and the measured surface water temperature  $T_{w,obs}$  (EAWAG dataset). For wind speed and temperature,

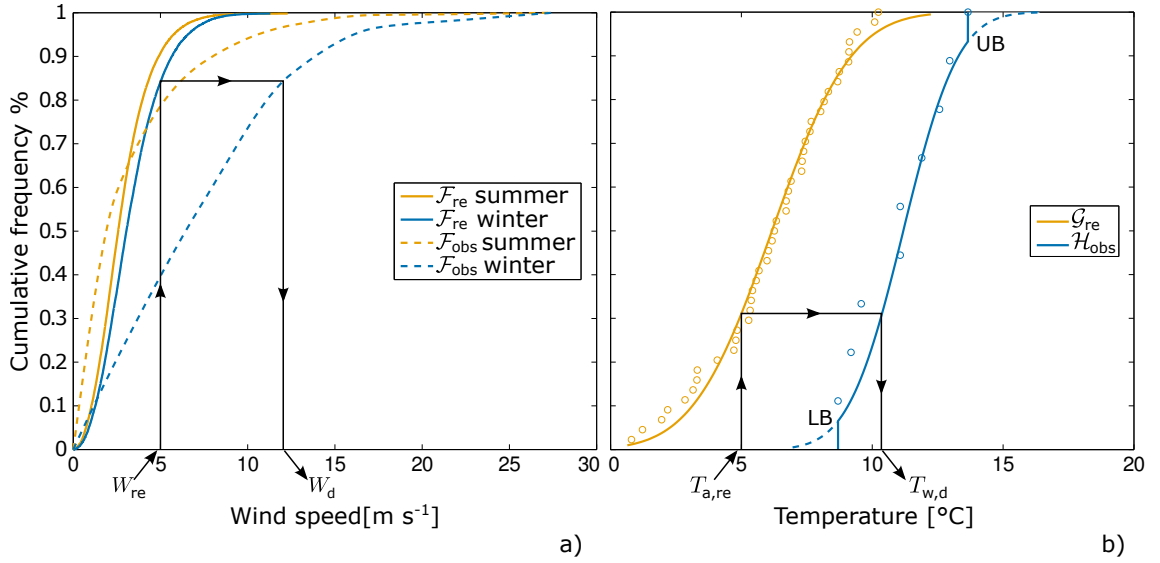


Figure 5.6: Graphical illustration of quantile-mapping downscaling for a) wind speed, and b) temperature (15 of September, daytime).  $W_{re}$  and  $T_{a,re}$  are the re-analysis data in input, while  $W_d$  and  $T_{w,d}$  represent the downscaled variables. For the specific case of  $T$ ,  $T_{a,re}$  refers to air, while  $T_{w,d}$  to surface water, which has been allowed to vary from the minimum (LB = lower bound) to the maximum (UB = upper bound) observed values.

Equation (5.2) can be rewritten as:

$$W_d = (\mathcal{F}_{obs})^{-1}(\mathcal{F}_{re}(W_{re})), \quad (5.3)$$

$$T_{w,d} = (\mathcal{H}_{obs})^{-1}(\mathcal{G}_{re}(T_{a,re})), \quad (5.4)$$

where the subscript *re* again indicates re-analysis (i.e., global scale), the subscript *obs* stays for observations (local scale) and *d* indicates the downscaled variable. For the sake of compactness, the CDFs of wind speed  $W$ , air temperature  $T_a$  and surface water temperature  $T_w$  are denoted as  $\mathcal{F}$ ,  $\mathcal{G}$  and  $\mathcal{H}$ , respectively. The superscript  $-1$  indicates the inverse function of each CDF, which is defined in the range  $[0,1]$ . Figure 5.6 schematically illustrates the downscaling procedure.

The two CDFs in Equations (5.3) and (5.4) have been constructed assuming different time scales for  $W$  and  $T$ , depending on the specific properties of the two meteorological variables. Since wind speed shows distinct seasonal distribution patterns [Rzheplinsky and Sorokina, 1977; Shimaraev et al., 1994], two different CDFs have been used, one for the warm season (mid February-September) and the other for the cold season (October - mid February), coherently with the CDFs of observations shown in Figure 5.2. On the other hand, half-daily CDFs have been considered for the downscaling/conversion of temperature, which correspond to the time step used for the

computation. Owing to the fact that the measurements of air and, to a larger extent, of surface water temperature are not sufficient to reconstruct detailed half-daily CDFs, the data have been assumed to be normally distributed, which appears to be a fairly good approximation (see Figure 5.6). Furthermore, in order to retain only reliable values of surface water temperature,  $T_{w,d}$  has been bounded according to the minimum and maximum observed values,  $T_{w,obs}$  (see Figure .

It is worth noting that other approaches might be proposed to tackle the problem of reconstructing  $T_w$ . One of them is to calculate the water temperature directly from the heat exchange through the lake-atmosphere interface, relying on the knowledge of all heat flux components (e.g., solar radiation, long wave radiation, sensible heat, latent heat). Unfortunately, as already discussed in Chapter 4, a lot of data would be required to implement such a complex method, whereas we can only rely on few measurements, not enough to estimate all these components with sufficient accuracy. For this reason, the approach described above appeared to be the most appropriate, as it allows for a suitable assessment of  $T_w$  at a sub-daily time scale (12 hours), ensuring the description of the seasonal hysteresis cycle between air and surface water temperature. The downscaling/conversion procedure is performed by accounting for the main statistical properties of the observations, which makes the whole procedure robust and physically consistent.

### 5.2.2 Future scenarios

As already mentioned, the standard quantile-mapping approach is not indicated for climate change studies, as it is stationary in the variance and skewness of the distribution, and only the mean changes [Li *et al.*, 2010]. In order to account for modifications in higher moments, it is necessary to include some information from the variation of the probabilistic distribution of the future scenarios datasets. This operation is not straightforward because future CNRM-CM5 data cannot be considered as a continuation of the re-analysis series (see Figure 5.5) due to their different derivation: the two datasets cannot be directly compared. This difficulty has been overcome by first assessing projected climate trends by analyzing CNRM-CM5 data, and only successively applying future modifications to present conditions, which are represented by re-analysis data.

Since detailed CNRM-CM5 data are not available in continuous but only for limited periods, a stepwise climate trend analysis has been carried out. For each period  $p$  ( $p = 0$  from 1960 to 2005,  $p = 1$  from 2026 to 2046 and  $p = 2$  from 2081 to 2101) and scenario  $s$  (viz., historical, RCP2.6, RCP4.5 and RCP8.5), mean annual cycles of  $W$  and  $T_a$  ( $\overline{W}_p^s$  and  $\overline{T}_{a,p}^s$ , respectively) have been defined by averaging the corresponding climate variables over the entire duration of  $p$ . For each of these mean annual cycles, the corresponding CDFs have been calculated:  $\mathcal{F}_p^s$  and  $\mathcal{G}_p^s$  for wind and air temperature, respectively. Future climate changes have been successively estimated by comparing projected climate conditions to those characterizing the historical period. Successively,



these stepwise climate modifications have been linearly interpolated to annual resolution

$$X_{int}^s = X_{p-1}^s + (X_p^s - X_{p-1}^s) \frac{y - y_{p-1}}{y_p - y_{p-1}}, \quad (5.5)$$

where  $X$  is the generic function to be interpolated, the subscript *int* denotes the interpolated value in year  $y$ ,  $y_p$  represents the middle year of each period ( $y_0 = 1982$ ,  $y_1 = 2036$  and  $y_2 = 2091$ ),  $y_{p-1}$  and  $y_p$  are the middle years of the periods before and after year  $y$ . The procedures devised to determine the future scenarios of  $W$  and  $T_w$  are presented in detail in the next sections.

**Wind speed** As far as  $W$  is concerned, a novel downscaling procedure has been developed, which is basically an extension of the quantile-mapping method, in which also information about the future distribution of  $W$  is included. Analogously to the procedure described in Section 5.2.1, the downscaling has been based on two seasonal CDFs of wind speed, one for the warm period (mid February-September) and the other for the cold season (October-mid February). For the sake of simplicity, the procedure is presented here only for one case.

In order to construct future scenarios of  $W$ , the following preliminary operations are required.

1. For all the scenarios and periods covered by CNRM-CM5 data, the corresponding cumulative distribution functions,  $\mathcal{F}_p^s$ , are defined (see Figure 5.7a).
2. The impact of climate change on  $W$  is estimated through the definition of a “change function”  $r_p^s$ , which is calculated as the ratio between the projected and historical wind speed values corresponding to the same quantile, thus having the same probability to occur (Figure 5.7b)

$$r_p^s = \frac{W_p^s}{W_0} = \frac{(\mathcal{F}_p^s)^{-1}}{(\mathcal{F}_0)^{-1}}. \quad (5.6)$$

In order to simplify the notation, all variables or functions referring to the historical period are denoted only by the subscript 0.

3. Each mean annual cycle of wind speed,  $\overline{W}_p^s$ , is converted into the corresponding mean annual distribution of quantile values,  $Q_p^s$ , which describes the seasonality of wind forcing (Figure 5.7c)

$$Q_p^s = \mathcal{F}_p^s(\overline{W}_p^s). \quad (5.7)$$

The quantities  $r_p^s$  and  $Q_p^s$  are provided as inputs to the model, together with the CDFs of observed local wind speed,  $\mathcal{F}_{obs}$  (dashed lines in Figure 5.6). For each year  $y$  during the simulation period,  $r_p^s$  and  $Q_p^s$  are interpolated using Equation (5.5), obtaining  $r_{int}^s$  and  $Q_{int}^s$ , which represent the

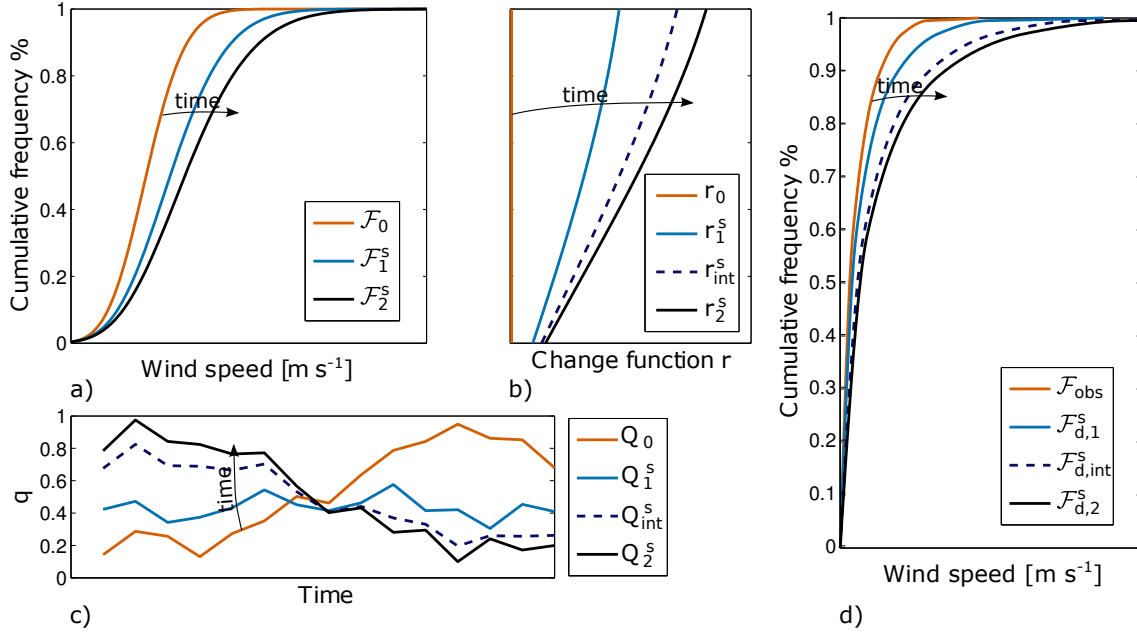


Figure 5.7: Curves used for the downscaling of wind speed, under the generic climate change scenario  $s$ . a) cumulative distribution functions of wind speed; b) “change function”  $r$ ; c) mean annual distribution of quantile values  $Q$ ; d) modified cumulative distribution functions of observed wind speed. For an easier interpretation of this figure and of the following ones, refer also to Table 5.4.

climate conditions to an annual resolution.  $r_{int}^s$  is then used to adjust  $\mathcal{F}_{obs}$ , aiming at updating the range of wind speed observations from historical to future climate conditions (Figure 5.7d):

$$(\mathcal{F}_{d,int}^s)^{-1} = r_{int}^s (\mathcal{F}_{obs})^{-1}, \quad (5.8)$$

where the subscript  $d$  (downscaled) denotes that the CDF on the right hand side refers to the lake scale.

Once the climate conditions of the generic simulation year  $y$  are defined (dark blue, dashed lines in Figure 5.7), all the information required for setting up the downscaling procedure is available. Only the series of wind speed values to be downscaled is not known yet. An obvious choice would be to use CNRM-CM5 wind speed data. However, this dataset does not cover the entire future period and, as already discussed, does not provide series of meteorological events with a reliable temporal sequence. Moreover, Figure 5.5b shows significant discrepancies with re-analysis data. In order to overcome this deficiencies, re-analysis data have been used, which ensure the provision of a more reliable information about the actual sequence of natural events. For the generic  $n$ -year long simulation, the series of wind events in input is generated by sampling (with replacement)  $n$  times

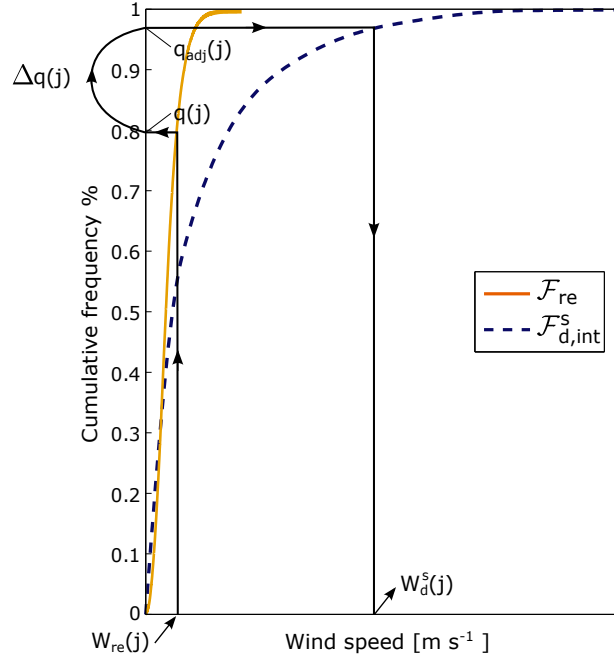


Figure 5.8: Graphical illustration of the procedure used for the downscaling of wind speed, under the generic scenario  $s$ .

an entire year from the ECMWF ERA-40 dataset. Successively, at every  $j$ th simulation time step ( $\Delta t = 12 h$ ) the corresponding wind speed value,  $W_{re}(j)$ , is downscaled by applying the following procedure (Figure 5.8).

1. The quantile value,  $q(j)$ , associated to  $W_{re}(j)$  is calculated from the CDF of re-analysis data,  $\mathcal{F}_{re}$ , as

$$q(j) = \mathcal{F}_{re}(W_{re}(j)) . \quad (5.9)$$

2. In order to account for the potential shift/change of the seasonal distribution of the events,  $q(j)$  is adjusted by

$$q_{adj}(j) = q(j) + \Delta q(j) , \quad (5.10)$$

where  $\Delta q(j) = \mathcal{Q}_{int}^s(j) - \mathcal{Q}_0(j)$  is the correction of the quantile between future and historical conditions. Is worth noting that the adjustment given by Equation (5.10) only determines the redistribution of wind events throughout the year, without modifying the associated CDF. As a matter of fact, the integral of  $\Delta q$  over the year is equal to zero.

3. Finally, the downscaled future wind speed,  $W_d^s(j)$ , is determined as that value

$$W_d^s(j) = (\mathcal{F}_{d,int}^s)^{-1}(q_{adj}(j)) \quad (5.11)$$

corresponding to a probability of  $q_{adj}(j)$  in the updated CDF of observations,  $\mathcal{F}_{d,int}^s$ , which has been defined in Equation (5.8).

For the sake of clarity in the graphical representation, the curves shown in Figures 5.7 and 5.8 are idealized and do not refer to the actual curves used in this work.

**Surface water temperature** In Section 5.2.1 the quantile-mapping approach has been applied to contemporaneously downscale and convert air temperature,  $T_a$ , into surface water temperature,  $T_w$ . This procedure aims at post-processing re-analysis outputs in order to be used as inputs (i.e., boundary conditions) for the downwelling model. In the case of future scenarios, no information about projected surface water temperature is available, thus the method used for current conditions is not applicable. Hence, a more elaborated procedure has been devised, which combines the simplified method to convert  $T_a$  into  $T_w$  described in Chapter 4 with two classical statistical downscaling methods: the quantile-mapping and the delta methods.

The first step is to assess the future climate impact on air temperature. This operation has been performed by using the change factor methodology, a simple and widely used statistical downscaling approach [e.g. *Minville et al.*, 2008; *Diaz-Nieto and Wilby*, 2005; *Hay et al.*, 2000]. In the simplest case (delta method), such an approach essentially modifies the observed historical time series by adding the difference between the future and actual climate patterns as simulated by GCMs. The main drawback of this method is that the variance of the climatic variables remains unchanged, while only the mean value changes from present to future conditions. In this case, the delta method has been applied to correct re-analysis air temperature data, including the information given by CNRM-CM5 data. Future modifications of air temperature,  $\Delta T_{a,p}^s$ , have been estimated as the difference between future and current mean annual cycles,  $\overline{T}_{a,p}^s$  and  $\overline{T}_{a,0}$  respectively (for the meaning of the subscripts, see the previous paragraph: “Wind speed”):

$$\Delta T_{a,p}^s = \overline{T}_{a,p}^s - \overline{T}_{a,0}. \quad (5.12)$$

Then, the re-analysis mean annual cycle of air temperature,  $\overline{T}_{a,re}$ , has been projected to future conditions,  $\overline{T}_{a,p}^{*s}$ , adding the correction  $\Delta T_{a,p}^s$  (see Figure 5.9):

$$\overline{T}_{a,p}^{*s} = \overline{T}_{a,re} + \Delta T_{a,p}^s; \quad (5.13)$$

At this point, the same physically-based approach discussed in Chapter 4 has been used to convert  $\overline{T}_{a,p}^{*s}$  into reliable values of the associated surface water temperature. For the sake of precision, this operation has been performed by adopting a previous version of the temperature conversion model, since the final version (that is, the one described in Chapter 4) has been developed successively, and has been terminated at the same time this thesis was written. However, the two

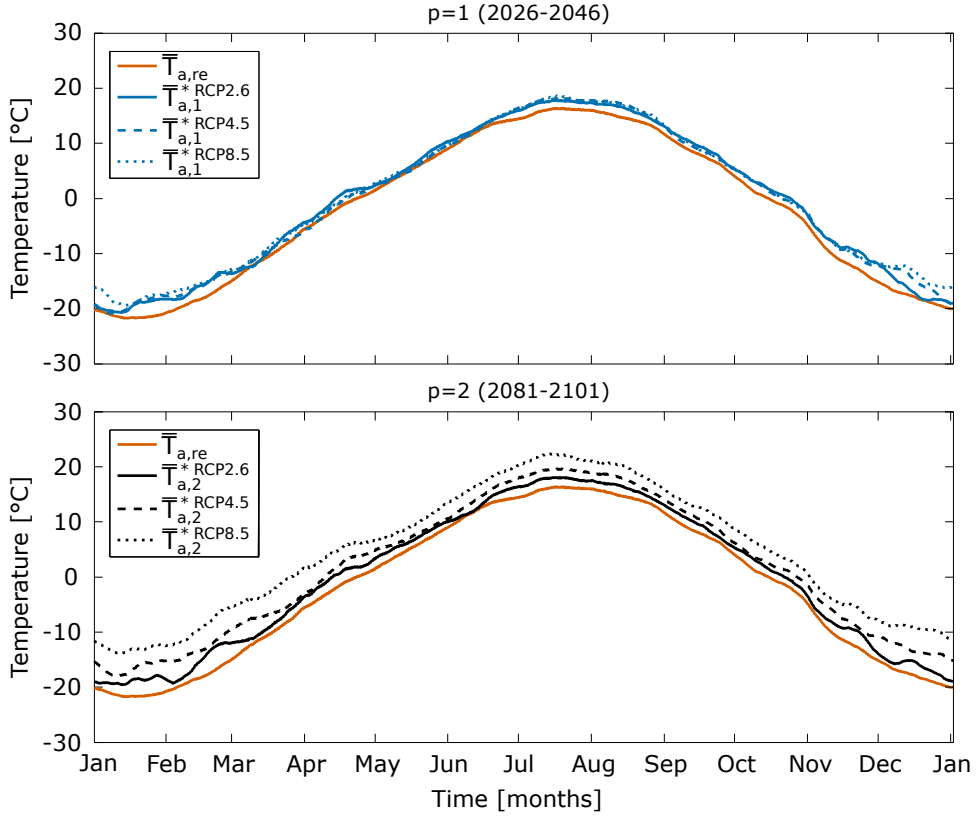


Figure 5.9: Re-analysis mean annual cycles of air temperature projected to future conditions,  $\overline{T_{a,p}^{*s}}$ . Results for both future periods ( $p = 1$  above and  $p = 2$  below) and all different scenarios (denoted by the different curves) are shown. For the sake of clarity, data are filtered with a 1 month moving average.

versions of the model present the same general structure, which is summarized by Equation (4.12), and hence are conceptually analogous.

The calibration of the temperature conversion model has been carried out using air temperature data provided by the re-analysis dataset in input, and the measurements of surface water temperature as reference series of data. In particular, since the historical periods of the two datasets do not coincide (re-analysis data are available for the period 1958-2002, whereas surface water measurements have been collected from 2000 to 2008), thus a direct correspondence of the two chronological series of data does not exist, the calibration has been performed according to the mean annual cycles of temperature ( $\overline{T_{a,re}}$  and  $\overline{T_{w,obs}}$  for air and water temperature, respectively). This calibration procedure has been previously tested for the case of Lake Superior for which concomitant long-term data series of  $T_a$  and  $T_w$  are available for validation (see Section 4.7), and has been shown to provide remarkable results both as far as the seasonal trend and the inter-annual

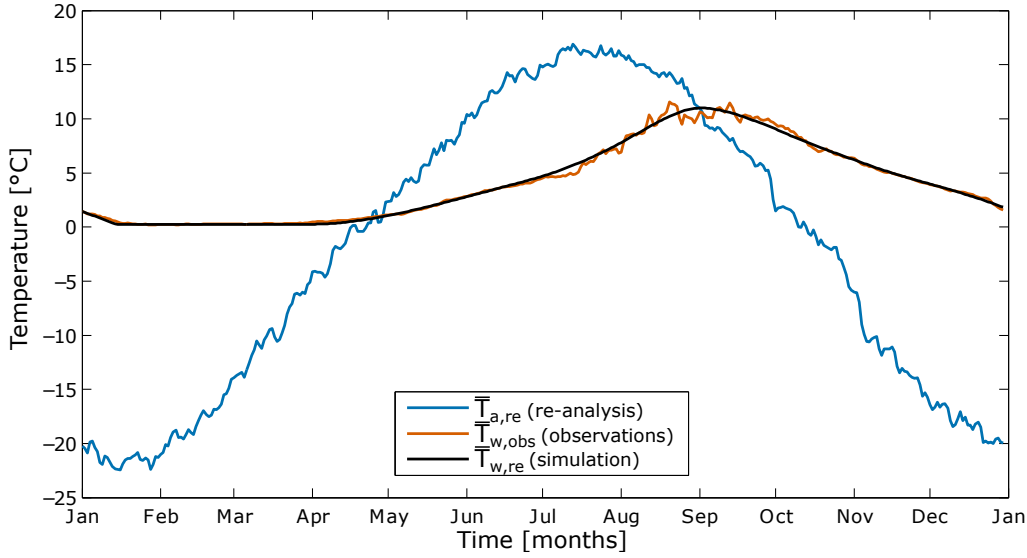


Figure 5.10: Mean annual cycles of air  $\overline{T}_{a,re}$  (re-analysis data) and surface water  $\overline{T}_{w,obs}$  (measurements, courtesy of A. Wüest) temperature used to calibrate the temperature conversion model. The estimated surface water temperature cycle,  $\overline{T}_{w,re}$ , is shown as well.

fluctuations of  $T_w$  are concerned. The mean annual cycles of temperature used for the calibration are shown in Figure 5.10, which also illustrates the cycle of surface water temperature estimated by the model,  $\overline{T}_{w,re}$  (the subscript *re* indicating that  $\overline{T}_{a,re}$  has been used as input forcing). A close agreement between measurements and simulation can be observed, which is confirmed by Figure 5.11 where the corresponding hysteresis cycles between air and surface water temperature are compared.

Once the model has been calibrated, the future projections of surface water temperature,  $\overline{T}_{w,p}^s$ , have been constructed using  $\overline{T}_{a,p}^{*s}$  in input (Figure 5.12).  $\overline{T}_{w,p}^s$  have been successively interpolated to annual resolution using Equation (5.5), thus obtaining the corresponding mean annual cycle of surface water temperature  $\overline{T}_{w,int}^s$ . The interpolated change of surface water temperature has been then estimated as  $\Delta T_{w,int}^s = \overline{T}_{w,int}^s - \overline{T}_{w,re}$ .

Finally, for the generic  $n$ -year long numerical simulation, the series of air temperatures used in input is that corresponding to the sequence of wind speed, which has been generated by sampling with replacement from the ECMWF ERA-40 dataset (see the previous paragraph: “Wind speed”). At every  $j$ th simulation time step, the air temperature value  $T_{a,re}(j)$ , is downscaled and converted into the associated value of surface water temperature,  $T_{w,d}^s(j)$ , applying the quantile-mapping approach (same procedure shown in Figure 5.6b) and adding the expected correction  $\Delta T_{w,int}^s$

$$T_{w,d}^s(j) = (\mathcal{H}_{obs})^{-1} (\mathcal{G}_{re}(T_{a,re}(j))) + \Delta T_{w,int}^s. \quad (5.14)$$

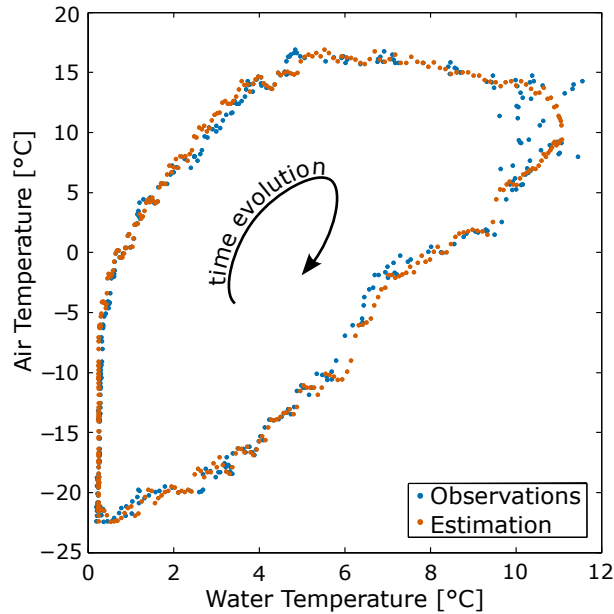


Figure 5.11: Comparison of the hysteresis cycles between air and surface water temperatures, as derived by the data and by the temperature conversion model. Hysteresis cycles refer to the mean annual, calculated using re-analysis data (1958-2002) and measurements (2000-2008, courtesy of A. Wüest) for  $T_a$  and  $T_w$ , respectively (see Figure 5.10).

For each season of the year, Table 5.2 summarizes the expected increase of water temperature for the different periods and scenarios analyzed, according to the estimations of the mean annual cycles of surface water temperature illustrated in Figure 5.12. Furthermore, for each period and scenario, Table 5.2 lists the duration of ice cover, the dates of ice formation and break-up and the mean annual surface water temperature. Ice cover properties have been calculated according to the threshold temperature for ice formation introduced in Section 5.1.1, which we recall is equal to  $1^{\circ}\text{C}$ .

In the first period  $p = 1$  (2026-2046), all scenarios are characterized by a modest increase in temperature, which primarily occurs in autumn and winter, during the descending branch of the annual cycle of temperature, after the maximum temperature is reached and before the formation of ice (see also Figure 5.12). The duration of ice cover is expected to reduce by about 20%, primarily due to a delay in the timing of freeze-up.

On the other hand, in the second period  $p = 2$  (2081-2101) the three climate scenarios show considerably distinct behaviors. Except for the RCP2.6, which does not differ significantly from the previous period ( $p = 1$ ), water temperature is expected to undergo a marked warming for both the RCP4.5 and, to a larger extent, the RCP8.5 scenarios. In the case of RCP4.5, the only season that experiences a mild increase in temperature is spring ( $+0.4^{\circ}\text{C}$ ), while during the rest of the year

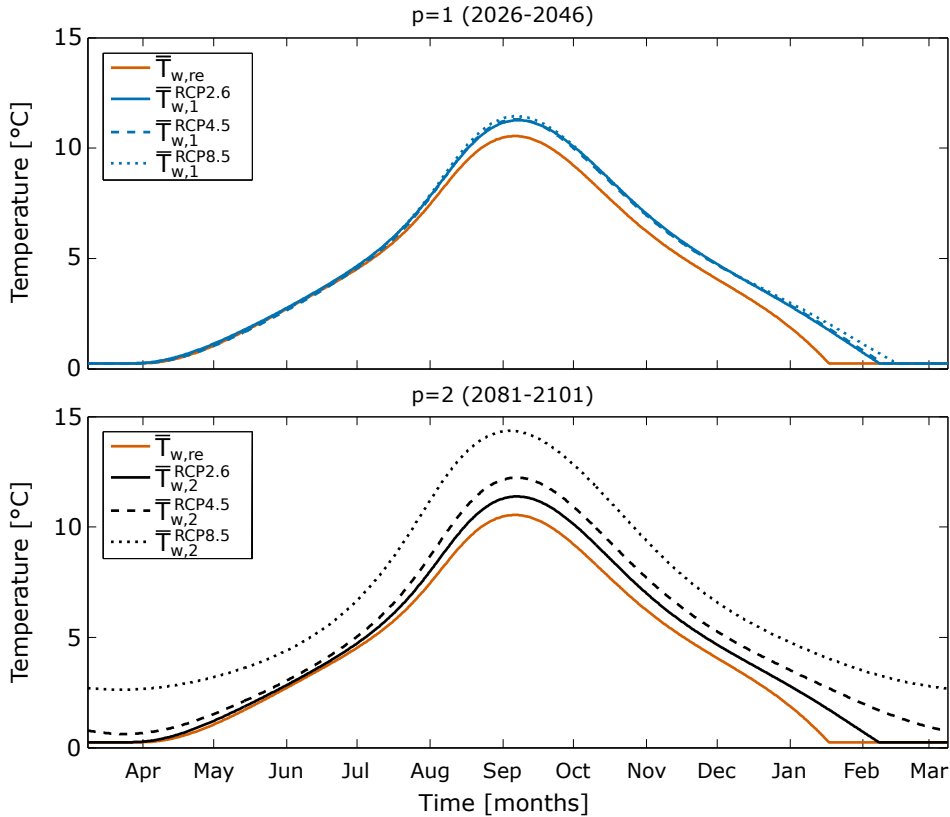


Figure 5.12: Future projections of surface water temperature,  $\overline{T}_{w,p}^s$ , for the different periods ( $p = 1$  above and  $p = 2$  below) and scenarios (denoted by the different curves).

surface water is expected to rise by about  $1.3^{\circ}\text{C}$ . As a consequence, the duration of ice cover is expected to reduce significantly (by more than a half).

Different are the results for the RCP8.5 scenario, which is characterized by a marked, well distributed increase in surface water temperature during all seasons, with a mean annual warming estimated at  $2.9^{\circ}\text{C}$ . This scenario represents an extreme case of climate change that should be confirmed, for example by applying the same procedure described here with longer series of data representing current climate conditions. This would allow for a more robust calibration of the temperature conversion model, and hence is likely to produce more reliable projections especially under severe future climate change scenarios, as is the case of the RCP8.5. In general, however, the projected variations of surface water temperature presented here are in fairly accordance with the trends of past decades, which suggest an increase of about  $4^{\circ}\text{C}$  in summer and  $2^{\circ}\text{C}$  in fall in the upper 25 m [Hampton *et al.*, 2008].

The most significant feature, which clearly distinguishes the RCP8.5 scenario from the others, is the fact that surface water temperature has been estimated to be always above  $1^{\circ}\text{C}$  (see Figure 5.12),



which is the threshold temperature for the formation of ice. In the light of these results, it is hard to determine whether Lake Baikal will actually not freeze under this scenario. As a matter of fact, the uncertainties in the interpretation of the results are significant, and are primarily ascribable to the not obvious definition of a threshold temperature for ice formation under different climate conditions. In this regard, further work is needed to set up a simple model able to simulate the future evolution of ice dynamics on the basis of the few available data. However, note that a scenario that assumes the progressive reduction of ice cover until its complete disappearance represents an interesting case study, which can provide valuable information for the general understanding of deep ventilation, in particular with regard to its dependence on the conditions at the atmosphere-lake interface.

Table 5.2: Expected increase of surface water temperature for the future periods and scenarios.

Scenario	Spring [ $^{\circ}\text{C}$ ]	Summer [ $^{\circ}\text{C}$ ]	Autumn [ $^{\circ}\text{C}$ ]	Winter [ $^{\circ}\text{C}$ ]	Mean annual [ $^{\circ}\text{C}$ ]
p=1 (2026-2046)					
RCP2.6	$\sim 0$	0.4	0.8	0.5	0.4
RCP4.5	$\sim 0$	0.4	0.7	0.5	0.4
RCP4.5	$\sim 0$	0.5	0.8	0.7	0.5
p=2 (2081-2101)					
RCP2.6	0.1	0.6	0.8	0.5	0.5
RCP4.5	0.4	1.2	1.4	1.3	1.1
RCP4.5	2.1	3.4	3.0	2.9	2.9

Table 5.3: Characteristic properties of surface water under current conditions, and for future periods and different scenarios.

Scenario	Ice cover [days]	Ice formation	Ice break up	Mean annual $T_w$ [ $^{\circ}\text{C}$ ]
p=0 Current conditions				
-	111	Jan 10	Apr 30	4.0
p=1 (2026-2046)				
RCP2.6	91	Jan 28	Apr 28	4.5
RCP4.5	92	Jan 29	Apr 30	4.4
RCP4.5	86	Feb 3	Apr 29	4.5
p=2 (2081-2101)				
RCP2.6	90	Jan 27	Apr 26	4.5
RCP4.5	50	Feb 27	Apr 17	5.1
RCP4.5	0	-	-	6.9

### 5.3 Concluding remarks

For the purposes of this study, the availability of long-term series of data is crucial. This is particularly true as far as wind forcing and surface water temperature data are concerned. As a

## 5. Available datasets and data processing

Table 5.4: Guidelines for the interpretation of Figures 5.7 - 5.9 and 5.12 in this section, and figures in Section 6.

Format (color/style)	Meaning
<b>Red line</b>	Present state
<b>Blue line</b>	First period (2026-2046)
<b>Dark blue, dashed line</b>	Generic simulation year $y$
<b>Black line</b>	Second period (2081-2101)
<b>Green line</b>	Equilibrium state (2101 - 3000, in Section 6.3)
Continuous line	Present state (red line) or RCP2.6 scenario (black or blue)
Dashed line	RCP4.5 scenario
Dotted line	RCP8.5 scenario

matter of fact, these information are required as boundary conditions in the 1D simplified model to investigate deep ventilation, which is formulated in Section 3. Unfortunately, although numerous field expeditions have been organized in the past and some permanent measurement stations have been installed during the last few decades, we can only rely on incomplete data and/or short measuring periods. Therefore, available measurements and observations were supplemented with additional, longer time series, and re-analysis data have been chosen for this purpose. In addition, three widely accepted climate change scenarios (RCP2.6, RCP4.5 and RCP8.5, corresponding to three different projections of greenhouse gasses concentration provided by the Intergovernmental Panel on Climate Change - IPCC) have been considered to reconstruct the input of the model over the whole 21<sup>th</sup> century.

Besides presenting the data used in this study, in the present chapter we described the operations that have been required in order to prepare the input data for the model, and properly define the boundary conditions associated to re-analysis series and climate change scenarios. The attention has been primarily focused on the downscaling of data from their coarse spatial resolution to a more suitable lake scale resolution. This operation also allowed for the removal of the biases that affect climate model outputs. Furthermore, since these datasets do not provide information concerning temperature of water, but only air temperature is available, particular attention has been devoted to suitably convert the series of air temperature into the corresponding series of surface water temperature. Different downscaling procedures have been used depending on the nature of data: wind speed or air temperature, re-analysis or future climate projections.

Re-analysis data have been downscaled using the well-known quantile-mapping approach, applied to both wind speed and air temperature. In the latter case, the downscaling provided the contemporaneous conversion from air into surface water temperature.

In the case of climate change scenarios, two different statistical downscaling procedures have been devised. Concerning wind speed, a novel procedure has been developed, which is still based

on the quantile-mapping approach, but also accounts for potential modifications in both intensity and seasonality of wind speed, thus resulting suitable to be applied to climate change studies. As regards water temperature, the downscaling/conversion of air temperature series has been carried out through the following steps. First, the simple physically-based model to convert air temperature into surface water temperature described in Chapter 4 has been used to assess the possible impact on lake temperature. Then, the current mean annual cycle of surface water temperature has been corrected accounting for these modifications. Finally, the downscaling has been obtained by implementing the standard quantile-mapping approach, as for the case of re-analysis data.

The majority of the measurements analyzed in this chapter have been extracted from the literature, with the exception of the 9-year long dataset of water temperature and both re-analysis data and future climate projections. We gratefully thank the research group headed by Prof. A. Wüest at EAWAG (Kastanienbaum, Switzerland), which provided the temperature records. These data were fundamental for the actual implementation of the model and the overall investigation presented in this thesis. Furthermore, special thanks to Dr. Samuel Somot and Dr. Clotilde Dubois at the CNRM, Mètèo-France for extracting the ECMWF ERA-40 re-analysis dataset from the ECMWF Data Server and for providing the future climate scenarios provided by the CNRM-CM5 model.

5. Available datasets and data processing

---

## 6 Results: deep ventilation under different climatic conditions

**Abstract** - *In Chapter 3 we presented a simplified one-dimensional model to investigate the phenomenon of deep ventilation in profound lakes. The model has been suitably designed in order to take into account the main physical factors controlling deep ventilation (e.g. thermobaric instability) and the major seasonal dynamics influencing the transport and mixing processes within a lacustrine system.*

*In this chapter, the effectiveness and consistency of the core algorithms and the general performance of the model are assessed by applying it to investigate deep ventilation in the South Basin of Lake Baikal. The calibration of the internal parameters of the model is presented and the main results are reported and discussed. In particular, the analysis of numerical results has been finalized to the description of the mixing and thermal regimes of the lake, and to an in-depth characterization of deep ventilation. Numerical simulations have been performed under different climate conditions (i.e. current and projected), thus allowing to assess the future behavior of the lake in response to the expected climate changes. All simulations have been carried out by using the available data and implementing the downscaling procedures discussed in Chapter 5.*

*The chapter is organized in three main parts. In Section 6.1, the calibration of the internal parameters of the model is presented. For this purpose, a medium-term simulation has been performed over a historical period (40 years, from 1958 to 1998), and numerical results have been compared with the available measurements (mainly temperature and CFC-12 profiles). An indirect validation of the model and a sensitivity analysis of the calibration process are also presented. Section 6.2 is devoted to the description of the behavior of the lake under current climate conditions. For this purpose a 1000-year simulation has been performed, by maintaining current climate conditions unchanged. Numerical results allowed for a detailed description of the mixing regime and thermal dynamics of the lake (e.g. seasonality of temperature and diffusivity profiles), and to a statistical characterization of deep ventilation (e.g. mean annual downwelling volume and temperature, deep ventilation timing). Finally, in Chapter 6.3 the model has been applied to investigate the impacts that climate change is likely to have on deep water renewal and on the general behavior of the lacustrine system. For this purpose, three well accepted climate change scenarios have been investigated, and results are discussed in the light of their differences compared to current conditions.*

6. Results: deep ventilation under different climatic conditions

---

## 6.1 Model calibration and validation

The 1D model formulated in Chapter 3 has been applied to investigate the phenomenon of deep ventilation in the South Basin of Lake Baikal. For this purpose, the first step is the calibration of the internal parameters of the model. We recall here that the key calibration parameters are: the coefficients  $\xi$  and  $\eta$  required for the estimates of energy input and downwelling volume respectively, the reference diffusivity profile  $D_{z,r}$ , and the mixing coefficients  $c_{mix}$  and  $c'_{mix}$  (see Chapter 3 for further details).

As already discussed in Chapter 5, the seasonality of temperature profiles and the past evolution of *CFC-12* concentration along the water column have been used as main calibration targets. Dissolved oxygen concentration profiles have been used as well, but since uncertainties exist concerning oxygen depletion rate along the water column, they have been used only as secondary calibration tracers. The definition of boundary conditions and the reconstruction of external forcing (primarily surface water temperature, *CFC-12* concentration at the surface and wind speed) have been based upon the data presented in Chapter 5.

The calibration procedure has been carried out over a 40-year historical period ranging from 1958 (starting date of ECMWF ERA-40 re-analysis data) to 1998, thus comprehending the period for which *CFC-12* profiles have been measured (1988-1996). In order to account for the fact that *CFC-12* was first introduced into the atmosphere in the 1940's, an initial condition for the vertical profile of *CFC-12* concentration in the lake is required. Since no measurements are available for the 1958, the initial condition for *CFC-12* has been estimated by running a preliminary 18 year simulation (i.e. 1940-1958), starting with a constant *CFC-12* profile equal to  $0 \text{ pmolkg}^{-1}$  and assigning the boundary conditions by randomly extracting 18 years from the re-analysis dataset.

Once all initial and boundary conditions have been defined, a set of medium-term simulations have been run over the period 1958-1998. A large number (several thousand) of simulations have been performed, setting up a robust iterative procedure aimed at calibrating the main parameters and at the same time continuously improving the core algorithms of the model. This procedure continued until we get to the current version of the model (which is that described in Chapter 3) and to the values of the calibration parameters shown in Table 6.1 (see Figure 3.7 for the calibrated profile of reference diffusivity  $D_{z,r}$ ), which is the set of parameters that allowed for the best match between measurements and simulations (see results in Section 6.1.1).

The calibration of the model has been successively tested performing a long-term simulation (i.e. 1000 years, see Section 6.1.2) starting from completely different initial conditions, and verifying the achievement of an asymptotic equilibrium of the system. Finally, a sensitivity analysis has been carried out on the main parameters of the model, revealing a robust calibration (Section 6.1.3).

Table 6.1: Calibrated values of the model parameters.

Parameter	Value	Units
$\xi$	30	$[kg\ m^{-2}\ s^{-1}]$
$\eta$	0.347	$[km\ h]$
$c_{mix}$	10%	$[-]$
$c'_{mix}$	6‰	$[-]$

### 6.1.1 Medium-term simulations

Hereafter, we present the numerical results obtained by running the model with the set of parameters listed in Table 6.1 and the reference diffusivity profile,  $D_{z,r}$ , shown in Figure 3.7. Simulations have been performed over the 40-year period ranging from 1958 to 1998, which is the historical period used for calibration.

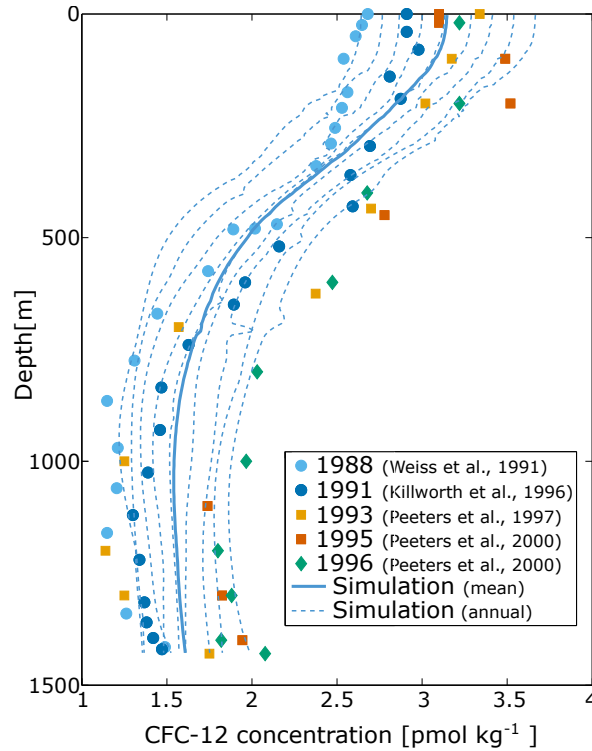


Figure 6.1: Comparison of simulated  $CFC-12$  profiles with measured data [Weiss *et al.*, 1991; Killworth *et al.*, 1996; Peeters *et al.*, 1997, 2000] during the period from 1988 to 1996. Different markers refer to measurements collected in different years; dashed lines correspond to the mean annual numerical profiles at each year in the considered period (progressively increasing from left - 1988 - to right - 1996), while the continuous line represents the numerical  $CFC-12$  profile averaged over the period from 1988 to 1996.



Figure 6.1 shows the numerical results for *CFC-12* concentration profiles. Simulations are compared with measurements, for the period ranging from 1988 to 1996. The thick line represents the average *CFC-12* profile during this time window, while dashed lines correspond to each single year, in order to allow for a detailed comparison with the different series of measurements. The overall agreement is reasonably good, although a slight model underestimation is visible around 500m depth. This is likely due to the fact that the model does not account for the possible exchanges among the South Basin and the Central Basin which can occur above the sill elevation. *CFC-12* concentrations are slightly different in the two basins, with relatively higher values in the Central Basin [Peeters *et al.*, 2000]. The possible exchange between the two basins is confirmed by the small deviation of *CFC-12* that is visible in the measurement profiles at about 400m depth. The overall evolution of *CFC-12* concentrations from 1958 to 1998 is shown in Figure 6.2.

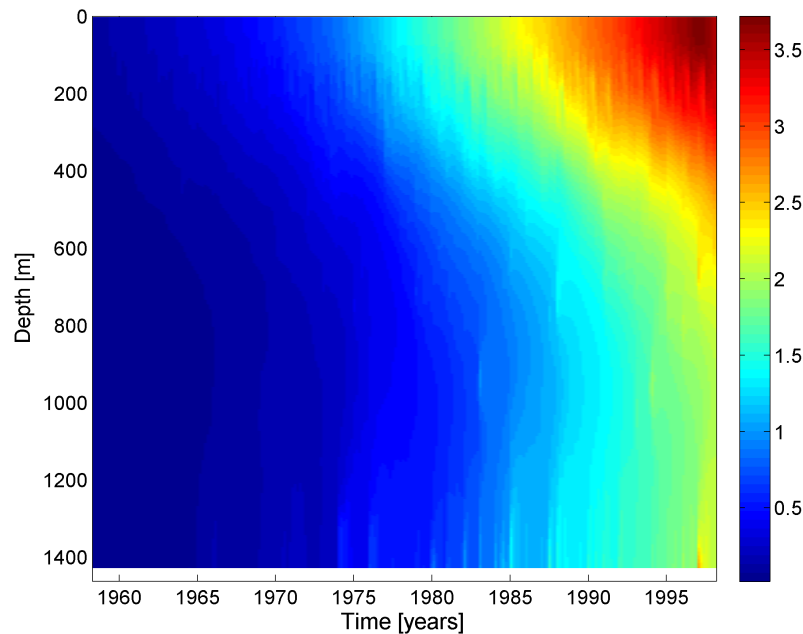


Figure 6.2: Overall evolution of *CFC-12* concentrations from 1958 to 1998.

In Figure 6.3, the modeled temperature profiles are compared with temperature measurements (symbols) in typical winter (15 February) and late summer (15 September) conditions. A temperature profile averaged over all simulation years is shown with the continuous line, while the range of variation is shown by dashed lines, allowing for an easy assessment of the confidence interval of the model predictions. Both in summer and winter time, a remarkable agreement between simulations and measurements is achieved, suggesting a reliable performance of the model. The main features

## 6. Results: deep ventilation under different climatic conditions

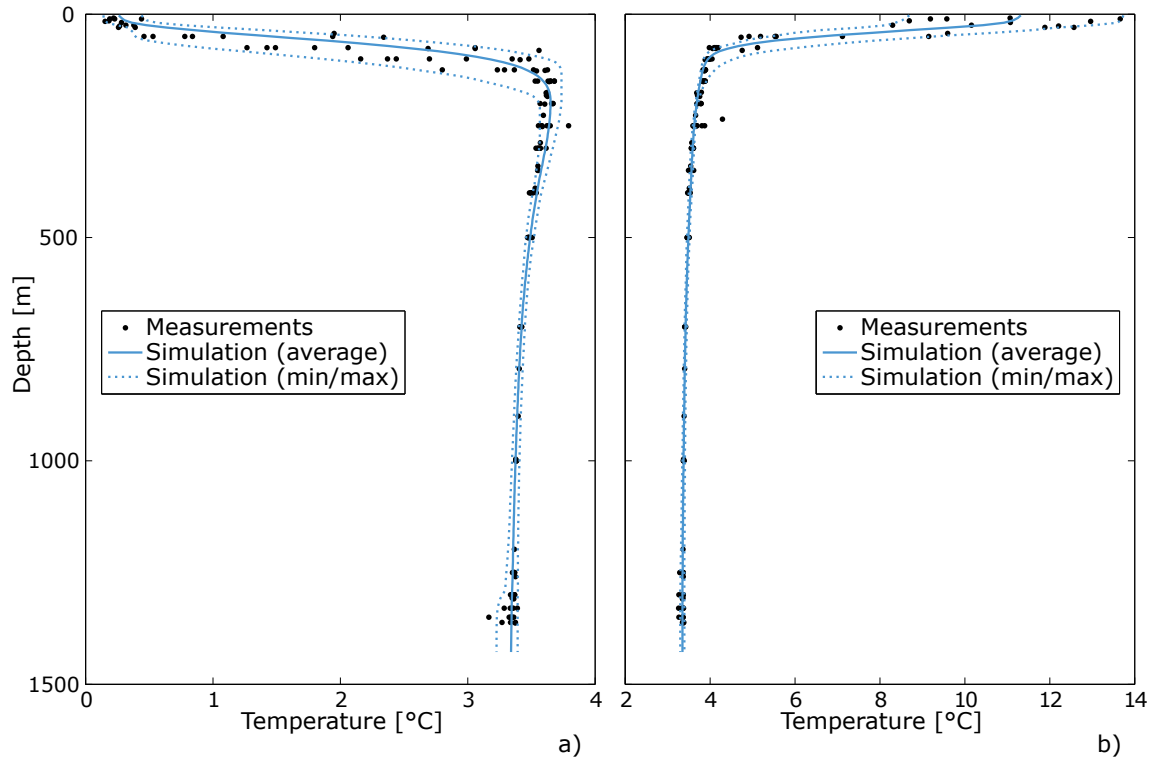


Figure 6.3: Comparison of simulated temperature profiles with measured data (courtesy of A. Wüest), for the 40-years simulation ranging from 1988 to 1996: a) winter conditions (28 February); and b) late summer conditions (15 September).

of the water column are well captured, as for example the thickness and the shape of the thermocline and the typical weak stratification of the hypolimnion.

Figure 6.4 shows the time evolution of water temperature beneath 500 *m* depth, from 1958 to 2002 (the whole period covered by re-analysis data). The occurrence of cold water deep downwellings is evident. According to numerical results, the period between 1958 and 1974 is characterized by small (in terms of volume) and relatively warm downwelling events. On the contrary, starting from 1974 the lake is subjected to an intense deep water renewal activity, which determines a significant cooling of the layers beneath 1000 *m* depth. Unfortunately, the available data do not allow to properly validate the timing of deep ventilation simulated by the model, as temperature data start in 2000. However, some information can be extracted from the literature. According to *Wüest et al.* [2005] and *Shimaraev et al.* [2011b], a strong downwelling event occurred in 1997, which is also clearly evident in Figure 6.4. From 1993 to 1997 the South Basin did not experience the occurrence of significant downwellings, which is in agreement with the numerical results as well. Before the 1990s few information are available, but a last conclusion can be addressed by observing the profiles presented by [*Weiss et al.*, 1991] for 1988 and 1991. In the

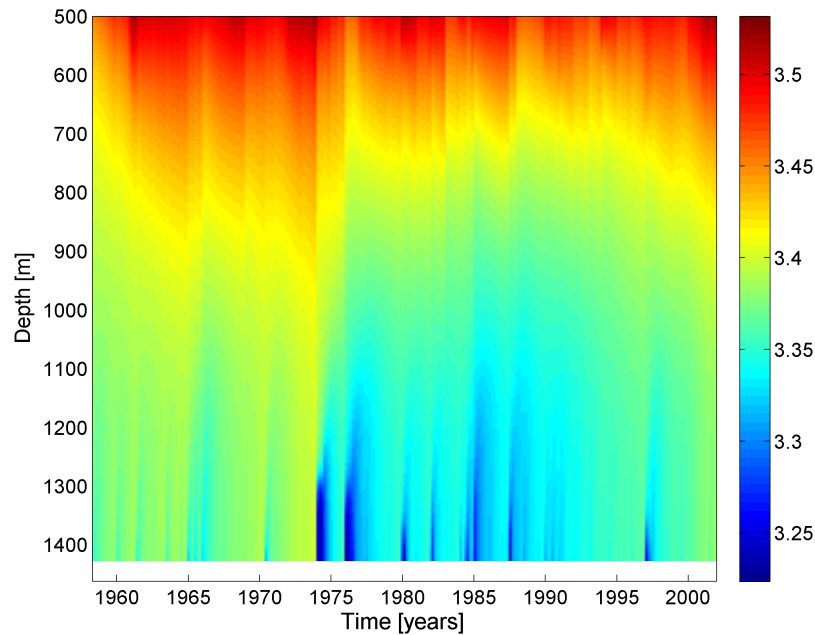


Figure 6.4: Time evolution of deep water temperature, from 1958 to 2002.

first case, deep water has a lower temperature and a higher oxygen content, which suggests that a relevant downwelling is likely to have occurred around the time measurements were collected. Also in this case, numerical results are in accordance with observations.

Finally, in Figure 6.5 the numerically simulated dissolved oxygen profile (solid line) is compared with measurements (symbols). As for the case of temperature, results have been averaged over the whole simulation (continuous line) and the envelope curves of *DO* variations have been calculated (dashed lines). Concerning the maximum value envelope curve, discontinuities are due to deep downwellings that stop along the water column (note that the envelope curves have been determined on the basis of *DO* profiles sampled at every time step). The *DO* profiles have been obtained assuming the oxygen consumption rate curve shown in Figure 3.5, which has been determined through the calibration procedure according to estimates that are available in the literature.

As a whole, we can conclude that results are consistent with the available measurements, which are however affected by non-negligible uncertainties (e.g. see the implausible decrease of *CFC-12* concentration beneath 700 *m* depth in 1993, and the non-calibrated temperature sensor at about 250 *m* depth).

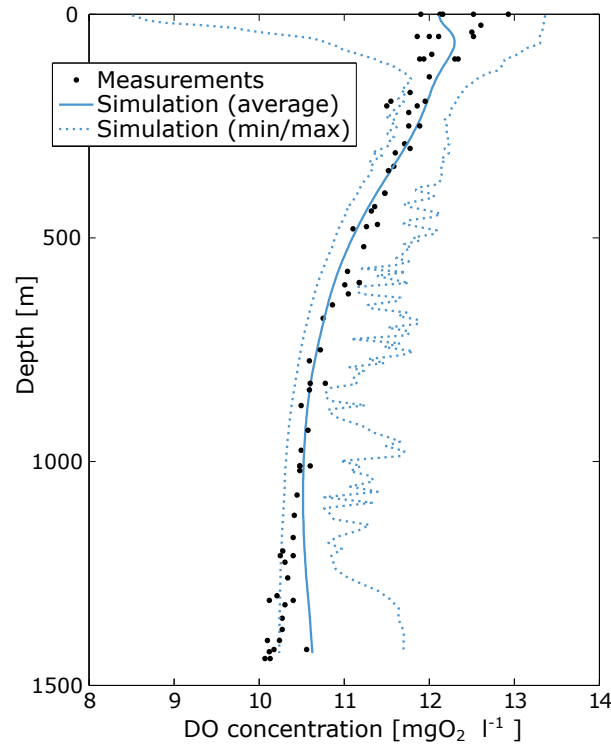


Figure 6.5: Comparison of simulated  $DO$  profile with measured data [Killworth *et al.*, 1996; Peeters *et al.*, 2000], for the 40-years simulation. Discontinuities in the upper envelope curve are due to deep downwellings that stop along the water column.

### 6.1.2 Long-term simulations

A classical validation of this model with an independent set of data is not obvious because of the quite limited information that is available, and that was used to obtain a reliable calibration. In order to have an independent (although indirect) test of the model results, we have decided to run a long-term simulation, which eventually leads to equilibrium profiles of the main variables ( $T$  and  $DO$ ). Equilibrium profiles are determined by the prescribed boundary conditions and, for a sufficiently long-term simulation, are likely to be independent of the initial conditions. Based upon the specific features of the equilibrium conditions achieved throughout the simulation, some considerations can be drawn concerning the robustness of the model formulation and calibration.

Therefore, a 1000-year simulation has been performed with arbitrarily set initial conditions, and the same external forcing (boundary conditions) as that derived for the calibration has been maintained. A constant temperature profile (corresponding to the temperature of maximum density at the surface,  $T \simeq 3.98^\circ C$ ) and a completely anoxic profile ( $DO = 0 \text{ mgO}_2 \text{ l}^{-1}$ ) have been assumed as initial conditions for  $T$  and  $DO$ , respectively. Boundary conditions have been specified consid-

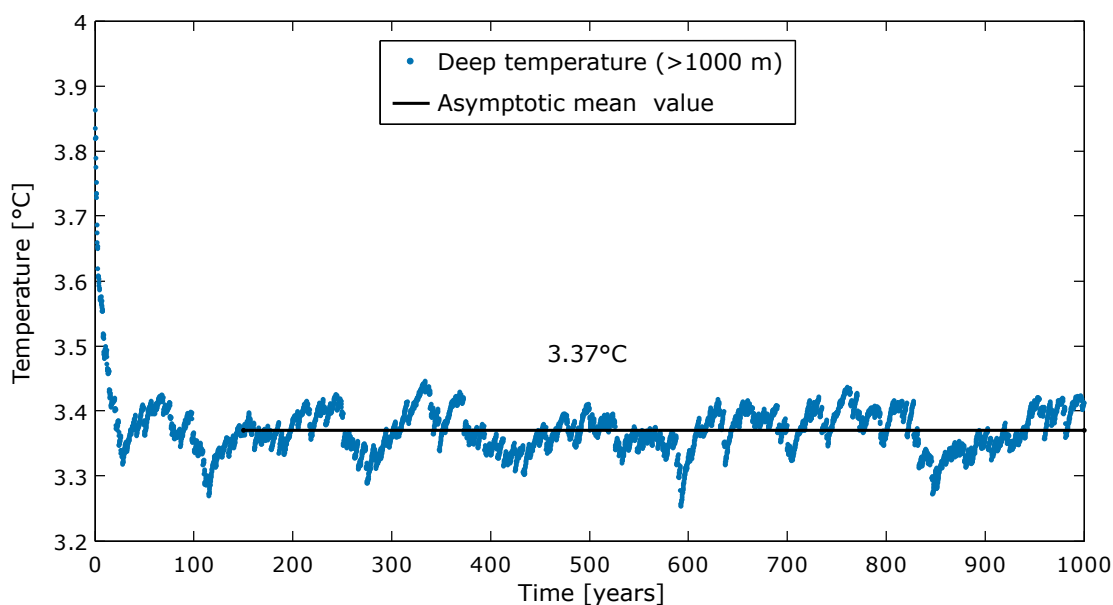


Figure 6.6: Long-term evolution of deep water temperature (averaged values beneath 1000 *m* depth, for a 1000-year simulation). An asymptotic equilibrium fully reached after an adjustment phase depending on the initial conditions.

ering a sequence of years randomly extracted from the same 40-year re-analysis dataset used to perform the medium-term (i.e. 40-year long) simulations.

Taking advantage from the fact that the current temperature profile did not change noticeably in the period when data are available (at least considering average conditions), we assume that it is not far from equilibrium conditions. This is also confirmed by the small changes noticed in the 40-year simulations run in the calibration phase (see the confidential range of temperature in Figure 6.3). In the light of these evidences, and since the system is subjected to the same external forcing as those of current conditions, if the model's algorithms properly describe the fundamental processes, it is expected that the numerical results match the actual observed conditions after an adjustment phase depending on the initial conditions. If the profiles resulting from long-term simulations are significantly different, either the model is not suitable to describe such a complex system, or the calibration has not been correctly carried out.

Figure 6.6 shows the evolution of deep water temperature averaged beneath 1000 *m* depth, over the 1000-year long simulation. An asymptotic equilibrium is completely reached after an adjustment phase depending on the initial profiles, confirming the goodness of the model. The asymptotic mean value of deep water temperature is  $\sim 3.37^{\circ}\text{C}$  (calculated after 150 years, in order to exclude the possible effect of initial conditions), which is in full agreement with measurements [e.g. see also *Wüest et al.*, 2005; *Schmid et al.*, 2008].

## 6. Results: deep ventilation under different climatic conditions

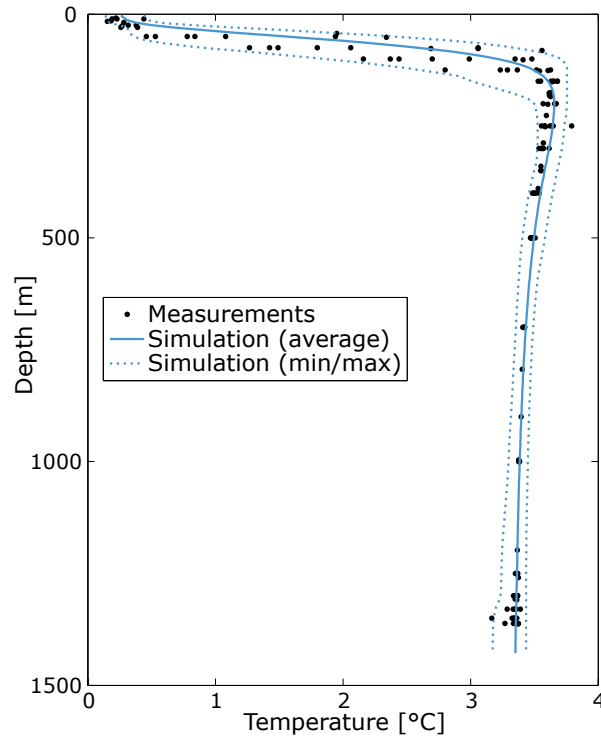


Figure 6.7: Comparison of simulated temperature profile and measured data (courtesy of A. Wüest) for typical winter conditions (28 February), for a 1 000-year simulation starting from an isothermal profile at  $T = 3.98^{\circ}\text{C}$ .

Model results have been analyzed evaluating the average, minimum and maximum profiles of  $T$  and  $DO$  over the asymptotic part of the simulation (150-1 000 years). In Figure 6.7, the simulated temperature profile is compared with measurements for a typical winter period (28 February), while Figure 6.8 shows the results for  $DO$  profile. In both cases the profiles predicted by the model closely match measurements.

Finally, the mean annual cycles of the vertical thermal structure of the South Basin have been determined, both for the 1 000-year long numerical simulation (Figure 6.9) and the 9-year long record of measurements (Figure 6.10). Since measurements are available only for a few years, in order to smooth the possible irregularities due to data scarcity the cycles of temperature profiles have been filtered with a one month moving average. The two cycles show a remarkable agreement: the overall vertical thermal structure is well simulated and the seasonal patterns are correctly reproduced (e.g. the evolution of the epilimnion). Note that the seasonal asymmetry in measured deep water temperature is likely due to the numerous cold water intrusions that occurred in winter time (i.e. between December and February), during the observation period [Schmid *et al.*, 2008; Shimaraev *et al.*, 2011b]. Such an asymmetric feature is absent in numerical results, as a

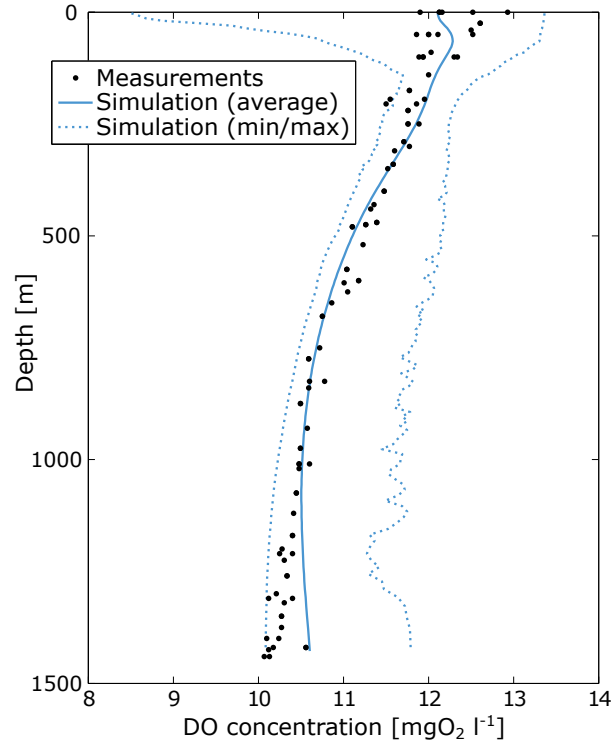


Figure 6.8: Comparison of simulated  $DO$  profile with measured data [Killworth *et al.*, 1996; Peeters *et al.*, 2000], for a 1000-year simulation starting from an anoxic profile,  $DO = 0\text{mgO}_2\text{l}^{-1}$ .

consequence of the high heterogeneity of deep downwellings that evidently characterizes long-term simulations. The good visual agreement is corroborated by Figure 6.11, which illustrates the map of residuals between model results and measurements. The major differences can be observed within the upper 200  $m$  depth layer, which is the part of the lake mostly affected by seasonality and external forcing. Nevertheless, the overall performance of the model is noticeable, the root mean square error, mean absolute error and maximum absolute error being  $RMSE \simeq 0.07^\circ\text{C}$ ,  $MAE \simeq 0.03^\circ\text{C}$  and  $MaxAE \simeq 0.78^\circ\text{C}$ , respectively ( $RMSE \simeq 0.09^\circ\text{C}$ ,  $MAE \simeq 0.04^\circ\text{C}$  and  $MaxAE \simeq 1.83^\circ\text{C}$ , in case the cycles are not filtered with a one month moving average).

### 6.1.3 Sensitivity analysis

A sensitivity analysis has been carried out aimed at evaluating the robustness of the calibration and the role played by each of the main parameters of the model. A new set of 40-year simulations has been run changing  $\xi$ ,  $\eta$ ,  $c_{mix}$  and  $c'_{mix}$  between 0.5 and 1.5 times the initial values. Different simulations have been performed changing one by one individual parameters, while all remaining

## 6. Results: deep ventilation under different climatic conditions

---

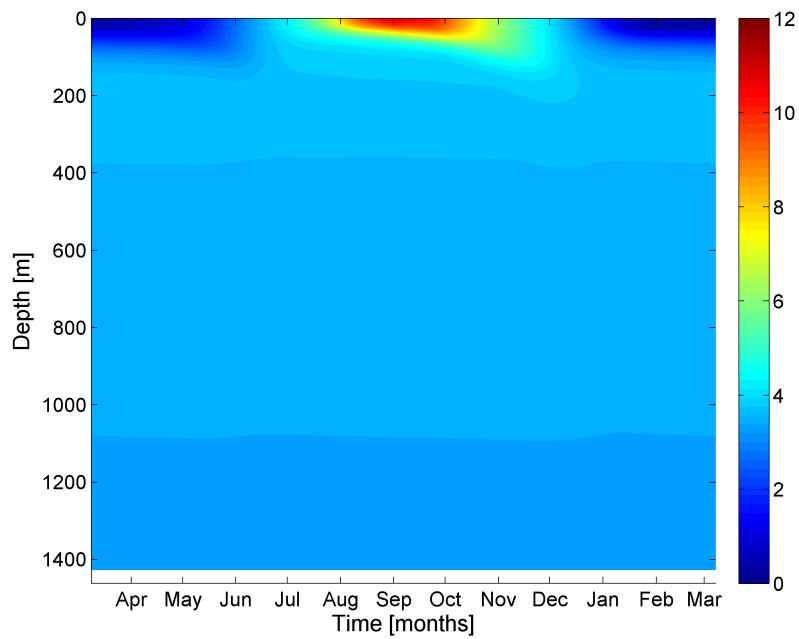


Figure 6.9: Mean annual cycle of model calculated vertical temperature profiles.

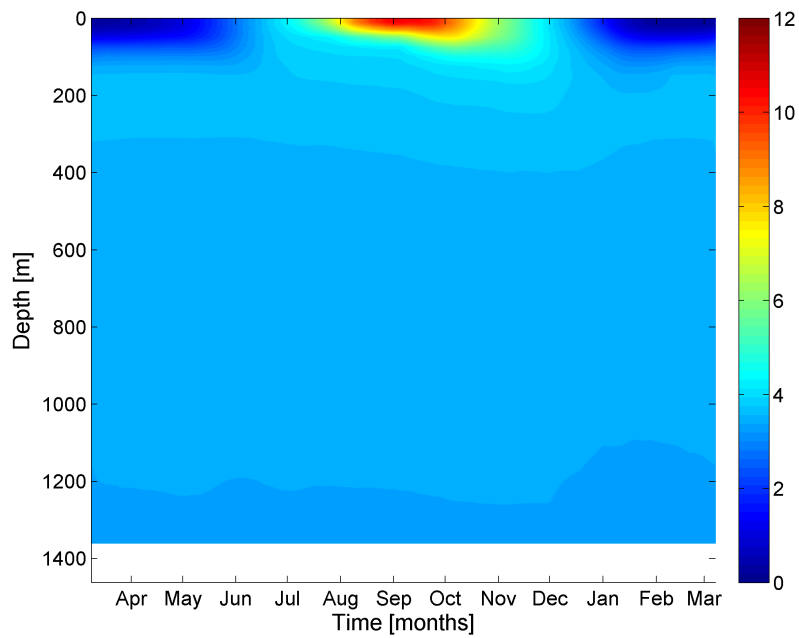


Figure 6.10: Mean annual cycle of measured vertical temperature profiles (data filtered with a one month moving average; data courtesy of A. Wüest).



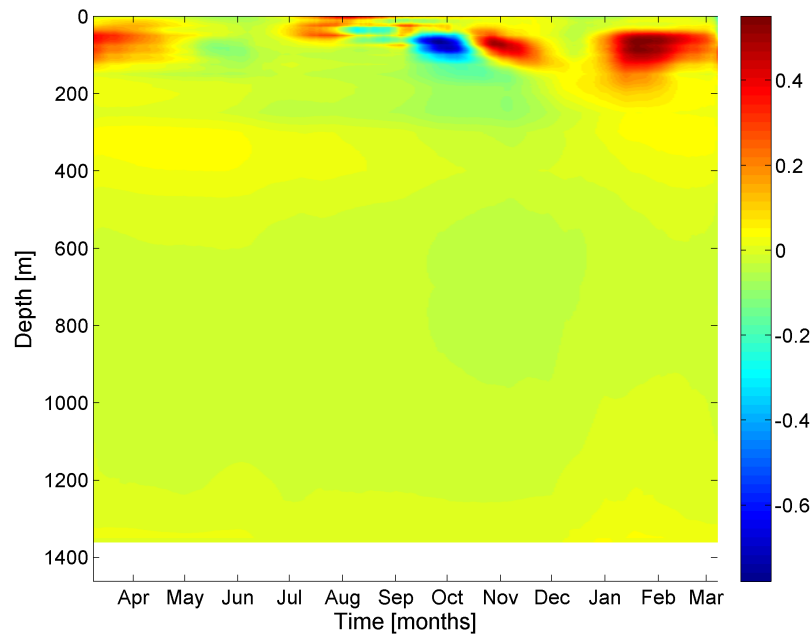


Figure 6.11: Map of residuals between the mean annual cycles of modeled and measured temperature profiles.

parameters were held at the initial values given in Table 6.1. The results of the sensitivity analysis are shown in Figure 6.12 and Figure 6.13, in which temperature and *CFC-12* profiles are plotted, respectively. The solution obtained using the calibrated set of parameters is plotted using a thick line marked with letter C, while numerical results obtained changing the set of parameters are plotted using thin lines labeled with numbers that refer to the combination of parameters listed in Table 6.2.

Note that profiles 3, 4 and 5 apparently show a better fit with measurements, if *CFC-12* profiles are analyzed. Nevertheless, the temperature profiles obtained with the same set of parameters deviate significantly from measurements. As a whole, modifications of the calibration parameters cause numerical results to significantly differ from measurements, suggesting that a proper calibration has been achieved. At the same time, no dramatic changes are observed as a consequence of the different values assigned to the parameters, indicating the suitability and robustness of the fundamental algorithms at the basis of the model.

## 6. Results: deep ventilation under different climatic conditions

Table 6.2: Different sets of parameters used in the sensitivity analysis.

id.	$\xi [kg m^{-2} s^{-1}]$	$\eta [km h]$	$c_{mix}$	$c'_{mix}$
C	30	0.347	0.10	0.006
1	15	0.347	0.10	0.006
2	30	0.174	0.10	0.006
3	30	0.347	0.05	0.003
4	45	0.347	0.10	0.006
5	30	0.694	0.10	0.006
6	30	0.347	0.15	0.009

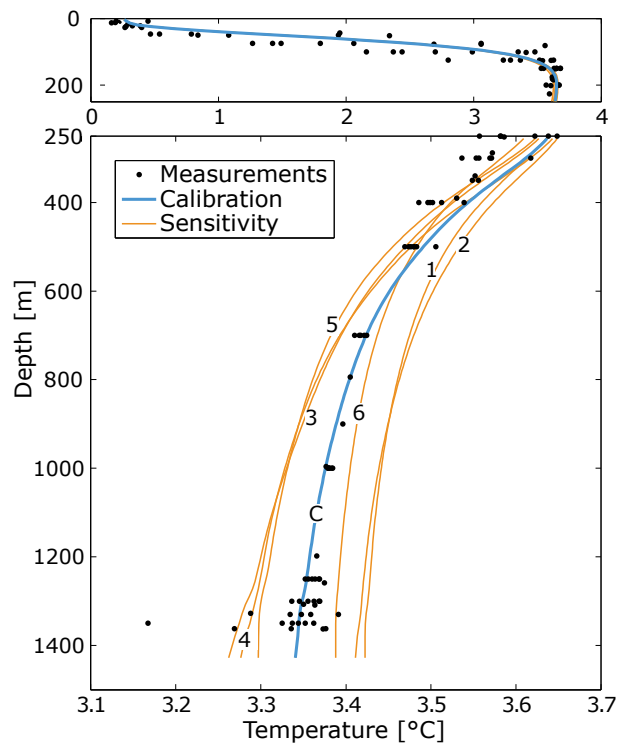


Figure 6.12: Sensitivity analysis on the temperature profile for a 40-year simulation: the thick line (C) shows the solution for the calibrated set of parameters, thin lines (from 1 to 6) refer to the sets of parameters listed in Table 6.2, and dots indicates measured profiles (courtesy of A. Wüest).

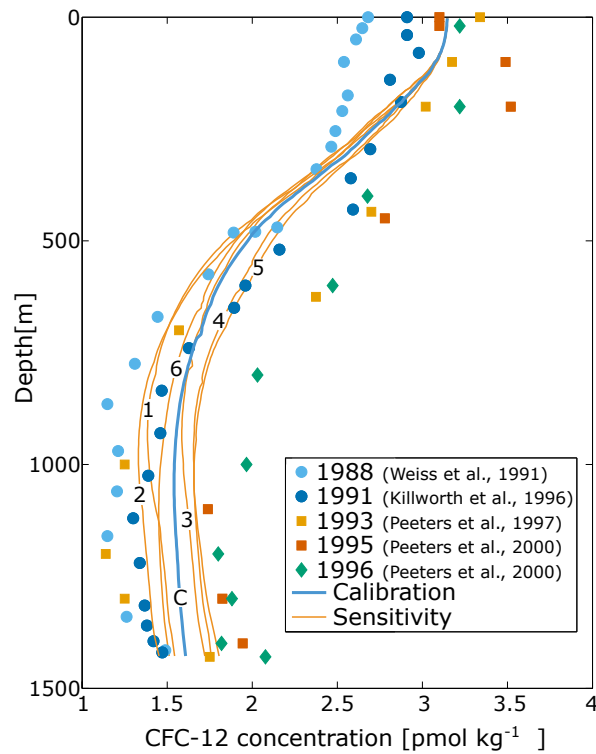


Figure 6.13: Sensitivity analysis on the *CFC-12* profile for a 40-year simulation: the thick line (C) shows the solution for the calibrated set of parameters, thin lines (from 1 to 6) refer to the sets of parameters listed in Table 6.2, and symbols indicate measured profiles [Weiss *et al.*, 1991; Killworth *et al.*, 1996; Peeters *et al.*, 1997, 2000].

## 6.2 Current climate conditions

In the previous section, the calibration and validation of the model have been presented, and its good capability in simulating deep ventilation in profound lakes has been demonstrated. Here, we discuss in detail the results obtained by running the calibrated model over a 1 000-year period under current climate conditions. The simulation is essentially the same as that used for model validation (see Section 6.1.2), the only difference lying in the choice of the initial conditions. In this case, the actual observed profiles of temperature and dissolved oxygen have been imposed, thus eliminating the adjustment phase due to arbitrarily chosen initial conditions (which is evident in Figure 6.6).

The long (*i.e.* one millennium) simulation period allowed to carry out a proper statistical description of deep ventilation, and an in-detail characterization of the mixing and thermal regime typical of the South Basin of Lake Baikal. These information are discussed in the following pages, where, unless differently specified, results are presented according to the mean year calculated over the whole simulation period (*i.e.* data associated with the same calendar day are averaged together).

### 6.2.1 Seasonal dynamics

Figures 6.14 - 6.19 show the mean annual cycles of the main variables involved in the model: temperature,  $T$ , dissolved oxygen,  $DO$ , Brunt-Väisälä buoyancy frequency,  $N^2$ , squared shear frequency,  $S^2$ , Richardson number,  $Ri$  and diapycnal diffusivity profile,  $D, z$ . Some insights about the major physical dynamics that occur in the South Basin can be gathered by analyzing the seasonal evolution and the vertical variations of these physical quantities and parameters.

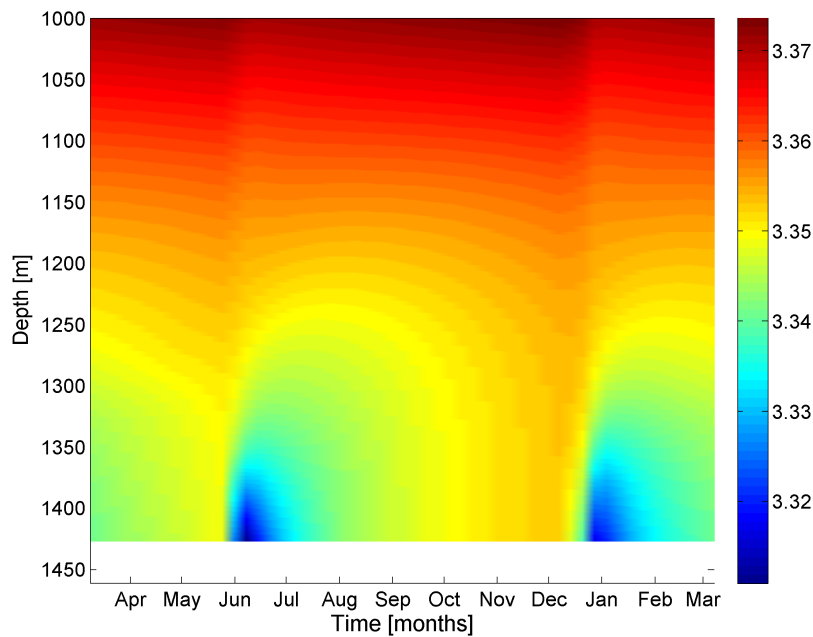


Figure 6.14: Mean annual cycle of temperature profile,  $T$ , within the hypolimnion (beneath 500  $m$  depth).

Concerning temperature, the mean annual cycle associated to the reference 1000-year simulation is inherently equivalent to that already presented in Figure 6.9 and commented in Section 6.1.2. Therefore, here we focus on the seasonal evolution of deep water temperature, which is shown in Figure 6.14 for depths greater than 1000  $m$ . Looking at this figure, it is evident that the interior of the lake does not experience meaningful variations in temperature throughout the seasons, but, on the contrary, is characterized by a typical profile that remains almost unchanged over the year. On the other hand, the deepest part of the hypolimnion (i.e. the last  $\sim 200 m$ ) is clearly subjected to a periodic variability: deep water is cooled twice per year, in correspondence to the occurrence of deep ventilation. According to numerical results, such a cooling effect is able to bump the temperature down to  $\sim 3.31^\circ\text{C}$  on average. The seasonal cooling of deep water is progressively

dissipated by diffusion on a time scale of about 2 to 4 months (for summer and winter cooling, respectively), in general accordance with *Wüest et al.* [2005]; *Schmid et al.* [2008]; *Shimaraev et al.* [2011a]. Some visual differences can be observed between the cooling of deep water in late spring/early summer and in late autumn/early winter: the second being more pronounced both concerning average vertical extension and time duration. However, from this figure we cannot infer anything about the reasons of this imbalance, which, in principle, could be determined by seasonal asymmetries concerning the volume, temperature, timing and frequency of downwellings. A more detailed analysis of deep ventilation is deferred to Section 6.2.2.

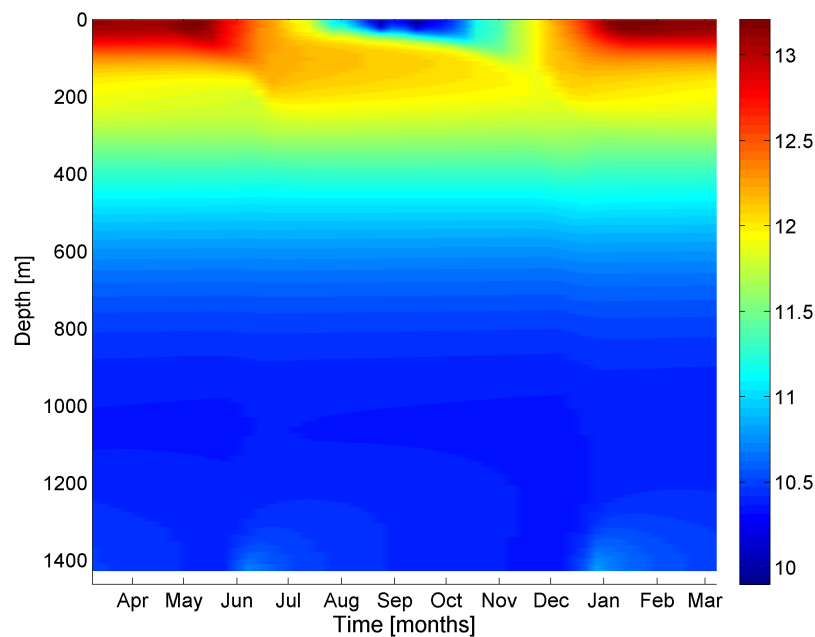


Figure 6.15: Mean annual cycle of dissolved oxygen concentration profile,  $DO$ .

Figure 6.15 shows the annual cycle of dissolved oxygen concentration,  $DO$ , along the water column. As for the case of temperature, the major seasonal variations are confined within the upper  $\sim 200\text{ m}$  layer, whilst deep water presents nearly the same conditions over the year, with  $DO$  concentrations ranging between  $12\text{ mg l}^{-1}$  and  $10\text{ mg l}^{-1}$ , moving from  $200\text{ m}$  depth to the bottom of the lake. Since temperature plays the primary role in controlling the exchanges of oxygen between atmosphere and lake ( $DO$  saturation concentration being inversely proportional to water temperature, see Equation (5.1)),  $DO$  concentration is strongly influenced by the seasonal cycle of surface water temperature. Indeed, as can be observed in the figure,  $DO$  concentration is lower in summer, when the epilimnion is warm, and higher in winter, when surface water is cold. The

highest peaks in  $DO$  concentration occur immediately before and after ice formation and break up, respectively, whereas during the period in which the lake is ice covered (from mid January to the end of April) the exchanges with the atmosphere is inhibited by the presence of the ice sheet, and hence  $DO$  concentration undergoes a progressive (slight) decrease due to oxygen consumption.

Due to convective mixing,  $DO$  concentration is vertically re-distributed within the superficial well-mixed layer, which, when surface water temperature approaches  $T_{p,max}$  (in June and December), reaches a thickness of  $\sim 200 - 250 m$ . Under these conditions,  $DO$  concentration at the surface is considerably high thanks to the low temperature of water, and hence the deepening of the well-mixed layer allows for a complete oxygenation of the entire uppermost part of the lake. As a consequence of the epilimnetic mixing that occurs in June, relatively high  $DO$  concentrations between 100 and 200  $m$  depth still persist during the warm season, when, on the contrary,  $DO$  within the uppermost layer progressively diminishes as temperature of water rises.

Finally, the effect of deep ventilation is evident in the very deep layers of the lake, where an increase of  $DO$  concentration can be observed during the downwelling periods. This increase is estimated at about  $0.4 mg l^{-1}$  at the very bottom of the lake (first 10  $m$  above the bottom of the lake), which is in fairly good accordance with the observations available in the literature [e.g. *Peeters et al.*, 2000].

The mean annual cycle of the logarithm (base 10) of the squared Brunt-Väisälä buoyancy frequency,  $N^2$ , is presented in Figure 6.16. The seasonal variation of  $N^2$  reflects the stratification conditions that occur throughout the year: higher values of  $N^2$  characterize the epilimnion in summer and winter when the lake is stratified (directly and inversely, respectively), whereas lower values can be observed during the transition periods, when the epilimnion deepens and the upper layer is well mixed. Furthermore, as a consequence of the fact that stratification is stronger during summer than in winter (i.e. vertical temperature gradients are higher during the warm season compared with those typical of the lake when it is inversely stratified), the warm season time is characterized by higher values of  $N^2$ .

As far as the internal part of the lake is concerned, there the water column is very weakly stratified, with a mean value of  $N^2 \simeq 3 \times 10^{-8} s^{-2}$  calculated between 400 and 1000  $m$  depth.

Note that when the lake is inversely stratified (roughly from December to July), the minimum of  $N^2$  is localized slightly beneath the mesothermal maximum (i.e. the depth where the temperature profile crosses the  $T_{p,max}$  line, see Section 2 for further details), which is depicted with a red line in the figure. As a matter of fact, in this region of the lake the static stability of the water column is inherently low, since the vertical temperature gradients are almost vertical [e.g. *Boehrer and Schultze*, 2008].

Finally, the effect of deep downwellings is evident in the very deep layers of the lake, where

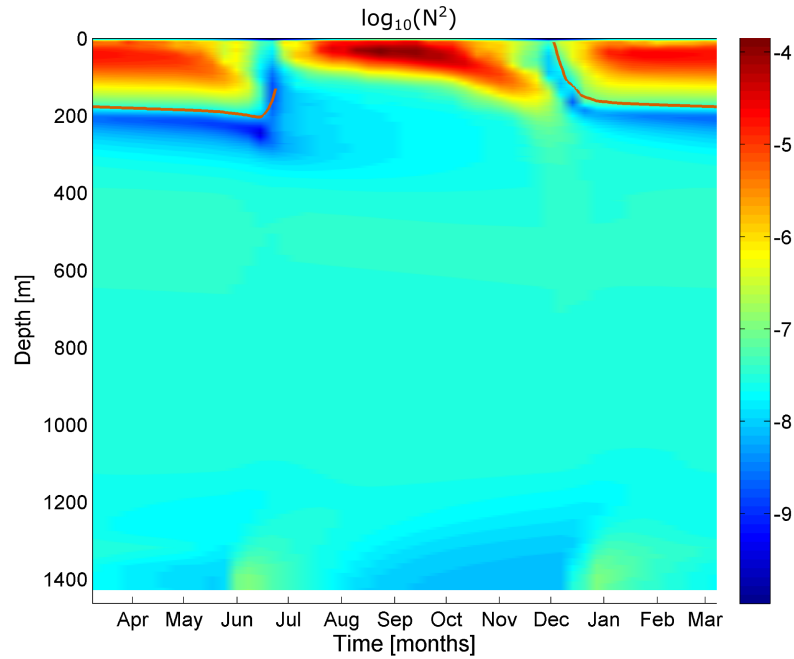


Figure 6.16: Mean annual cycle of the squared Brunt-Väisälä buoyancy frequency,  $N^2$ . The seasonal variation of the mesothermal maximum depth is depicted by the red line.

$N^2$  increases during the downwelling periods as a consequence of the stabilizing effect due to the cooling of deep water (which results in an increase of the vertical temperature gradient). During the remaining of the year,  $N^2$  progressively decreases as the cooling is dissipated by diffusion and deep water is warmed by geothermal heat flux.

Figures 6.17 and 6.18 show the logarithm (base 10) of the squared shear frequency  $S^2$  and of the Richardson number,  $Ri$ , respectively. Concerning  $S^2$ , as one would expect, the highest values occur when the lake is ice free. As a matter of fact, under these conditions shear stress is generated directly by the action of wind blowing at the surface (in the very upper part of the lake -  $S_{lw}^2$ ) and by wind-induced internal waves (in correspondence of the thermocline -  $S_{iw}^2$ ). On the contrary, as ice starts to appear at the surface,  $S^2$  progressively diminishes until, eventually, it asymptotically decays to a background value  $S_{bg}$  (see Section 3.4.2 for the meaning of  $S_{lw}^2$ ,  $S_{iw}^2$  and  $S_{bg}^2$ ). This background value also characterizes the interior of the lake, where only a small fraction of the turbulent energy available from the wind is transferred [Ravens *et al.*, 2000].

By definition, the Richardson number,  $Ri$ , combines the information of  $N^2$  and  $S^2$  (see Section 3.4.1). The outline of the mean annual cycle of  $Ri$  is qualitatively similar to that of  $N^2$ : the higher values of  $Ri$  occurs within the top 200 m depth, when the lake is stratified, in summer and in winter.

## 6. Results: deep ventilation under different climatic conditions

---

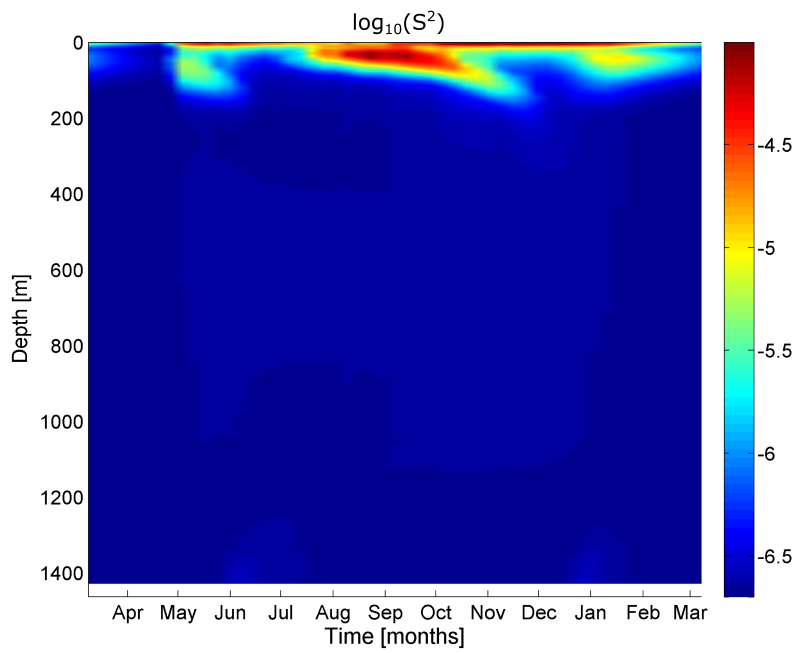


Figure 6.17: Mean annual cycle of the squared shear frequency,  $S^2$ .

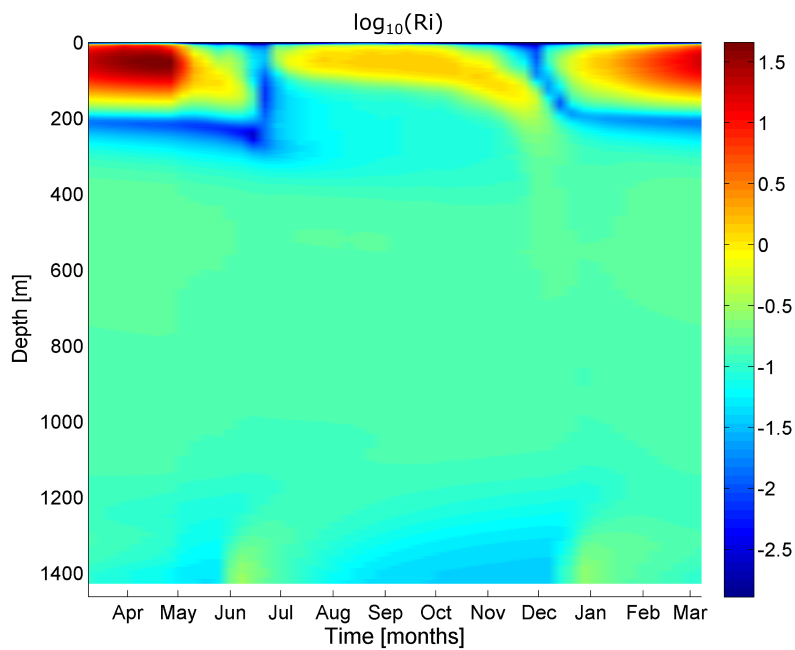


Figure 6.18: Mean annual cycle of the Richardson number,  $Ri$ .



However, note that during the period of direct stratification, in summer,  $Ri$  is lower than in winter, whereas we observed the opposite trend in the case of  $N^2$  (see Figure 6.16). This difference is due to the relevant values of  $S^2$  at the surface of the lake during the warm season (when the lake is ice free and hence the wind-induced shear stress is significant), which, on the contrary, are very low in winter when the lake is ice covered.

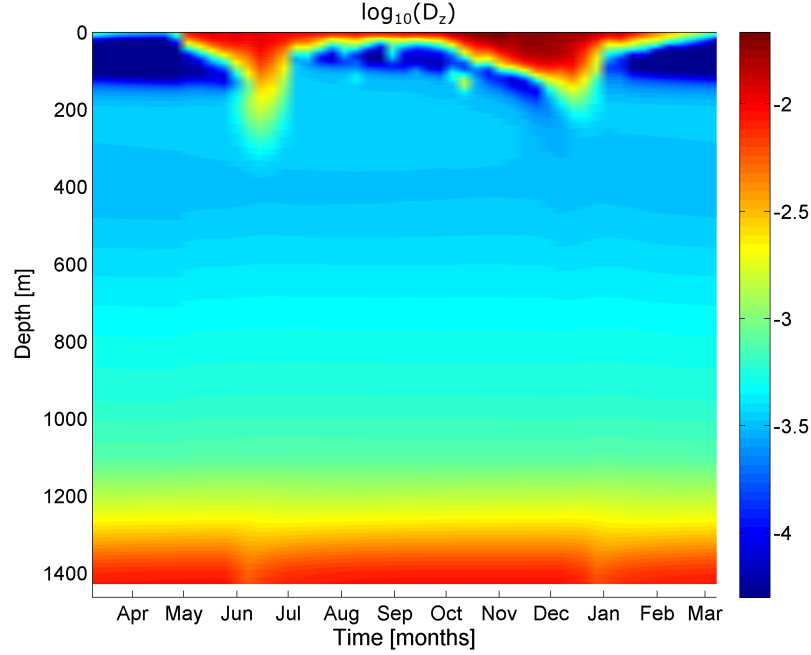


Figure 6.19: Mean annual cycle of the diapycnal diffusivity profile,  $D_z$ .

The mean annual cycle of the logarithm (base 10) of the diapycnal diffusivity,  $D_z$ , is presented in Figure 6.19. At every time step,  $D_z$  is calculated by means of the Richardson number-based scheme given in Equation (3.22) and discussed in Section 3.4.1. Therefore, the vertical variation and seasonal evolution is closely related to the corresponding pattern of  $Ri$ .

The interior of the lake is characterized by a nearly constant diffusivity profile over the year, with a mean value of  $\sim 4.5 \times 10^{-4} \text{ m}^2 \text{ s}^{-1}$  calculated between 400 and 1000 m depth. Beneath 1000 m depth  $D_z$  progressively increases accounting for the turbulent processes within the benthic boundary layer, as already discussed in Section 3.4.3.

As for the other variables and parameters discussed so far, the most interesting variations of  $D_z$  throughout the year occur within the upper part of the lake. Figure 6.20 shows in detail the vertical profiles of  $D_z$  within the upper 400 m, which provides a comprehensive summary of the features typically observed in the South Basin of Lake Baikal [Shimaraev *et al.*, 1994] and already

## 6. Results: deep ventilation under different climatic conditions

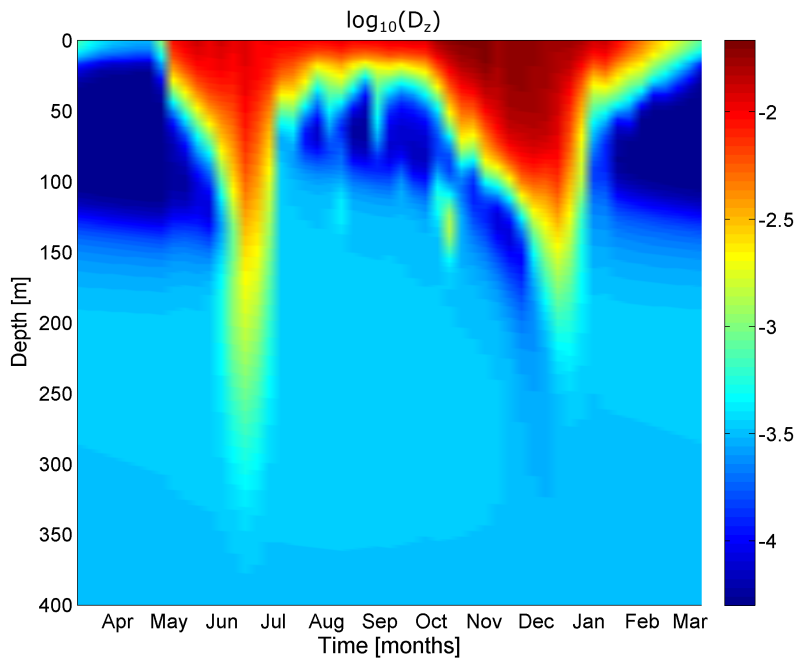


Figure 6.20: Mean annual cycle of the diapycnal diffusivity profile,  $D_z$ , within the uppermost 400 m.

discussed in Section 2. The well-mixed layer reaches a maximum thickness of about 200 – 250 m twice a year, in June and December, when the surface water temperature approaches 4°C. Under these conditions, the weak stratification of the water column and the action of wind forcing, which is particularly intense in these periods [Rzheplinsky and Sorokina, 1977; Shimaraev et al., 1994], determines high values of  $D_z$  within the whole upper layer of the lake (see Figure 6.21a). Starting from the end of June, the summer thermocline develops and the thickness of the mixing layer progressively reduces, confining the turbulent mixing within the uppermost  $\sim 50$  m depth layer. Beneath that depth, the water column is stably stratified, thus turbulent convection is inhibited and  $D_z$  drops to very low values (see Figure 6.21b). As summer is over, from the end of September, the surface mixed layer starts to deepen again, until eventually it reaches a thickness of  $\sim 200$  m in December. This is the period of the year when  $D_z$  achieves its maximum values at the surface (see Figure 6.21a). Successively, the mixing layer reduces and  $D_z$  steadily declines while winter stratification develops under the ice. The presence of the ice sheet inhibits the action of wind, and  $D_z$  progressively decreases to the lowest values of the year. The seasonal cycle starts again, when the convective mixed layer develops in spring as a combined effect of solar heating and wind-induced mixing, after the melting of ice. Finally, note the mixed zone of approximately 100 m thickness that appears between 200 and 250 m depth, immediately beneath the depth of the

mesothermal maximum, where the water column is not stratified (see also the discussion of Figure 6.16).

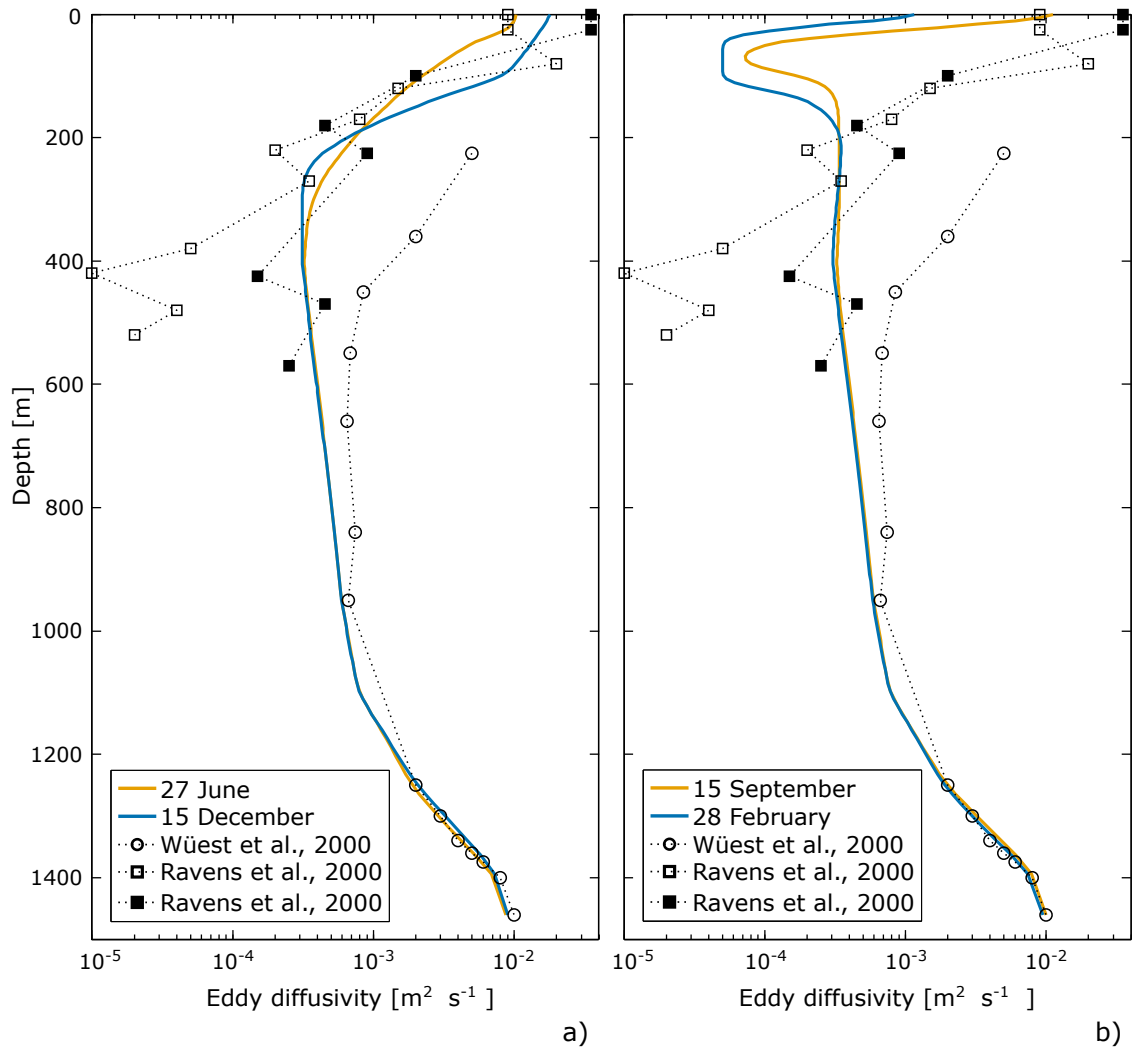


Figure 6.21: Typical diapycnal diffusivity profiles in different periods of the year: a) when the lake is near isothermal conditions, in early summer (27 June) and late autumn (15 December), and b) when the water column is stratified, in late summer (15 September) and winter (28 February).  $D_z$  profiles in the literature refer to measurements collected between 26 and 28 June, 1996.

In general, we can affirm that the simple Richardson number-based scheme used in this work to calculate diapycnal diffusivity provides a reliable description of the turbulent mixing processes occurring in Lake Baikal. This is confirmed by the fairly good agreement between our estimates and the vertical diffusivities simulated with the  $\kappa$ - $\epsilon$  model by *Schmid et al.* [2007] (compare our Figure

## 6. Results: deep ventilation under different climatic conditions

6.20 with their Figure 8). Furthermore, in Figure 6.21 we compared our estimates to the  $D_z$  profiles available in the literature [Ravens *et al.*, 2000; Wüest *et al.*, 2005]. Simulated profiles refer to four significant periods of the year: the seasons of deep convective mixing in June and December (Figure 6.21a), and the periods during which the lake is stratified in February and September (Figure 6.21b). On the other hand, profiles in the literature refer only to the period of deep convective mixing in June, as they have been calculated on the basis of measurements collected between the 26th and 28th of June, 1996. A reasonable agreement can be observed between the profiles proposed in the literature and the profiles estimated by our model. In particular, the increase of  $D_z$  within the upper  $\sim 250$  m due to seasonal convective mixing in June (the date corresponds to the same period when measurements were collected: the 27th of June) and December is suitably reproduced.

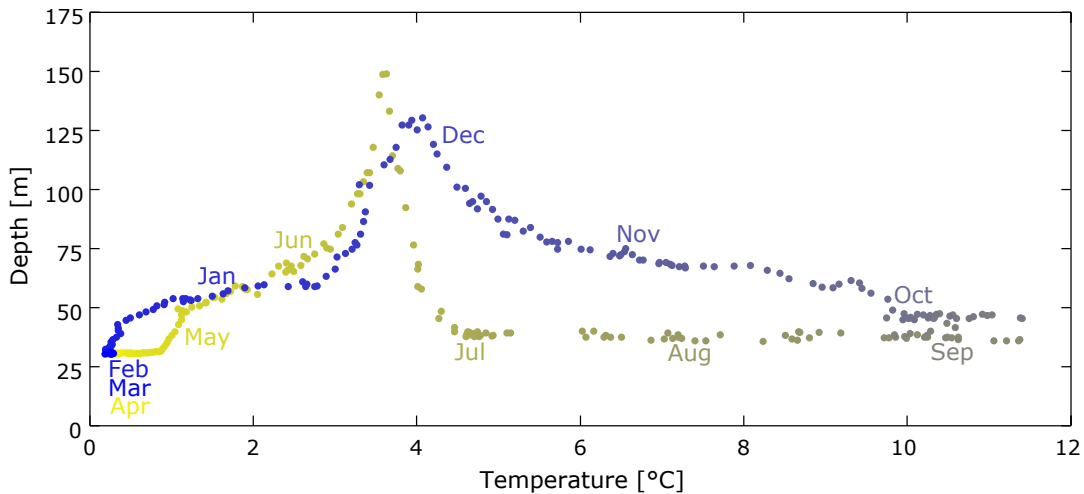


Figure 6.22: Annual evolution of the thickness of the epilimnion plotted versus surface water temperature. Colors from yellow to blue indicate the progression of time, from April to March.

Finally, in order to complete the analysis of the mixing dynamics of the lake, the annual evolution of the epilimnion is presented in Figure 6.22. The depth of the epilimnion is plotted versus surface water temperature, which provides a measure of the strength of the stratification when compared to the temperature of water beneath the seasonal mixed layer. At this depth ( $\sim 250$  m) water temperature is nearly constant throughout the year (see Figure 6.9 and 6.10) and equal to about  $\sim 3.6^\circ\text{C}$ . It is evident that when surface water temperature approaches this value, stratification weakens and the epilimnion thickens (in June and December). On the contrary, as surface water temperature departs from this reference temperature, stratification becomes progressively stronger and the epilimnion thinner. The overall evolution of the thickness of the epilimnion is clearly shown in Figure 6.22 and follows the same behavior of  $D_z$  illustrated in Figures 6.19 and 6.20 and already discussed above. The thickness of the epilimnion has been defined as the upper portion of the lake

that results unstable according to the stability algorithm formulated in Section 3.2.2.

### 6.2.2 In-depth analysis of deep ventilation

In the attempt to provide an in-depth characterization of deep ventilation occurring in the South Basin of Lake Baikal, the results of the 1 000-year simulation discussed in the previous section are analyzed here. Interesting insights into this phenomenon have been obtained concerning the extent and timing of downwellings and the energetics of the process.

Figure 6.23 shows the timing of deep ventilation throughout the year. Downwelling occurrences have been divided into spring and winter events, depending on the period they occur, and into shallow and deep, depending on the depth they reach. During the analysis that follows in this section, a threshold depth at 1 300 *m* has been considered. Therefore, deep downwellings are considered all those events that sink down towards the last  $\sim 150$  *m* of the water column. During the warm season, deep downwellings are expected to occur between May 23 and June 13, while in winter between December 6 and January 4, which are the periods when the water column approaches a nearly homogeneous temperature, thus the conditions for the occurrence of deep ventilation are the most favorable (see also Chapter 2 and Section 6.2.1). The probability of occurrence of deep downwellings is different in the two seasons, in the warm period being about 87% whereas in winter 78%.

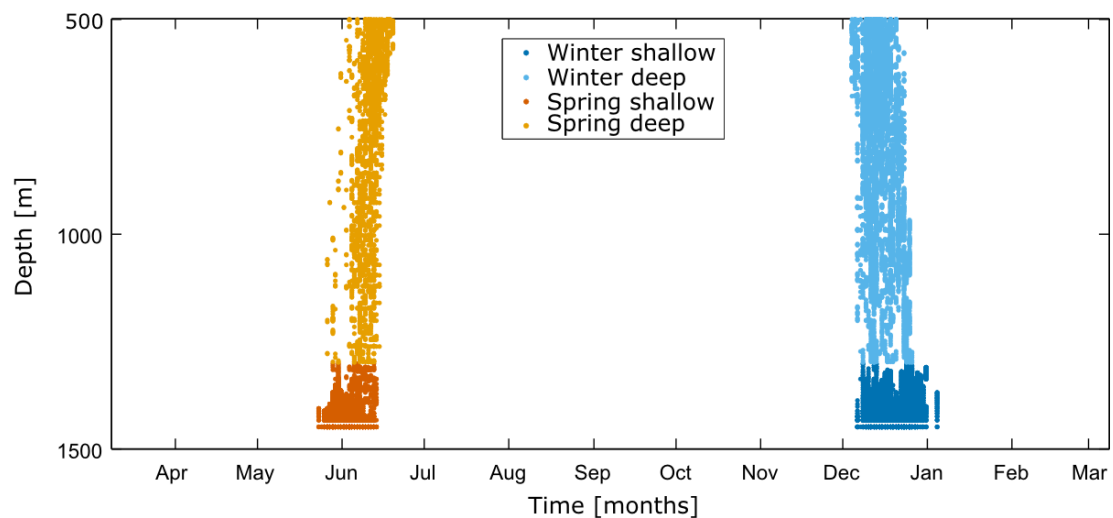


Figure 6.23: Typical timing of deep downwellings throughout the year. The threshold depth chosen to discriminate between shallow and deep downwellings is 1 300 *m*.

The arrival depth corresponding to each downwelling event depends on both the temperature of the sinking volume and the temperature profile of the water column. Based upon these conditions,

## 6. Results: deep ventilation under different climatic conditions

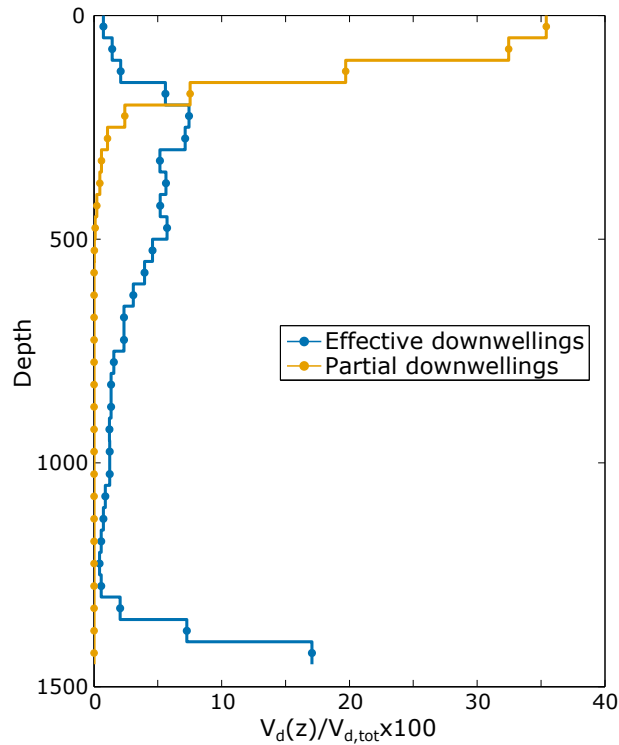


Figure 6.24: Vertical distribution of partial and effective downwellings along the water column. For each vertical layer of the lake (considering a constant thickness of 50 m), the figure indicates the percentage of total downwelling volume that stops there. Dots are centered in each layer.

downwellings can reach either their equilibrium depth (which is defined as the depth where the temperature of the sinking water volume equals the temperature of local water) or the bottom of the lake (see Figure 2.9a,b). It is evident that an estimate of the typical distribution of downwellings along the water column can provide useful information about the vertical fluxes of mass and energy induced by deep ventilation. This vertical distribution is shown in Figure 6.24, both for “effective” and “partial” downwellings. With the term “effective” we indicate the downwellings that reach and overcome the compensation depth, thus effectively give rise to deep ventilation (mechanism shown in Figure 2.9a,b). On the contrary, the term “partial” indicates the cases in which the sinking volume is displaced until a depth shallower than the compensation depth, where it is still buoyant and hence is forced to rise back (see Figure 2.9c). Partial downwellings also include the wind-induced convective instabilities that develop when surface water temperature is warmer than  $T_{p,max}$  (see Figure 2.9d). Note that also in the case of partial downwellings the final position of the generic sinking volume does not necessarily coincide with its initial position, as a consequence of the mixing processes that take place during its vertical displacement (see the definition of  $c'_{mix}$  in

Section 3.2.3).

Concerning effective downwellings, nearly 26% of the total sinking volume reaches depths greater than 1300 m (which motivates the choice of a threshold depth of 1300 m to discriminate between deep and shallow events). The remaining percentage is mainly distributed between 150 and 900 m ( $\sim 63\%$ ), with a peak at about 200 – 250 m that is due to the numerous shallow and relatively warm events that occur as soon as the water column approaches a nearly homogeneous temperature. The downwelling distribution between 150 and 600 m well reflects the typical shape of the temperature profile which is distinctly identifiable in Figure 6.12. Finally, the downwellings that stop within the upper 150 m are those events that occur when the mesothermal maximum and, as a consequence, the compensation depth progressively get shallower, following the  $T_{\rho,max}$  line (see Figure 2.10).

On the other hand, partial downwellings do not reach depths greater than 500 m, and nearly 98% of total events are distributed within the upper 250 m depth, which corresponds to the depth of the seasonal mixing layer. The deepest contributions occur when the temperature profile is nearly vertical and the sinking water is slightly warmer than the temperature of the water column. Under these conditions, only partial downwellings can occur (see Figure 2.9d), which are likely to reach great depths. During their vertical displacement, the downwelling volumes mix with ambient water, until eventually the temperature difference between sinking and local water vanishes, and the convection stops.

The mean annual sinking volume ( $\bar{V}_d$ ) and the mean annual downwelling temperature ( $\bar{T}_d$ ) are the main parameters characterizing the cooling effect of deep ventilation. A proper statistical analysis of these parameters has been allowed thanks to the availability of the long-term series of simulation results. Both model and literature quantitative estimates are given in Table 6.3. The first row shows the mean and the standard deviation values as estimated by the model. Estimates refer to deep downwellings, which, following the definition given above, refer to the events that reach depths greater than 1300 m. Concerning the values available in the literature, downwelling temperatures refer to measurements collected near the bottom of the lake, whereas the estimates of the typical downwelling volumes are not defined with respect to an univocal reference depth, but rather depend on the single events.

For a better comparison between model and literature estimates, Table 6.3 is supplemented with Figure 6.25 which shows the boxplots of  $\bar{V}_d$  and  $\bar{T}_d$  for the whole year, and warm and cold seasons. Evidently, the ranges of variation estimated by the model, both for  $\bar{V}_d$  and  $\bar{T}_d$ , are wider than those suggested in the literature. This is due to the fact that literature estimates (for  $V_d$ ) and measurements (for  $T_d$ ) refer to relatively short observational periods (from a few years to a decade), whereas the statistics proposed here have been carried out over a much longer time horizon (i.e. 1 millennium). During this long simulation period the lake could experience several different

## 6. Results: deep ventilation under different climatic conditions

Table 6.3: Comparison between numerical results (for downwellings beneath 1300 m depth) and literature estimations of the main parameters characterizing deep ventilation in Lake Baikal: mean annual sinking volume,  $\bar{V}_d$ , and typical downwelling temperature,  $\bar{T}_d$ . Estimates from the literature indicate ranges of variation.

	$\bar{V}_d [km^3]$	$\bar{T}_d [^\circ C]$
Present model	91.6 (mean) 73.0 (std)	3.27 (mean) 0.06 (std)
<i>Wüest et al.</i> [2005]	10 ÷ 30	3.15 ÷ 3.27
<i>Schmid et al.</i> [2008]	50 ÷ 100	3.03 ÷ 3.28
<i>Shimaraev et al.</i> [2011a]	1 ÷ 72	-

conditions, thus spanning a wider range of possible downwelling occurrences. Furthermore, in general the downwelling volumes calculated in the literature are probably underestimates, as the effective cooling of deep water is likely to be larger than the observed heat deficit [*Wüest et al.*, 2005; *Schmid et al.*, 2008]. Besides the extreme values and in the light of these considerations, as a whole model results are coherent with the existing measurements, which are however affected by non negligible uncertainties.

Some relevant information concerning the differences between downwelling occurrences in warm and cold seasons can be extracted from Figure 6.25. The most remarkable aspect is the strong dissimilarity between the typical downwelling volumes in the two periods. Indeed, downwellings that occur in the warm season are characterized by significantly smaller volumes compared to those that occur in winter. The entire range of variation of  $\bar{V}_d$  in the first case roughly corresponds to the interquartile range of winter volumes, and the mean value of  $\bar{V}_d$  in spring is approximately one-half of the mean value of  $\bar{V}_d$  in winter. The imbalance in the seasonal distributions of  $\bar{V}_d$  is primarily due to the fact that the strongest winds occur from October to December [*Rzheplinsky and Sorokina*, 1977], and hence, according to Equation (3.17), the volumes of water that can be vertically displaced along the water column are much larger in autumn/winter than in spring. Analogously, according to Equation (3.16), also the specific (i.e. per unit volume) energy input at the lake surface is proportional to the wind speed. Therefore, the amount of wind energy available to trigger deep ventilation is higher from October to December than in spring. Notwithstanding, looking at Figure 6.25b, colder downwellings are likely to occur during the warm season, when available wind energy is lower. This may seem contradictory, as in principle the colder are downwellings, the deeper is the compensation depth,  $h_c$ , and thus the larger is the amount of wind energy input required to overcome the potential energy barrier. The relationship between downwelling temperature,  $T_d$ , and the energy per unit volume required to reach the compensation depth,  $e_c$ , is illustrated in Figure 6.26. As expected, the figure confirms an inverse proportion between  $T_d$  and  $e_c$  (which is well fitted by an exponential curve), but also reveals that for a given value of  $T_d$  the associated  $e_c$  is significantly lower in spring than in winter.



## 6. Results: deep ventilation under different climatic conditions

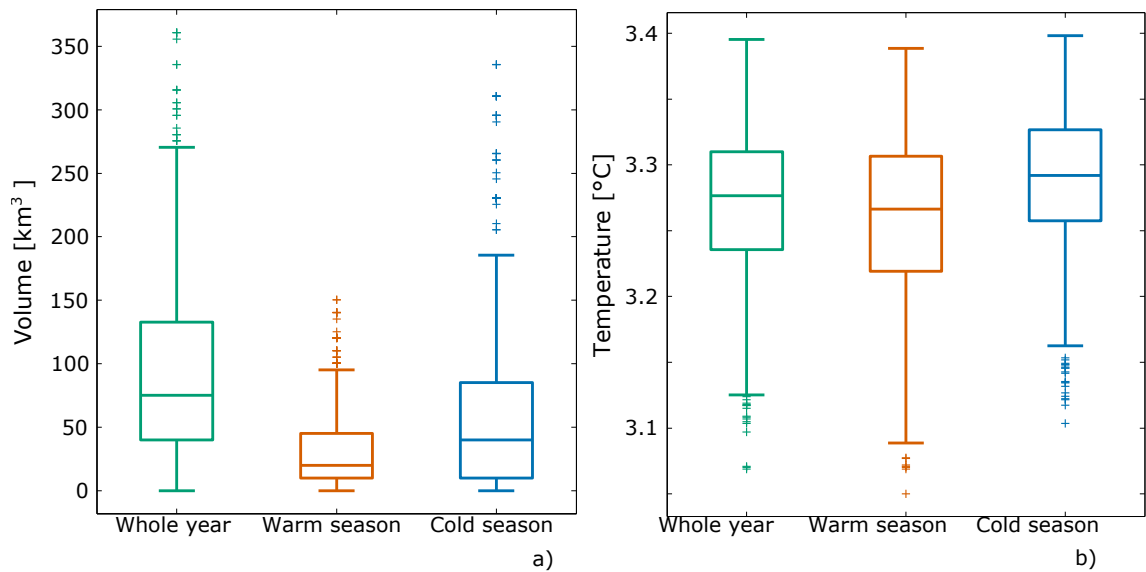


Figure 6.25: Boxplots of a) mean annual sinking volume,  $\bar{V}_d$ , and b) the mean annual downwelling temperature,  $\bar{T}_d$ , for the whole year, and warm and cold seasons. The central mark is the median, the edges of the box are the 25<sup>th</sup> and 75<sup>th</sup> percentiles, the whiskers are placed at 1.5 interquartile range, signs indicate the outliers. Statistics refer to deep downwellings: beneath 1300 m depth.

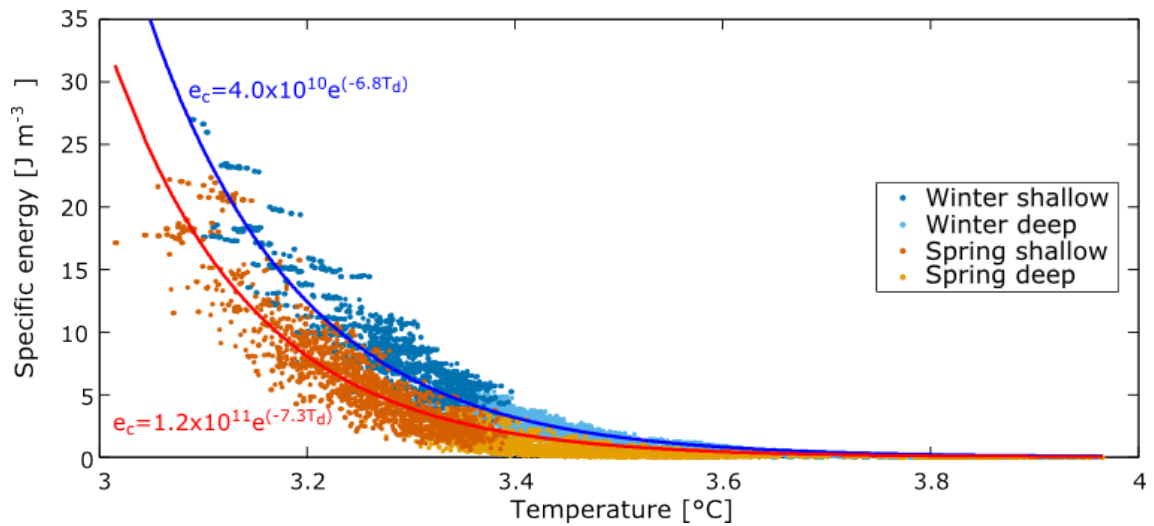


Figure 6.26: Relationship between downwelling temperature ( $T_d$ ) and the energy per unit volume required to reach the compensation depth ( $e_c$ ). Curves are shown for downwellings events occurring during warm and cold season, and for deep and shallow events. Exponential best fitting curves are also shown.

## 6. Results: deep ventilation under different climatic conditions

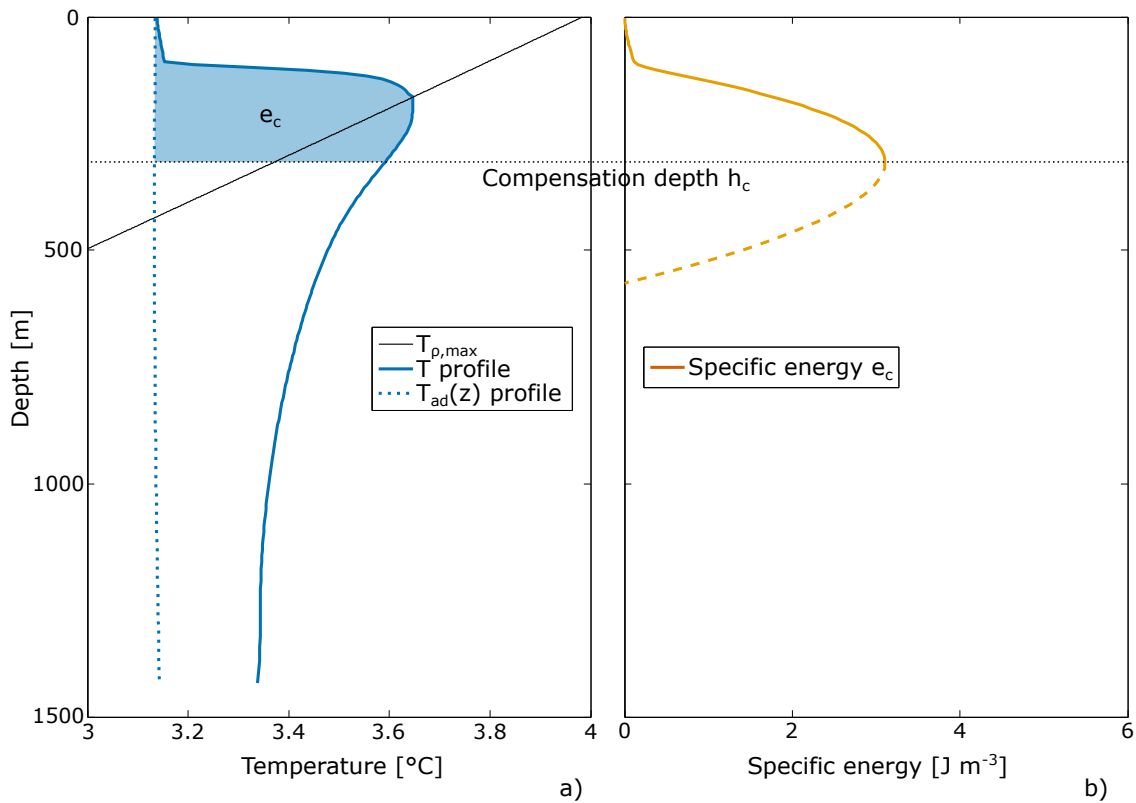


Figure 6.27: Relationship between temperature profile and the energy per unit volume required to move surface water to the compensation depth: warm season. a) simulated temperature profile on May 25, 1992, and b) energy per unit volume  $e_c$ .

The reason for the existence of a marked seasonality of  $e_c$  stems from the typical thermal structure of the upper part of the lake, which is inherently different during the two periods of the year. Figures 6.27 and 6.28 show the simulated temperature profiles on May 25, 1992 and December 17, 1992, respectively, when surface water temperature is roughly the same in the two cases ( $\sim 3.14^\circ\text{C}$ ). The right side of each figure shows the energy per unit volume,  $e_c$ , that the uppermost parcel of water would require to reach the compensation depth.  $e_c$  has been calculated using Equation (3.11), and graphically corresponds to the area between the temperature profile and the adiabatic path which lies above the compensation depth,  $h_c$  (light blue area in the figures). Besides in both cases  $h_c$  approximately correspond to  $\sim 310$  m (since surface water temperature is the same and temperature profile in the lake's interior does not change significantly throughout the year), in winter  $e_c$  is about the double compared to the warm season. This remarkable difference is essentially due to two main reasons: 1) during the cold season, the upper part of the lake is strongly stratified, whereas a thick well-mixed layer develops in spring, and 2) the mesothermal maximum is warmer and more pronounced in winter than in spring. Both these features contribute

## 6. Results: deep ventilation under different climatic conditions

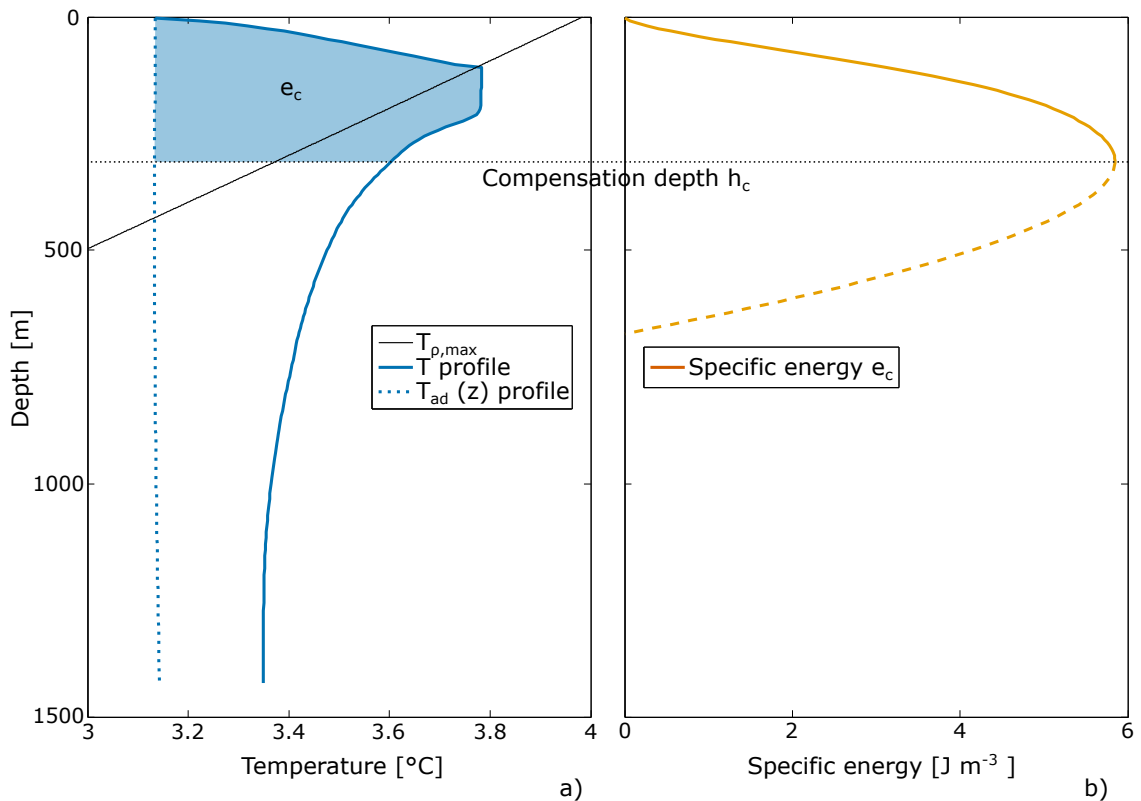


Figure 6.28: Relationship between temperature profile and the energy per unit volume required to move surface water to the compensation depth: cold season. a) simulated temperature profile on December 17, 1992, and b) energy per unit volume  $e_c$ .

to a substantial increase of  $e_c$  in winter (for a visual assessment, compare the light blue areas plotted in the figures). As a side remark, note that a direct comparison between information contained in Figures 6.27 and 6.28 and Figure 6.26 is not possible since in the first case temperature refer to surface water, whereas in the second case to downwelling temperature,  $T_d$ .

In conclusion, combining the information contained in Figures 6.25 and 6.26, and in the light of the results shown in Figures 6.27 and 6.28, the following remarks can be pointed out: 1) in winter, strong winds allow for the sinking of large volumes of water, which however are characterized by (slightly) warmer temperatures than in the warm season since the potential energy barrier is higher; 2) during the warm season, the lower energy required to trigger deep ventilation overcompensates the relatively smaller amount of available wind energy, thus permitting the occurrence of colder downwellings, which anyway are characterized by small volumes.

These considerations also clarify the results presented in Figure 6.14: the cooling of deep water which results from deep ventilation is more pronounced in winter than in spring, as a consequence of the larger sinking volumes that are likely to reach the bottom of the lake in this period of the year.

Note that since the major differences between spring and winter downwellings concerns  $V_d$ , any possible effect due to the seasonal variability of  $T_d$  assumes secondary importance. Furthermore, these results are coherent with the fact that downwellings have been mainly observed in winter time [e.g. *Wüest et al.*, 2005; *Schmid et al.*, 2008; *Shimaraev et al.*, 2011a,b], indeed, thanks to their large extent, these events are likely to be more easily detectable if only few permanent measuring stations are installed in the lake.

### 6.3 Climate change projections

In this section, the mixing and thermal dynamics of the South Basin of Lake Baikal are investigated under the different climate scenarios provided by the CNRM-CM5 dataset, which have been described in Chapter 5. For each future scenario, a 1000-year simulation has been performed, which consists of two parts. The first part covers the period for which CNRM-CM5 climate projections are available, thus it runs from 1982 to 2091 (i.e. from  $y_0$  to  $y_2$ , following the notation introduced in Section 5.2.2). During this period, the progressive evolution of the external forcing has been included according to the procedures discussed in Section 5.2.2 for wind speed and surface water temperature. Successively, the external conditions achieved at the end of the first part of the simulation (i.e. in  $y_2$ ) have been kept unchanged till the end of the run. For comparison purposes, an additional 1000-year simulation has been carried out, in which present conditions have been kept unchanged (hereafter referred to as null scenario or null simulation) during the entire simulation period.

In order to properly compare the results obtained for the different scenarios, the boundary conditions associated to each simulation have been constructed on the basis of the same sequence of weather events, which has been obtained by sampling (with replacement) from the re-analysis dataset (see Section 5.2.2 for further details). In this way, any differences in the results are entirely imputable to the dissimilarities between the climate scenarios, and not to the use of different chronological series of forcing conditions. Furthermore, note that the only difference between the null simulation introduced here and the long term run analyzed in Section 6.2 is about the chronological sequence of weather events, while the results provided by the two simulations are statistically the same.

In the following sections, the possible impact of climate change on lake dynamics is assessed by comparing numerical results obtained under present and future climate conditions. For the sake of a fair comparison between the different simulations, the profiles of water temperature (Figure 6.29) and dissolved oxygen (Figure 6.30), as well as the parameters listed in Table 6.4, have been obtained by averaging numerical results over the second part of each run ( $\sim 900$  years). These averaged values are representative of the ideal stationary state that would occur if the projected

climate conditions would remain unchanged after 2091, and provides a significant description of the impact that each scenario is expected to have on the lake. All figures presented here have been plotted following the color and style coding in Table 5.4.

### 6.3.1 Vertical profiles

Figure 6.29 shows the temperature profiles in winter (Figure 6.29a) and late summer (Figure 6.29b). Concerning the upper part of the temperature profile, all the scenarios agree in forecasting a general increase of temperature within the seasonal well mixed surface layer (upper 250 m), accordingly to the estimated rising of surface water temperature shown in Figure 5.12. As far as the deep water temperature is concerned, different behavior can be observed depending on each scenario. The RCP2.6 and RCP4.5 scenarios do not show any strong variation from current conditions (null scenario), although an opposite trend is expected: the first scenario being characterized by a slight increase of temperatures, while the second by a modest cooling. In particular, deep water temperature beneath 500 m is expected to increase by approximately  $0.10^{\circ}\text{C}$  in the first case, and to decrease by about  $0.06^{\circ}\text{C}$  in the second case, on average. On the contrary, for the RCP8.5 scenario the results show a general trend toward an evident decrease of deep water temperature, up to approximately  $0.33^{\circ}\text{C}$ , calculated as average beneath 500 m. Moreover, the mesothermal maximum is expected to deepen, thus modifying significantly the temperature profile, and consequently the amount of energy required to trigger deep ventilation (as discussed in the concluding part of Section 6.2.2).

Concerning dissolved oxygen concentration, the mean annual profiles shown in Figure 6.30 are characterized by a clear decrease of *DO* within the upper part of the lake. This behavior is common to all scenarios, and it is a direct consequence of the expected rise of water temperature at the surface. As a matter of fact, *DO* concentration within the uppermost layer of the lake is strongly affected by the exchanges between air and water, which, in turn, are primarily controlled by temperature. We recall that the upper boundary condition for *DO* in the model is the saturation concentration, which, according to Equation (5.1), is inversely proportional to temperature. As for the case of temperature profiles shown in figure 6.29, the dissolved oxygen profiles expected for the RCP2.6 and RCP4.5 scenarios do not depart significantly from present conditions. The typical shape that characterizes the current *DO* profile does not undergo marked modifications, and the mean *DO* concentration beneath 500 m is not expected to change much in these two scenarios compared to the present value of about  $10.70\text{mgO}_2\text{l}^{-1}$ . On the contrary, major changes can be observed for the RCP8.5 scenario, which predicts a stronger oxygenation of the hypolimnion compared to current conditions. A considerable increase of *DO* along the entire water column is evident, except than in the upper layer as already mentioned. In particular, the mean *DO* concentration beneath 500 m is expected to rise from the present value of  $10.70\text{mgO}_2\text{l}^{-1}$  to  $11.67\text{mgO}_2\text{l}^{-1}$ . At a first

## 6. Results: deep ventilation under different climatic conditions

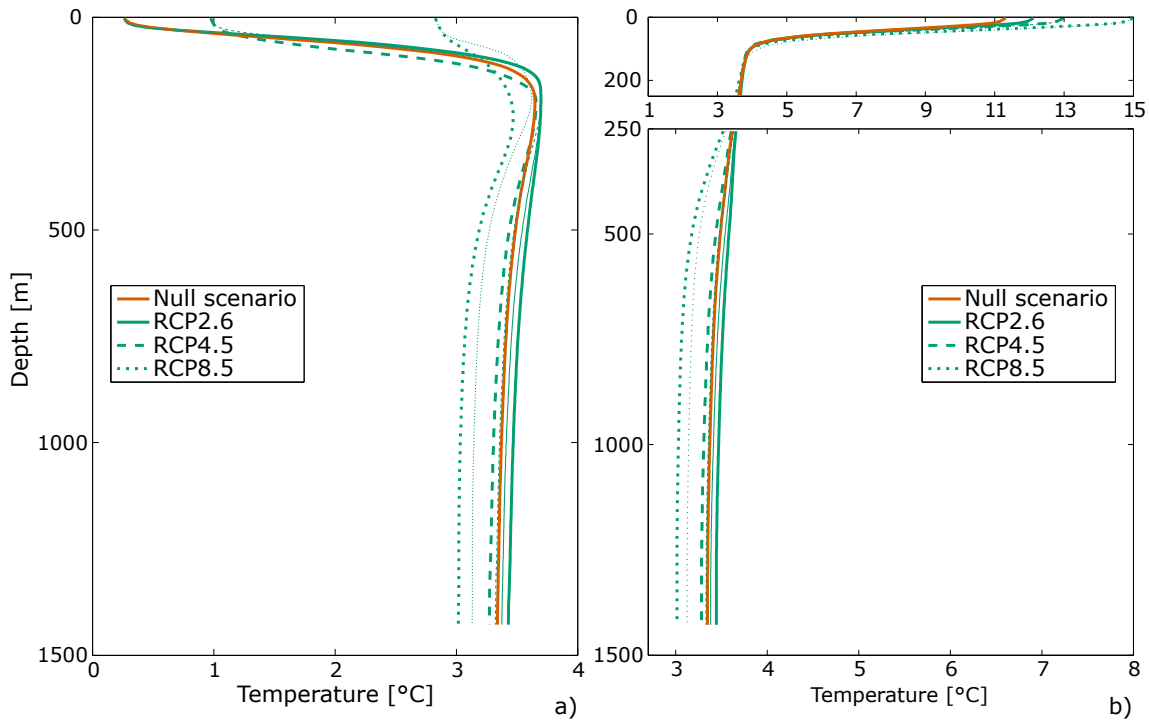


Figure 6.29: Comparison between temperature profiles simulated under the different climate scenarios (different line types) and current conditions (null scenario): a) winter period (28 February), and b) summer period (15 September). Thinner lines refer to climate scenarios where the correction (5.10) associated to  $\Delta q$  has not been considered, thus neglecting the temporal shifts in the distribution of wind events.

glance, the *DO* concentration profile simulated for the RCP8.5 scenario may seem anomalous, as concentrations are higher at the bottom than at the surface. The reasons for this apparent anomaly are elucidated in the following, and stem from the fact that the figure shows annually averaged simulated profiles. The occurrence of strong downwelling events during cold periods (when *DO* concentration at the surface is high) tends to accumulate large volumes of oxygenated water along the water column and in the deep layers. The intensity of the downwellings is sufficient to balance deep water oxygen depletion, thus the hypolimnion is constantly, highly oxygenated throughout the whole year. On the contrary, at the surface *DO* concentration varies according to the annual cycle of temperature, which is expected to be considerably warmer under this scenario. This explains the significant reduction of the mean annual *DO* concentration within the upper layers of the lake.

For the sake of completeness, it is opportune to clarify that the vertical profile of oxygen depletion rate has been kept unchanged for all scenarios and throughout the entire simulation period, and assumed equal to present conditions (see Figure 3.5). This assumption is likely to be unrealistic, since a significant rise of surface temperature would probably lead to a stimulation of primary

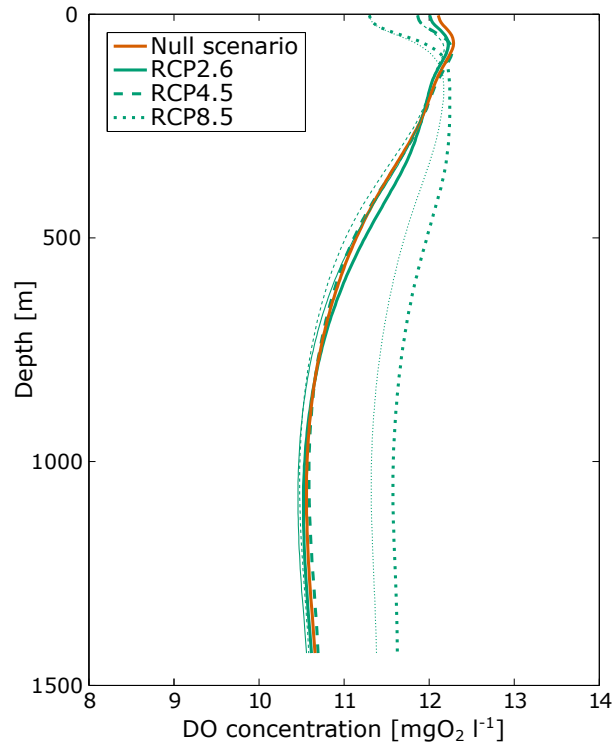


Figure 6.30: Comparison between mean annual dissolved oxygen profiles simulated under the different climate scenarios (different line types) and current conditions (null scenario). Thinner lines refer to climate scenarios where the correction (5.10) associated to  $\Delta q$  has not been considered, thus neglecting the temporal shifts in the distribution of wind events.

production [Adrian *et al.*, 2009], thus to the consequent modification of the oxygen consumption rates along the water column. However, an accurate representation of these dynamics would require the development of a suitable sub-model for the biogeochemical processes, which goes beyond the scope of this work. For this reason, *DO* profiles shown in Figure 6.30 can be used to get only a first approximation estimate of the impact of future climate modifications on *DO* concentrations in deep water. Nevertheless, these results provide useful information to assess the general evolution of the vertical exchanges between epilimnion and hypolimnion. In particular, the increase of *DO* concentrations in deep water that is expected for the RCP8.5 scenario suggests an enhancement of downward fluxes following an increase of deep ventilation activity. This hypothesis is confirmed in the next section, where the main characteristics of deep downwellings are compared for the different cases.

### 6.3.2 Downwelling characterization

In order to characterize the impact of climate change on deep ventilation, the mean annual sinking volume,  $\bar{V}_d$ , and the typical downwelling temperature,  $\bar{T}_d$ , have been calculated for each scenario, and compared to present conditions. The values of these parameters are given in Table 6.4, together with the dates and the corresponding duration of downwelling periods. Note that for current conditions the slight difference between these values and those reported in Table 6.3 is essentially due to the different chronological series of meteorological forcing used to construct the boundary conditions. Notwithstanding, as already discussed at the beginning of Section 6.3, differences are negligible, and results are statistically equivalent.

Concerning the RCP2.6 scenario, the cooling and oxygenation of deep water resulting from deep convection mixing are expected to slightly decrease compared to current conditions. These tendencies are evident in Figures 6.29 and 6.30, and are due to the slight decrease of the typical downwelling volume,  $\bar{V}_d$ , and the contemporaneous increase in downwelling temperatures,  $\bar{T}_d$  (see Table 6.4). Concerning the RCP4.5 scenario,  $\bar{V}_d$  will increase slightly and  $\bar{T}_d$  is expected to undergo a mild cooling, determining the corresponding decrease of temperature within the hypolimnion that can be seen in Figure 6.29. The major changes are expected in the case of the RCP8.5 scenario, for which deep ventilation is expected to increase significantly: downwelling volumes will be much larger (with an increase of approximately 60%) and colder ( $\bar{T}_d$  will diminish by approximately 9%) compared to current estimates. These changes in the downwelling characteristics are at the basis of the evident modifications of both temperature and dissolved oxygen profiles shown in Figures 6.29 and 6.30.



Table 6.4: Main parameters characterizing deep ventilation the different scenarios and current conditions. Values refer to deep downwellings (i.e. beneath 1300m). Values refer to the second part of each simulation (~ 900 years).

	$\bar{V}_d [km^3]$				$\bar{T}_d [^{\circ}C]$				Warm period				Cold period			
	Mean	Std	Mean	Std	Start	End	Duration [d]	Start	End	Duration [d]	Start	End	Duration [d]	Start	End	Duration [d]
Current conditions	92.3	73.2	3.27	0.05	23 May	13 Jun	22	6 Dec	4 Jan	30						
RCP2.6	85.4	60.5	3.35	0.06	22 May	13 Jun	23	9 Dec	12 Jan	35						
RCP4.5	98.1	74.8	3.21	0.05	16 May	8 Jun	24	26 Dec	24 Jan	30						
RCP8.5	147.3	99.5	2.99	0.03	22 Feb	14 Apr	53	-	-	-						

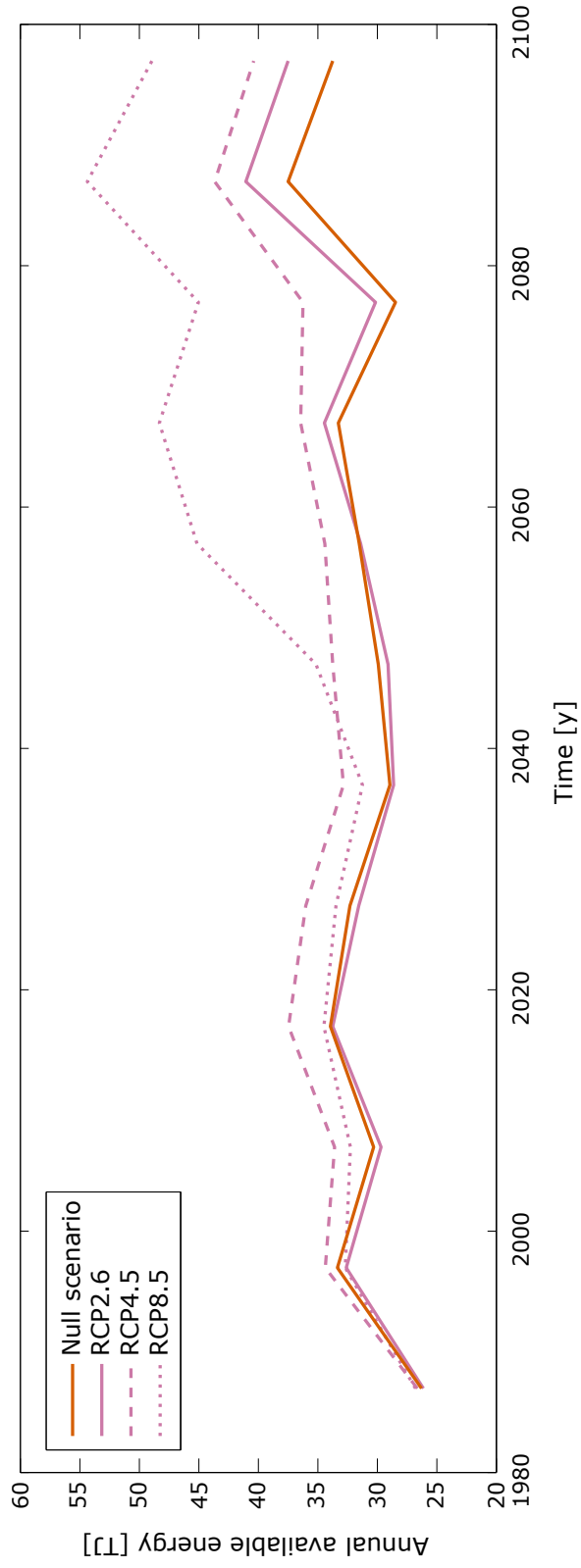


Figure 6.31: Evolution of the annual cumulative energy input provided by the wind, during the 21<sup>st</sup> century. For a better comparison values have been averaged over one decade.

## 6. Results: deep ventilation under different climatic conditions

---

The comparison between the values of  $\bar{V}_d$  and  $\bar{T}_d$  obtained for the different scenarios provides an adequate quantification of the impact of climate change on deep ventilation. Notwithstanding, it does not provide any information about the causes of such modifications, and also does not explain the role played in the future by the major external factors that are involved in the process: wind action and the annual cycle of surface water temperature. We recall here that wind represents the primary source of energy input for deep ventilation. Furthermore, wind driven circulations influence the vertical stratification within the upper part of the lake, thus possibly affecting the amount of energy that is necessary to trigger deep ventilation. On the other hand, the annual cycle of surface water temperature plays a fundamental role in regulating the seasonal evolution of the surface well-mixed layer and the timing of deep ventilation. Indeed, the seasonality and duration of the downwelling periods depend on when and how long surface water temperature varies within a certain range of values, whose boundaries depend on the specific conditions of the overall system, namely: the available energy (i.e. wind action) and the potential energy barrier (i.e. thermal structure). In turn, the thermal structure of the lake's interior is controlled by deep ventilation, thus giving rise to the existence of complex feedback loops between the intrinsic properties of the lacustrine system (i.e. thermal structure, diapycnal diffusivity profile) and the internal lake dynamics (i.e. deep convective mixing, seasonal evolution of the surface well-mixed layer). In conclusion, under given climate conditions, the equilibrium state of the lake is determined and maintained by the interaction between numerous physical processes, which are primarily controlled by the external forcing (see Figure 6.32 for a schematic). It is therefore evident that possible modifications in the climate conditions could alter the existing equilibrium of the system, affecting the overall processes of transport (of momentum, energy and mass) and mixing in the lake [Piccolroaz and Toffolon, 2012b]. Changes on the typical cycle of surface temperature can yield, for example, to the shortening or prolongation of deep downwelling periods, depending on whether the rates of surface water warming/cooling are expected to hasten or slow down, respectively (note that warm and cold season do not necessarily have to follow the same tendency). Furthermore, since generally winds follow seasonal patterns, a significant shift in time of downwelling periods may modify the amount of wind energy available for deep ventilation. In the following, we analyze the expected changes on wind action and annual surface water temperature cycle, in the attempt to evaluate their possible effects on deep ventilation.

**Wind energy** - Figure 6.31 shows the evolution of the available wind energy input to the lake during the 21<sup>st</sup> century, which corresponds to the period covered by the CNRM-CM5 future projections. The curves represent the trend of the cumulative annual energy provided by the wind, which have been calculated as the sum of the product between Equations (3.18 and (3.19) over each year. Values have been averaged over a period of one decade for easier comparison between

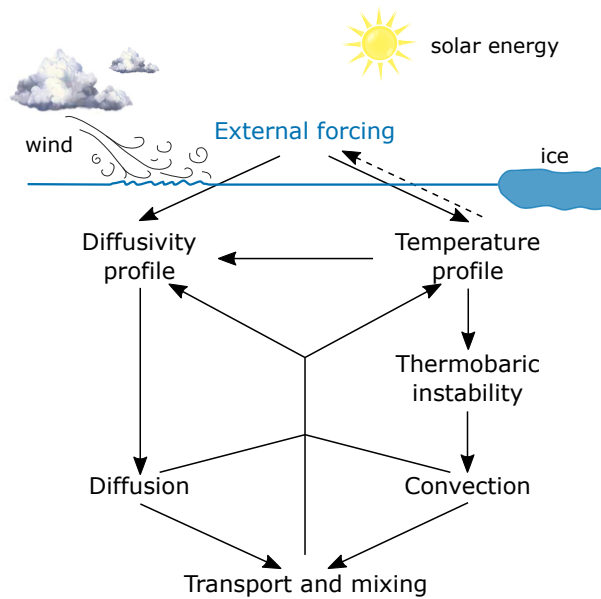


Figure 6.32: Schematic representation of the main physical processes and their interactions controlling transport and mixing in the lake.

the different scenarios. Concerning the RCP2.6 scenario, during the whole first part of the 21<sup>st</sup> century the total wind energy input at the lake surface roughly corresponds to that available under current conditions, whereas it will progressively increase towards the end of the century. During the stationary part of the simulation (i.e. after 2100) such increase is estimated at  $\sim 11\%$ . The RCP4.5 scenario is characterized by a well distributed increase of wind energy over the whole century, up to  $\sim 19\%$  during the stationary part of the simulation. Even greater changes are expected for the RCP8.5, for which the increase of wind energy input is estimated at  $\sim 52\%$  (for the stationary part of the simulation). In this case, the major changes will occur during the second part of the 21<sup>st</sup> century, whereas, before, wind energy availability is expected to undergo only a slight increase.

**Deep ventilation timing -** In order to characterize the future modifications on the timing of deep ventilation, the seasonality of downwelling periods and the corresponding duration have been calculated for each scenario and for current conditions. On the basis of the values listed in Table 6.4, the total annual duration of the downwelling period does not change significantly between the various climate conditions. In all cases the overall duration of the periods favorable for the occurrence of deep ventilation is equal to about 50 days, thus the effect that the future increase of temperatures has on deep water renewal seems to be limited. Notwithstanding, marked differences can be observed concerning the typical downwelling seasons. As a consequence of the general increase of temperature that is projected under the future climate scenarios, spring and winter

downwellings are expected to occur earlier and later, respectively. In the case of RCP2.6 and RCP4.5 scenarios, this time shift is more marked for the winter downwellings, and especially in the latter scenario. Concerning the RCP8.5 scenario, as a consequence of the considerable increase of surface water temperature, the seasonality of deep ventilation is expected to undergo an evident modification: a single, long downwelling period between February and April, instead of two distinct periods in late spring/early summer and late autumn/early winter.

In the light of the results discussed above, wind speed seems to be the main meteorological variable influencing future modifications on deep water renewal. On the contrary changes on surface water temperature seem to play a secondary role, which anyway are not relative to a shortening/lengthening of the downwelling periods, but rather to their seasonality.

As a final comment, note the RCP8.5 is the only scenario in which the lake is expected to not freeze during the cold season. Indeed, the annual cycle of surface water temperature shown in Figure 5.12 is always warmer than the threshold temperature for ice formation, which, according to temperature measurements and ice cover observations, has been conveniently assumed equal to 1°C (see Section 5.1.1 for further details). This threshold value has been kept unchanged for all the climate change scenarios, due to the lack of information about the future dynamics of ice formation and melting. This choice is fully justified for the RCP2.6 and RCP4.5 scenarios, which are characterized by a slight increase of surface water temperature. On the contrary, in principle it represents a stronger assumption for the RCP8.5 scenario. In this regard, we would like to stress that the RCP8.5 scenario represents an extreme case of climate change, which should be confirmed once more data are available to characterize current conditions, and hence to set up a robust downscaling of future climate projections. Notwithstanding, thanks to its peculiarities, this scenario represents an interesting case study that is worthwhile to investigate with the purpose to deeply understand deep ventilation and its dependence on climate conditions.

### **6.3.3 Effect of wind intensity and seasonality**

In the previous Section, future changes in wind forcing have been found to play the primary role in affecting the energy balance that controls deep water renewal. Indeed, all future projections agree in estimating a negligible modification of the duration of downwelling periods and an increase of the mean annual wind energy input at the lake surface (see Figure 6.31). In general, modifications in wind conditions can concern both wind intensity and the seasonality distribution of the events, and these changes jointly contribute to the overall impact on deep ventilation. In the following, each of the two factors are investigated separately, in the attempt to quantify their relative influence to the overall impact on the lake.

For this purpose, an additional 1 000-year simulation has been performed for each scenario, in

which the expected variations on wind annual distribution have been neglected, while retaining the changes in wind intensity. These “halfway” scenarios have been obtained by simply modifying the downscaling procedure formulated in Section 5.2.2, neglecting the correction associated to wind seasonality (i.e. by imposing  $\Delta q = 0$ , in Equation (5.10)). Results for temperature and dissolved oxygen are shown in Figures 6.29 and 6.30 (thin lines), together with the corresponding results obtained under the full scenarios (thick lines) and already discussed in Section 6.3.1. A first estimate of the relative importance of the two effects (namely, changes in wind speed compared to changes in wind seasonality) can be assessed by comparing thick and thin profiles to null scenario profile. For a given scenario, the closer is the thin line to the null scenario profile, the more relevant are future changes in wind seasonality compared to future changes in wind speed; whereas, on the contrary, the closer is the thin line to the corresponding thick line, the higher is the importance of future modifications in wind intensity compared to future changes in the annual wind distribution.

By analyzing Figures 6.29 and 6.30 on the basis of these considerations, we can conclude that in the case of the RCP2.6 and RCP4.5 scenarios the expected changes in wind seasonality are likely to provide the greatest contribution to the overall impact on the lake. On the contrary, the future evolution of wind intensity is predominant under the RCP8.5 scenario. These different tendencies have been interpreted according to Figure 6.33, which shows the change function of wind intensity,  $r$ , and the quantile correction,  $\Delta q$ , relative to the second period ( $p = 2$ , 2081-2101) of each scenario (see Section 5.2.2 for the definitions of  $r$  and  $\Delta q$ , and for more details). In the case of RCP2.6 and RCP4.5 scenarios the changes in wind intensity are milder ( $r$  close to unity) if compared to the RCP8.5 scenario. On the other hand, under the third scenarios, wind intensity is expected to increase significantly, especially during the cold season (Figure 6.33c) and for the strongest winds in the warm period (Figure 6.33b). In particular, this latter effect is the primary cause of the future increase of deep ventilation activity discussed in the previous section, as downwellings are expected to occur during the warm season (from the end of February to mid April, see Table 6.4). Concerning  $\Delta q$ , as a consequence of the seasonal redistribution of wind events, stronger winds (associated to positive values of  $\Delta q$ ) are expected to concentrate during the future downwelling periods (see Table 6.4) to the detriment of the remaining part of the year. The only exception is for the warm downwelling period in the RCP2.6 scenario. As a side remark, note that the discontinuities of  $\Delta q$  in Figure 6.33a are only due to the distinction between summer and winter CDFs of wind speed, and do not affect the chronological series of wind events that, on the contrary, preserve a continuous structure.

## 6. Results: deep ventilation under different climatic conditions

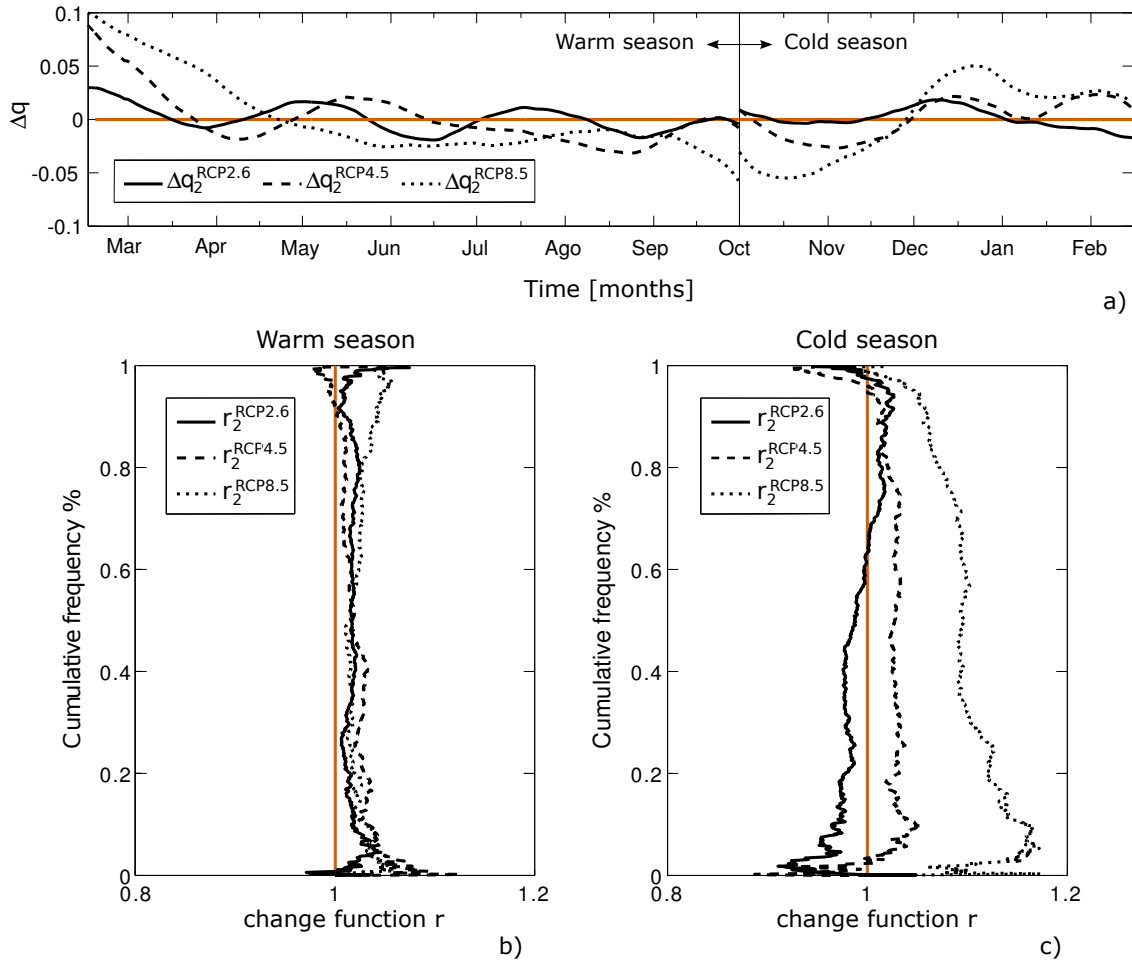


Figure 6.33: Correction functions associated to the different scenarios: a) quantile correction for wind seasonality,  $\Delta q$ ; (b,c) wind intensity change factor  $r$  in summer b) and in winter c).

## 6.4 Concluding remarks

In this chapter the simplified 1D model presented in Chapter 3 has been applied to investigate deep ventilation in the South Basin of Lake Baikal.

The model has been calibrated performing a medium-term simulation over a 40-year period ranging from 1958 to 1998, which is fully covered by the re-analysis dataset described in Chapter 5. The calibration procedure has been primarily focused on the reproduction of the seasonality of thermal stratification and on the historical (from 1988 to 1996) evolution of *CFC-12* concentrations along the water column. Numerical results showed a remarkable agreement with measurements, confirming the general suitability of the model to properly simulate the main processes that take

place in the lake. Due to the considerable lack of long-term series of data, a full validation of the model was not possible. For this reason, a 1 000-year simulation has been performed under current climate conditions, which allowed for a statistical description of the main physical features of the lake (e.g. thermal regime, diffusivity profiles, seasonal patterns, timing and characteristics of deep ventilation). A good correlation between numerical results and available literature estimates and observation has been obtained, which served as an indirect validation of the model. Finally, a sensitivity analysis has been carried out aimed at testing the robustness of the calibration and the role played by each parameter of the model. Results showed that a proper calibration has been performed and further confirmed the suitability and robustness of the fundamental algorithms at the basis of the model.

A considerable portion of the chapter has been devoted to the description and analysis of the lake under current climate conditions. The entire analysis has been based on the results of the 1 000-year simulation in which present external conditions have been kept unchanged. Seasonal dynamics and deep convective mixing have been examined in detail, providing valuable insights into the major physical processes that occur in the lake. An in-depth characterization of deep ventilation has been presented, which mainly concerns: timing, typical volumes and temperatures, energy balance and vertical distribution of downwelling occurrences. In particular, deep downwellings have been estimated to have a mean annual sinking volume of  $91.6 \pm 73.0 \text{ km}^3$  and a mean annual temperature of  $3.27 \pm 0.06 \text{ }^\circ\text{C}$ . The general agreement between our estimates and those available in the literature is reasonable, although the significant degree of uncertainty concerning the latter estimates makes the comparison not straightforward. Furthermore, numerical results allowed for a comprehensive description of the thermal and mixing regime of the lake, and for the assessment of the effects of deep ventilation on the whole system.

In the last part of the chapter, the model has been applied to assess the consequences of climate change on deep water renewal, and, in general, on the overall conditions of the lake. For this purpose, three different climate change scenarios have been considered for the 21<sup>st</sup> century (RCP2.6, RCP4.5 and RCP8.5). The numerical results obtained for the different scenarios gave significant information about the future evolution of the lacustrine system. The main changes are expected for the RCP8.5 scenario, for which the results suggest an evident enhancement of deep water renewal, characterized by larger and colder downwelling volumes. As a consequence of the increased downward transport, the hypolimnion will become colder and the dissolved oxygen concentration will increase along the entire water column, except than in the epilimnion where it is reduced as a consequence of the warming of surface water due to climate change. On the other hand, the RCP2.6 and RCP4.5 scenarios are likely to have a minor impact, essentially due to the milder changes in the meteorological forcing. In all cases, the major impact on deep ventilation is expected from modifications of the wind forcing, including both wind speed and seasonality. The variations of

## 6. Results: deep ventilation under different climatic conditions

---

surface water temperature have been found to contribute to a smaller extent, although they are expected to play a crucial role in defining the periods of the year during which downwelling events are likely to occur. In this regard, results support previous speculations [*Schmid et al.*, 2008]. Besides the direct consequences induced by the meteorological forcing, complex interactions exist between external factors and internal properties of the limnic system, which may potentially have significant effects on the overall lake dynamics. Some preliminary evidence of these feedback loops was found, although this aspect deserves further investigation. Finally, results concerning dissolved oxygen concentrations may be affected by the lack of estimates about the modification of oxygen consumption rate, but they provide an appropriate quantification of the exchange fluxes along the water column.



## 7 Conclusions and future developments

In this work, a simplified, one-dimensional numerical model has been developed to investigate the phenomenon of deep ventilation in profound lakes. The model takes into account the main physical factors controlling deep ventilation (e.g. thermobaric instability) and the major dynamics that influence the transport and mixing processes along the water column. Besides the mutual interactions between these processes are complex, the computational structure of the model has been deliberately kept simple. For this purpose, most efforts have been spent in the design and definition of appropriate algorithms and parameterizations with the aim to develop a robust numerical tool, while retaining significant computational simplicity.

The most significant physical processes and their inter-relations are suitably reproduced by the three key modules that constitute the model: 1) a standard algorithm for the diffusion of temperature and other tracers along the vertical, 2) a sorting algorithm to handle the re-arrangement of unstable vertical regions, and 3) an original algorithm for the simulation of deep ventilation triggered by thermobaric instability. In the attempt to properly simulate the convective mixing processes, the last two algorithms have been developed following a Lagrangian scheme.

Furthermore, the effects of seasonal and interannual climate variability are self consistently taken into account, not only assuming evolving external forcing but also coherently adapting the internal properties of the lake. For this purpose, a novel and expeditious dynamical procedure has been developed with the purpose of reconstructing the diapycnal diffusivity profile at every computational time step. At the same time, suitable parameterizations and closure relationships have been formulated, as for example for the evaluation of the wind energy input and the estimation of the downwelling volumes.

The final result is the simplified but comprehensive numerical tool described in Chapter 3, which is found to effectively simulate the numerous physical processes occurring in deep lakes (e.g. deep ventilation, buoyancy-driven convection, wind-induced mixing, turbulent diffusion, surface well-mixed layer evolution), capturing their mutual interactions and relative contributions to the overall lake dynamics. Thanks to its simple structure, the model is suitable to perform long-term simulations (i.e. from decades to centuries) with significantly low computational efforts (e.g. a 1000-year simulation with a half day time step and adopting Intel(R) Xeon(R) CPU X5680 @

3.33GHz takes about 9 h; the code is implemented in Matlab).

The model has been used to investigate deep ventilation in the South Basin of Lake Baikal (Southern Siberia), where deep water renewal has been widely observed. Notwithstanding, owing to the large extension of Lake Baikal and the fact it is located in a remote region, long-term measurements are extremely scarce (especially as regards wind forcing). In order to deal with this problem, the model has been developed to require only few input data. For this reason, for example, since a reasonable amount of surface water temperature measurements were available (courtesy of A. Wüest and his research team), the temperature itself has been prescribed as upper boundary condition instead of determining the net heat exchange between the lake and the atmosphere. This choice offered the key advantage to avoid the uncertainties in the estimation of the heat budget at the surface, which are likely to be relevant in all those cases where the available data are scarce and hence significant hypotheses and simplifications are introduced. In conclusion, the only information the model requires to impose the upper boundary conditions concerns surface water temperature and wind action.

The main parameters of the model (the coefficients  $\xi$  and  $\eta$  required for the estimates of energy input and downwelling volume respectively, the reference diffusivity profile  $D_{z,r}$ , and the mixing coefficients  $c_{mix}$  and  $c'_{mix}$ ) have been calibrated by performing a 40-year simulation over a historical period (i.e. from 1958 to 1998), and comparing numerical results with the available measurements. Due to its high chemical stability and its widespread application as a tracer to analyze deep ventilation in oceans and lakes, *CFC-12* has been chosen, together with temperature, as the main tracer for model calibration. In particular, the calibration process focused on adequately simulating the seasonality of the thermal structure of the lake, and on reproducing the past evolution of *CFC-12* concentrations along the water column (data are available between 1988 and 1996). Therefore, since the aim is to simulate specific historical conditions actually occurred in the past, the boundary conditions (i.e. wind speed and surface water temperature) have been suitably reconstructed on the basis of re-analysis data covering the period of interest (ECMWF ERA-40 data, available from 1958 to 2002, for the lake region). For this purpose, a well-known quantile-mapping downscaling approach has been implemented to transform coarse-resolution data to a finer scale.

In general, a very good agreement has been obtained between measurements and simulation results. The calibration of the model has been tested performing a long-term simulation (i.e. 1000 years) in which present meteorological forcing has been kept unchanged and initial conditions have been arbitrary chosen, and verifying the achievement of an asymptotic equilibrium of the system. After an adjustment phase depending on the initial profiles ( $\sim 150$  years), numerical results have been found to match the actual observed conditions, verifying that model's algorithms properly describe the fundamental processes. In addition, a sensitivity analysis has been carried out on the

main calibration parameters, confirming a proper calibration and corroborating the suitability and robustness of the core algorithms.

Numerical results based on the calibrated model allowed for a detailed description of the seasonal thermal and mixing dynamics of the lake: typical thermal structure, timing and strength of stratification, deep convective mixing, evolution of the surface mixing layer, seasonality of the diapycnal diffusivity profile. Concerning the chemical properties of the lake, the annual evolution of dissolved oxygen concentration along the water column has been successfully simulated. In this regard, a vertical profile of oxygen consumption rate has been evaluated for the entire water column, as a result of the calibration procedure and accounting for previous estimates available in the literature. The overall good performance of the model further confirmed the effectiveness and consistency of the core algorithms in simulating deep convective mixing and the main physical processes that take place within the lacustrine system.

Furthermore, the analysis of results led to an in detail description of the lake dynamics and deep water renewal. The outcomes of this analysis provided valuable insights that clarify the complex interactions between external forcing and deep ventilation, yielding to a deeper understanding and exhaustive quantification of the phenomenon. As a matter of fact, although deep ventilation in the South Basin of Lake Baikal has been widely observed and studied, still significant uncertainties exist about its proper characterization, in particular concerning the estimate of downwelling volumes. In this regard, the model, once calibrated, represents a valuable alternative tool for the assessment of deep downwellings, which overcomes the limitations of temporal and vertical resolution of measurements that, on the contrary, are at the basis of the non negligible uncertainties that affect the existing estimates. Deep downwellings have been estimated to have a mean annual sinking volume of  $91.6 \pm 73.0 \text{ km}^3$  and a mean annual temperature of  $3.27 \pm 0.06 \text{ }^\circ\text{C}$ . Typical downwelling temperatures are in accordance with available observations, and the overall agreement between our downwelling volume estimates and those available in the literature is reasonable. However, in the latter case a proper comparison is not straightforward since values in the literature are characterized by significant discrepancies between different authors.

Other interesting features of deep ventilation have been investigated, as for example: the vertical distribution of sinking volumes, the timing of deep ventilation and the energy balance between wind energy input and the potential energy barrier. Concerning this last aspect, some interesting insights have been raised about the role that the seasonal evolution of thermal conditions of the lake (e.g. thickness of the surface well-mixed layer, strength of the thermal stratification, depth of the mesothermal maximum) play on the occurrence of deep water renewal.

Besides the study of lake dynamics under present conditions, three different climate change scenarios associated with widely accepted projections of greenhouse gases emissions (provided

## 7. Conclusions and future developments

---

by the Intergovernmental Panel on Climate Change - IPCC) have been investigated. All future scenarios (namely, RCP2.6, RCP4.5 and RCP8.5) are based on the numerical outputs provided by the General Circulation Model (GCM) CNRM-CM5, and consist of future projections of wind speed and air temperature for the 21<sup>th</sup> century.

In order to properly define the boundary conditions associated to each scenario, the information provided by the GCM outputs has been preliminary downscaled from their coarse spatial resolution to a more suitable lake scale resolution. Furthermore, since GCM outputs do not provide a reliable chronological series of meteorological events, in performing the downscaling procedures re-analysis data, which provide a realistic temporal sequence of events, have been combined with CNRM-CM5 data, which give the information about the expected evolution of climate. Two different statistical downscaling procedures have been adopted for wind speed and surface water temperature, respectively. Concerning wind speed, a novel downscaling procedure has been developed on the basis of the quantile-mapping approach (used for the downscaling under current climate conditions). The procedure accounts for potential modifications in both intensity and seasonality of wind speed, thus resulting suitable to be applied to climate change studies. As regards water temperature, the downscaling procedure has been designed to contemporaneously move from global to local scale and convert air temperature (provided by the GCM) into surface water temperature (required by the deep ventilation model). In order to estimate future changes in surface water temperature of the lake, a simple, physically-based model has been developed, which is able to estimate the epilimnetic temperature on the basis of air temperature only. The model has been previously tested on Lake Superior, for which long-term series of air and water temperature measurements are available. Results suggested that this simple model is suitable to capture the thermal hysteresis between air and water temperatures, and to effectively reproduce interannual variations. In general, the model could represent a valuable tool in climate change impact studies allowing for predictions of future trends of lake surface water temperature, given future projections of air temperature only.

The analysis of the results obtained under the different scenarios allowed for a quantitative assessment of the impacts of climate change on deep water renewal and the general characterization of Lake Baikal (say, temperature and dissolved oxygen vertical profiles) under different climatic conditions. Results suggest that the major impact on deep ventilation is expected from modifications of the wind forcing, which can concern both wind intensity and seasonality. On the contrary, the variations of surface water temperature are expected to contribute to a smaller extent, although they are crucial in defining the periods of the year during which deep downwellings are likely to occur. In this regard, results are in accordance with previous speculations. Concerning the RCP2.6 and RCP4.5 scenarios, future changes in climate are not expected to have a strong impact on deep ventilation and the overall lake dynamics, essentially because of the relatively small variations of meteorological forcing. A significantly larger impact has been estimated under the RCP8.5

scenario, due to the considerable increase of wind intensity. Under this scenario, the cooling and oxygenation effects of deep ventilation are expected to increase as a result of larger and colder downwelling volumes.

The major limitation of this work was the scarcity of long-term series of data. Besides the deep ventilation model has been developed to deal with a limited amount of information (mainly concerning the upper boundary conditions), the lack of long-term series of measurements did not allowed for a direct validation of the model and for its application to investigate in detail the past evolution of the lake. Furthermore, the contemporaneous availability of air temperature and contextual surface water temperature for the same, sufficiently long, time period (say, at list a couple of years) would have permitted a more robust calibration of the temperature conversion model described in Chapter 4. As a consequence, this would have allowed us to produce more reliable future projections especially under severe future climate change scenarios, as is the case of the RCP8.5. In this regard, we would like to stress that the RCP8.5 scenario represents an extreme case of climate change, which should be confirmed once more data are available to characterize current conditions. Notwithstanding, thanks to its peculiarities, this scenario offered an interesting case study, which provided useful guidelines for a better understanding of deep ventilation and its dependence on climate conditions.

Further research is expected to explore the coupling of physical and biological processes (e.g. plankton dynamics), in order to assess the role of deep convective mixing in affecting the lake ecosystem. For this purpose, future work should be focused on the development of *ad hoc* sub-modules to simulate the cycling of nutrients and the vertical distribution of biological and chemical constituents. These improvements should be able to take into account the possible influence of climate change, in order to allow for a robust characterization of the biogeochemistry of the whole lake under different climate conditions.

Moreover, further research is needed to better understand the complex network of interactions between the numerous physical processes that take place in the lake, possibly highlighting their dependence on the external forcing. Some preliminary evidence about the existence of important feedback loops has been found, and additional work could provide valuable insights into the response of the lacustrine system to climate change.

Finally, in the light of the main results, the simplified, one-dimensional model presented here could be an appropriate tool to investigate the convective dynamics in the other very deep lakes in the world (e.g. Lake Tanganyika, Crater Lake) and possibly also in some deep alpine lakes (e.g. Lake Tahoe, Lake Como, Lake Geneva, Lake Garda).

## 7. Conclusions and future developments

---

# Acknowledgements

I deeply thank my supervisor Dr. Marco Toffolon for his invaluable guidance during these three years. I warmly thank him for the precious advice and support, for the useful discussions and ideas, and for the friendship. Thank you for having introduced me to the stimulating world of scientific research.

I would like to extend sincere thanks to the research group headed by Prof. Alfred Wüest at EAWAG (Kastanienbaum - Switzerland) for the stimulating discussions about Lake Baikal, for providing the fundamental water temperature data used in this work and for the kind hospitality during a research period I spent at the Departments of Surface Waters - Research and Management, EAWAG. Many thanks for having hosted me in the village of Horw, along the shores of the calming Vierwaldstättersee. In particular, Prof. Alfred Wüest, Dr. Martin Schmid and Chrysanthi Tsimitri are gratefully acknowledged.

Special thanks to Prof. Bernard Laval and Prof. Geoffrey Shladow for the precious comments and suggestions they gave me during these years, which I found very helpful for my research.

I wish to thank Dr. Samuel Somot and Dr. Clotilde Dubois at the CNRM, Mètèo-France (Toulouse - France) for providing re-analysis and future projection CNRM-CM5 datasets.

I am grateful to the NOAA (National Oceanic and Atmospheric Administration) for providing the air and water temperature data for Lake Superior, which have been used in Chapter 4.

Dr. Bruno Majone is gratefully acknowledged for the fruitful discussions and its contribution to the work presented in Chapter 4.

I would like to thank my friends and colleagues from the Department of Civil, Environmental and Mechanical Engineering of the University of Trento for these three years spent together. In particular, special thanks go to all friends I have shared the office with during these years.

I am deeply grateful to Laura Martuscelli for her precious assistance, support and willingness.

Finally, I also would like to thank Professors Masataka Okabe and Kei Ito for the helpful guideline on how to make colorblind-friendly figures, which I followed for producing all the plots (web link: [jfly.iam.u-tokyo.ac.jp/html/color\\_blind](http://jfly.iam.u-tokyo.ac.jp/html/color_blind)).

## Acknowledgements

---



## Bibliography

- Adrian, R., et al., Lakes as sentinels of climate change, *Limnology and Oceanography*, 54, 2283–2297, 2009.
- Afanasyev, A. N., and V. D. Leksakova, The water balance of lake baikal, in *Hydrology of Lakes*, 109, pp. 170–175, IAHS Publ, 1973.
- Akitomo, N., K. Tanaka, K. Awaji, and T. Imasato, Deep convection in a lake triggered by wind: Two-dimensional numerical experiments with a nonhydrostatic model, *Journal of Oceanography*, 51, 171–185, 1995.
- Arhonditsis, G. B., M. T. Brett, C. L. DeGasperi, and D. E. Schindler, Effects of climatic variability on the thermal properties of Lake Washington, *Limnology and Oceanography*, 49, 256–270, 2004.
- Balkhanov, V. K., Y. B. Bashkuev, and V. B. Khaptanov, Formation of circular rings on the snow-covered ice field of Lake Baikal, *Technical Physics*, 55, 1266–1269, 2010.
- Bennington, V., G. A. McKinley, N. Kimura, and C. H. Wu, General circulation of Lake Superior: Mean, variability, and trends from 1979 to 2006, *115*, 2010.
- Benyahya, L., F. Cassie, A. St-Hilaire, T. B. Ourada, and B. Bobée, A Review of Statistical Water Temperature Models, *Canadian Water Resources Journal*, 32, 179–192, 2007.
- Beven, K. J., A manifesto for the equifinality thesis, *Water Resources Research*, 320, 18–36, 2006.
- Beven, K. J., and A. M. Binley, The future of distributed models: Model calibration and uncertainty prediction, *Hydrological Processes*, 6, 279–288, 1992.
- Bilello, M. A., Method for predicting river and lake ice formation, *Journal of Applied Meteorology*, 3, 38–44, 1964.
- Boehrer, B., and M. Schultze, Stratification of lakes, *Reviews of Geophysics*, 46, 2008.

## Bibliography

---

- Boehrer, B., R. Fukuyama, and K. Chikita, Stratification of very deep, thermally stratified lakes, *Geophysical Research Letters*, 35, 2008.
- Bolton, D., The Computation of Equivalent Potential Temperature, *Monthly Weather Review*, 108, 1046–1053, 1980.
- Bonalumi, M., F. S. Anselmetti, A. Wüest, and M. Schmid, Modeling of temperature and turbidity in a natural lake and a reservoir connected by pumped-storage operations, *Water Resources Research*, 48, 2012.
- Bondarenko, N. A., A. Tuji, and M. Nakanishi, A comparison of phytoplankton communities between the ancient Lakes Biwa and Baikal, *Hydrobiologia*, 568, 25–29, 2006.
- Botte, V., and A. Kay, A model of the wind-driven circulation in Lake Baikal, *Dynamics of Atmospheres and Oceans*, 35, 131–152, 2002.
- Bradbury, J. P., Y. V. Bezrukova, G. R. Chernyaeva, S. M. Colman, G. Khursevich, J. W. King, and Y. V. Likoshway, A synthesis of post-glacial diatom records from Lake Baikal, *Journal of Paleolimnology*, 10, 213–252, 1994.
- Brunello, A. J., V. C. Molotov, B. Dugherkhuu, C. Goldman, E. Khamaganova, T. Strijhova, and R. Sigman, Lake Baikal. Experience and Lessons Learned Brief, 2006, (Available at [www.iwlearn.net/iw-projects/1665/experience-notes-and-lessons-learned/lakebaikal\\_2005.pdf/view](http://www.iwlearn.net/iw-projects/1665/experience-notes-and-lessons-learned/lakebaikal_2005.pdf/view)).
- Chen, C. T., and F. J. Millero, The use and misuse of pure water PVT properties for lake waters, *Nature*, 266, 707–708, 1977.
- Chen, C. T., and F. J. Millero, Precise thermodynamic properties for natural-waters covering only the limnological range, *Limnology and Oceanography*, 31, 657–662, 1986.
- Chen, J., B. P. Brisette, and R. Leconte, Uncertainty of downscaling method in quantifying the impact of climate change on hydrology, *Journal of Hydrology*, 401, 190–202, 2011.
- Crawford, G. B., and R. W. Collier, Observations of a deep-mixing event in Crater Lake, Oregon, *Limnology and Oceanography*, 42, 299–306, 1997.
- Crisp, D. T., and G. Howson, Effect of Air Temperature upon Mean Water Temperature in Streams in the North Pennines and English Lake District, *Freshwater Biology*, 12, 359–367, 1982.
- Deardorff, J. W., Empirical Dependence of the Eddy Coefficient for Heat upon Stability Above the Lowest 50 m, *Journal of Applied Meteorology*, 6, 631–643, 1967.

- Diaz-Nieto, J., and R. L. Wilby, A comparison of statistical downscaling and climate change factor methods: impacts on low flows in the River Thames, United Kingdom, *Climatic Change*, 69, 245–268, 2005.
- Dorofeeva, R. P., and S. V. Lysak, Geothermal profiles of the lithosphere in Central Asia, *Tectonophysics*, 164, 165–173, 1989.
- England, M. H., *Encyclopedia of Ocean Sciences*, chap. Ocean process tracers: tracers and large-scale models, Academic Press, 2001.
- Fang, X., and H. G. Stefan, Long-term lake water temperature and ice cover simulations/measurements, *Cold Regions Science and Technology*, 24, 289–304, 1996.
- Fang, X., and H. G. Stefan, Projections of climate change effects on water temperature characteristics of small lakes in the contiguous U.S., *Climatic Change*, 42, 377–412, 1999.
- Farmer, D. M., and E. Carmack, Wind Mixing and Restratification in a Lake near the Temperature of Maximum Density, *Journal of Physical Oceanography*, 11, 1516–1533, 1981.
- Galaziya, G. I. (Ed.), *Baikal Atlas*, Roskartografiya, Moscow, 1993, (in Russian).
- Garwood, R. W., S. M. Isakari, and P. Gallacher, Thermobaric convection, in *The Role of the Polar Oceans in Shaping the Global Environment*, edited by O. Johannessen, R. Muench, and J. Overland, vol. 85 of *Geophysical Monograph*, pp. 199–209, 1994.
- Gill, A. E., *Atmosphere-ocean dynamics*, Academic Press, 1982.
- Gleckler, P. J., K. E. Taylor, and C. Doutriaux, Performance metrics for climate models, *Journal of Geophysical Research*, 113, D06,104, 2008.
- Golubev, V. A., Geothermal Field and Distribution for Earthquake Source Depths in the Baikal Rift Zone, *Doklady Earth Sciences*, 433, 2010.
- Goudsmit, G. H., H. Burchard, F. Peeters, and A. Wüest, Application of k- $\epsilon$  turbulence models to enclosed basins: The role of internal seiches, *Journal of Geophysical Research: Oceans*, 107, 23–1–23–13, 2002.
- Goyette, S., and M. Perroud, Interfacing a one-dimensional lake model with a single-column atmospheric model: Application to the deep Lake Geneva, Switzerland, *Water Resources and Research*, 48, W04,507, 2012.

## Bibliography

---

- Goyette, S., N. A. McFarlane, and G. M. Flato, Application of the Canadian regional climate model to the Laurentian great lakes region: Implementation of a lake model, *Atmosphere-Ocean*, 38, 481–503, 2000.
- Hampton, S. E., L. R. Izmet'eva, M. V. Moore, S. L. Katz, B. Dennis, and E. A. Silow, Sixty years of environmental change in the world's largest freshwater lake - Lake Baikal, Siberia, *Global Change Biology*, 14, 2008.
- Hay, L. E., R. L. Wilby, and G. H. Leavesley, A comparison of delta change and downscaled GCM scenarios for three mountainous basins in the United States, *Journal Of The American Water Resources Association*, 36, 387–397, 2000.
- Henderson-Sellers, B., A simple formula for vertical eddy diffusion coefficients under conditions of nonneutral stability, *Journal of Geophysical Research*, 87, 5860–5864, 1982.
- Henderson-Sellers, B., Calculating the surface energy balance for lake and reservoir modeling: A review, *Reviews of Geophysics*, 24, 625–649, 1986.
- Hewitson, B. C., and R. G. Crane, Consensus between gcm climate change projections with empirical downscaling: precipitation downscaling over south africa, *International Journal of Climatology*, 26, 1315–1337, 2006.
- Hohmann, R., R. Kipfer, F. Peeters, G. Piepke, D. M. Imboden, and M. N. Shimaraev, Deep-water renewal in Lake Baikal, *Limnology and Oceanography*, 42, 841–855, 1997.
- Hornberger, G. M., K. J. Beven, B. J. Cosby, and D. E. Sappington, Shenandoah watershed study: calibration of a topography-based, variable contributing area hydrological model to a small forested catchment, *Water Resources and Research*, 21, 1841–1850, 1985.
- Hutchinson, D. R., A. J. Golmshtok, L. P. Zonenshain, T. C. Moore, C. A. Scholz, and K. D. Klitgord, Depositional and tectonic framework of the rift basins of Lake Baikal from multichannel seismic data, *Geology*, 20, 589–592, 1992.
- Hutchinson, G. E., and H. Löffler, The thermal classification of lakes, *Proceedings of the National Academy of Sciences of the United States of America*, 42, 84–86, 1956.
- Imboden, D., and A. Wüest, *Physics and Chemistry of Lakes*, chap. 4 Mixing Mechanisms in Lakes, pp. 83–138, Springer-Verlag, 1995.
- IPCC, *Towards New Scenarios for Analysis of Emissions, Climate Change, Impacts, and Response Strategies: IPCC Expert Meeting Report 19-21 September, 2007*, Noordwijkerhout, The Netherlands, IPCC Secretariat, 2008.

- Ivanov, A. Y., Unique phenomena in Lake Baikal, Russia, imaged and studied with SAR and multi-sensor images, *International Journal of Remote Sensing*, 33, 7579–7598, 2012.
- Kashiwaya, K., S. Ochiai, H. Sakai, and T. Kawai, Orbit-related long-term climate cycles revealed in a 12-Myr continental record from Lake Baikal, *Nature*, 410, 71–74, 2001.
- Kettle, H., R. T. N. J. Anderson, and D. M. Livingstone, Empirical modeling of summer lake surface temperatures in southwest Greenland, *Limnology and Oceanography*, 49, 271–282, 2004.
- Khlystov, O. M., et al., Oil in the lake of world heritage, *Doklady Earth Sciences*, 415, 682–685, 2007.
- Killworth, P. D., E. C. Carmack, R. F. Weiss, and R. Matear, Modeling deep-water renewal in Lake Baikal, *Limnology and Oceanography*, 41, 1521–1538, 1996.
- Klerkx, J., M. D. Batist, J. Poort, R. Hus, P. V. Rensbergen, O. Khlystov, and N. Granin, Tectonically controlled methane escape in lake baikal, in *Advances in the Geological Storage of Carbon Dioxide*, edited by S. Lombardi, L. K. Altunina, and S. E. Beaubien, vol. 65 of *Nato Science Series: IV: Earth and Environmental Sciences*, pp. 203–219, Springer Netherlands, 2006.
- Kontorovich, A. E., V. A. Kashirtsev, V. I. Moskvina, L. M. Burshtein, T. I. Zemskaya, E. A. Kostyreva, G. V. Kalmychkov, and O. M. Khlystov, Petroleum potential of Baikal deposits, *Russian Geology and Geophysics*, 48, 1046–1053, 2007.
- Kothandaraman, V., and R. L. Evans, Use of Air-Water Relationships for Predicting Water Temperature, *Tech. rep.*, Illinois State Water Survey, Urbana, 1972, report of Investigation 69.
- Kouraev, A. V., S. V. Semovski, M. N. Shimaraev, N. M. Mognard, B. Legrésy, and B. Rémy, The ice regime of Lake Baikal from historical and satellite data: Relationship to air temperature, dynamical, and other factors, *Limnology and Oceanography*, 52, 1268–1286, 2007a.
- Kouraev, A. V., S. V. Semovski, M. N. Shimaraev, N. M. Mognard, B. Legrésy, and B. Rémy, Observations of Lake Baikal ice from satellite altimetry and radiometry, *Remote Sensing of Environment*, 108, 240–253, 2007b.
- Kullenberg, G., On vertical mixing and the energy transfer from the wind to the water, *Tellus B*, 28, 2011.
- Landau, L. D., and L. M. Lifshitz, *Fluid Mechanics*, Pergamon Press, 1987.
- Large, W. G., J. C. McWilliams, and S. C. Doney, Oceanic vertical mixing: A review and a model with a nonlocal boundary layer parameterization, *Reviews of Geophysics*, 32, 363–403, 1994.

## Bibliography

---

- Lawrence, S. P., K. Hogeboom, and H. L. Le Core, A three-dimensional general circulation model of the surface layers of Lake Baikal, *Hydrobiologia*, 487, 95–110, 2002.
- Lesne, O., W. Calais, and J. Deverchère, Finite element modelling of crustal deformation in the Baikal rift zone: new insights into the active-passive rifting debate, *Tectonophysics*, 289, 327–340, 1998.
- Lewis, W. M., A Revised Classification of Lakes Based on Mixing, *Canadian Journal of Fisheries and Aquatic Sciences*, 40, 1779–1787, 1983.
- Li, H., J. Sheffield, and E. F. Wood, Bias correction of monthly precipitation and temperature fields from Intergovernmental Panel on Climate Change AR4 models using equidistant quantile matching, *Journal of Geophysical Research*, 115, D10,101, 2010.
- Livingstone, D. M., Ice break-up on southern Lake Baikal and its relationship to local and regional air temperatures in Siberia and to the North Atlantic Oscillation, *Limnology and Oceanography*, 44, 1486–149, 1999.
- Livingstone, D. M., and D. M. Imboden, The prediction of hypolimnetic oxygen profiles: a plea for a deductive approach, *Canadian Journal of Fisheries and Aquatic Sciences*, 53, 924–932, 1996.
- Livingstone, D. M., and A. F. Lotter, The relationship between air and water temperatures in lakes of the Swiss Plateau: a case study with palæolimnological implications, *Journal of Paleolimnology*, 19, 181–198, 1998.
- Livingstone, D. M., and J. Padisák, Large-scale coherence in the response of lake surface-water temperatures to synoptic-scale climate forcing during summer, *Limnology and Oceanography*, 52, 896–902, 2007.
- Livingstone, D. M., A. F. Lotter, and R. W. Ian, The Decrease in Summer Surface Water Temperature with Altitude in Swiss Alpine Lakes: A Comparison with Air Temperature Lapse Rates, *Arctic, Antarctic, and Alpine Research*, 31, 341–352, 1999.
- Ljungemyr, P., N. Gustafsson, and A. Omstedt, Parameterization of lake thermodynamics in a high-resolution weather forecasting model, *Tellus A*, 48, 608–621, 1996.
- Lorke, A., F. Peeters, and A. Wüest, Shear-induced convective mixing in bottom boundary layers on slopes, *Limnology and Oceanography*, 50, 1612–1619, 2005.
- Løyning, T. B., and J. Weber, Thermobaric effect on buoyancy-driven convection in cold seawater, *Journal of Geophysical Research*, 1997.

- Lysak, S. V., Terrestrial heat flow in zones of active faults in Southern East Siberia, *Russian Geology and Geophysics*, 43, 791–803, 2002.
- MacKay, M. D., A Process-Oriented Small Lake Scheme for Coupled Climate Modeling Applications, *Journal of Hydrometeorology*, 13, 1911–1924, 2012.
- MacKay, M. D., et al., Modeling lakes and reservoirs in the climate system, *Limnology and oceanography*, 54, 2315–2329, 2009.
- Majone, B., A. Bertagnoli, and A. Bellin, A non-linear runoff generation model in small Alpine catchments, *Journal of Hydrology*, 385, 300–312, 2010.
- Majone, B., C. I. Bovolo, A. Bellin, S. Blenkinsop, and H. J. Fowler, Modeling the impacts of future climate change on water resources for the Gállego river basin (Spain), *Water Resources and Research*, 48, W01,512, 2012.
- Martin, J. L., and S. McCutcheon, *Hydrodynamics and Transport for Water Quality Modeling*, CRC Press, 1998.
- Martin, P., Lake baikal, *Archiv für Hydrobiologie Beiheft Ergebnisse der Limnologie*, 44, 3–11, 1994.
- Martynov, A., L. Sushama, and R. Laprise, Simulation of temperate freezing lakes by one-dimensional lake models: performance assessment for interactive coupling with regional climate models, *Boreal Environment Research*, 15, 143–164, 2010.
- Martynov, A., L. Sushama, R. Laprise, K. Winger, and B. Dugas, Interactive lakes in the Canadian Regional Climate Model, version 5: the role of lakes in the regional climate of North America, *Tellus A*, 64, 2012.
- McCombie, A. M., Some Relations Between Air Temperatures and the Surface Water Temperatures of Lakes, *Limnology and Oceanography*, 4, 252–258, 1959.
- McDougall, T. J., Thermobaricity, Cabbeling, and Water-Mass Conversion, *Journal of Geophysical Research*, 93, 5448–5464, 1987.
- McDougall, T. J., and Y. You, Implications of the nonlinear equation of state for upwelling in the ocean interior, *Journal of Geophysical Research*, 95, 13,263–13,276, 1990.
- Mearns, L. O., I. Bogardi, F. Giorgi, I. Matyasovszky, and M. Palecki, Comparison of climate change scenarios generated from regional climate model experiments and statistical downscaling, *Journal of Geophysical Research*, 104, 6603–6621, 1999.

## Bibliography

---

- Mellor, G. L., Retrospect on oceanic boundary layer modeling and second moment closure, in *The parameterization of Small-Scale Processes*, edited by P. Müller and D. Henderson, pp. 251–272, 1989.
- Minville, M., F. Brissette, and R. Leconte, Uncertainty of the impact of climate change on the hydrology of a nordic watershed, *Journal of Hydrology*, 358, 70–83, 2008.
- Moore, M. V., S. E. Hampton, L. R. Izmet'seva, E. A. Silow, E. V. Peshkova, and B. K. Pavlov, Climate Change and the World's "Sacred Sea" - Lake Baikal, Siberia, *BioScience*, 59, 405–417, 2009.
- Morrill, J. C., R. C. Bales, and M. Conklin, Estimating Stream Temperature from Air Temperature: Implications for Future Water Quality, *Journal of Environmental Engineering*, 131, 139–146, 2005.
- Munk, W. H., and E. R. Anderson, Notes on a theory of the thermocline, *Journal of Marine Research*, 7, 276–295, 1948.
- Nash, J. E., and J. V. Sutcliffe, River flow forecasting through conceptual models 1. A discussion of principles, *Journal of Hydrology*, 10, 282–290, 1970.
- Osborn, T. R., and P. H. LeBlond, Comments on "static stability in freshwater lakes", *Limnology and Oceanography*, 19, 544–545, 1974.
- Pacanowski, R. C., and S. G. Philander, Parameterization of vertical mixing in numerical models of tropical oceans, *Journal of Physical Oceanography*, 11, 1443–1451, 1981.
- Panofsky, H. A., and G. W. Brier, *Some applications of statistics to meteorology*, Earth and Mineral Sciences Continuing Education, College of Earth and Mineral Sciences, 1968.
- Peeters, F., G. Piepke, R. Kipfer, R. Hohmann, and D. M. Imboden, Description of stability and neutrally buoyant transport in freshwater lakes, *Limnology and Oceanography*, 41, 1711–1724, 1996.
- Peeters, F., R. Kipfer, R. Hohmann, M. Hofer, D. M. Imboden, G. G. Kodenev, and T. Khozder, Modeling transport rates in Lake Baikal: Gas exchange and deep water renewal, *Environmental Science & Technology*, 31, 2973–2982, 1997.
- Peeters, F., R. Kipfer, M. Hofer, D. M. Imboden, and V. M. Domysheva, Vertical turbulent diffusion and upwelling in Lake Baikal estimated by inverse modeling of transient tracers, *Journal of Geophysical Research - Oceans*, 105, 14,283, 2000.



- Peeters, F., D. M. Livingstone, G. H. Goudsmit, R. Kipfer, and R. Forster, Modeling 50 years of historical temperature profiles in a large central European lake, *Limnology and Oceanography*, 47, 186–197, 2002.
- Piccolroaz, S., and M. Toffolon, A simplified model for deep water renewal in Lake Baikal, in *XV International Workshop on Physical Processes in Natural Waters: Fluids and Environments*, 2011, Burlington (Ontario, Canada), 11-14 July 2011.
- Piccolroaz, S., and M. Toffolon, A simplified physically-based model to calculate surface water temperature of lakes from air temperature in climate change scenarios, 2012a, American Geophysical Union (AGU) - Fall Meeting, San Francisco (California, USA), 3-7 December 2012.
- Piccolroaz, S., and M. Toffolon, The subtle equilibrium between external forcing, thermobaric instability and turbulent diffusivity in deep lakes, 2012b, ASLO Aquatic Sciences Meeting: Voyages of Discovery, Lake Biwa (Shiga, Japan), 8-13 July 2012.
- Piccolroaz, S., and M. Toffolon, Riuscirà il cambiamento climatico ad alterare la ventilazione profonda nel Lago Baikal? (in Italian), in *XXXIII Convegno Nazionale di Idraulica e Costruzioni Idrauliche*, 2012c, Brescia (Italy), 10-15 September 2012.
- Piccolroaz, S., and M. Toffolon, Deep ventilation in Lake Baikal: A model for long term analyses, 2013, submitted to *Journal of Geophysical Research - Oceans*.
- Piccolroaz, S., M. Toffolon, and B. Majone, A physically-based probabilistic model to convert air temperature into surface water temperature in lakes, 2013a, submitted to *Hydrology and Earth System Sciences*.
- Piccolroaz, S., M. Toffolon, M. C. Sighel, and M. Bresciani, On the impact of climate change on surface water temperature of Lake Garda, 2013b, European Geosciences Union (EGU) - General Assembly, Vienna (Austria), 7-12 April 2013.
- Pitman, A. J., A simple parameterization of sub-grid scale open water for climate models, *Climate Dynamics*, 6, 99–112, 1991.
- Ravens, T. M., O. Kocsis, A. Wüest, and N. Granin, Small-scale turbulence and vertical mixing in Lake Baikal, *Limnology and Oceanography*, 45, 159–173, 2000.
- Rodhe, B., On the Relation between Air Temperature and Ice Formation in the Baltic, *Geografiska Annaler*, 34, 175–202, 1952.

## Bibliography

---

- Rzheplinsky, G. V., and A. I. Sorokina, *Atlas of wave and wind action in Lake Baikal*, Gidrometeoizdat (in Russian), 1977.
- Samuelsson, P., E. Kourzeneva, and D. Mironov, The impact of lakes on the European climate as simulated by a regional climate model, *Boreal Environmental Research*, 15, 113–129, 2010.
- Schmid, M., M. D. Batist, N. G. Granin, V. A. Kapitanov, D. F. McGinnis, I. B. Mizandrontsev, A. I. Obzhirov, and A. Wüest, Sources and sinks of methane in Lake Baikal: A synthesis of measurements and modeling, *Limnology and Oceanography*, 52, 2007.
- Schmid, M., N. M. Budnev, N. G. Granin, M. Sturm, M. Schurter, and A. Wüest, Lake Baikal deepwater renewal mystery solved, *Geophysical Research Letters*, 35, 2008.
- Scholz, C. A., and D. R. Hutchinson, Stratigraphic and structural evolution of the Selenga Delta Accommodation Zone, Lake Baikal Rift, Siberia, *International Journal of Earth Sciences*, 89, 212–228, 2000.
- Scholz, C. A., K. D. Klitgord, D. R. Hutchinson, U. S. ten Brink, L. P. Zonenshain, A. Y. Golmshtok, and T. C. Moore, Results of 1992 seismic reflection experiment in Lake Baikal, *Eos Transactions AGU*, 74, 465, 1993.
- Schwab, B. J., G. A. Leshkevich, and G. C. Muhr, Automated Mapping of Surface Water Temperature in the Great Lakes, *Journal of Great Lakes Research*, 25, 468–481, 1999.
- Sharma, S., S. C. Walker, and D. A. Jackson, Empirical modelling of lake water-temperature relationships: a comparison of approaches, *Freshwater Biology*, 53, 897–911, 2008.
- Sheng, J., and Y. R. Rao, Circulation and thermal structure in Lake Huron and Georgian Bay: Application of a nested-grid hydrodynamic model, *Continental Shelf Research*, 26, 1496–1518, 2006.
- Shimaraev, M. N., and L. N. Starygin, Lake Baikal: zonal atmospheric circulation, climate and hydrological processes (1968-2007), *Geography and Natural Resources*, 31, 245–250, 2010.
- Shimaraev, M. N., V. I. Verbolov, N. G. Granin, and P. P. Sherstyankin, *Physical Limnology of Lake Baikal: A Review*, Baikal International Center for Ecological Research, Irkutsk-Okayama, 1994.
- Shimaraev, M. N., E. S. Troitskaya, V. V. Blinov, V. G. Ivanov, and R. Y. Gnatovskii, Upwellings in Lake Baikal, *Doklady Earth Sciences*, 442, 272–276, 2012.
- Shimaraev, M. N., N. G. Granin, and A. A. Zhdanov, Deep ventilation of Lake Baikal waters due to spring thermal bars, *Limnology and Oceanography*, 38, 1068–1072, 1993.

- Shimaraev, M. N., E. S. Troitskaya, and R. Y. Gnatovskii, Modern Climate Changes and Deep Water Temperature of Lake Baikal, *Doklady Earth Sciences*, 427, 804–808, 2009.
- Shimaraev, M. N., R. Y. Gnatovskii, V. V. Blinov, and V. G. Ivanov, Renewal of Deep Waters of Lake Baikal Revisited, *Doklady Earth Sciences*, 438, 652–655, 2011a.
- Shimaraev, M. N., A. A. Zhdanov, R. Y. Gnatovskii, V. V. Blinov, and V. G. Ivanov, Specific Features of Cold Bottom Intrusion in Baikal According to Observations in 1993-2009, *Water Resources*, 38, 169–174, 2011b.
- Shuter, B. J., D. A. Schlesinger, and A. P. Zimmerman, Empirical Predictors of Annual Surface Water Temperature Cycle in North American Lakes, *Canadian Journal of Fisheries and Aquatic Sciences*, 40, 1838–1845, 1983.
- Stefan, H. G., X. Fang, and M. Hondzo, Simulated climate change effects on year-round water temperatures in temperate zone lakes, *Climatic Change*, 40, 547–576, 1998.
- Sundaram, T. R., and R. G. Rehm, Formation and Maintenance of Thermoclines in Temperate Lakes, *AIAA Journal*, 9, 1322–1329, 1971.
- The INTAS Project 99-1669 Team, A new bathymetric map of Lake Baikal, Open-File Report on CD-Rom, 2002.
- Timoshkin, O. A., Biodiversity of Baikal fauna: state-of-the-art (Preliminary analysis), in *New Scope on the Boreal Ecosystems in East Siberia*, edited by E. Wada, O. A. Timoshkin, N. Fujita, and K. Tanida, pp. 35–76, Siberian Branch, Russian Academy of Sciences, 1997.
- Todd, M. C., and A. W. Mackay, Large-Scale Climatic Controls on Lake Baikal Ice Cover, *Journal of Climate*, 16, 3186–3199, 2003.
- Tsvetova, E. A., Mathematical modelling of Lake Baikal hydrodynamics, *Hydrobiologia*, 407, 37–43, 1999.
- UNESCO, Convention Concerning the Protection of the World Cultural and Natural Heritage: Report from 20th Session, 1996, (Available at [www.whc.unesco.org/archive/repcom96.htm](http://www.whc.unesco.org/archive/repcom96.htm) # 754).
- Venayagamoorthy, S. K., and D. D. Stretch, On the turbulent Prandtl number in homogeneous stably stratified turbulence., *Journal of Fluid Mechanics*, 644, 359–369, 2010.
- Voltaire, A., et al., The CNRM-CM5.1 global climate model: description and basic evaluation, *Climate Dynamics*, pp. 1–31, 2012.

## Bibliography

---

- Watts, S. J., and R. G. Walker, A three-dimensional numerical model of deep ventilation in temperate lakes, *Journal of Geophysical Research*, *100*, 22,711–22,731, 1995.
- Webb, M. S., Surface Temperatures of Lake Erie, *Water Resources Research*, *10*, 199–210, 1974.
- Webb, M. S., P. D. Clack, and D. E. Walling, Water-air temperature relationships in a Devon river system and the role of flow, *Water Resources Research*, *17*, 3069–3084, 2003.
- Weber, J. E., and T. B. Løyning, Thermobaric effect on slantwise convection in cold seawater, *Tellus*, *58*, 385–391, 2006.
- Weiss, R. F., The solubility of nitrogen, oxygen and argon in water and seawater, *Deep Sea Research and Oceanographic Abstracts*, *17*, 721–735, 1970.
- Weiss, R. F., E. C. Carmack, and V. M. Koropalov, Deep-water renewal and biological production in Lake Baikal, *Nature*, *349*, 665–669, 1991.
- Wu, J., Wind-stress coefficients over sea-surface from breeze to hurricane, *Journal of Geophysical Research-Oceans and Atmospheres*, *87*, 9704–9706, 1982.
- Wüest, A., and A. Lorke, Small-scale hydrodynamics in lakes, *Annual Review of Fluid Mechanics*, *35*, 373–412, 2003.
- Wüest, A., G. Piepke, and D. C. V. Senden, Turbulent kinetic energy balance as a tool for estimating vertical diffusivity in wind-forced stratified waters, *Limnology and Oceanography*, *45*, 1388–1400, 2000.
- Wüest, A., T. M. Ravens, N. G. Granin, O. Kocsis, M. Schurter, and M. Sturm, Deep water renewal in Lake Baikal matching turbulent kinetic energy and internal cycling, *Terra Nostra*, *9*, 60–74, 2000.
- Wüest, A., T. M. Ravens, N. G. Granin, O. Kocsis, M. Schurter, and M. Sturm, Cold intrusions in Lake Baikal: Direct observational evidence for deep-water renewal, *Limnology and Oceanography*, *50*, 184–196, 2005.